VIRTUAL INERTIA CONTROL FOR IMPROVING FREQUENCY STABILITY IN HYBRID POWER SYSTEMS USING SPARROW SEARCH ALGORITHM WITH MOUNTAIN GAZELLE OPTIMIZATION

By

BASHAR ABBAS FADHEEL AL-MURSHEDI

Thesis Submitted to the School of Graduate Studies, Universiti Putra Malaysia, in Fulfilment of the Requirements for the Degree of Doctor of Philosophy

September 2024

FK 2024 16

DEDICATION

This thesis is gratefully dedicated to:

My beloved wife for her unwavering support, patience, and understanding throughout this journey, and to my beloved children.

&

To my beloved father, whose memory continues to inspire me, and to my cherished mother, whose love, wisdom, and guidance remain a constant source of strength.

&

To my supportive community, whose encouragement and belief in my abilities have fueled my determination.

Abstract of thesis presented to the Senate of Universiti Putra Malaysia in fulfilment of the requirement for the degree of Doctor of Philosophy

VIRTUAL INERTIA CONTROL FOR IMPROVING FREQUENCY STABILITY IN HYBRID POWER SYSTEMS USING SPARROW SEARCH ALGORITHM WITH MOUNTAIN GAZELLE OPTIMIZATION

By

BASHAR ABBAS FADHEEL AL-MURSHEDI

September 2024

Chairman : Noor Izzri bin Abdul Wahab, Ir, PhD
Faculty : Engineering

The increasing need for energy, coupled with the diminishing availability of fossil fuels, has driven the widespread utilization of Renewable Energy Sources (RESs). These resources are recognized for their eco-friendliness and economic viability and are increasingly integrated into interconnected power systems for widespread use. This development has been primarily facilitated by progress in electricity networks. However, stabilizing the frequency in microgrids is challenging due to the intermittent behavior of RESs. Over-penetration of RESs can lead to challenging frequency oscillations, making system stability harder to maintain. Moreover, integrating RESs into isolated MGs requires power electronic devices, such as static converters, which lack rotational mass and reduce overall system inertia. This thesis aims to enhance the frequency response in a smart multi-microgrid power system integrated with renewable energy sources by utilizing advanced virtual inertia control techniques. At the outset, this study considers a Proportional-Integral-Derivative (PID) controller whose parameters are tuned using a hybrid sparrow search algorithm-grey wolf optimizer (SSAGWO) for a multi-area Load Frequency Control (LFC) problem. Results from the analysis of the multi-area multi-source demonstrate that the proposed SSAGWO-optimized PID controller outperforms other state-of-the-art algorithms presented in the literature, showing improvements of 53%, 60%, 20%, and 70% in terms of settling time, peak undershoot, control effort, and steady-state error values, respectively. Although the results show the proposed approach effectively manages renewable impacts on system stability, combining lower-rated RES with higher-rated conventional generators does not clearly indicate an effect on system inertia. A robust control approach of a Fractional Derivative Virtual Inertia Controller (FDVIC), integrated with a modified demand response controller, has been introduced for an islanded low inertia Multi-Microgrid (MMG) system. Fractional Order Proportional Integral Derivative (FOPID) controllers have been employed to regulate the active power output of the biodiesel generators and the Geothermal station of the proposed Microgrid (MG). Optimal parameters for the three-loop controller were determined using a new hybrid Sparrow Search and Mountain Gazelle Optimizer (SSAMGO). SSAMGO's performance was then evaluated against other optimization algorithms across various scenarios. The results demonstrate that the estimated value of the virtual inertia and virtual damping when using SSAMGO-optimized the proposed controller is less than other optimization techniques. The estimated value of the virtual inertia has a very significant impact on the size of the capacity of the Energy Storage System (ESS) that is used to support the MG power system with instant active power. In other words, the minimum value of the virtual inertia constant means reducing the size of the battery and leading to a reduction in the cost. Furthermore, the achieved outcomes exhibited substantial improvements in terms of settling time, peak undershoot, control effort, and steady-state error values compared to other optimization algorithms.

Moreover, the system's stability is analyzed in the frequency domain through the utilization of Bode analysis. Finally, the validation of the power system is ultimately achieved by utilizing both the New England IEEE-39 bus test system and conducting Real-Time Digital Simulation experiments using the Opal-RT simulator.

Keywords: energy, frequency stability, hybrid optimization algorithm, renewable energy sources, virtual inertia control.

SDG: GOAL 7: Affordable and clean energy, GOAL 11: Sustainable cities and communities, GOAL 13: Climate action.

Abstrak tesis yang dikemukakan kepada Senat Universiti Putra Malaysia sebagai memenuhi keperluan untuk ijazah Doktor Falsafah

KAWALAN INERSIA MAYA UNTUK MENINGKATKAN KESTABILAN FREKUENSI SISTEM KUASA HIBRID MENGGUNAKAN ALGORITMA PENGOPTIMUMAN PENCARIAN PIPIT DENGAN GAZEL GUNUNG

Oleh

BASHAR ABBAS FADHEEL AL-MURSHEDI

September 2024

Pengerusi : Noor Izzri bin Abdul Wahab, Ir, PhD
Fakulti : Kejuruteraan

Keperluan tenaga yang semakin meningkat, bersama dengan pengurangan ketersediaan bahan api fosil, telah mendorong penggunaan meluas Sumber Tenaga Boleh Diperbaharui (RES). Sumber-sumber ini dikenali atas kelebihan mesra alam dan keberkesanan kos, serta semakin banyak diintegrasikan ke dalam sistem kuasa bersambungan untuk penggunaan secara meluas. Perkembangan ini didorong terutamanya oleh kemajuan dalam rangkaian elektrik. Namun, kestabilan frekuensi dalam mikrogrid menghadapi cabaran disebabkan oleh sifat tidak menentu RES. Penembusan RES yang berlebihan boleh menyebabkan ayunan frekuensi yang tidak stabil, yang menyukarkan usaha mengekalkan kestabilan sistem. Tambahan pula, integrasi RES ke dalam MG yang terasing bergantung pada penggunaan peranti elektronik kuasa, termasuk penukar statik. Namun, penukar ini tidak mempunyai jisim putaran, yang menyumbang kepada pengurangan inersia keseluruhan sistem. Tesis ini bertujuan untuk meningkatkan respons frekuensi dalam sistem kuasa mikrogrid pelbagai yang pintar yang diintegrasikan dengan sumber tenaga boleh diperbaharui

melalui penggunaan teknik kawalan inersia maya yang canggih. Pada awalnya, kajian ini mempertimbangkan pengawal Kadar-Integral-Terbitan (PID) yang parameternya ditala menggunakan algoritma hybrid Pengoptimuman Pencarian Pipit - Serigala Kelabu (SSAGWO) untuk masalah Kawalan Frekuensi Beban (LFC) berbilang kawasan. Hasil analisis untuk sumber berbilang kawasan menunjukkan bahawa pengawal PID yang dioptimumkan oleh SSAGWO mengatasi algoritma canggih lain yang dibentangkan dalam literatur, dengan peningkatan 53%, 60%, 20%, dan 70% dalam masa penyelesaian, puncak penurunan, usaha kawalan, dan nilai ralat keadaan mantap, masing-masing. Walaupun hasilnya menunjukkan keberkesanan pendekatan yang dicadangkan dalam menguruskan kesan RES terhadap kestabilan sistem, menggabungkan RES berkadar rendah dengan penjana konvensional berkadar tinggi tidak menunjukkan kesan pada inersia sistem. Pendekatan kawalan yang mantap untuk Pengawal Inersia Maya Pecahan Derivatif (FDVIC), yang digabungkan dengan pengawal tindak balas permintaan yang diubah suai, telah diperkenalkan untuk sistem Mikrogrid Berbilang (MMG) yang berinersia rendah dan terasing. Pengawal Kadar Integral Terbitan Nisbah Pecahan (FOPID) telah digunakan untuk mengawal keluaran kuasa aktif penjana biodiesel dan stesen geoterma pada mikrogrid (MG) yang dicadangkan. Parameter optimum untuk pengawal tiga-gelung ini ditentukan menggunakan algoritma baru hibrid iaitu teknik Pengoptimuman Pencarian Pipit dan Gazel Gunung (SSAMGO). Selain itu, penilaian menyeluruh terhadap prestasi SSAMGO telah dijalankan dengan membandingkannya dengan beberapa algoritma pengoptimuman lain dalam pelbagai senario. Hasil menunjukkan bahawa nilai anggaran inersia maya dan peredaman maya menggunakan SSAMGO adalah lebih rendah berbanding teknik pengoptimuman lain. Nilai anggaran inersia maya mempunyai kesan yang sangat signifikan pada saiz kapasiti Sistem Penyimpanan

Tenaga (ESS) yang digunakan untuk menyokong sistem kuasa MG dengan kuasa aktif serta-merta. Dalam kata lain, nilai minimum pemalar inersia maya bermaksud pengurangan saiz bateri dan membawa kepada pengurangan kos. Tambahan pula, hasil yang dicapai menunjukkan peningkatan yang ketara dalam masa penyelesaian, puncak penurunan, usaha kawalan, dan nilai ralat keadaan mantap berbanding algoritma pengoptimuman lain. Selain itu, kestabilan sistem dianalisis dalam domain frekuensi melalui penggunaan analisis Bode. Akhirnya, pengesahan sistem kuasa dicapai dengan menggunakan sistem ujian New England IEEE-39 bas dan menjalankan eksperimen Simulasi Digital Masa Sebenar menggunakan simulator Opal-RT.

Kata Kunci: tenaga, kestabilan frekuensi, algoritma pengoptimuman hybrid, sumber tenaga boleh diperbaharui, kawalan inersia maya.

SDG: MATLAMAT 7: Tenaga bersih dan berpatutan, MATLAMAT 11: Bandar dan komuniti mampan, MATLAMAT 13: Tindakan memerangi perubahan iklim.

ACKNOWLEDGEMENTS

Firstly, I would like to express my sincere gratitude to my thesis advisor Assoc. Prof. Ir. Dr. Noor Izzri bin Abdul Wahab, for his immense support and supervision throughout my PhD program.

Besides, I would like to express my appreciation for the guidance and coaching of co-supervisors, Prof Dr. Mohd Amran b. Mohd Radzi, Assoc. Prof. Ts. Dr. Azura binti Che Soh, and Prof. Dr. Ali Jafer Mahdi for their profound and carefully aimed comments and suggestions of this study.

I am incredibly grateful to all staff members of Department of Electrical and Electronics Engineering and Faculty of Engineering (Electrical), especially many thanks also extended to my colleagues in the Advanced Lightning Power and Energy Research (ALPER) group for their companionship, helpful insights, and friendly working environment.

I would like to express my gratitude to the Iraqi Ministry of Higher Education and the University of Kerbala for their financial support and for granting me study leave at UPM.

Last but not the least, I would like to thank my family and friends for supporting me spiritually throughout writing this thesis.

This thesis was submitted to the Senate of the Universiti Putra Malaysia and has been accepted as fulfilment of the requirement for the degree of Doctor of Philosophy. The members of the Supervisory Committee were as follows:

Noor Izzri bin Abdul Wahab, PhD
Associate Professor, Ir
Faculty of Engineering
Universiti Putra Malaysia
(Chairman)

Mohd Amran bin Mohd Radzi, PhD
Professor
Faculty of Engineering
Universiti Putra Malaysia
(Member)

Azura binti Che Soh, PhD
Associate Professor, Ts
Faculty of Engineering
Universiti Putra Malaysia
(Member)

Ali Jafer Mahdi, PhD
Professor
College of Information Technology Engineering
Al-Zahraa University for Women
Iraq
(External Member)

ZALILAH MOHD SHARIFF, PhD
Professor and Dean
School of Graduate Studies
Universiti Putra Malaysia

Date: 13 January 2025

TABLE OF CONTENTS

LIST OF TABLES

LIST OF FIGURES

LIST OF ABBREVIATIONS

2D-SLCSCA	2D Sine Logistic map-based chaotic sine cosine algorithm
ACE	Area Control Error
AGC	Automatic Generation Control
AI	Artificial Intelligence
ALFC	Automatic Load Frequency Control
ANN	Artificial Neural Networks
apf	Participation Factor
AVR	Automatic Voltage Regulators
BD	Boiler Dynamics
BES	Battery Energy Storage
BEO	Bald Eagle Optimizer
BS	Best Score
CGO	Chaos Game Optimizer
CIO	Cohort Intelligence Optimizer
CLTF	Close Loop Transfer Function
cpf	Contract Participation Factor
CRPSO	Craziness-based Particle Swarm Optimization
CTO	Class Topper Optimization
D	Damping Coefficient
DCT	Derivative Control Technique
DE	Differential Evolutionary
DERs	Distributed Energy Resources
DFIG	Doubly-Fed Induction Generator
DGs	Distributed generators
DISCOs	Distribution Companies

DGA-BFA	Dynamic Genetic Algorithm and Bacteria Forging Optimizer
DPM	DISCOs Participation Matrix
DR	Demand Response
DRC	Demand Response Controller
ESS	Energy Storage System
ET	Elapsed Time
EVs	Electric vehicles
FDVIC	Fractional Derivative Virtual Inertia Control
FLC	Fuzzy Logic Control
FOPID	Fractional Order Proportional-Integral-Derivative
GA	Genetic Algorithm
GDB	Governor Dead Band
GENCOs	Generation Companies
GRC	Generation Rate Constraint
GWO	Grey Wolf Optimizer
H	Inertia Constant
HIL	Hardware-in-the-Loop
HIO	Hybrid Intelligent Optimization
ICA	Independent Contract Administration
IAE	Integral Absolute Error
ISE	Integral Square Error
ITAE	Integral Time Absolute Error
ITSE	Time Weighted Squared Error
IMC	Internal Model Control
IO	Integer Order
J	Objective Function

JSO	Jellyfish Search Optimizer
LFC	Load Frequency Control
LSPS	Large Scale Power System
MA	Mayfly Algorithm
MFO	Moth Flame Optimization
MGO	Mountain Gazelle Optimizer
MGs	Microgrids
MMG	Multi-Microgrid
MPA	Marine Predator Algorithm
MPC	Model Predictive Controller
MPSOGA	Modified Particle Swarm Optimization and Genetic Algorithm
OS	Overshoot
PFMPID	Predictive Functional Modified Proportional Integral Derivative
PI	Proportional plus Integral
PID	Proportional-Integral-Derivative
PIDA	Proportional-Integral-Derivative-Acceleration
PIs	Performance Indices
P_L	Demand Load
P_m	Mechanical Power
PSO	Particle Swarm Optimization
PSOGSA	Particle Swarm Optimization based on Gravitational Search Algorithm
PSS	Power System Stabilizers
PV	Photo Voltaic
QOSCA	Quasi-Oppositional Sine Cosine Algorithm
R	Droop Gain
RESs	Renewable Energy Resources

RFB	Redox Flow Battery
RoCoF	Rate of Change of Frequency
RT	Rise Time
RTDS	Real-Time Digital Simulator
SG	Synchronous Generator
SMC	Sliding Mode Control
SMES	Superconducting Magnetic Energy Storage
PV	Solar Photovoltaic
SSA	Sparrow Search Algorithm
SSAGWO	A hybrid Sparrow Search Algorithm-Grey Wolf Optimizer
SSAMGO	Hybrid Sparrow Search Algorithm-Mountain Gazelle Optimizer algorithm
SSE	Steady State Error
SSO	Salp Swarm Optimization
ST	Settling Time
STES	Solar Thermal Energy System
STH	Solar Thermal
STPP	Solar Thermal Power Plants
TRANSCOS	Transmission Companies
US	Undershoot
VI	Virtual Inertia
VIC	Virtual Inertia Control
VSG	Virtual Synchronous Generator
WOA	Whale Optimization Algorithm
WT	Wind Turbine
Z-N	Ziegler-Nichols

CHAPTER 1

INTRODUCTION

1.1 Background

The increasing integration of RESs, such as wind turbines, solar systems, and geothermal power, into MGs has posed significant challenges in maintaining system frequency due to their intermittent nature (Murugesan. et al., 2023; Daraz et al., 2022). This integration, whether in grid-connected or islanded modes, often results in precarious frequency oscillations and instability, especially with the over-penetration of RESs (Irudayaraj et al., 2023). Additionally, the use of power electronic devices, such as static converters, in the integration process leads to a reduction in overall system inertia, as these converters lack the rotating mass and damping characteristics of traditional generators (Roy et al., 2022).

To overcome the challenge of reduced inertia in MGs, Virtual Inertia Control (VIC) has emerged as an effective solution by mimicking the dynamic behaviour of synchronous generators without relying on physical rotating mass (Sørensen et al., 2023). VIC, integrated with ESS, delivers fast-active power support, with the static converter's reference power regulated by the rate of change of system frequency (Saxena et al., 2021). Accurate optimization of the virtual inertia and damping coefficients is essential for maintaining system stability.

Furthermore, Demand Response Controller (DRC) techniques have recently gained significant attention for their potential in enhancing grid frequency stability. These techniques have been explored to improve the frequency performance of interconnected hybrid power systems (Hosseini et al., 2022; Saxena & Shankar, 2022).

Automatic Load Frequency Control (ALFC) regulates system frequency by adjusting generation to match load demand, ensuring smooth operation of interconnected power networks. Maintaining nominal system frequency within ±0.2 Hz and scheduled tie-line power exchange requires robust control techniques (Veerasamy et al., 2022). While PID controllers are widely used due to their simplicity and robustness (Boopathi et al., 2023), their performance diminishes under varying conditions. To overcome this, a FOPID controller has been developed, offering improved adaptability and enhanced performance under fluctuating system parameters (Fathy & Alharbi, 2021).

On the other hand, numerous heuristic techniques have been employed to tune controller parameters for LFC in interconnected power systems. However, optimizing controller gain values remains a significant challenge due to uncertainties in power generation and system load. To address these challenges, researchers are increasingly developing Artificial Intelligence (AI) approaches to improve system performance through the optimization of controller gains (Karnavas & Nivolianiti, 2023). Hybrid algorithms, which combine features from multiple algorithms, are gaining popularity for their effectiveness in solving complex optimization problems (Sundararaju et al., 2022).

To enhance the frequency response and minimize variations in tie line power during load disturbances in a low-inertia MG integrated with RESs, a new FDVIC has been developed. This technique is combined with DRC to further improve frequency response and alleviate stress on the ESS during charging and discharging. In the secondary control loop, FOPID controllers are employed to regulate the active power output of conventional generators. The optimal values of these control parameters are determined using a hybrid optimization algorithm proposed in this study, which efficiently identifies the most suitable controller settings.

Ensuring the effectiveness of power system frequency controller techniques prior to implementation is crucial. The IEEE 39-bus New England test system provides a realistic network representation for validation, while the Opal-RT digital simulator enables real-time simulation for high-fidelity modeling, prototype testing, and performance evaluation.

1.2 Problem Statement

With the rising demand for energy and the need to reduce reliance on fossil fuels, RESs are increasingly integrated into electrical power systems as sustainable alternatives (Naderipour et al., 2021). However, their intermittent nature in MGs complicates the stabilization of system frequency. Over-penetration of RESs can lead to significant frequency oscillations, posing challenges to system stability (Irudayaraj et al., 2023). The integration of RESs through power electronic devices, such as static converters, reduces overall system inertia due to the absence of rotating mass (Roy et al., 2022). To mitigate frequency deviations, LFC is employed, often using centralized PID or FOPID control loops in the secondary control layer to enhance stability and minimize tie-line power variations (Latif et al., 2021; Veerasamy et al., 2022). Additionally, VIC provides necessary inertia and damping characteristics, utilizing a derivative technique based on grid frequency (Magdy et al., 2021).

Nevertheless, conventional PID controllers often fail to maintain system performance under varying operating conditions. To overcome this, the FOPID controller has been developed, incorporating fractional terms in the integral and derivative components (Babu & Saikia, 2021). This design provides additional tuning parameters, enhancing flexibility and control (Tepljakov et al., 2021). The FOPID controller effectively reduces frequency deviations and tie-line errors in MG applications, offering significant advantages over conventional controllers due to its unique structure with two extra tuning parameters (Fathy & Alharbi, 2021).

To address the lack of inertia in interconnected power systems integrated with RESs, the VIC technique is a significant solution that mimics the performance of synchronous generators without requiring rotating mass. The reference power for static converters is based on the rate of change of system frequency. VIC is crucial for managing frequency control during system faults, as it helps restore frequency promptly after disturbances (Kerdphol et al., 2018; Nour et al., 2023; Rakhshani et al., 2016). However, the influence of damping coefficients on frequency response has often been overlooked, impacting the duration needed to mitigate oscillations. Addressing this, simulating the effects of virtual damping coefficients is necessary to enhance both transient and steady-state stability (Kerdphol et al., 2019; Kerdphol et al., 2021; Khooban, 2021; Mandal & Chatterjee, 2021). Therefore, it is essential to develop a new VIC technique and approach for estimating the inertia constant based on observed frequency response, explicitly addressing the effects of inertia and damping coefficients, which are critical for the stability of microgrid power systems integrated with RESs.

Furthermore, there has been increasing attention on DRC techniques for frequency control, which are promising for enhancing grid frequency stability (Bharti et al., 2022). Research indicates that incorporating a suitably sized ESS can significantly improve dynamic stability through its active participation in demand response measures (Al-Hinai et al., 2021; Hosseini et al., 2022; Kerdphol et al., 2016). However, these studies often neglect the stress on the ESS during charging and discharging, which can impact its lifespan and overall performance. Thus, a new approach is needed that integrates demand-side and generation-side controls to effectively reduce frequency deviations and enhance power system stability.

On the other hand, obtaining optimal controller parameters in power systems with RESs integration is essential. Traditionally, tuning gain parameters has relied on methods such as Ziegler-Nichols (Z-N), Cohen-Coon, and Åström-Hägglund (Åström & Hägglund, 2001). However, these conventional approaches become inadequate in the presence of substantial uncertainties in load and generation dynamics, which challenge the effectiveness of the Z-N method. Therefore, alternative control strategies must be explored to address these complexities and improve system performance. Heuristic-based stochastic optimization techniques have been implemented to optimize gain parameters in LFC applications (Guha et al., 2016; Guha et al., 2020; Paliwal et al., 2022). While these algorithms offer advantages such as minimal function evaluations and ease of use, they often risk stagnating in local optima, complicating the balance between exploration and exploitation to find the global optimum (Lu et al., 2021). Consequently, it is crucial to investigate the appropriate type and design of controller parameters, as they significantly influence the system's performance and stability.

The previously mentioned problem statements can be summarized as follows:

1. Existing methods for tuning controller parameters in interconnected power systems with RESs are inadequate, especially under the uncertainties and non-linearities introduced by renewable generation, posing challenges for reliable frequency regulation in hybrid power systems.

2. Current control strategies lack effectiveness in regulating frequency for both islanded and grid-connected MMG systems, particularly with high RES integration that reduces system inertia. This emphasizes the need for advanced control that estimates optimal virtual inertia and damping to handle diverse modes and frequency disturbances.

3. Conventional VIC techniques lack integration with demand-side management, essential for reducing stress on ESS, enhancing frequency response, and extending ESS lifespan by minimizing unnecessary active power adjustments.

4. Existing validation approaches for virtual inertia control schemes do not include real-world testing under complex conditions, such as those represented by the IEEE 39-bus New England test system. Real-time simulation is needed to validate practical performance and reliability.

1.3 Objectives

This research aims to develop a virtual inertia controller to enhance frequency stability in MG power systems integrated with RESs. The controller is designed to provide inertia support during disturbances, thereby improving system stability. The objectives are as follows:

1. To propose an intelligent hybrid optimization technique for tuning the controller parameters to regulate the frequency of the hybrid power system integrated with RESs.

2. To develop a fractional virtual inertia controller to enhance frequency regulation in both islanded and grid-connected MMG systems based on an enhanced hybrid optimization technique.

3. To integrate the proposed fractional virtual inertia controller with an improved demand response controller to enhance the frequency response of MMG systems.

4. To validate the proposed virtual inertia control scheme with the IEEE 39-bus New England test system and real-time simulator of the Opal-RT lab.

1.4 Scope of the Study

The scope and limitations of this research work are as follows:

1. While the secondary PID/FOPID controller possesses the ability to control both active and reactive power, the current investigation is constrained to the regulation of the active power alone. This limitation is imposed as the controller primarily influences the frequency component of the system.

2. Despite the intrinsic complexity and uncertainties associated with real-world nonlinear systems, the study adopts linearized small-signal transfer function models for system analysis. The decision to simplify nonlinear and uncertain systems into linear mathematical models serves the purpose of reducing control efforts while maintaining performance.

3. The FDVIC model, proposed to provide the necessary inertia for the interconnected power system, is adaptable for operation within both MG systems and large-scale power systems. However, the investigation is limited to supplying inertia support exclusively to MG systems in both islanded and grid-connected modes.

4. The controller developed for this study is constrained to integer and fractional order PID controllers. Moreover, the research entails optimizing the parameters of the FOPID controller using the proposed hybrid optimization algorithm.

1.5 Thesis Outline

This dissertation is structured into five chapters. Each chapter comprises essential sections, namely introduction, literature review, methodology, results and discussion, and conclusions.

In Chapter 1, the research work is introduced with a focus on providing a brief discussion of the background, problem statement, objectives, scope, and research contributions. After that, Chapter 2 starts with an in-depth literature review that comprehensively explores the existing system models utilized for LFC application, encompassing single-area, multi-area, MG, and MMG systems. The literature review covers the hierarchical control architecture, control schemes, as well as the implementation of various inertia control techniques. Additionally, the consideration of demand response control techniques for LFC is included. Furthermore, a review of optimization algorithm techniques used to tune the controller parameters for LFC applications is provided. Through this review, significant gaps in the current research on LFC and inertia controllers have been identified. These gaps will be addressed in the subsequent chapters of this study.

Next, Chapter 3 provides an overview of the methodology adopted to achieve the research objectives. The focus lies on optimizing control parameters for the Virtual Inertia Controller and supplementary controllers through AI techniques. Initially, a novel hybrid SSAGWO optimization algorithm is employed to tune the PID controller for LFC within a large-scale interconnected power system integrated with RESs operating under both deregulated and regulated environments. Subsequently, a new hybrid SSAMGO algorithm is developed to estimate optimal values for virtual inertia and damping while adjusting controller parameters for the proposed Fractional-Derivative Virtual Inertia Controller, FOPID controller, and Droop Ratio Control controller within an integrated MMG power system. Finally, validation of these techniques is conducted through Real-Time Digital Simulation Experiments utilizing the Opal-RT simulator.

Chapter 4 presents a clear illustration of the results derived from the methodology outlined in Chapter 3. Initially, a novel hybrid optimization algorithm is introduced to tune the gain values of a decentralized secondary PID controller for a RESs-integrated power network. The simulation outcomes and quantitative findings are meticulously compared with those obtained from various optimization algorithms and real-time variations of RESs. Then, a novel virtual inertia controller is developed to enhance low-inertia MMG systems, providing adequate inertia to mitigate frequency fluctuations during uncertainty. It integrates demand response control with inertia control to reduce stress on the ESS during active periods. Additionally, the control technique's performance is improved using a hybrid SSAMGO algorithm, with results compared to SSAGWO. Finally, the controller strategy, employing the SSAMGO algorithm, integrates MMG into a large-scale power system. The modified New England IEEE 39 bus system is chosen as the test platform to validate the effectiveness of the approach.

Finally, Chapter 5 presents a conclusion of the research study's findings, along with suggestions for future work.

CHAPTER 2

LITERATURE REVIEW

2.1 Introduction

Power system stability refers to the electric power system's ability, under specific initial operating conditions, to restore a state of operational equilibrium after experiencing a physical disturbance. During this restoration process, the system ensures that most variables are bounded, thereby preserving the overall integrity of the entire system (Bevrani, 2014; Shair et al., 2021). Diverse aspects define power system stability, with transient stability, dynamic stability, and static stability being prominent categories as illustrated in Figure 2.1. Transient stability defines the system's capacity to recover its normal conditions after a significant disturbance, usually discernible within a few seconds. Dynamic stability, in contrast, addresses the system's ability to return to its equilibrium state following a minor disturbance, known as small signal stability. Lastly, static stability refers to the system's inherent stability without the need for any external control interventions (Hatziargyriou et al., 2021; Kundur et al., 2004).

Rotor angle and voltage stability can be categorized into small and large disturbance stability. Rotor angle stability involves mitigating power swings within subsystems and between interconnected grid subsystems, while voltage stability focuses on controlling voltage excursions that exceed specified threshold levels (Rezaei et al., 2022). To minimize the risk of angle and voltage instability, employing effective control devices within the power system is crucial. Power System Stabilizers (PSS) and Automatic Voltage Regulators (AVR) play vital roles in enhancing stability. Generators are commonly operated at a constant voltage with an AVR, controlling excitation through an electric field exciter. The exciter supplies direct current to the synchronous machine's field winding, generating the needed rotor flux. While, PSS acts as an additional control loop, working in conjunction with the turbine-governing system, to enhance the AVR system of a generating unit (Kundur, 1965).

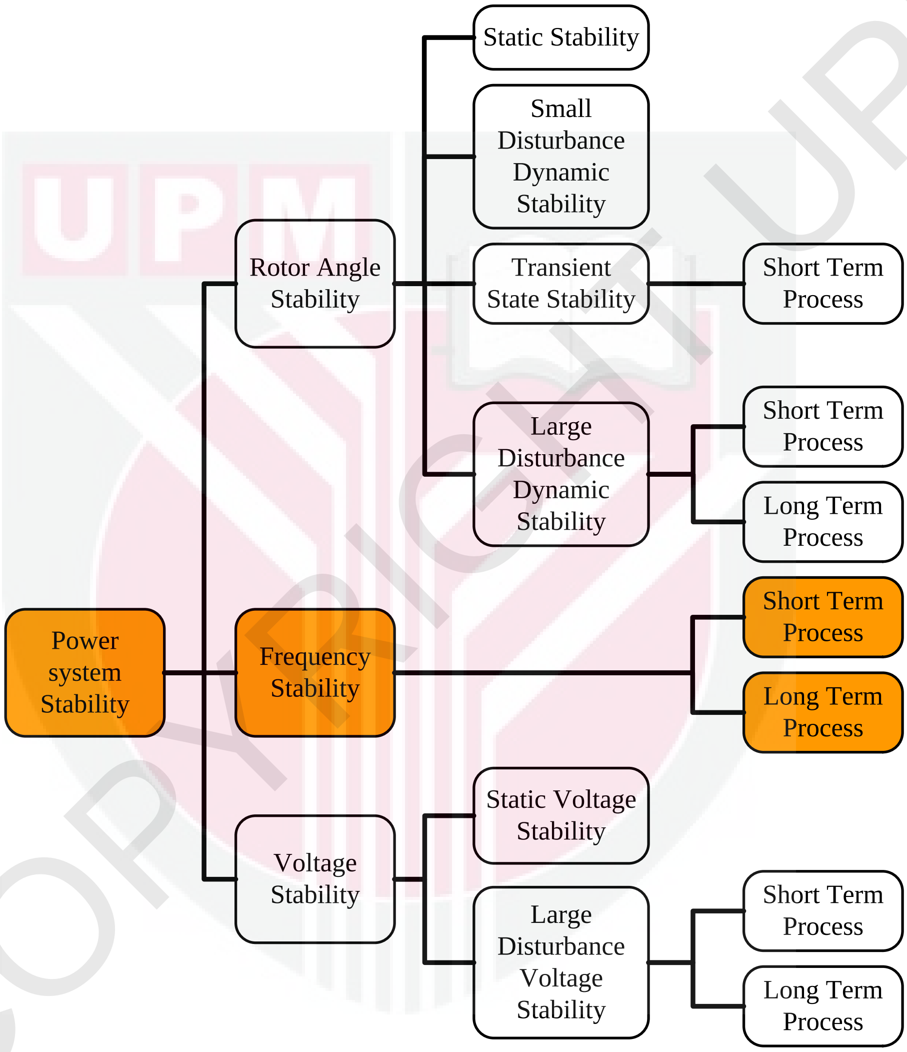

Figure 2.1 : Classification of Power System Stability

Intense system stress causing a generation-load imbalance significantly degrades power system performance and stability, beyond conventional transient and voltage stability studies. Frequency deviation directly reflects the imbalance between electrical load and generated power, serving as a useful index for assessing generation-load disparities. During load imbalance or load fluctuation events, inertia plays an important role in maintaining the frequency of the power system (Saxena et al., 2020). Synchronous generators (rotating mass) are the main sources of inertia in the conventional power system. The inertia control loop, droop frequency control (primary frequency control), and supplementary control loop (secondary frequency control) are the three stages of conventional frequency control operation. The inertia control stage is the first line of defense against load fluctuations to reduce the frequency deviation of the power system. The inertia constant of the conventional system is calculated as a function of the kinetic energy stored in the generator's rotating parts (Rafiee et al., 2021). The inertia (H) can be calculated as follows:

$$H = \frac{E_{Kinetic}}{S} = \frac{J\omega^2}{2S} \tag{2.1}$$

where $E_{Kinetic}$ is the stored kinetic energy in the rotor, J is the moment of inertia in kgm^2, ω is the rotor angular velocity in rad/s, and S is the rated power of the power system in VA.

This thesis focuses on load frequency control, the process that realigns frequency to the desired level. It specifically focuses on frequency stability, rather than voltage stability and rotor angle stability. Furthermore, the integration of RESs involves the use of power electronic devices like static converters. These converters operate without rotating mass, leading to a reduction in the overall system inertia (Roy et al., 2022).

In less than 10 seconds, inertia power compensation in rotating units responds to counter the initial frequency deviation. Following this, the primary control loop in a governor-turbine unit is activated within 3 seconds and fully integrated into the system within 10 seconds. This support, if required, is maintained for up to 20–40 seconds (Kerdphol et al., 2021). Upon achieving stability, the system frequency rebounds to a predetermined value. However, this value may differ from the nominal value due to the proportional action of the generator droop. Subsequently, the secondary control is initiated, following the timescales of inertia compensation and primary control, and can remain active for up to 30 minutes after a disturbance (Zaman et al., 2018). This control redistributes power to restore the nominal frequency and exchanged power. During critical disturbances, if the system frequency rapidly drops to a crucial level, tertiary and emergency controls become essential for recovery. Tertiary control addresses potential congestions, replenishes secondary control reserves, and restores frequency and tie-line power to fixed values when secondary control reserves are inadequate. Figure 2.2 depicts the frequency dynamic control timescale for traditional power systems primarily governed by synchronous generators.

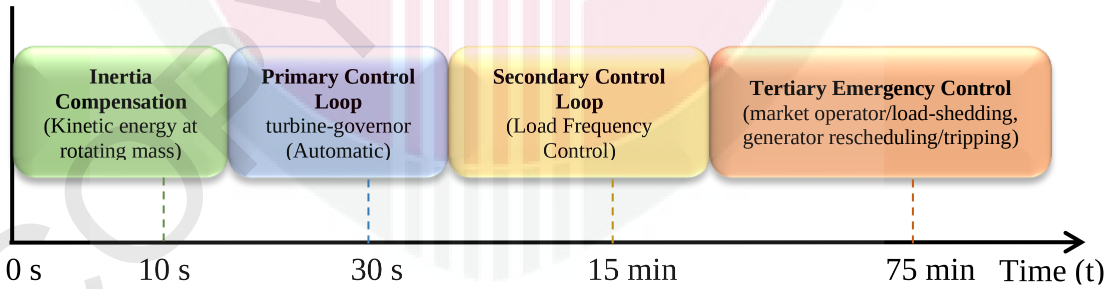

Figure 2.2 : The time scale for the dynamic response of conventional power system synchronous generators

2.2 Load Frequency Control

Automatic generation control (AGC) plays a crucial role in power systems, contributing to the effective management of the balance between generation and load at an optimal cost within a power system. The AGC approach addresses the regulation of frequency, control of power exchange, and economic dispatch within power systems. Additionally, it manages the adjustment of megawatt power across multiple generators situated in various power plants in response to changes in load (Mishra et al., 2023). Primarily, AGC operates as a closed-loop scheme designed to regulate both frequency and exchange power within power systems. Crucially, two parameters, frequency, and voltage, play a pivotal role in maintaining the balance between generation and load within the power network.

Therefore, to regulate frequency deviation, the LFC loop, an essential mechanism, is employed (Shafei et al., 2022). Nevertheless, another control loop, the AVR, is utilized to regulate voltage levels. The incorporation of both the LFC and AVR control loops extends the functionality of AGC, addressing both frequency and voltage as control parameters. In many instances, researchers have referred to LFC as AGC (Oshnoei et al., 2021). This is because frequency control takes precedence over voltage control in terms of addressing frequency deviation. Typically, the power frequency can only handle deviations of up to ±0.5 hertz. Deviations beyond this range risk the collapse of the power network or may lead to a blackout. Therefore, extensive research has been conducted over the past few decades to emphasize load frequency control.

2.2.1 Inertia Control Loop

The kinetic energy stored in the rotating mass (rotor) of a synchronous generator, known as inertia power, is pivotal in mitigating frequency oscillations and actively maintaining system frequency stability during disturbances. A decrease in system inertia can lead to a notably faster fluctuation in the system frequency, ultimately compromising the overall stability of the frequency (Sørensen et al., 2023).

In conventional power systems where synchronous machines prevail, synchronous generators produce active power and kinetic energy, playing a crucial role in regulating the system frequency. In the rotor of a synchronous machine, the rotating mass generates inertia power, quantified in units Joule-seconds (J·s) or Watt-square seconds ($W \cdot s^2$), to mitigate disturbances. This inertia power is essential for ensuring the stable frequency of the system (Kerdphol et al., 2021). Inertia originates from the spinning mass, or rotor, of a synchronous generator, persisting unless intentionally slowed or halted. The system's inertial response is largely enhanced by the physical rotating mass linked to the power outputs of synchronous generators. Therefore, ensuring a minimum level of total system inertia is crucial for addressing two primary dynamic challenges. Firstly, it mitigates the initial rate of change of frequency (RoCoF) following significant disturbances such as generator or load disconnections, thus averting cascading disconnections. Secondly, it helps stabilize the frequency decay and restrict the frequency nadir after events like generator trips or load increases (Sørensen et al., 2023). In addition, inertia is utilized to restrain the increase in frequency and mitigate the frequency peak following a load trip or generation increase. The emulation of the typical swing equation of a synchronous generator (SG) in the control of an inverter relies on capturing the system's inertia. This equation can be expressed as follows:

$$\Delta P_m - \Delta P_e = \frac{2H}{f_o} \cdot \frac{d\Delta f}{dt} \tag{2.2}$$

where ΔP_m is the change in the input mechanical power [p.u.], ΔP_e is the change in the output electrical power [p.u.], H is the inertia constant of the SG in second, f_o is the rated frequency [Hz], and f is the power system frequency [Hz]. The notation $\frac{d\Delta f}{dt}$ is widely recognized as representing the RoCoF within the power system. When considering the influence of the damping coefficient component impact (mechanical friction losses and electrical losses in both the stator field and damper windings), Equation (2.2) is transformed as follows (Kerdphol et al., 2019):

$$\Delta P_m - \Delta P_e = \frac{2H}{f_o} \cdot \frac{d\Delta f}{dt} + D\frac{\Delta f}{f_o} \tag{2.3}$$

where D is the damping coefficient of the power system [p.u./Hz].

The swing equation elucidates how the system frequency changes in relation to the balance between the mechanical power input ΔP_m and the electrical power output ΔP_e. This equilibrium dictates whether the frequency increases or decreases. When the difference between mechanical power input P_m and electrical power output P_e is positive, the system frequency tends to increase, and conversely, when it is negative, the frequency decreases. At a steady-state operating point, the balance between generation and load is regulated to maintain the system frequency. This is achieved through a speed governing system implemented in the SG units. The conceptualization of virtual inertia control is grounded in the swing equation delineated previously. There are several proposed configurations for emulating virtual inertia.

A VIC, employing the Derivative Control Technique (DCT), has been introduced to improve the frequency deviation response in a power system model. This model includes a traditional power station integrated with RESs. The DCT is utilized specifically to regulate the power of ESS, effectively mimicking inertia characteristics (Kerdphol et al., 2018; Kerdphol et al., 2019). Therefore, VIC based on an ESS does not provide any physical rotational inertia and it can be considered as a fast-active power supply to the power system. The ability to provide the effect of virtual damping control loop in the structure of the controllers, which significantly affects the frequency deviation oscillations has been considered by Kerdphol et al. (2019), Kerdphol et al. (2021), Khooban (2021), and Mandal & Chatterjee (2021b), which significantly affects the transient and steady-state stability of the performance of the system frequency. Nevertheless, all these configurations share a common primary goal: to incorporate additional inertia into the power system virtually through the use of a power electronics interface. Typically, the VIC system comprises an energy source, an inverter, and appropriate control mechanisms for emulating virtual inertia. The fundamental concept of the virtual inertia control system is depicted in Figure 2.3.

Additional energy sources, like solar photovoltaic (PV) (Saxena et al., 2021), and wind turbines (WT), could also be integrated with VI controller. The process of emulating virtual inertia through wind turbines, specifically doubly-fed induction generator (DFIG) wind turbines, is commonly known as "synthetic inertia". Nonetheless, for enhanced operational versatility, employing an ESS as the energy source is preferable.

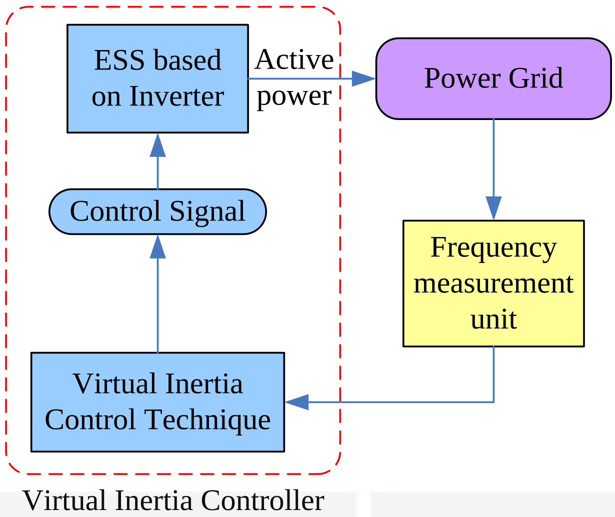

Figure 2.3 : The basic schematic of the virtual inertia control system

The concept of VI revolves around incorporating the swing equation of an SG into the inverter of inverter-based ESS units. This enables the control of the inertia-less inverter to mimic the inertia characteristics of an SG. The term 'virtual inertia' signifies the emulation of the inertia characteristic of an SG without relying on any rotating mass. The control mechanism for VI emulation is employed to ascertain the necessary inertia power output from the VIC system (Hou et al., 2020). To mimic the VI characteristic of an SG, the fundamental approach involves adjusting the reference power of the static converter based on the derivative of the system frequency's rate of change. In this method of VI emulation, the virtual inertia power is calculated using Equation (2.4), derived from Equation (2.3):

$$\Delta P_{inertia} = H_{virtual}\frac{d\Delta f}{dt} + D_{virtual}\Delta f \tag{2.4}$$

where $\Delta P_{inertia}$ is the output VI active power of VIC units, $H_{virtual}$ is the virtual inertia constant, and $D_{virtual}$ is the virtual damping coefficient constant.

The total equivalent inertia constant of the conventional power system is a function of all the inertia constants of the synchronous generators; therefore, this parameter will decrease by removing any synchronous generator from the system. While in the MG system, including multi-distribution generators, the equivalent inertia constant of the system decreases with the increased number of RESs connected through static converters (Rafiee et al., 2021). The equivalent inertia of the MG system integrated with RESs can be estimated as follows:

$$H_{equiv.} = \frac{\sum_{i=1}^{N} H_i S_i}{\sum_{i=1}^{N} S_i + \sum_{i=1}^{R} P_i} \tag{2.5}$$

$$D_{equiv.} = \frac{\sum_{i=1}^{N} D_i S_i}{\sum_{i=1}^{N} S_i + \sum_{i=1}^{R} P_i} \tag{2.6}$$

where H_i is the inertia constant of the ith MG distributed generators (DGs) (i = 1, 2, …. N); N is number of DGs; S_i is the rating power of the ith MG distributed generators; D_i is the damping coefficient of the ith MG distributed generators; P_i is the injected real power by the ith RESs connected to MG by static converters (zero inertia); R is number of RESs.

A variety of control strategies have been proposed in the literature. The conventional VIC technique utilizes the derivative of system frequency deviation as a control signal for ESS to provide the necessary inertia, as demonstrated in several studies (Kerdphol et al., 2018; Kerdphol et al., 2019; Rakhshani et al., 2016; Sockeel et al., 2020). The controller has since been upgraded to incorporate the effect of the damping coefficient, effectively introducing virtual damping in studies (Abubakr et al., 2021; Kerdphol et al., 2019; Kerdphol et al., 2021; Khooban, 2021; Mandal & Chatterjee, 2021a). Additionally, Oshnoei et al. (2021) proposed a VIC technique that integrates droop control effects. Furthermore, Bhowmik & Rout (2019) and Kerdphol et al. (2019) explored the use of fuzzy logic to optimize the inertia constant. Saxena et al. (2021) presented a VIC that does not rely on any ESS, instead utilizing sunlight to provide the necessary inertia during daylight hours. While previous studies primarily employed integer-order derivatives of frequency deviations, the techniques proposed in this study utilize fractional derivatives, offering a broader range of controller parameter values and enabling more precise support for the power system by accurately determining the necessary reduction in ESS capacity.

2.2.2 Primary and Secondary Control Loop

The frequency of a power system is determined by the balance of real power. Changes in real power demand at any point in the network cause corresponding shifts in frequency across the system. Therefore, system frequency serves as a valuable indicator of generation and load imbalances within the system (Bevrani, 2014). An instantaneous shift in system frequency occurs due to any short-term energy imbalance, initially compensated by the kinetic energy of rotating machinery. A substantial generation loss, without prompt system intervention, can lead to frequency excursions beyond the operational limits of the plant (Tripathi et al., 2023).

The generator's active power output relies on the mechanical energy generated by the turbine, sourced differently from various input sources. For instance, in thermal and hydroelectric plants, the turbine is known respectively as a steam turbine and a hydro-turbine. Moreover, in thermal and hydroelectric plants, steam and water serve as the primary inputs to the turbine, responsible for generating mechanical power. Despite this, the input (steam or water) can be regulated by the valve through the regulator to meet the required active power demand (Mishra et al., 2023).

The primary loop's basic block diagram is illustrated in Figure 2.4. Within this loop, the speed governor functions as a speed sensor, detecting the speed or frequency through feedback from the steam/hydro turbine. It then issues commands to the hydraulic amplifier to adjust the valve position, either raising or lowering it, in accordance with the desired frequency (Akram et al., 2020).

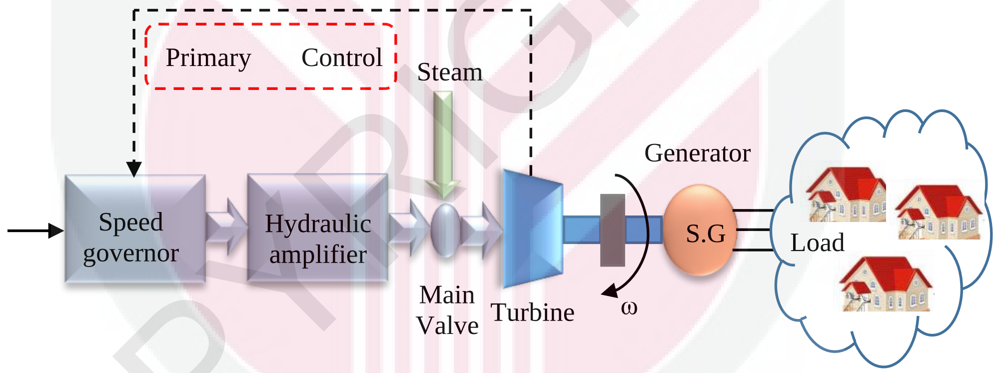

Figure 2.4 : Schematic block diagram of the primary control loop (Mishra et al., 2023)

In practical application, the primary loop implements a locally programmed control, providing backup power in response to frequency fluctuations. Nevertheless, it has been confirmed that this loop is incapable of maintaining frequency at a fixed level in power systems with multiple areas. Consequently, a secondary loop is necessary to adjust the set point via the speed changer and controller.

The secondary loop comprises the primary loop integrated with a speed regulator and controller, as depicted in Figure 2.5. This loop's significance lies in its feedback control mechanism, which utilizes the frequency deviation output to enhance the primary loop's ability to accurately regulate frequency changes. Additionally, the speed changer motor serves as a regulator, responding to set point commands from the controller (Khooban, 2021).

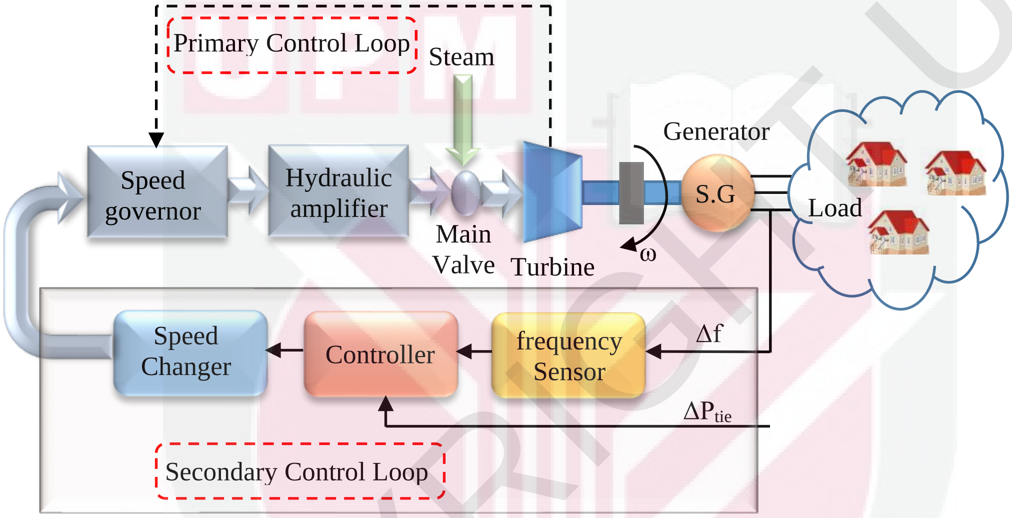

Figure 2.5 : Schematic block diagram of the secondary control loop (Mishra et al., 2023)

In practical power system applications, the proportional plus integral (PI) controller is often utilized as a dynamic controller. This mechanism enables the AGC to promptly adjust frequency levels in response to various disruptive events over a broad range. The relationship between the incremental mismatch power and the system frequency deviation in the generator-load dynamic system can be mathematically described by a swing differential equation as follows:

$$\Delta P_m(t) - \Delta P_L(t) = 2H\frac{\Delta f(t)}{dt} + D\Delta f(t) \qquad (2.7)$$

where ΔP_L is the change in demand load.

Based on Equation (2.7), a change in load (ΔP_L) induces a transient alteration in frequency (Δf). Subsequently, the feedback mechanism is initiated, generating a signal to adjust the turbine's operation (ΔP_m) in response to the load, thereby restoring the system frequency. Expressed typically as a percentage change in load for a 1% change in frequency, the damping coefficient is a crucial parameter. For instance, if D equals 1.5, it signifies that a 1% alteration in frequency results in a 1.5% adjustment in load. Employing the Laplace transform, Equation (2.7) can be reformulated as (Xiong et al., 2020):

$$\Delta P_m(s) - \Delta P_L(s) = 2Hs\Delta f(s) + D\Delta f(s) \quad (2.8)$$

The representation of Equation (2.8) can be visualized through a block diagram, as demonstrated in Figure 2.6. This model of generator-load dynamics offers a simplified version of the closed-loop synchronous generator schematic presented in Figure 2.5 (Hadi, 1999).

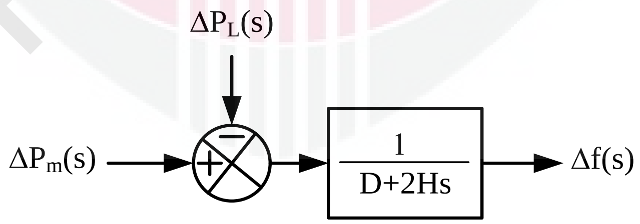

Figure 2.6 : Generator-load model block diagram

The governor-generator system of the reheat turbine generator is simplified in earlier studies by Hadi (1999), and its model is depicted in Figure 2.7. This model provides a foundation for analyzing power system frequency and designing control strategies.

The governor-turbine dynamics are expressed through first-order transfer functions. The droop gain (R) can be expressed as the ratio of the change in frequency (Δf) to the change in generator power output (ΔP). The turbine-governor control system aims to regulate the system frequency at the desired level by adjusting the mechanical power output of the turbine (Bevrani, 2014). Equation (2.9) describes the relationship between frequency and power for turbine-governor control,

$$\Delta P_g = \Delta P_c - \frac{1}{R}\Delta f \tag{2.9}$$

The droop gain is defined in Equation (2.9) as,

$$-R = Slop = \frac{\Delta f}{\Delta P_g - \Delta P_c} \tag{2.10}$$

Governors utilize droop control to manage generator power output in reaction to frequency deviations. This system serves as the primary frequency control and is autonomously executed by the governors. For example, when demand power rises (or generation power declines), causing a frequency drop, the governors react by supplying low-frequency service, and conversely (Abazari et al., 2018). Moreover, the realistic aspects of reheat power systems are considered by accounting for physical constraints such as the Generation Rate Constraint (GRC), Governor Dead Band (GDB), and the boiler effect (Veerasamy et al., 2022). To ensure the realism of load frequency control in power systems, it's essential to consider the GRC. This factor is incorporated to address the sensitivity of the power generator turbine (Irudayaraj et al., 2022). Systems with GRC exhibit notable effects on dynamic response compared to those without it, showing larger overshoots and extended settling times. Typically, the GRC limitation ranges between 3 to 10% per minute (Veerasamy et al., 2022). The speed governor dead band significantly affects the dynamic performance and stability of power systems during sudden load changes. This dead band introduces a nonlinear backlash, causing a time lag in the performance of the governor transfer function (Ramachandran et al., 2018).

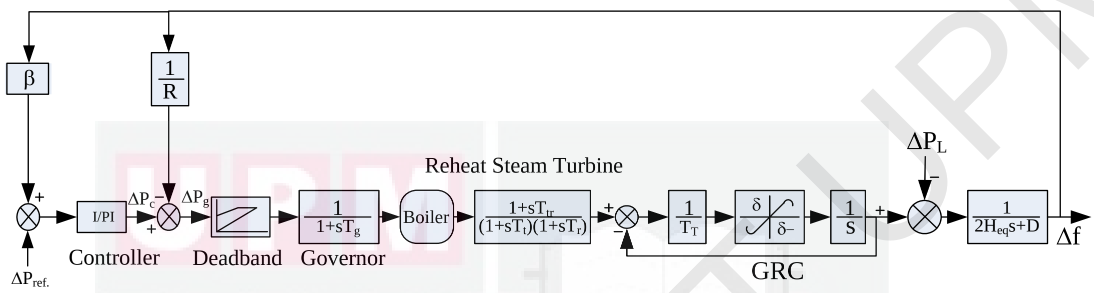

Figure 2.7 : Transfer function model of the single area reheat turbine generator

In thermal power plants, a boiler dynamics (BD) arrangement is utilized to generate steam under high pressure. This model considers the long-term process of steam flow in the boiler drum as combustion control. The block diagram configuration of the boiler dynamics is depicted in Figure 2.8, with parameters for boiler-type gas or oil-fired systems listed in Table 2.1 (Naidu et al., 2014; Sahu et al., 2015).

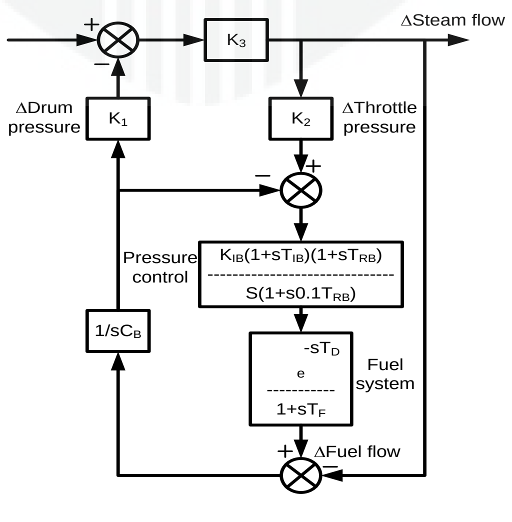

Figure 2.8 : Block diagram of the boiler dynamics configuration system

Table 2.1 : Boiler dynamics parameters

Boiler Parameters	Value	Boiler Parameters	Value
K_1	0.85	K_{IB}	0.03
K_2	0.095	T_{IB}	26
K_3	0.92	T_{RB}	69
C_B	200	T_F	10
T_D	0		

Within this mechanism, the AGC effectively regulates frequency levels following disturbances across a wide spectrum. Nevertheless, during extreme events, the secondary controller's capabilities may prove insufficient to fully rectify frequency deviations, potentially resulting in power outages. Consequently, integration of a demand response control loop becomes imperative to address such critical scenarios and maintain system stability.

2.2.3 Demand Response Control Loop

In recent years, there has been a significant focus on DRC techniques for frequency control. These techniques have gained considerable attention due to their potential in addressing the challenges associated with maintaining grid frequency stability (BAO et al., 2017). Saxena & Shankar (2022) introduces a DR control technique aimed at improving the frequency performance of interconnected hybrid power systems. While the study provides valuable insights, it is important to note that the uncertainties related to RESs output have not been accounted for. These uncertainties can have a notable impact on the dynamic response of the proposed model. While Hosseini et al. (2022) investigated the application of an ESS with optimized size and its potential contribution to load frequency control. The study demonstrated that incorporating an ESS into the system significantly improved the dynamic stability by actively participating in DR measures.

Moreover, Kerdphol et al. (2016) proposes a method that combines a particle swarm optimization algorithm (PSO) with a DRC technique to improve system stability through the optimization of the battery energy storage system's size. The effectiveness of this approach is evaluated by comparing it with the results obtained using the simulated annealing technique for determining the optimal size of the energy storage system. However, it's important to note that certain aspects have not been taken into account in this research. Specifically, the authors did not consider the island operating condition mode, which refers to the scenario where the power system operates in isolation from the main grid. Additionally, the study did not account for the challenges posed by high uncertainties in RES penetration, which can impact the overall performance and reliability of the system.

In addition, Al-Hinai et al. (2021) propose an approach that integrates the ESS control loop with the LFC system. By doing so, they aim to enhance the overall system stability and mitigate frequency deviations. To achieve this, the PSO algorithm is utilized to determine the optimal parameters for the Fuzzy controller within the secondary control loop. This optimization process aims to improve the performance and effectiveness of the integrated ESS-LFC system in maintaining grid stability and frequency regulation. The studies mentioned earlier propose a combination of the DRC technique with ESS units integrated into LFC to improve system stability. However, it is important to note that these studies do not consider the potential benefits of this technique in reducing stress on the ESS during discharging and charging periods. Such stress on the ESS can significantly impact the battery's lifetime and overall performance.

2.3 Frequency Response Model of the Multi-Area System

Power systems exhibit a complex, nonlinear, and time-varying behaviour. Nevertheless, when analyzing frequency control amidst load disturbances, a simplified low-order linearized model is commonly employed. Unlike voltage and rotor angle dynamics, the dynamics influencing frequency response unfold over relatively slower time scales, typically spanning from seconds to minutes (Bevrani, 2014). Moreover, complex numerical methods are required to encompass both fast and slow power system dynamics, accounting for detailed generation and load dynamics. These methods enable the adjustment of simulation time steps based on the magnitude of system variable fluctuations. Simplifying the model by neglecting fast dynamics, such as voltage and angle variations, streamlines the modeling process, reduces computational complexity, and minimizes data requirements. This simplification also facilitates easier analysis of results (Hadi, 1999).

To generalize the model for interconnected power systems, the concept of control areas is essential. A control area represents a cohesive grouping of generators and loads. Within each control area, all generators respond collectively to changes in load or speed changer settings. It is assumed that the frequency remains uniform across all locations within a control area (Yan & Xu, 2020). In a multi-area power system, regions are linked via high-voltage transmission lines or tie-lines. The frequency trend observed within each control area serves as an indication of the trend in mismatched power across interconnections, rather than solely within the individual control area.

In a multi-area power system, each control area's secondary frequency control system must manage not only the local frequency but also the interchange power with other areas (Kalyan & Rao, 2021). Consequently, the dynamic LFC system model illustrated in Figure 2.7 needs modification to integrate the tie-line power signal. Figure 2.9 presents a simplified block diagram for a multi-area control power system.

In a multi-area power system, secondary control not only regulates area frequency but also maintains scheduled net interchange power levels with neighboring areas. Typically, achieving this involves incorporating tie-line flow deviation into the secondary feedback loop alongside frequency deviation. The mathematical expression for power transmission through the tie-line from area i to area j can be rewritten as follows:

$$P_{tie,ij} = \left(\frac{V_i V_j}{X_{ij}}\right)\sin\left(\delta_i - \delta_j\right) \tag{2.11}$$

where, V_i and V_j refer to the voltages of area i and area j, respectively, expressed in per unit (p.u.). δ_i and δ_j represent the power angles of the equivalent machines in areas i and j, and X_{ij} denotes the reactance of the tie line connecting area i and area j.

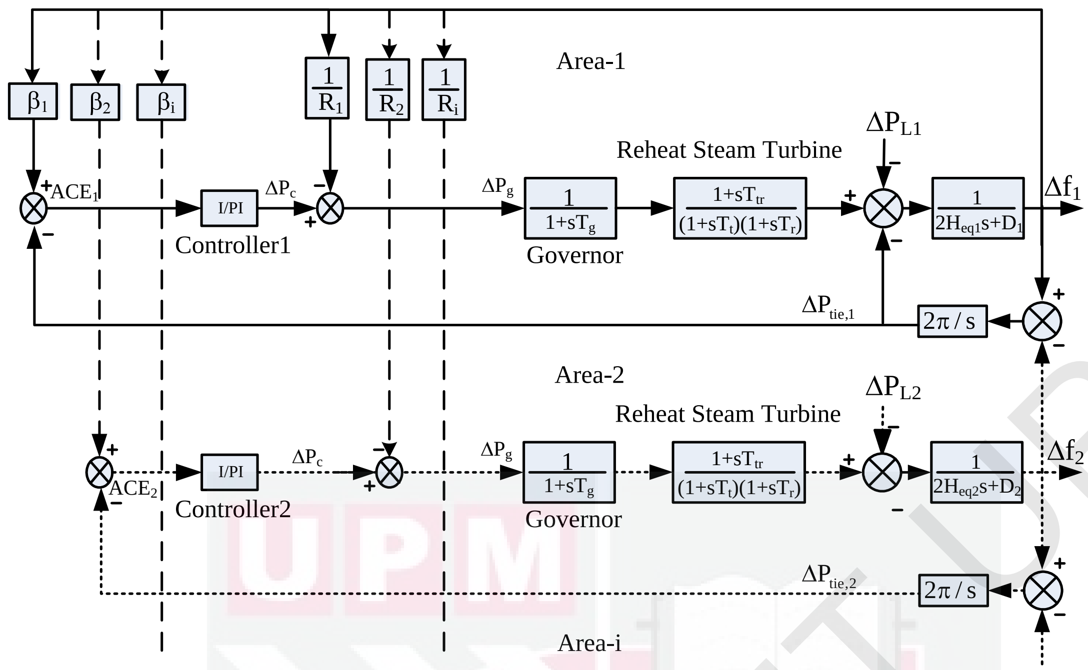

Figure 2.9 : Linearized transfer function model for a multi-area power system, highlighting the interconnections between different areas (Bevrani, 2014)

Linearizing equation (2.11) around an equilibrium point (δ_i^0 , δ_j^0) involves approximating the behaviour of the system near this equilibrium point by its linearized form.

$$\Delta P_{tie,ij} = T_{ij}(\Delta\delta_i - \Delta\delta_j) \tag{2.12}$$

where, T_{ij} denotes the synchronizing torque coefficient, which is defined as (Bevrani, 2014):

$$T_{ij} = \left(\frac{|V_i||V_j|}{X_{ij}}\right)\cos(\delta_i^{\,0} - \delta_j^{\,0}) \tag{2.13}$$

By incorporating the connection between the area power angle and frequency, Equation (2.12) can be reformulated as:

$$\Delta P_{tie,ij} = 2\pi T_{ij}(\int \Delta f_i - \int \Delta f_j) \tag{2.14}$$

where, the frequency deviations in areas i and j are designated as Δf_i and Δf_j, respectively. The Laplace transform of equation (2.14) indicates the derivation of $P_{tie,ij}(s)$ is,

$$\Delta P_{tie,ij} = \frac{2\pi}{s} T_{ij}(\Delta f_i - \Delta f_j) \tag{2.15}$$

The total change in tie-line power between area i and other areas can be expressed as:

$$\Delta P_{tie,i} = \sum_{\substack{j=1 \\ j\neq i}}^{i} \Delta P_{tie,ij} = \frac{2\pi}{s}\left(\sum_{\substack{j=1 \\ j\neq i}}^{i} T_{ij}\Delta f_i - \sum_{\substack{j=1 \\ j\neq i}}^{i} T_{ij}\Delta f_j \right) \tag{2.16}$$

The block diagram in Figure 2.9 illustrates Equation (2.16), demonstrating that modifying the tie-line power for a specific area is akin to adjusting that area's load. Therefore, the tie-line power change $\Delta P_{tie,i}$ should be appropriately added to the mechanical power change ΔP_m and area load change ΔP_L with the correct sign.

Another consideration is the secondary control loop when a tie-line is present. In an isolated control area, this loop is driven by feedback from the control area's frequency deviation via a simple dynamic controller, as depicted in Figure 2.5. While, in a multi-area power system, secondary control is responsible not only for regulating area frequency but also for ensuring that the net interchange power with neighboring areas stays at designated levels. Achieving this typically involves incorporating a tie-line flow deviation into the frequency deviation within the secondary feedback loop. The resultant linear combination of frequency and tie-line power changes for area i is referred to as the Area Control Error (ACE) (Irudayaraj et al., 2022). The ACE_i signal is computed as per Equation (2.16) and then utilized in the controller.

$$ACE_i = \Delta P_{tie,i} + \beta_i \Delta f_i \tag{2.17}$$

where, β represents a bias factor, which can be determined based on the influence of the damping coefficient and droop gain factor, as follows:

$$\beta_i = \frac{1}{R_i} + D_i \tag{2.18}$$

The considerations of local load modifications and interactions with neighboring areas are appropriately acknowledged as two input signals. Within each control area, monitoring of tie-line power flow and frequency takes place at the area control center. The ACE signal is calculated and assigned to the controller. Subsequently, the resultant control action signal is implemented on the turbine-governor unit. Hence, the secondary control depicted in Figure 2.9 is anticipated to effectively fulfill the fundamental LFC objectives and uphold area frequency and tie-line interchange at predetermined values. The parameters of the simplified interconnected power system are presented in Table 2.2:

Table 2.2 : Simplified power system parameters

System Parameters	Value
Equivalent system inertia $H_{equ.}$	5 s
Governor time constant T_g	0.2 s
Turbine time constant T_T	0.3 s
Time constant of the Reheat T_r	10 s
Governor adjustment deviation coefficient R	2.4 Hz/p.u.
The frequency response coefficients β	0.425 p.u./Hz
Damping coefficient D	0.00833 p.u./Hz

(Irudayaraj et al., 2022b), (Ramachandran et al., 2018b)

2.4 Frequency Response Model of the Microgrid System

The development of conventional power generation and transmission line, alongside the utilization of RES, is garnering significant attention within environmental initiatives. The utilization of RES involves power electronic converters such as PV, wind, micro turbine, and ESS (Bevrani, 2014). By integrating RES with power-saving techniques, system stability is improved, leading to enhanced resource usability. MG constructs efficient infrastructure to integrate RES into the power grid at the distribution level (Sen & Kumar, 2018). An MG is a portion of the electrical grid that contains Distributed Energy Resources (DERs) such as DGs, RES, ESS, and various load demands (Shuai et al., 2016).

MGs consist of decentralized energy producers and consumers, usually integrated and synchronized with the conventional wide-area synchronization grid. They possess the flexibility to disconnect and operate independently in "island mode," driven by either physical or economic considerations (Jirdehi et al., 2020). Through this approach, diverse distributed generation sources can be efficiently incorporated. A microgrid connects to the main grid at a common coupling point through a static switch, ensuring its current matches that of the main grid. This switch can disconnect the MG autonomously, whether for maintenance or in the event of a fault or contingency (D’silva et al., 2020).

Several research studies have focused on addressing frequency stability in islanded MG systems. For instant, Yang et al. (2019) examined a two-area AC MG power system with a PV system and ESS, utilizing a supercapacitor to enhance system inertia. Abubakr et al. (2021) investigated a MMG system with various DGs, implementing a VIC based on frequency changes, along with controllers for EVs and a secondary control loop. Sockeel et al. (2020) developed a MG integrating a diesel generator, PV, WT, and ESS, employing a virtual inertia emulator to support system inertia. Rafiee et al. (2021) analyzed a configuration with a diesel generator and fuel cell, using quantitative feedback theory for tuning inertia controller parameters and implementing a PID controller for the diesel generator's secondary control loop. Mandal & Chatterjee (2021) focused on a MG consisting of a thermal power plant, PV, WT generator, and ESS, optimizing controller parameters with a genetic algorithm. Oshnoei et al. (2023) proposed a two-layer model predictive control approach for a MG system, enhancing frequency performance through ESS control based on frequency deviations.

Moreover, several studies have focused on frequency stability in grid-connected MG systems. Wu et al. (2017) investigated a DC microgrid comprising DGs, ESS, and PVs, highlighting the bidirectional converter's role in maintaining power balance and simulating synchronous generator behavior for DC bus voltage stability. Teng et al. (2021) analyzed the impact of grid-connected inverters on frequency stability, using an integral sliding mode and backstepping control approach to simulate virtual inertia and damping. Santhoshkumar & Senthilkumar (2020) utilized a hybrid optimization algorithm to adjust controller parameters for frequency regulation in a synchronous generator and ESS setup. Lastly, Zhang et al. (2023) implemented a bidirectional VIC in a hybrid AC/DC MG, enhancing frequency stability by regulating active power between subgrids through a PI controller.

2.5 Deregulated Power Systems

In the landscape of an open energy market, LFC continues to be indispensable, ensuring the regulation of frequency to its designated value and the minimization of tie-line power deviations between control areas. The development of the electricity market, encompassing privatization, the formation of free markets, and the quest for economic efficiency and reliability, has prompted the deregulation of regulatory structures within power systems. The global power industry is being deregulated from a vertically integrated market into several enterprises in each power system continuum. Several deregulated electricity businesses can trade in the same or a diverse control region (Farooq et al., 2022).

The new power system market will include many generation companies called is (GENCOs), many distribution companies called (DISCOs), and several transmission companies known as (TRANSCOS). ICA is the independent contract administration that is responsible for managing all the market participation (Marzbali, 2020). The industry discusses three different types of market operations: poolco, bilateral, and contract violation transactions. These contracts are predicated on a pricing scheme and market demand (Kumari & Shankar, 2020). The norms and procedures for bidding between GENCOs and DISCOs are provided by ICA, and the organization utilizes three different agreements (poolco, bilateral, and contract violation) (Babu & Saikia, 2021).

In the power system market under deregulated environment, in order to achieve a balance between GENCOs and DISCOs, ICA creates a contract based on the rules between the cooperating companies (Shiva & Mukherjee, 2016). These contracts should be deals with all possibilities of the operating scenarios like bilateral, poolco, and contract violation or a combination of them (Shankar et al., 2016). Under the rules of the poolco agreement, each DISCO is required to fulfill its power requirements using only the generators located inside its own area. However, the bilateral agreement allows each DISCO to negotiate contracts with any GENCO in any region (Kumar et al., 2022). The progressive rise in power production within a region is influenced by its ACE, with the ACE participation factor (apf) determining the contribution of each GENCO's (Dutta & Prakash, 2022).

Donde et al. (2001) provided an exposition on the intricacies of the Disco Participation Matrix (DPM), utilized to represent various contracts in matrix format. DPM consists of a number of rows equal to the number of GENCOs and a number of columns equal to the number of DISCOs. Every cell in the DPM is denoted as a contract participation factor (cpf), indicating the proportion of each GENCO's involvement relative to the total DISCO demand as illustrated in Figure 2.10:

	$DISCO_1$	$DISCO_2$	$DISCO_3$	$DISCO_4$	$DISCO_5$	$DISCO_n$
$GENCO_1$	cpf_{11}	cpf_{12}	cpf_{13}	cpf_{14}	cpf_{15}	cpf_{1n}
$GENCO_2$	cpf_{21}	cpf_{22}	cpf_{23}	cpf_{24}	cpf_{25}	cpf_{2n}
$GENCO_3$	cpf_{31}	cpf_{32}	cpf_{33}	cpf_{34}	cpf_{35}	cpf_{3n}
$GENCO_4$	cpf_{41}	cpf_{42}	cpf_{43}	cpf_{44}	cpf_{45}	cpf_{4n}
$GENCO_5$	cpf_{51}	cpf_{52}	cpf_{53}	cpf_{54}	cpf_{55}	cpf_{5n}
$GENCO_n$	cpf_{n1}	cpf_{n2}	cpf_{n3}	cpf_{n4}	cpf_{n5}	cpf_{nn}

Figure 2.10 : Disco participation matrix in general form

An analysis of a conventional generating unit in two areas is conducted within a deregulated environment using DPM. Tan et al. (2012) introduced a Decentralized PID controller for a multi-area conventional power system within a deregulated environment. The design incorporates local load frequency controllers utilizing internal model control based on PID controllers. Numerous studies have been conducted within deregulated power systems without incorporating (Jain & Bhaskar, 2024; Kumar et al., 2022; Kumar & Sharma, 2020; Kumari & Shankar, 2020). The analysis of the LFC for the multi-sources in the two-area power system was expanded by Shankar et al. (2016). This involved integrating thermal, hydro, and gas power stations alongside ESS within a deregulated power market framework. There is a scarcity of literature that comprehensively integrates large-scale RES into realistic deregulated power systems. Dutta & Prakash (2022) presented an analysis of a hybrid power system for two areas power system, incorporating a steam turbine generator and a hydropower station integrated with RESs such as PV and biomass. Electric vehicles (EVs) are employed to address the intermittency of solar power. Another study introduced a two-area power system integrating thermal, hydro, and gas power stations alongside a wind turbine generator (WTG) within a deregulated environment, utilizing a grasshopper optimization algorithm (Biswas et al., 2023).

2.6 System Control Strategies

The decentralized control is more favourable for large-scale interconnected systems due to its ability to distribute control tasks among multiple local controllers, reducing the burden on a central controller and enhancing system robustness and scalability (Magdy et al., 2019). It provides benefits over conventional centralized control methods by reducing computational demands and streamlining control processes.

Additionally, it demonstrates a heightened ability to overcome obstacles in communication and adapt to alterations in the system's structure (Khayat et al., 2019). Regarding control, each DG within the system maintains its own local frequency information, which contributes to the overall regulation of the system frequency. Figure 2.11 provides an illustration of decentralized control in the MG system.

In a similar vein, the author Saxena & Hote (2016) utilized a decentralized PID controller in a multi-area power system. The design approach of the PID controller relied on the Kharitonov theorem and stability boundary locus. The objective of the research was to tackle the issues of inter-area oscillations and frequency fluctuations. Likewise, the authors in the study Jagatheesan et al. (2017) utilized PID control integrated with a stochastic PSO algorithm, with each technique being applied distinctly within separate control areas of a multi-area power system. In an alternative approach within the MG power system context, Sabahi et al. (2021) utilized type-2 fuzzy tuning for PID controller parameters. Stability was secured using a Lyapunov function, which also facilitated the derivation of tuning laws for both the output scaling factors and the consequent parameters, ultimately contributing to the system's improved performance. Alahmadi et al. (2021), evaluated another hybrid controller that integrates PID with fuzzy logic techniques for a microgrid system. Singh et al. (2018), suggested an Internal Model Control (IMC) technique to adjust the gain values of a decentralized PID controller, tailored specifically for single and two-area high-order power systems.

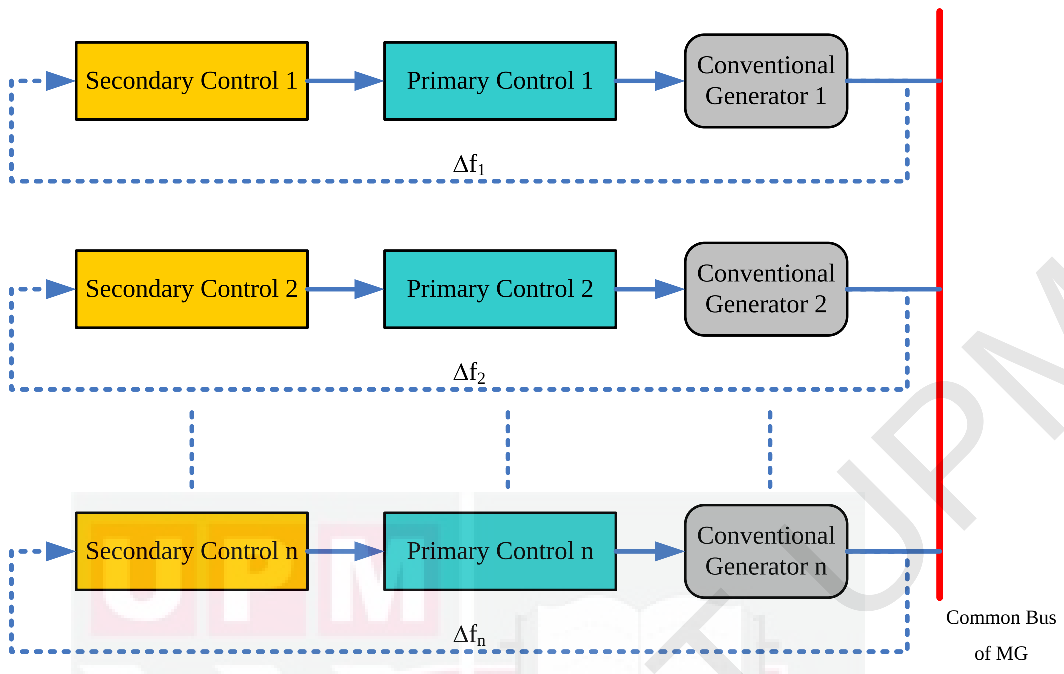

Figure 2.11 : Configuration of the decentralized control of the MG system

Moreover, nonlinear controllers like Sliding Mode Control (SMC), $H_2/H\infty$ controllers, and Model Predictive Controller (MPC) are employed to manage the frequency of multi-area, multi-source, and multi-microgrid power systems. Wang et al. (2021), proposed an integral SMC utilized to achieve LFC within the interconnected power system. The study also focused on integrating wind power and EVs into a multi-region interconnected power system to enhance stability and mitigate load frequency deviations. Similarly, Mohamed et al. (2020), a frequency control system was proposed, which integrates adaptive MPC and recursive polynomial model estimators, along with double-fed induction generator wind turbines. Mohseni & Bayati (2022), implemented a decentralized control strategy a robust multi-objective $H_2/H\infty$ delayed feedback controller for LFC in a multi-area interconnected power system. The study addresses the challenge of achieving more accurate modeling and analysis by considering limitations such as valve position, governor response, and transmission delays, ensuring the stability of the LFC system in practical applications.

In addition, the integration of RESs in recent years has resulted in larger and more structurally complex power systems. Linear controllers alone are insufficient to attain the desired level of precision in operation. To address this challenge, advanced techniques such as artificial neural networks (ANN), fuzzy logic, and meta-heuristic-based optimization algorithms have been widely adopted, effectively mitigating this issue. Furthermore, accurate tuning of the PID controller parameters is vital for a comprehensive dynamic hybrid power system model. Inadequate tuning may lead to system instability and insufficient dynamic response in frequency regulation. To address this challenge, numerous studies in the literature have aimed to optimize the PID controller's gain values using ANN (Safari et al., 2021), and Fuzzy Logic Control (FLC) (Shakibjoo et al., 2022). Although beneficial, implementing these techniques in actual LFC systems is limited by the computational time needed for rule selection in fuzzy logic and the large training dataset required for ANN. Moreover, the selection process lacks precise mathematical interpretation, occasionally leading to subpar LFC performance.

However, with the rapid growth of MMG systems and the unpredictable variations in RESs and load demand, there is a pressing need for an even more efficient controller to effectively manage these uncertainties. Conventional approaches struggle and degrade in performance with exponential uncertainty growth and lacking MG inertia impact. Maintaining stability in MG power systems remains a significant challenge due to the lack of optimal control parameter settings. To address this, researchers have introduced an alternative control concept of FOPID to enhance the performance of classical integer order controllers and increase robustness in the face of uncertainties.

The effectiveness of conventional PID controller is significantly reduced in improving system performance by changing the operating conditions and system parameters. Therefore, in order to be insistent and flexible despite all of these conditions, a FOPID has been constructed. This controller employs fractional terms in the integral and differential terms of integer order PID controllers (Babu & Saikia, 2021). The additional tuning parameters of differential-integral operators introduce a high degree of freedom (Oshnoei, et al., 2021; Tepljakov et al., 2021). The FOPID controller demonstrates significant advantages over conventional controllers in multi-microgrid power systems applications, as it effectively enhances system response by minimizing both frequency deviations and tie-line errors. The FOPID controller stands out from conventional PID controllers due to its incorporation of two extra knobs, specifically designed for controlling the integral and differential terms. These additional features contribute to its distinctive performance in various applications (Fathy & Alharbi, 2021).

In conjunction with intelligence-based heuristic methods, the FOPID controller has demonstrated significant effectiveness in diverse LFC applications for MG power systems such as using Quasi-Oppositional Sine Cosine Algorithm (QOSCA) tuned FOPID gain parameters in Guha et al. (2020), Jellyfish Search Optimizer (JSO) in Karnavas & Nivolianiti (2023), Bald Eagle Optimizer (BEO) in Agwa et al. (2022), Chaos Game Optimizer (CGO) in Barakat (2022), Cohort Intelligence Optimizer (CIO) in (Murugesan. et al., 2023).

2.7 Optimization Algorithm Techniques for Load Frequency Control

To ensure reliable control and achieve desired dynamic system performance, researchers extensively employ optimization algorithms in LFC studies (Bose & Auxillia, 2021). These algorithms are instrumental in tuning the parameters of secondary control loops, virtual inertia control loops, and demand response control loops. Over the past decade, researchers have explored the control and stability of power systems employing various algorithms. The output of the designed controller can be influenced by various factors, including the membership function, transfer function order, the number of input and output layers, and the chosen method for training the network. Therefore, to obtain the gain parameters of classical controllers for LFC in single/multi-area interconnected, and multi-microgrid power systems integrated with RES, researchers employ population-based evolutionary computational intelligence approaches such as Genetic Algorithm (GA) (Mythreyee & Nalini, 2023), PSO (Rojin & Linda, 2022), grey wolf optimization algorithm (GWO) (Singh & Gope, 2021), Mayfly Algorithm (MA) (Boopathi et al., 2023), Moth Flame Optimization (MFO) (Sanki et al., 2021), 2D Sine Logistic map-based chaotic sine cosine algorithm (2D-SLCSCA) (Khokhar et al., 2021), and numerous other methods. Various heuristic strategies have been employed to optimize PID controller parameters within LFC applications, focusing on enhancing control performance for different power system models. These approaches utilize either standard or modified PID configurations and leverage advanced optimization algorithms to achieve improved stability and dynamic response. Additionally, each method presents unique challenges and limitations, underscoring the need for continuous innovation in control techniques for LFC systems.

A review of various optimization algorithms applied to LFC in power systems reveals distinct approaches and limitations. Guha et al. (2016) employed a PID controller with the GWO in a two-area interconnected thermal power system; however, this study did not account for GRC, GDB, or nonlinearities, which often results in the algorithm becoming trapped in local optima. Nosratabadi et al. (2019) utilized a Predictive Functional Modified Proportional Integral Derivative (PFMPID) controller with the Grasshopper Optimization Algorithm (GOA) for a three-area multi-source power system that included various energy sources; nonetheless, the GOA's exploration of the search space was limited due to its initial population setup. Rai & Das (2020) explored a two-area system with PID control and the Class Topper Optimization (CTO) algorithm, finding that non-conventional power resources were not incorporated, and the CTO's extensive parameter initialization posed challenges. Paliwal et al. (2022) also utilized a PID controller with GWO for a single-area system; however, this study excluded RESs and suffered from local optima issues.

Furthermore, Sobhy et al. (2021) applied a PID controller with the Marine Predators Algorithm (MPA) to analyze two-area systems, noting that MPA's slow convergence rate limited its effectiveness. In a two-area setup with reheat turbines, Gupta et al. (2021) used PID control combined with the Hybrid Intelligent Optimization (HIO) algorithm, neglecting RESs entirely. Wang et al. (2020) adopted a PID controller with Differential Evolutionary (DE) for a two-area multi-source system but faced limitations due to nonlinearities being disregarded. Yakout et al. (2021) investigated a two-area thermal non-reheat system using a PID controller and MPA, omitting RESs, GRC, BD, and GDB in their study. Guha & Banerjee (2020) highlighted the limitations of the Whale Optimization Algorithm (WOA) in their PID-controlled two-area reheat thermal system, particularly the tendency for rapid convergence to local optima. Finally, Hasanien & El-Fergany (2019) examined a two-area thermal system with GRC and GDB using a PID controller and the Salp Swarm Optimization (SSO) algorithm, but noted that the update rule of SSO fails when certain dimensions are constrained below zero.

Individual algorithms are advantageous due to their minimum requirement for function evaluation and ease of usage throughout the whole optimization process. One notable optimization intelligence algorithm among them is the Sparrow Search Algorithm (SSA), introduced in Xue & Shen (2020), which emulates sparrows' foraging behaviour to address specific optimization problems. SSA stands out from other intelligent optimization algorithms due to its remarkable search accuracy, rapid convergence time, enhanced stability, and resilience. However, as noted in Yuan et al. (2021), SSA tends to encounter local optima issues during the later stages of convergence because of inadequate exploitation. These problems directly affect SSA's optimization, hindering the discovery of the optimal global solution.

Another widely adopted swarm intelligence algorithm is GWO, introduced by Mirjalili et al. (2021), which has gained significant traction in the optimization domain. This algorithm mimics the natural hunting and dominance behaviour of grey wolves. GWO has garnered attention for its simplicity, ease of implementation, and effectiveness in addressing various real-time optimization challenges. However, when confronted with complex, high-dimensional, and unimodal problems, GWO may become trapped in local optima due to its limited exploration capabilities (Yuan et al., 2021). Therefore, to enhance convergence speed and mitigate these issues, GWO can be combined with an algorithm possessing superior exploration abilities.

2.7.1 Grey Wolf Optimization

GWO stands out as a widely recognized swarm intelligence optimization technique. Inspired by the predatory behaviour of Grey Wolves, the algorithm mimics the process of tracking, surrounding, and hunting. Within a wolf pack, there exist various types of members distinguished by their level of dominance, such as α, β, δ, and ω. Among them, α, β, and δ represent the top three solutions, with ω leading the pack. Grey wolves collaborate within the pack to effectively hunt prey, employing a technique of chasing and surrounding their target (Sun et al., 2020). The mathematical model describing the encircling behaviour of grey wolves is captured by the following equations:

$$\vec{X}(t+1) = \frac{\vec{X}_1 + \vec{X}_2 + \vec{X}_3}{3} \tag{2.19}$$

$$\vec{X}_1 = \vec{X}_\alpha(t) - \vec{A}\cdot\vec{D}_\alpha,\ \vec{X}_2 = \vec{X}_\beta(t) - \vec{A}\cdot\vec{D}_\beta, \text{and } \vec{X}_\delta = \vec{X}_\delta(t) - \vec{A}\cdot\vec{D}_\delta \tag{2.20}$$

$$\vec{D}_\alpha = \left|\vec{C}_1\cdot\vec{X}_\alpha - \vec{X}\right|,\ \vec{D}_\beta = \left|\vec{C}_2\cdot\vec{X}_\beta - \vec{X}\right|, \text{and } \vec{D}_\delta = \left|\vec{C}_3\cdot\vec{X}_\delta - \vec{X}\right| \tag{2.21}$$

$$\vec{A} = 2\vec{a}\cdot\vec{r}_1 - \vec{a} \tag{2.22}$$

$$\vec{C} = 2\cdot\vec{r}_2 \tag{2.23}$$

$$\vec{a} = 2 - t\left(\frac{2}{T}\right) \tag{2.24}$$

where $\vec{X}(t)$ represents the current position of the grey wolf, $\vec{A}$ is a coefficient vector, $\vec{D}$ represent the distance that varies according to the place of the prey, $\vec{a}$ is a factor that reduces from 2 to 0 linearly during optimization, $\vec{r}_1$ and $\vec{r}_2$ are random number between 0 and 1, t represent as the current iteration, and T is the maximum iteration (Narinder & Singh, 2017).

To anticipate the prey's location, we consider the alpha wolf as the best solution, leading the pack and knowing the prey's whereabouts. The β and δ wolves represent the second and third-best solutions, respectively, in the current iteration (Xie et al., 2021). A is a random number in the gap $\left[-2a, 2a\right]$. The wolves move to attack the prey when the value of $|A| < 1$. Exploration is the ability to search for prey, while exploitation is the ability to attack the prey. The arbitrary values of A are used to force the wolves to move away from the prey. Furthermore, when the value of $|A| > 1$, the wolves are forced to diverge from the prey (local minimum).

2.7.2 Mountain Gazelle Optimizer

Mountain Gazelle Optimizer (MGO) is a meta-heuristic optimization technique that mimics the behaviour of mountain gazelles. It simulates gazelle's adaptive feeding and escaping strategies to solve complex optimization issues. The algorithm has been widely praised for its efficiency in a wide range of practical settings, and it was offered as a nature-inspired way to overcome the constraints of conventional optimization techniques (Abdollahzadeh et al., 2022).

Moreover, this algorithm models the behaviour of gazelles by incorporating several critical components. The gazelles' methods of foraging, evasion, and locomotion are all part of these categories (Abbassi et al., 2023). While out gathering food, gazelles constantly reorient themselves to make use of the best available data, both locally and globally. Because of this exploration-exploitation process, the algorithm is able to thoroughly investigate the whole space of possible solutions and quickly focus on the most promising regions (Sarangi & Mohapatra, 2023).

In addition, the algorithm mimics gazelles' escape from predators in the fleeing phase. Exploring diverse search space regions promotes population diversity. The algorithm can escape local optima and find globally optimal solutions by dynamically balancing the exploration and exploitation (Abdelsattar et al., 2024).

To further improve the exploration and exploitation, the MGO algorithm uses population growth, mutation, and crossover operators. The algorithm can adapt to varied issue landscapes and improve search efficiency with these strategies.

2.7.3 Sparrow Search Algorithm

SSA, a swarm intelligence optimization method, emulates sparrow foraging behaviour. It involves three types of individuals: discoverers, followers, and investigators, each updating their locations based on specific rules. Discoverers search for food and lead the community (Xue & Shen, 2020). Followers, upon discovering the location of discoverers, search for food around this area, updating their position according to Equation (2.25) (Liu et al., 2021; Zhu & Yousefi, 2021):

$$X_i^{t+1} = \begin{cases} Q \cdot \exp\left(\dfrac{X_{worst} - X_i^t}{}\right), & i > \dfrac{n}{2} \\ X_{best}^{t+1} + \left|X_i^t - X_{best}^{t+1}\right| \cdot A \cdot L, & i \le \dfrac{n}{2} \end{cases} \tag{2.25}$$

where X_{best} represents the best individual position, which it is means the best current location, X_{worst} is the current worst global location, A is a $d \times d_{matrix}$ which includes inside each factor randomly assigned 1 or -1, n represents the number of sparrows, when $i \leq \frac{n}{2}$, it proposes the ith entrant is searching for food close to the best location, if $i > \frac{n}{2}$, this implies that each member of the population needs to relocate to find food. Individuals are randomly selected from the population to act as investigators. In the event of predator attacks, signals are emitted, prompting sparrows to relocate to a secure area (Liu et al., 2021).

The mutation strategy in SSA plays a crucial role in determining convergence accuracy and speed. While SSA excels in tackling intricate optimization challenges, it suffers from drawbacks such as decreased population diversity and inadequate convergence accuracy. There's a risk of it getting trapped in local optima, thereby failing to reach the optimal solution for the problems.

However, there's a high chance of getting trapped in local optima, making it challenging for individual meta-heuristic algorithms to balance exploration and exploitation to reach the global optimum (Lu et al., 2021). Moreover, the optimization of controller gain values continues to pose a major challenge for researchers, primarily due to the increasing uncertainties in power generation and system load. To address this issue, meta-heuristic algorithms undergo various modifications aimed at enhancing their performance. A recent and widely adopted approach involves integrating chaos theory into these algorithms to boost global convergence speed and improve their exploration/exploitation capabilities, thereby fostering greater solution diversity. Another strategy involves hybridizing two algorithms.

2.8 Hybrid Optimization Algorithm Techniques for Load Frequency Control

Recently, hybrid algorithms have gained popularity and are being applied across various domains (Almotairi & Abualigah, 2022; Pozna et al., 2022; Sundararaju et al., 2022; Sureshkumar et al., 2022). Combining the characteristics and attributes of two distinct algorithms results in an optimization tool that is more reliable and powerful for addressing complex problems. It's acknowledged that amalgamating evolutionary algorithms can enhance their performance through problem-specific local searches (Gharehpasha et al., 2021). Ates & Akpamukcu (2022), proposed a hybrid monarchy butterfly optimization technique to solve the basic problem, while a stochastic multi-parameter divergence algorithm has been utilized to adjust the parameters of the basic algorithm. Zishan et al. (2022), present a particle swarm optimizer hybrid with a gravitational search optimization algorithm to obtain the PID controller parameters of the MG power system integrated with RESs. A hybrid whale optimization algorithm with ant lion optimization has been proposed in Santhoshkumar & Senthilkumar (2020) to adjust the parameters of the Virtual Synchronous Generator (VSG) in order to reduce the frequency of overshoots under sudden changes in load demand. A genetic algorithm-moth swarm optimization-based hybrid method is proposed in Mohamed & Mitani (2019) to obtain the PID controller parameters to maintain the system frequency at a minimum deviation of the islanded MG integrated with high penetration of WTG.

Similarly, in a particular study by Abdulkhader et al. (2019), the researchers presented a hybrid optimization approach that combines the dynamic genetic algorithm and bacteria forging optimizer (DGA-BFA). This algorithm was applied to determine the parameters of a type-2 fuzzy fractional PID controller. The aim was to enhance stability and improve the responsive behaviour of the MG power system. In another study by Sobhy et al. (2021), the authors introduced the MPA to determine PID controller parameters for an interconnected power system with integrated RES. The objective was to mitigate frequency deviation and heighten power system stability. Real input data from Malaysia and Egypt were employed to provide a realistic foundation for the proposed model. Similarly, a hybrid Craziness-based Particle Swarm Optimization (CRPSO) algorithm was proposed in Alayi et al. (2021) to obtain the PID controller parameters for the secondary control loop within a multi-microgrid power system integrated with RESs. The outcome of this approach was a responsive controller capable of tuning microgrid frequency and enhancing the dynamic response of the proposed model. Another innovative approach, as detailed in Elmelegi et al. (2021), hybrid Modified Particle Swarm Optimization and Genetic Algorithm (MPSOGA) is introduced. This approach is tailored for optimizing the secondary control loop parameters and VIC parameters within an interconnected power system that incorporates RESs. The low system inertia impact and the sensitivity to the load and generation fluctuations have been considered in this article. Additionally, a hybrid Particle Swarm Optimization based on Gravitational Search Algorithm (PSOGSA) was presented by Zishan et al. (2022). This algorithm is used to tune the parameters of a PID controller with the objective of minimizing frequency deviation in a MG incorporating RESs. The main objective of this research is to enhance the dynamic response of the MG and improve its stability during operation in island mode.

Collectively, these studies underscore a notable shift towards harnessing the potential of AI-based methodologies in effectively addressing the intricate challenge of optimizing controller gain values within the complex landscape of multi-microgrid systems. These innovative approaches hold the promise of not only addressing current uncertainties in power generation and load dynamics but also improving the stability, responsiveness, and performance of such systems.

2.9 Energy Storage System

Batteries are devices designed for the storage of electrical energy and operate using direct current. In order to impart inertia to the system, power electronic converters and algorithms simulating inertia are essential. The incorporation of an appropriate control algorithm alongside a battery enhances the frequency stability of a power system (Hassanzadeh et al., 2020). By quickly responding to imbalances between power generation and demand, ESS can help reduce frequency deviation and contribute to system stability (Sitompul et al., 2020). The battery is constructed of a series of cells that can change between chemical and electrical energy. There are several different types of batteries, including lead-acid, vanadium redox, sodium-sulfur, and lithium-ion.

Lead-acid stands out as the most established rechargeable battery technology, renowned for its reliability, affordability, and extended operational lifespan (Zhang et al., 2018; Zou et al., 2018). Lead-acid batteries have predominantly been employed in power system applications as uninterruptible power supplies, ensuring backup power availability. Nonetheless, their versatility extends to other recognized applications such as frequency regulation. Lead-acid batteries utilize lead, lead dioxide, and sulfuric acid as electrodes and electrolytes, respectively (Zhang et al., 2018). While their production is established and recycling rates are high, the materials pose environmental pollution risks due to their toxicity, flammability, and explosiveness. Consequently, their use in power system applications is constrained.

Vanadium-flow batteries are comprised of two cells that are partitioned by a membrane, and the electrolytes are stored remotely (Lucas & Chondrogiannis, 2016; Wang et al., 2023). The electrolytes contain electron pairs that are transported through the cells, where the electrochemical reaction occurs on immobile electrodes. Due to the fact that the electrolytes are stored remotely, there is a potential for achieving a remarkably high capacity, rendering this technology highly suitable for extensive energy storage purposes. However, vanadium-flow batteries encounter major drawbacks including high construction costs and limited availability of crucial materials for electrolytes, electrodes, and membranes (Nikolaidis & Poullikkas, 2018). They also suffer from lower energy density compared to other battery technologies, leading to constrained development with only a few ongoing projects.

Sodium-sulfur batteries exhibit distinct characteristics in comparison to conventional rechargeable batteries due to their utilization of liquid electrodes and a solid electrolyte. The negative and positive electrodes are comprised of molten sodium and sulfur, respectively, while a solid ceramic tube serves as the electrolyte, effectively separating the electrodes (Zhang et al., 2020). Operating at temperatures between 300-350 ^{o}C, sodium-sulfur batteries are classified as high-temperature batteries, necessary to maintain the electrodes in a liquid state. Sodium and sulfur, both economical, environmentally friendly, and plentiful, make sodium-sulfur batteries ideal for large-scale production (Al-Humaid et al., 2021). These batteries boast high energy density, efficiency, and usefulness in power system applications, particularly load leveling. However, practical drawbacks arise, notably the higher risk of fires due to their operating temperature of 300-350 ^{o}C, emphasizing the critical importance of safety.

Lithium-ion batteries are the most common type of battery used in LFC power applications due to their properties (quick response time, high power capacity, extended cycle life at partial cycles, low self-discharge rate, etc.) (El-Bidairi et al., 2020; Stroe et al., 2017). Lithium-ion batteries typically feature a graphite anode, a cobalt-based lithium metal oxide cathode, and an organic liquid electrolyte containing lithium salt. Their electrodes possess highly porous structures with multiple layers, facilitating the extensive storage of lithium ions. This capacity to accommodate ions elucidates why lithium-ion batteries exhibit the highest energy densities among all battery technologies (Yu et al., 2024).

However, the choice of battery and energy storage system is critical for maintaining frequency stability. As described by Delille et al. (2012), the ultra-capacitor-based distributed energy storage system stands out for its rapid response time, indicating its potential to enhance inertia emulation power. The frequency modulation of a standalone microgrid with significant RES penetration was studied in (Sanjareh et al., 2021; Dashtdar et al., 2022; Moradi & Amiri, 2021). Introducing batteries into low-inertia MGs could aid in maintaining stability. Conversely, a sudden demand for power from the grid puts strain on the battery. Therefore, to minimize stress on the battery during discharge and charging cycles and optimize its lifespan, a combination of controller techniques is required. These techniques should provide inertial response and maintain stability in the power system.

The dynamic expression of the ESS model can be represented as (Siti et al., 2022),

$$SOC(t+1) = SOC(t) + \eta_{ch} P_{ch}(t) - \eta_{des}^{-1} P_{des}(t) \tag{2.26}$$

where $P_{ch}(t)$ and $P_{des}(t)$ are the charging and discharging power flow of the ESS, respectively; SOC(t) is the state of charge; η_{ch} and η_{des} are the efficiency of the charging and discharging, respectively; t is the sampling time.

The transfer function of the ESS can be written as a first-order lag:

$$\Delta G_{ESS} = \frac{\Delta(P_{ch} - \Delta P_{des})}{\Delta\omega} = \frac{K_{ESS}}{1 + T_{ESS}} \tag{2.27}$$

where K_{ESS} and T_{ESS} are the gain constant and time constant of the ESS, respectively.

2.10 Controller Approach Validation Methods

Validating the performance of power system frequency controller techniques before implementation is essential. One important validation method is the IEEE 39-bus New England test system, which helps researchers verify the designed controller's effectiveness. Another crucial technique is using the Opal-RT digital simulator, a real-time simulation platform for high-fidelity plant simulation, prototype testing, performance evaluation, and embedded data acquisition and control.

2.10.1 New England IEEE-39 Bus Test System

The New England test system serves as a standard platform for testing new methodologies in power system analysis and control synthesis. The IEEE-39 bus system offers a realistic network representation and diverse load characteristics, making it an ideal platform for assessing the efficacy and performance of different LFC strategies (Bevrani, 2014; Patel & Beik, 2021; Ramachandran et al., 2021). Its intricate design provides researchers and practitioners with valuable insights into the complexities of frequency regulation in interconnected power grids. This aids in developing resilient and efficient control algorithms, essential for maintaining grid stability and reliability (Hussain et al., 2022; Mahmud et al., 2023). This approach is widely utilized by numerous researchers for testing load LFC techniques in power systems.

Ramachandran et al. (2021), utilized the New England 39-bus system to assess the efficacy of their proposed control technique in a multi-area power system. They employed a hybrid optimization algorithm, an extension of the Hopfield neural network, to derive the parameters of the FOPID controller for LFC in the proposed power system. Similarly, Cai et al. (2023), utilized a modified New England test system to evaluate the power system's stability under the frequency load-shedding control technique. The IEEE 39-bus New England test system was employed to assess the effectiveness of the proposed control strategy in various studies. In the study by Kumar & Pan (2022), a frequency-domain approach was utilized to design a FOPID controller cascaded with a first-order filter for LFC systems with communication delay. Additionally, an adaptive under-frequency load-shedding scheme was evaluated by Chandra & Pradhan (2021); Li et al. (2020). Moreover, in the study by Shakibjoo et al. (2022), an optimized Type-2 Fuzzy Frequency Control for Multi-Area Power Systems was tested.

2.10.2 Real-Time Digital Simulation

RT LAB software and MATLAB are integrated into the Opal-RT system for real-time simulation and further validation. RT LAB software supports MATLAB in building the real-time simulation platform and offers a communication mode between the host PC and the RT emulator (Mishra et al., 2023). For real-time simulation, the accuracy of the dynamic model and the time taken to produce outcomes determine computational precision. To validate a test system in real time, the emulator's variables must be precise, and the simulation outputs must match the time duration of their physical counterparts.

Opal-RT simulators have been widely used to validate various controller approaches proposed by researchers (Saxena & Shankar, 2022). For instance, they have been utilized to validate the technique proposed by Bubshait & Simões (2018; Karad et al. (2024), which optimizes wind turbine operation by de-loading turbine power by controlling both pitch angle and rotor speed. Acharya et al. (2018) employs Opal-RT to validate a proposed frequency control scheme that includes demand-side management for an islanded MG integrated with RESs. Meanwhile, Gheisarnejad & Khooban (2019) applies the same methodology to validate an adaptive secondary controller designed for a Multi-Microgrid system. This validation ensures that the controller can dynamically adjust to varying conditions within the interconnected MGs, maintaining stability and optimal performance across the system.

2.11 Summary

This chapter conducts a comprehensive survey of literature pertaining to LFC within power systems. It explores a wide array of topics, such as conventional power system models, and recent advancements in LFC methodologies—including inertia control loops, primary and secondary control loops, and their integration with demand response controllers—to address various aspects of modern power systems. These aspects include regulated systems, deregulated systems, MG, and MMG. Additionally, the chapter provides a concise overview of different control strategies utilized in LFC. Through the literature survey, the study has identified and addressed the following research gaps:

In the literature, various swarm intelligence optimization algorithms have been introduced and investigated to address the challenge of system frequency stability in both regulated and deregulated power systems. However, as convergence progresses, many of these optimization algorithms tend to encounter local optima due to inadequate exploitation. These challenges directly affect the optimization process, leading to difficulties in identifying the optimal global solution. Therefore, considering the strengths and weaknesses of optimization algorithms, employing a hybrid method emerges as a potential solution to overcome limitations and leverage the benefits of both algorithms simultaneously.

Numerous researchers have utilized derivative control methods with integer derivative orders to tackle the issue of insufficient equivalent system inertia. However, this strategy leads to an increase in the virtual inertia constant value for the VIC system.

Consequently, a greater ESS capacity is necessary to adequately mitigate active power fluctuations during disturbances.

The studies mentioned earlier propose a combination of the DR control technique with ESS units integrated into LFC to improve system stability. However, it is important to note that these studies do not take into account the potential benefits of this technique in reducing stress on the ESS during discharging and charging periods. Such stress on the ESS can significantly impact the battery's lifetime and overall performance.

The controller gain values obtained from the above classical method have improved MG system efficiency and robustness. However, with the rapid growth of multi-microgrid systems and the unpredictable variations in RESs and load demand, there is a pressing need for an even more efficient controller to effectively manage these uncertainties. To address this, researchers have introduced an alternative control concept of FOPID to enhance the performance of classical integer order controllers and increase robustness in the face of uncertainties.

CHAPTER 3

METHODOLOGY

3.1 Introduction

This chapter presents an overview of the methodology utilized in this research. The methodology is employed with the intention of achieving three specific objectives. The first objective is to develop an SSA optimization algorithm by integrating it with the GWO algorithm, creating a hybrid algorithm combining SSA and GWO named (SSAGWO). Initially, SSA is used to tune the PID parameters to regulate frequency deviation in a two-area interconnected power system under deregulated conditions. This system includes a reheat turbine generator in each area integrated with RESs. The proposed model considers nonlinearities such as GRC and GDB. Next, a two-area power system with integrated RESs is constructed in MATLAB/Simulink to evaluate the robustness of the proposed SSAGWO algorithm in tuning the PID controller parameters of the secondary control loop under regulated conditions.

The second objective focuses on developing a fractional virtual inertia control technique to support power systems with the required inertia. This objective involves the creation of a hybrid optimization algorithm (SSAMGO) by integrating the SSA and MGO algorithms. The proposed SSAMGO algorithm is designed to optimize controller parameters and estimate the optimal values of virtual inertia and virtual damping. The goal is to enhance frequency regulation in both islanded and grid-connected MMG systems integrated with RESs. Furthermore, SSAMGO is used to optimize the secondary LFC along with the VIC to mitigate frequency deviations in the microgrid.

The third objective aims to improve system stability by integrating the proposed FDVIC with a DRC. This integration is intended to enhance frequency stability, reduce the stress on ESS, and extend the battery life by minimizing the amount of active power drawn from ESS during charging and discharging periods. Additionally, it focuses on reducing the frequency variations and power fluctuations on tie lines during load disturbances in low-inertia MMG systems integrated with RESs, ultimately improving the overall system's frequency response.

Finally, the fourth objective addressed in this study involves validation through Real-Time Digital Simulation Experiments using the Opal-RT simulator. Two validation scenarios are considered to validate the optimization of the designed FDVIC controller parameters through the proposed SSAMGO. In the first scenario, the MMG power system operates in islanded mode, introducing uncertainty in the demand load. The second scenario entails two interconnected microgrid power systems with a large-scale power system in grid-connected mode, considering the capacity of the 39-bus IEEE New England test system. Figure 3.1 presents a schematic depiction of the research framework.

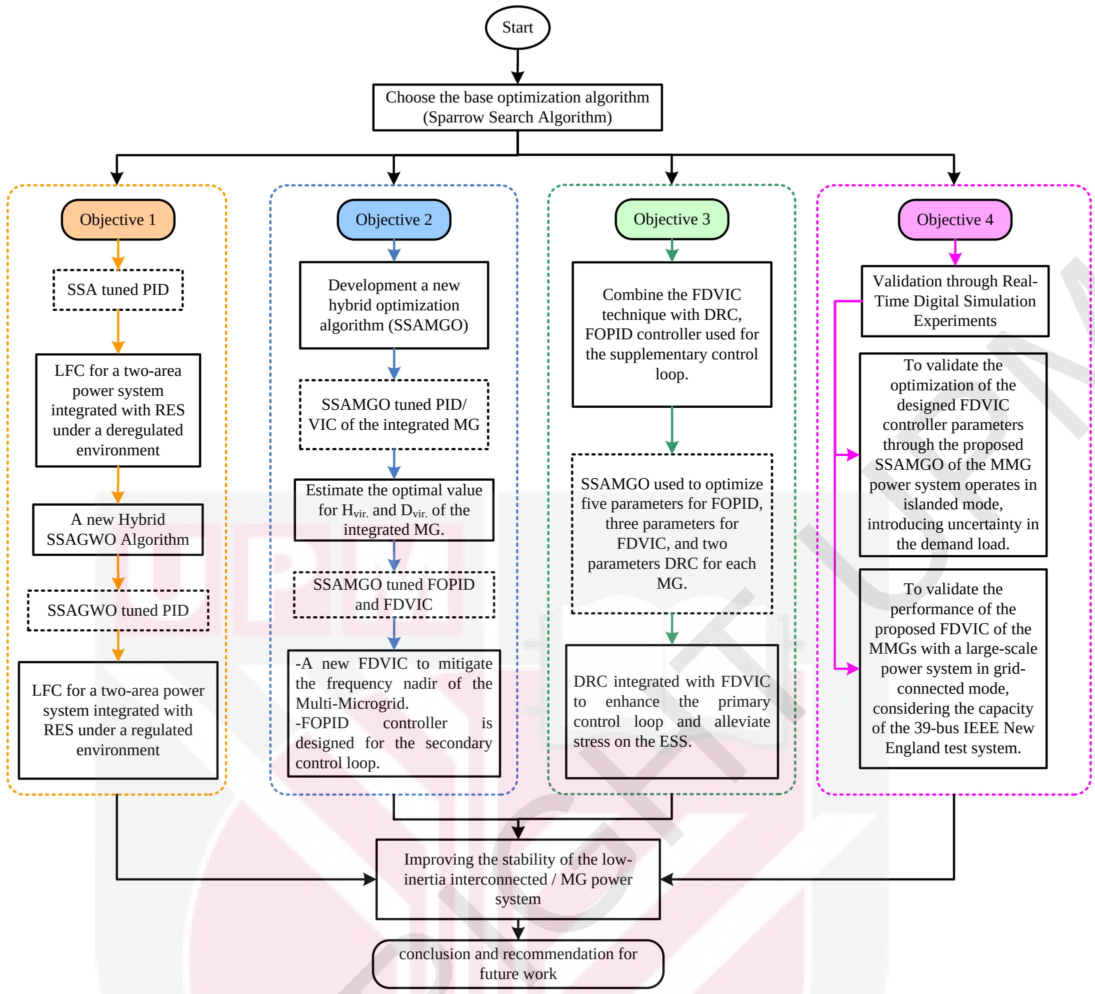

Figure 3.1 : A flowchart illustrating the entirety of the research process

3.2 LFC of the Interconnected Power System Based on SSAGWO Algorithm

The first objective of this study is to propose a new hybrid SSAGWO algorithm. First, SSA will used to optimize PID controller parameters to regulate frequency deviation in a two-area interconnected power system with reheat turbine generators and RESs under deregulated conditions. Then, SSAGWO's performance in tuning PID controller parameters for the secondary control loop of a two-area power system with RES integration under regulated conditions will be assessed.

3.2.1 LFC of the Deregulated Power System Based on SSA Algorithm

The first objective involves examining the deregulated energy system represented in Figure 3.2. This system consists of two equal areas, each with a capacity of 2000 MW. Base load power generation is facilitated by a reheat steam energy system in both areas, supplemented by renewable energy sources. Area 1 incorporates a solar thermal energy system (STES), while area 2 integrates a geothermal station. The parameters of the proposed power system model shown in Appendix A. This study involves GENCO1 and GENCO2 operating as generation companies, and DISCO1 and DISCO2 functioning as distribution companies in area-1. Meanwhile, in area-2, GENCO3, GENCO4, DISCO3, and DISCO4 serve as generation and distribution entities, respectively.

In order to achieve a balance between GENCOs and DISCOs, Independent Contract Administration (ICA) creates a contract based on the rules between the cooperating companies (Peddakapu et al., 2022). These contracts should be deals with all possibilities of the operating scenarios like bilateral, poolco, and contract violation or a combination of them (Marzbali, 2020). Under the rules of the poolco agreement, each DISCO is required to fulfill its power requirements using only the generators located inside its own area. However, the bilateral agreement allows each DISCO to negotiate contracts with any GENCO in any region (Kumar et al., 2022). DPM is used to derive a connection between GENCOs and DISCOs. DPM consists of a number of rows equal to the number of GENCOs and the number of columns equal to the number of DISCOs of the proposed power system. A standard description of the DPM for the system model under consideration is presented in Equation (3.1).

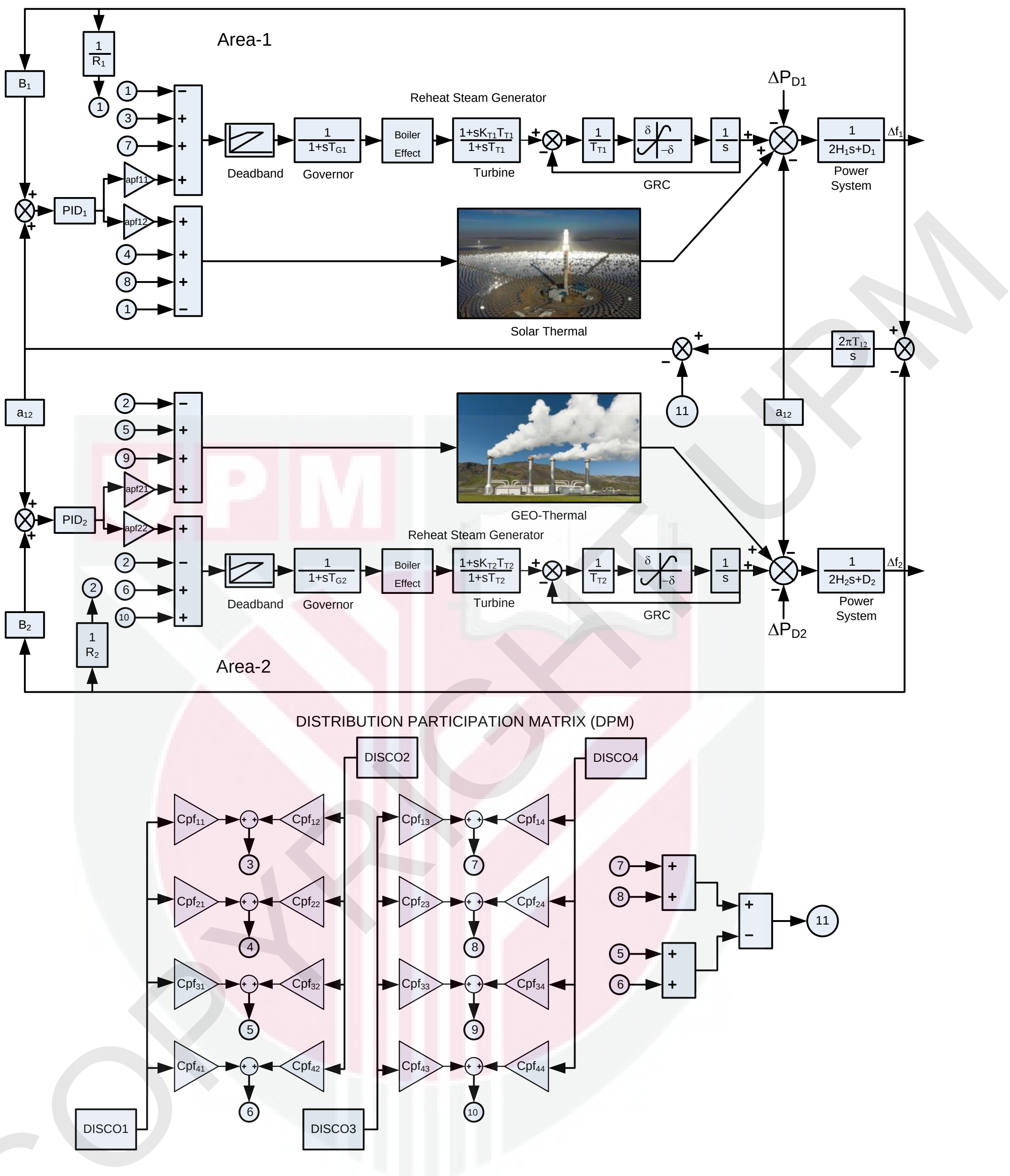

Figure 3.2 : Block diagram of the two areas deregulated energy system

$$\text{DPM}=\begin{bmatrix} cpf_{11} & cpf_{12} & cpf_{13} & cpf_{14} \\ cpf_{21} & cpf_{22} & cpf_{23} & cpf_{24} \\ cpf_{31} & cpf_{32} & cpf_{33} & cpf_{34} \\ cpf_{41} & cpf_{42} & cpf_{43} & cpf_{44} \end{bmatrix} \tag{3.1}$$

Each element in the DPM, denoted as cpf_{ij}, signifies the proportion of the total load demand contracted by DISCO 'j' from GENCO 'i'. The power generated by each GENCO should precisely match the cumulative demands from all DISCOs with whom power contracts are established. The total power delivered from GENCOs can be calculated from the Equation (3.2).

$$\Delta P_i = \sum_{j=1}^{k} cpf_{ij} \Delta P_{Lj} \tag{3.2}$$

where k is the number of DISCOs, ΔP_{Lj} is the contracted power demand.

Within a deregulated energy sector, DISCOs have the flexibility to contract with GENCOs within their area as well as in other areas. This leads to variability in the scheduled tie-line power of any given area, corresponding to fluctuations in DISCOs' demand. Thus, the net planned steady-state power flow from an area can be expressed as follows, with a mathematical formulation provided for determining the scheduled tie-line power flow connecting area 1 and area 2:

$$\begin{aligned} \Delta P_{tie12}^{scheduled} &= (\text{Demand of DISCOs in area 2 from GENCOs in area 1}) \\ &\quad - (\text{Demand of DISCOs in area 1 from GENCOs in area 2}) \end{aligned}$$

$$\Delta P_{tie12}^{scheduled} = \sum_{i=1}^{2}\sum_{j=3}^{4} cpf_{ij}\Delta P_{Lj} - \sum_{i=3}^{4}\sum_{j=1}^{2} cpf_{ij}\Delta P_{Lj} \tag{3.3}$$

To calculate the scheduled tie-line power of the proposed model, Equation (3.3) is solved as follows:

$$\begin{aligned} \Delta P_{tie12}^{scheduled} &= (cpf_{13}\,\Delta P_{L3} + cpf_{14}\,\Delta P_{L4} + cpf_{23}\,\Delta P_{L3} + cpf_{24}\,\Delta P_{L4}) \\ &\quad - (cpf_{31}\,\Delta P_{L1} + cpf_{32}\,\Delta P_{L2} + cpf_{41}\,\Delta P_{L1} + cpf_{42}\,\Delta P_{L2}) \end{aligned}$$

At any time, the tie-line power error is defined as:

$$\Delta P_{tie12}^{error} = \Delta P_{tie12}^{actual} - \Delta P_{tie12}^{scheduled} \tag{3.4}$$

where,

$$\Delta P_{tie12}^{actual} = (\Delta f_1 - \Delta f_2)\frac{T_{12} \cdot 2\pi}{s} \tag{3.5}$$

At the steady-state, the value of the tie-line power error should be equal to zero.

A PID controller is utilized for decentralized control in the proposed model. Figure 3.3 depicts the closed-loop control of the system. PID controllers are widely used in industrial automatic control applications due to their functional simplicity. Due to their simplicity and intuitive nature, PID controllers can deliver satisfactory performance across a broad spectrum of processes.

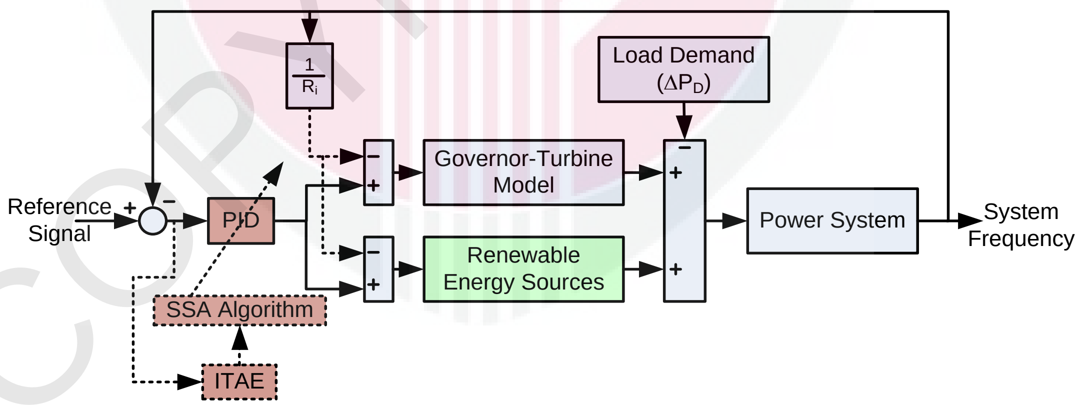

Figure 3.3 : Closed loop control system tuning of the deregulated energy system

The controllers' main control actions can be straightforwardly categorized as follows: proportional action, which depends on the current error value; integral action, which relies on the past error value; and derivative action, which is influenced by the future error value (Kerdphol et al., 2021). The decentralized PID controller's transfer function and control output are described accordingly:

$$K(t) = K_p + \frac{d}{dt}K_i + \int K_d dt \tag{3.6}$$

where K_p, K_i, and K_d denote the proportional, integral, and derivative gains of the PID controller, respectively. ACE, as depicted in the following equations, regulates both the frequency deviation and the error in tie-line power variation.

$$ACE_1 = B_1 \Delta f_1 + \Delta P_{tie12}^{error} \tag{3.7}$$

$$ACE_2 = B_2 \Delta f_2 + \Delta P_{tie21}^{error} \tag{3.8}$$

The feedback control signal of the proposed controller, denoted by u(t), can be represented as follows:

$$u(t) = (K_p + \frac{d}{dt}K_i + \int K_d dt) \times ACE \tag{3.9}$$

In this study, the integral time absolute error (ITAE) is utilized as the objective function (J) to adjust the parameters of the PID controller. Minimizing the ACE via ITAE improves performance by decreasing the settling time and undershoots of the controlled plant. The objective function is defined as:

$$J = ITAE = \int_0^t t \cdot |ACE_i| dt = \int_0^t t \cdot \{|\Delta f_i + \Delta P_{tie,ij}|\} dt \tag{3.10}$$

where i and j are the area numbers from 1,2,3, 4…. n with $i \neq j$. Under the conditions of the following inequalities:

$$K_p^{min} \leq K_{pi} \leq K_p^{max},\ K_i^{min} \leq K_{ii} \leq K_i^{max},\ K_d^{min} \leq K_{di} \leq K_d^{max} \tag{3.11}$$

An intelligent SSA is proposed to obtain the optimal values of the PID controller parameters to maintain the frequency deviation in the proposed two-area interconnected power system.

The SSA optimization technique is classified as a swarm intelligence optimization method. This technique simulates the foraging behaviour of sparrows. It includes three individual behaviour types: discoverer, follower, and investigator. The sparrows update their locations in accordance with their own rules (Wang et al., 2021). The discoverer looks for food and serves as a guide for the rest of the population (Ouyang et al., 2021). The discoverer's location is updated by Equation (3.12).

$$X_i^{t+1} = \begin{cases} X_i^t \times \exp\left(\dfrac{-i}{\alpha \cdot T_{max}}\right), & R_2 < ST \\ X_i^t + Q \cdot L, & R_2 \geq ST \end{cases} \tag{3.12}$$

where t denotes the current iteration; n is the population of sparrows; d represents the dimension of the variables; T_{max} is the iteration maximum number; X_i^t is the location of the i^{th} sparrow at iteration t; α is a random number between 0 and 1; R_2 is the alarm value which is $0 < R_2 \leq 1$; The safety threshold is ST and its value $0.5 \leq ST < 1$; L is a $1 \times d_{matrix}$; d_{matrix} is the matrix including 1 in each factor; Q is a random value with a mean of zero and a variance of one that follows the normal distribution; If $R_2 < ST$, it indicates that the foraging surroundings are safe, while $R_2 \geq ST$ denotes that some individuals already have faced dangerous animals and that all sparrows must flee to other safe locations as soon as possible (Liu et al., 2021).

After discovering the location by the discoverers, followers will conduct to search for food around this location. The follower's location will be updated according to Equation (3.13) (Zhu & Yousefi, 2021):

$$X_i^{t+1} = \begin{cases} Q \times \exp\left(\dfrac{X_{worst} - X_i^t}{i^2}\right), & i > \dfrac{n}{2} \\ X_{best}^{t+1} + \left|X_i^t - X_{best}^{t+1}\right| \cdot A \cdot L, & i \le \dfrac{n}{2} \end{cases} \tag{3.13}$$

where X_{best} represent as the best individual position which it is mean the best current location; X_{worst} is the current worst global location; A is a $d \times d_{matrix}$ which include inside each factor randomly assigned 1 or -1; n represent as the number of sparrows; when $i \le \frac{n}{2}$, it proposes the i^{th} entrant is searching for food close to the best location, if $i > \frac{n}{2}$, that's mean the i^{th} entrant need to fly to another location for food.

Individuals from the population are chosen at random to be investigators. When predators attack, they will send out signals that will cause sparrows to flee to a safe location (Liu et al., 2021). The following formula simulates the investigators' behaviour:

$$X_i^{t+1} = \begin{cases} X_{best}^t + \beta\left|X_i^t - X_{best}^t\right|, & f_i > f_b \\ X_{best}^{t+1} + K\dfrac{\left|X_i^t - X_{best}^t\right|}{(f_i - f_w) + \varepsilon}, & f_i = f_b \end{cases} \tag{3.14}$$

where β denotes the random step length control coefficient, which has a variance of 1 and a mean value of 0 and follows the normal distribution; K is random number between -1 and 1; f_i is the fitness value of the i^{th} individual; f_b is the current global best fitness; f_w is the current global worst fitness; To avoid the zero-division-error, ε represents the smallest parameter. When $f_i > f_b$, that's means the sparrow locate at the edge of the colony. If $f_i = f_b$, it means that the sparrows in the center of the colony are aware of the danger and should fly closer to a safe location (Yuan et al., 2021). The mutation strategy in SSA directly affects convergence accuracy and speed. The SSA shows better performance in solving complex optimization problems.

Two RESs are integrated into area 1 and area 2, serving as generation companies. Solar Thermal Generator (STH), in recent years, STH systems have been commonly used to generate heat energy and electricity. The solar thermal energy station consists of trough collectors, several dishes to reflect the sun's heat, a central receiver, and a linear fresnel reflector. These systems often concentrate the sun's rays into a narrow beam, which is then used to raise the temperature of a fluid (which is usually oil or melting salt due to their high boiling temperatures) (Barik & Das, 2019). The extremely heated fluids exchange heat with water to produce steam, which can turn a turbine to generate electricity. The transfer function of the solar thermal energy system is depicted in Equation (3.15) (Irudayaraj et al., 2022):

$$\Delta P_{STH} = \frac{K_T}{1+sT_T} \cdot \frac{K_S}{1+sT_S} \tag{3.15}$$

where K_T, T_T, Ks, and T_S are gain of the system turbine, the turbine charging time constant, solar collector gain, and time constant of the solar collector.

Geothermal power stations (GEO), which use the heat stored deep inside the earth to produce electricity, are another promising form of renewable energy. The high-pressure (> 7 bar), high-temperature (140-250 degrees Celsius) stream is injected straight into the geothermal power plant. According to the International GEO Association (IGA), the capacity that has been installed around the world is around 12.636 GW, and it has produced 73.549 GWh of electrical energy. The linearized transfer function model of the governor and turbine of the geothermal energy conversion is considered in this study as follows (Latif et al., 2019):

$$\Delta P_{Geo} = \frac{K_{gg}}{1+sT_{gg}} \cdot \frac{K_{tg}}{1+sT_{tg}} \tag{3.16}$$

where K_{gg}, T_{gg}, K_{tg}, and T_{tg} are governor gain, governor time constant, turbine gain, and turbine time constant.

3.2.2 LFC of Two-area Power System Based on Hybrid SSAGWO Algorithm

This section explores the enhancement of SSA performance through hybridization with the GWO algorithm. The hybrid optimization algorithm will be utilized to determine the optimal value of the controller parameters for the large-scale two-area power system integrated with RESs. The model will first be described in detail, including all non-linearity factors. Then, the control strategy employed will be discussed. Finally, the hybridization technique of the SSAGWO will be explained.

a. Two-area Power System Model Description

The model proposed in this study comprises a two-area reheat steam power turbine integrated with RESs such as PV and WT Power Generator conversion, as depicted in Figure 3.4. Two symmetrical power generator areas have been proposed with the parameters shown in Appendix A (Irudayaraj et al., 2020; Veerasamy et al., 2019).

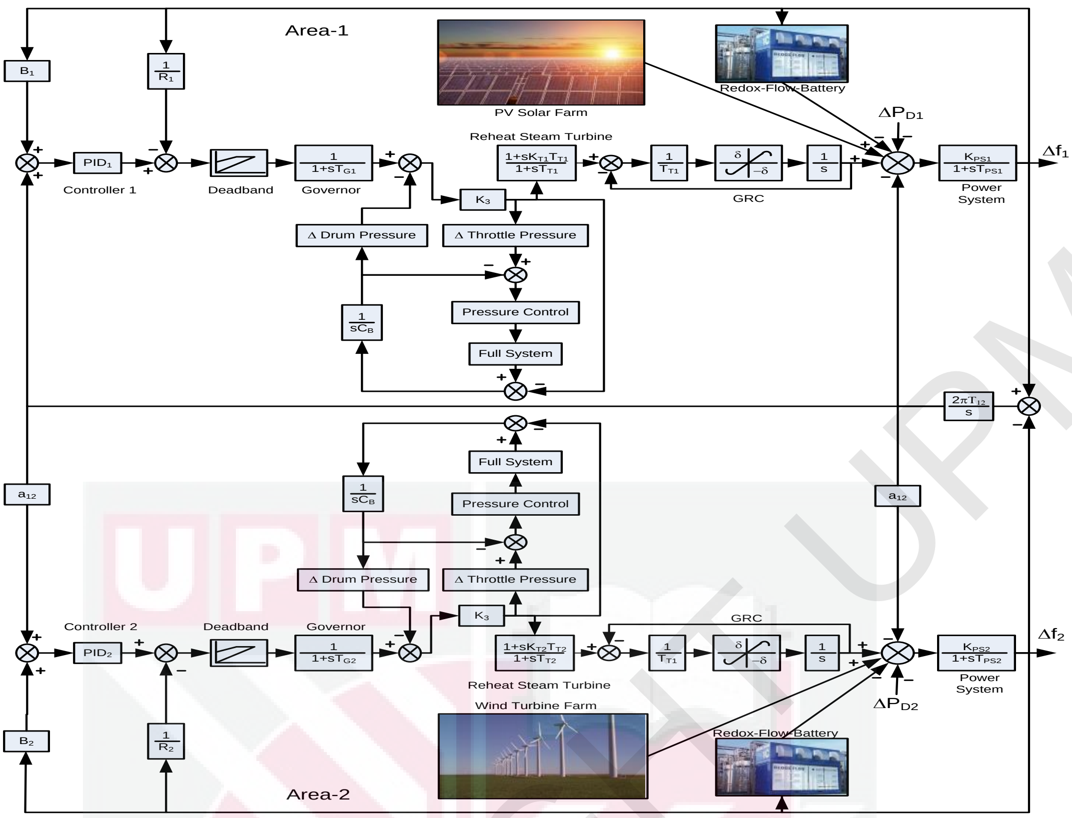

Figure 3.4 : Transfer function model of the two-area power system

In traditional steam plants, adjustments in power output are initiated through turbine control valves, while boiler controls promptly react to fluctuations in steam flow and pressure variances. The study incorporates the pressure effects of a drum-type boiler, which are a result of its dynamics in generating steam under pressure. The GRC is a vital factor for achieving realistic load frequency control in power systems. It accounts for the sensitivity of power generator turbines (Irudayaraj et al., 2022). Systems with GRC exhibit notable differences in dynamic response compared to those without, featuring larger overshoots and longer settling times. In this study, a GRC value of 0.05% is considered (Veerasamy et al., 2022). Conversely, the dead band in thermal steam units is a result of backlash in the linkage connecting the servo pistons to the camshaft. Thus, for this study, the maximum value of the dead band is established at

10%. The reheat thermal system and RES generation unit's nonlinearity are mathematically linearized around specific operating points, leading to a first-order transfer function described as follows:

PV cells, comprised of semiconductor materials, can convert photon energy directly into electrical energy. Power loss is also modelled because of the boundary and external contact, represented by series resistors, and a leakage current, represented by parallel resistance. PV power generation is intermittent and dependent on sun irradiation and temperature; thus, a random power source can represent PV behaviour (Abou El-Ela et al., 2021). The block diagram of the PV is shown in Figure 3.5. The linearized PV model, which is considered for the ALFC model, is given by:

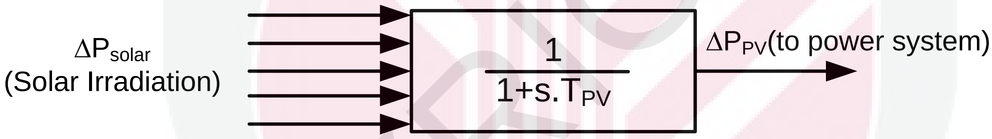

Figure 3.5 : Block diagram of PV dynamics system

where T_{PV} is the time constant of the PV, ΔP_{Solar} is the change in solar irradiation power, and ΔP_{PV} denotes the change in power generated from solar to the power system.

The mathematical model implementation for the wind power plant comprises a hydraulic pitch actuator, data fit pitch response, and blade characteristics, as shown in Figure 3.6. The pitch angle control mechanism keeps the pitch angle at the desired value based on wind speed. Thus, wind turbine production may be controlled by adjusting the pitch angle regardless of wind speed. The wind's mathematical modeling transfer function model can be given as (Oshnoei, et al., 2021):

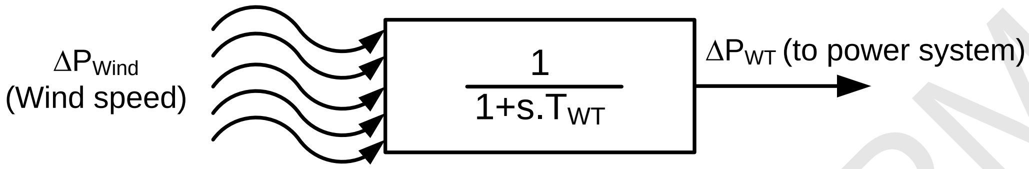

Figure 3.6 : Block diagram of Wind turbine dynamics system

where T_{WT} is the time constant of the Wind turbine, ΔP_{Wind} is the change in wind speed, and ΔP_{WT} is the change in power generated by the power system.

Redox Flow Battery (RFB) is a type of electrochemical energy storage device that converts energy between electrical and chemical forms through electrochemical reaction processes (Dhandapani et al., 2018). RFB is an efficient method for reducing frequency deviations and tie-line power, making it a fast and effective active power compensation device. The primary function of the RFB is to charge and store energy from the power system as a small load under normal operating conditions, and to discharge this stored energy during sudden load changes, thereby mitigating frequency fluctuations. The block diagram model of the RFB integrated with areas 1 and 2 is shown in Figure 3.7 (Oshnoei, et al., 2021).

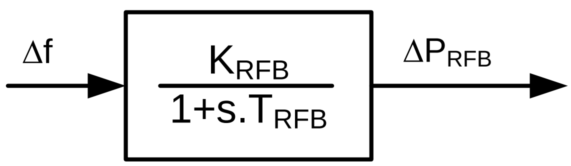

Figure 3.7 : Block diagram of Redox-Flow-Battery model

where T_{RFB} and K_{RFB} are the time constant and the gain of the RFB, respectively.

b. Control Strategy of the Hybrid Power System

The close loop of the two-area hybrid power system can be simplified as shown in Figure 3.8. Controller design and objective function selection for designing control parameters have a significant impact on power system performance. PID controller has been used for the secondary control loop.

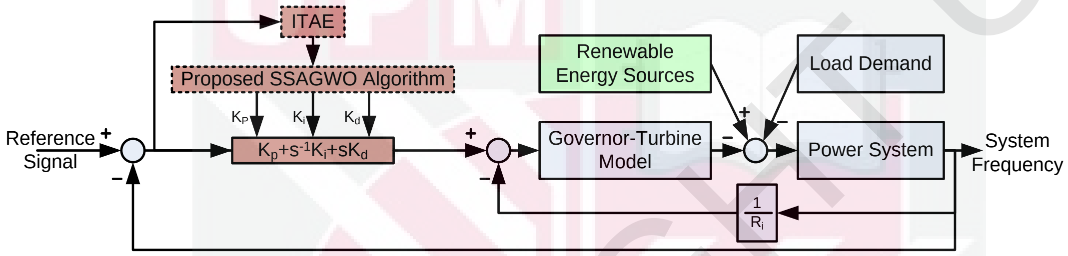

Figure 3.8 : Closed loop control system tuning

Designing a PID controller for regulating the frequency of a hybrid power system involves tuning the controller's gain values. Optimization methods offer a systematic approach to determining the most suitable values for these gains. This procedure usually entails defining ranges for each gain parameter and utilizing optimization algorithms to explore these ranges, aiming to minimize certain performance criteria. Usually, one or more performance indices (PIs) of the controller, such as Integral Absolute Error (IAE), Integral Time Absolute Error (ITAE), Integral Square Error (ISE), and Time Weighted Squared Error (ITSE), are utilized (Sundararaju et al., 2022).

ISE is often chosen in optimization-based design approaches for managing step changes in set-point or load because of its mathematical tractability. However, prioritizing smaller errors with ISE can lead to higher controller gains, oscillatory responses, and reduced robustness (Paliwal et al., 2022). To mitigate these issues, IAE or ITSE criteria can be utilized, offering a more balanced approach to tuning controller gains by giving greater weight to small errors. On the other hand, the ITAE is used to suppress the small errors that prolong for a longer time period. This is achieved, as time period (t) amplifies the integral value of small errors. If the error persists for a longer time period, then ITAE criteria can be used to tune the gain values of the controller. Also, this method reduces the settling time of the system response. Hence, the ITAE index has been chosen for tuning the gain parameters of the controller (Fathy & Alharbi, 2021).

The transfer function of the PID controller is given by:

$$C(s) = k_p + \frac{k_i}{s} + sk_d \tag{3.17}$$

where k_p is the proportional gain, k_i is the integral gain, and k_d is the derivative gain.

The PID controller output of the hybrid power system is as follows:

$$u_{1,2} = k_{pi}ACE_{1,2} + k_{ii}\int_0^t ACE_{1,2}dt + k_{di}\frac{d}{dt}ACE_{1,2} \tag{3.18}$$

The gain of the PID controller in this study is designed to minimize the steady-state error guides, such as the performance index ITAE as given below:

$$J = ITAE = \int_0^t t\left|ACE_i\right|dt = \int_0^t t\left\{\left|\Delta f_i + \Delta P_{tie,i-j}\right|\right\}dt \tag{3.19}$$

where i and j are the area numbers from 1,2,3, 4…. n with $i \neq j$.

This objective aims to minimize J by tuning the values of PID controller parameters by using the proposed new hybrid SSAGWO.

c. Proposed Hybrid SSA-GWO

In this section, an effort was made to develop a new hybrid metaheuristic algorithm that combines the strength of swarm-inspired algorithms like SSA with GWO to tune the values of the PID controller for a multi-area power system.

A new hybrid sparrow search algorithm based on the GWO, namely SSAGWO, is proposed in this study. Its features allow the SSAGWO to avoid the local optimum while improving convergence speed and accuracy. The exploitation capability of the GWO is introduced into the sparrow search algorithm to improve its exploitation ability. The modification in the structure of SSA is improving the exploitation ability by using the behaviour of exploration ability in GWO to compromise between exploitation and exploration. Improving the exploitation in SSA with the exploration effort should be achieved by hybridization between SSA and GWO. The variants of the position of SSA Equation (3.13) are mixed with the distance equation of GWO by new weight factor (θ) to keep the problem's final solutions near the optimal values. The modification-guided equations are rewritten as follows:

$$\vec{D}_\alpha = \left|\vec{C}_1 \cdot \vec{X}_\alpha - \theta\vec{X}\right|,\ \vec{D}_\beta = \left|\vec{C}_1 \cdot \vec{X}_\beta - \theta\vec{X}\right|,\ \text{and}\ \vec{D}_\delta = \left|\vec{C}_1 \cdot \vec{X}_\delta - \theta\vec{X}\right| \qquad (3.20)$$

where α, β, and δ are the best three solutions of the grey wolf who leads the pack, $\vec{D}$ represent the distance that varies according to the place of the prey, $\vec{X}$ represents the current position of the grey wolf, $\vec{C} = 2 \cdot \vec{r}_2$, $\vec{r}_2$ is a random number between 0 and 1.

The probability of shifting the position of all agents is calculated using Equation (3.21):

$$\Gamma\left[X(t+1)-X(t)\right]=\left|\frac{\left[X(t+1)-X(1)\right]}{\sqrt{\left[X(t+1)-X(t)\right]^{2}+1}}\right| \tag{3.21}$$

where Γ is the probability factor. If the result of $\left[X(t+1)-X(t)\right]$ is positive, the sparrows select the food, while if the result is negative, the sparrow moves far away from predators. It is worth noting that the correct position is quickly achieved by well-selecting the boundaries of the PID factors.

The specific procedures of the SSAGWO for tuning the parameters of the PID controller are outlined in detail as follows: First, the sparrow search population and its parameters are initialized. While the current iteration is less than maximum iteration, the sparrows are ranked according to their fitness values by minimizing J in Equation (3.19). The current best value, corresponding to the minimum fitness, and the current worst value, indicating the maximum fitness, are then identified.

Next, the location of the discoverer is updated using Equation (3.12). If the i^{th} individual at the current iteration is less than or equal to half the sparrow's population, the position of the followers is updated using Equation (3.13), followed by updating the investigator's location with Equation (3.14). If this condition is not met, the GWO algorithm is executed.

The values of a, A, and C are initialized, where a decreases linearly from 2 to 0 during the optimization process, $a=2-t\left(\frac{2}{T}\right)$. Here, t represents the current iteration, T is the maximum number of iterations, and $\vec{A}$ is a coefficient vector, $\vec{A} = 2\vec{a} \cdot r_1 - \vec{a}$, r_1 is a random number, C, between 0 and 1.

Following this, the first-best value of the alpha wolf, the second-best value of the beta wolf, and the third-best value of the gamma wolf are determined. The distance between the wolves and the prey is then calculated using Equation (3.20), followed by computing the new position using Equations (3.22) and (3.23).

$$\vec{X}(t+1) = \frac{\vec{X}_1 + \vec{X}_2 + \vec{X}_3}{3} \tag{3.22}$$

$$\vec{X}_1 = \vec{X}_\alpha(t) - \vec{A} \cdot \vec{D}_\alpha, \ \vec{X}_2 = \vec{X}_\beta(t) - \vec{A} \cdot \vec{D}_\beta, \text{ and } \vec{X}_3 = \vec{X}_\delta(t) - \vec{A} \cdot \vec{D}_\delta \tag{3.23}$$

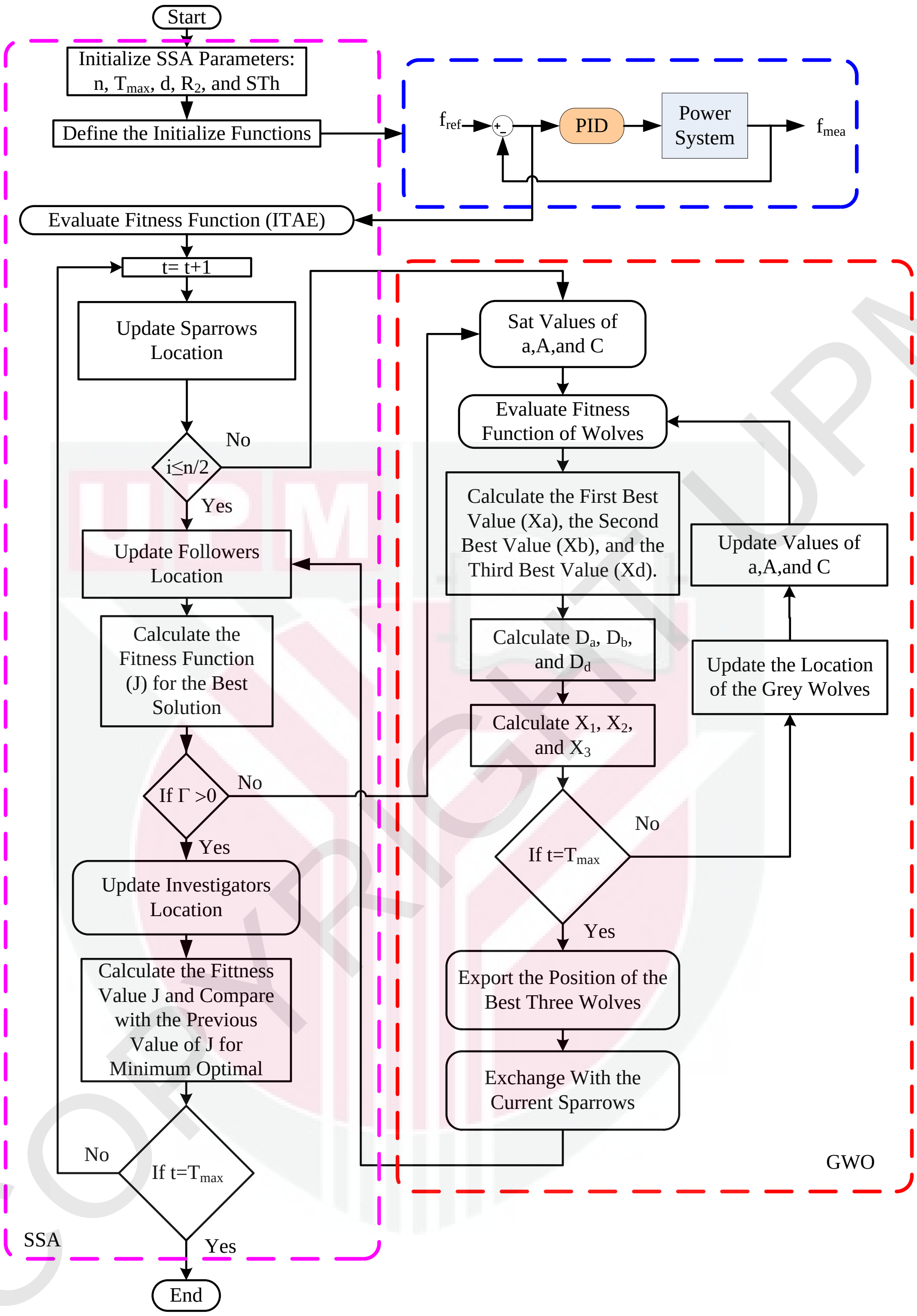

Figure 3.9 : Flow chart of the proposed hybrid SSAGWO algorithm technique

Finally, if the probability factor calculated using Equation (3.21) is positive, the fitness value is evaluated using Equation (3.19) and compared with the best fitness solution to determine the minimum optimal value. Conversely, if the probability factor is negative, the process reinitializes the values a, A, and C. The positions of the best three wolves are exported and exchanged with the current sparrows. The flowchart of the SSAGWO is illustrated in Figure 3.9.

The parameters of the proposed SSAGWO algorithm technique are initialized in this study at maximum iteration = 100, the number of search agents = 50, and the percentage of the total population size is selected as 0.2.

3.3 Virtual Inertia Controller Based on Hybrid SSAMGO Algorithm

This section extensively examines a newly developed approach aimed at achieving the second objective. It provides a detailed discussion of the innovative virtual inertia control technique. The initial phase involves estimating the optimal values for the inertia constant and damping coefficients of the conventional VIC for the islanded MG system integrated with RESs. This was achieved through a novel hybrid optimization algorithm, namely, the SSAMGO algorithm, which combines the SSA algorithm with the MGO algorithm. Additionally, SSAMGO is employed to tune the PID controller parameters of the secondary control loop combined with the VIC, aimed at alleviating frequency deviations within the MG system. In the subsequent phase, a novel Fractional Derivative Virtual Inertia Controller combined with damping coefficient impact (FDVIC) is devised to enhance the frequency response and minimize fluctuations in tie line power amidst load disturbances within a low-inertia islanded MMG system with integrated RESs. This approach employs a decentralized FOPID controller, with its gain values optimized through the proposed SSAMGO algorithm.

3.3.1 Virtual Inertia Control for Frequency Regulation of Microgrid

The integration of renewable energy sources in modern microgrid power systems has a significant impact on frequency stability due to reducing inertia and damping coefficient (Oshnoei et al., 2023). This study employs a virtual inertia control based on frequency deviation derivatives to emulate the system inertia and damping coefficient characteristics of traditional synchronous generators.

a. Design of the Islanded MG Model with VIC

The MG system presented in this study with a rated plant capacity of 1500 kW that consists of a Biodiesel Generator (BDG) with a rated power of 600 kW integrated with RESs. The RESs include a solar thermal energy system with a capacity of 550 kW and a WTG with 350 kW capacity. In addition, the MG system is capable of supplying a 600 kW residential load. Figure 3.10 shows the configuration structure of the proposed MG.

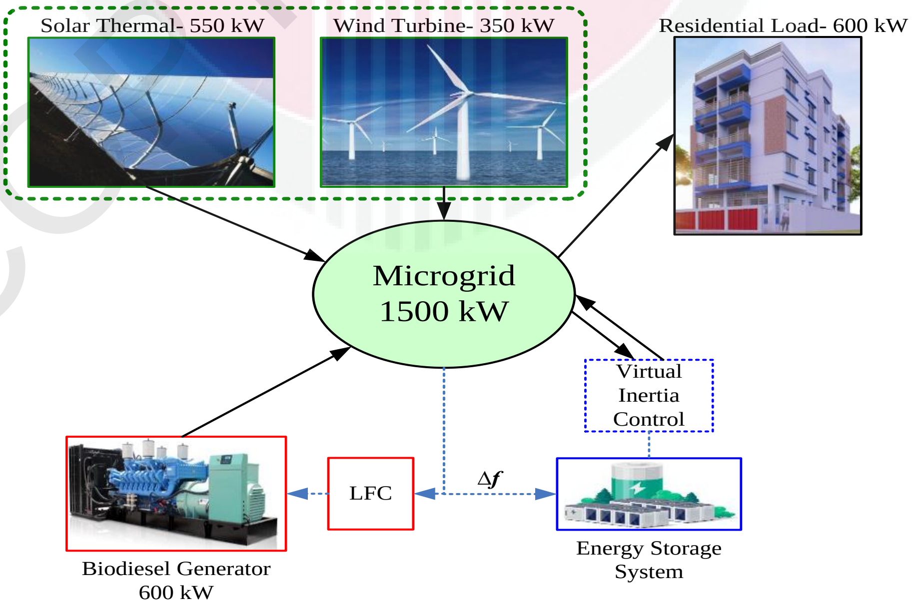

Figure 3.10 : Configuration of the studied MG

The RESs have a significant impact on the system's performance and stability due to its less inertia and damping properties of the system. To address this issue, the MG is provided with an integrated 300 kW ESS. The parameters of the MG power system shown in Appendix A.

The BDG is considered as a controlling unit in the MG system in order to regulate the system frequency. Moreover, the power of solar thermal station (ΔP_{STH}), wind power generation (ΔP_{WTG}), and the sudden change in the load demand load (ΔP_{Load}) are considered with varying power inputs. Figure 3.11 illustrates the LFC model of the proposed MG.

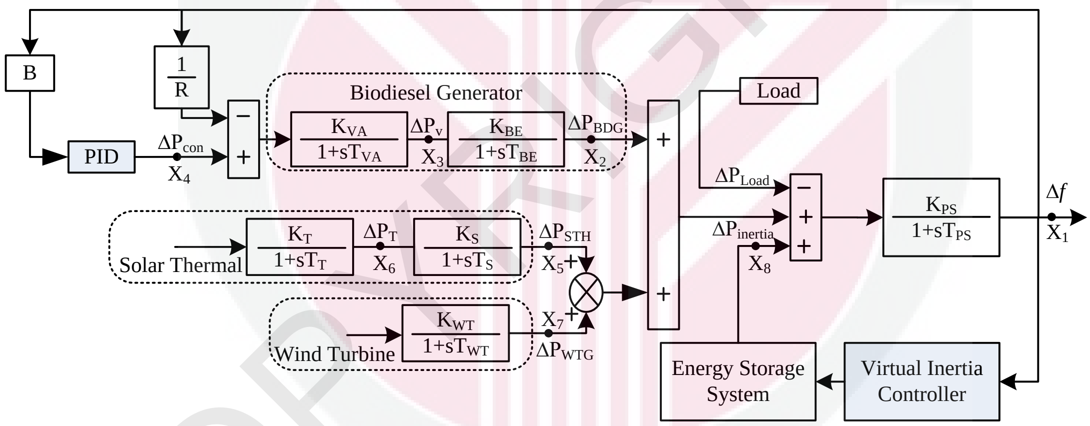

Figure 3.11 : Dynamic model of the proposed MG

The natural inertia response, the primary control loops, and the secondary control loops are the three stages of control units that have an effect on the dynamic response of the MG. The MG frequency deviation can be obtained as in Equation (3.24) (Saxena et al., 2021; Yildirim et al., 2022):

$$\Delta f(s) = \frac{K_{ps}}{1+sT_{ps}} \times \left[\Delta P_m + \Delta P_{STH} + \Delta P_{WTG} - \Delta P_{load}\right] \tag{3.24}$$

where K_{ps} and T_{ps} are the gain constant and time constant of the MG, respectively. ΔP_m is the output power from the BDG.

$$K_{ps} = \frac{1}{D_{equv.}} \tag{3.25}$$

$$T_{ps} = \frac{2 \times H_{equv.}}{f^{o} \times D_{equv.}} \tag{3.26}$$

where f^{o} is the MG nominal frequency.

After integration with RESs, both the MG gain constant and time constant are subject to change and are subsequently influenced. These alterations can be calculated using the equivalent MG inertia and damping coefficient derived from Equations (2.5) and (2.6).

In order to improve the frequency performance and enhance the stability of the MG, a VIC approach based on the derivative technique has been presented in (Mandal & Chatterjee, 2021; Moradi & Amiri, 2021; Saleh et al., 2022). The objective of the VIC is to provide the traditional generator with inertia and damping characteristics virtually during high penetration of RESs. The structure of this controller consists of ESS, the inverter, and an adequate inertia control technique. The control loop of VIC acts independently from primary and secondary control loops. For this reason, the ESS is required to support MG with active power to improve system stability at transient and steady-state operation. Figure 3.12, shows the block diagram of the VIC technique based on the proposed hybrid optimization algorithm.

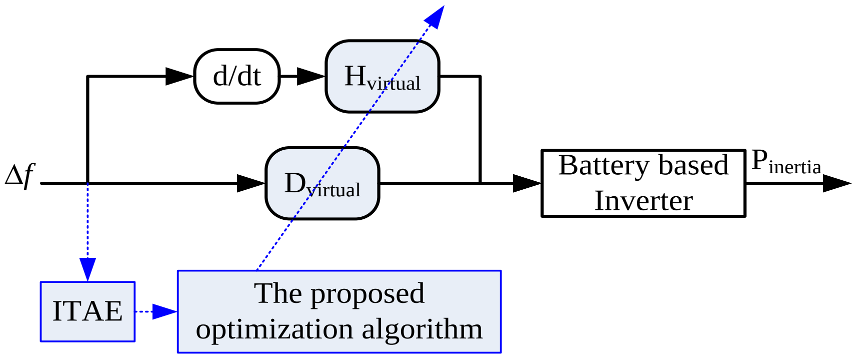

Figure 3.12 : Block diagram of VIC

The inertia power emulation is proportionally controlled by using the derivative technique of the deviation of the system frequency, d(Δf)/dt. The increasing value of $H_{virtual}$ will improve MG stability by reducing the maximum deviation and transient of the system frequency. Nevertheless, a significant increase in the H value leads to an increase in the settling time of the system frequency and an increase in the ESS capacity (Abubakr et al., 2021; Rafiee et al., 2021). The increasing value of $D_{virtual}$ will reduce the frequency deviation settling time and enhance a slight absorption in the frequency transient. However, excessive $D_{virtual}$ increases lead to large secondary overshoots (Xu et al., 2021). Thus, the $P_{inertia}$ emulated into the MG can be calculated as:

$$\Delta P_{inertia} = \left[H_{virtual} \cdot \frac{d(\Delta f)}{dt} + D_{virtual}(\Delta f) \right] \left[\frac{1}{1+T_{ESS}} \right] \tag{3.27}$$

where T_{ESS} is time constant of the ESS based on inverter.

b. Control Strategy of the Proposed MG

The closed-loop control of the low inertia single-area islanded MG power system integrated with RESs based in tandem with VIC technique can be presented as shown in Figure 3.13:

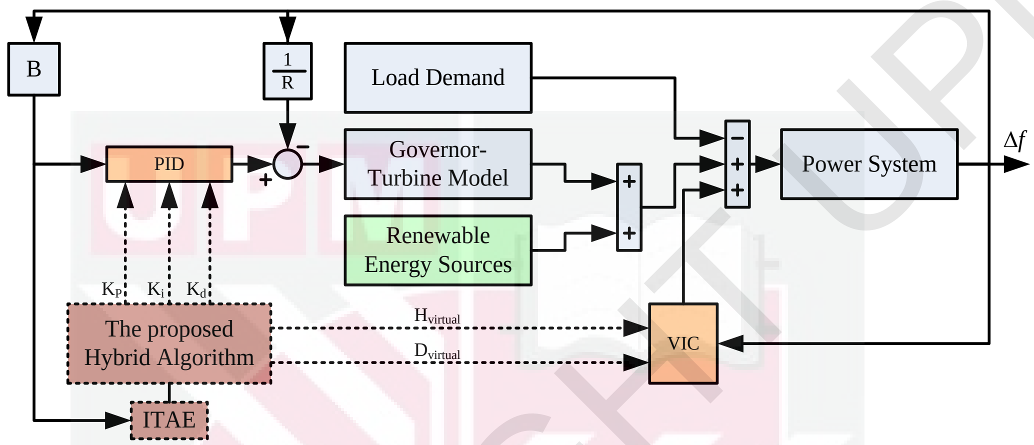

Figure 3.13 : Adapting a closed-loop control system

ACE is the signal fed into the PID controller. The ACE can be defined according to the frequency deviation of the power system as follows:

$$ACE = B \cdot \Delta f \tag{3.28}$$

The biodiesel governor control signal ($\Delta P_{gov.}$) can be given as:

$$\Delta P_{gov.} = k_p(ACE) + k_i\int_0^t (ACE)\,dt + k_d\frac{d(ACE)}{dt} \tag{3.29}$$

where k_p, k_i, and k_d are the proportional, integral, and derivative gains of the PID controller, respectively.

The controller's techniques (secondary loop and VIC) in this study are designed to minimize the steady-state error of the fitness function (J) given in Equation (3.30) by using the ITAE performance index:

$$J = ITAE = \int_0^t t \cdot |ACE| \, dt \tag{3.30}$$

where t is the simulation time.

A new hybrid optimization algorithm technique is used to tune the PID controller parameter gains and estimate the optimal value of the virtual inertia and damping of the VIC. The MATLAB code based on the SSAMGO algorithm has been run, and the results have been compared with the SSAGWO algorithm at the same operating conditions. The parameters assumed for optimizing the parameters of the controller of this model are population size = 30; and number of iterations = 50.

3.3.2 Virtual Inertia Control for Frequency Regulation of Multi-Microgrid Power System

In this section, a new robust virtual inertia controller combined with the impact of the damping coefficient factor is proposed for an islanded Multi-Microgrid (MMG) system, accommodating high levels of RESs. In these MGs, the low inertia in the system has an undesirable impact on the stability of MG frequency. As a result, it leads to a weakening of the MG's overall performance. A novel fractional derivative virtual inertia is integrated into the VIC loop to address this issue. This enhancement aims to fortify the MG's stability and robust performance, particularly when facing contingencies. Moreover, FOPID controllers have been employed to regulate the active power output of the biodiesel generators and the Geothermal station in the MG. The hybrid SSAMGO optimizes the parameters for the three-loop controller.

i. Design of the Islanded MMG Model with FDVIC

The development and economic growth of Malaysia have led to an increased demand for energy within the country. In response to this demand, Malaysia has emerged as a promising nation in the utilization of various RESs. These resources include biodiesel, wind energy, solar energy, and geothermal energy (Ashnani et al., 2014). In the present study, the MMG power system consists of an MG1 with a rated capacity of 2000 kW and an MG2 with a capacity of 1500 kW. MG1 consists of a BDG with a 600 kW rated power integrated with a 350 kW rated WTG, a 550 kW solar thermal generator (STH), and a 500 kW geothermal power station. MG2 consists of a 500 kW-rated WTG, a 400 kW-capacity PV, and a 600 kW-rated BDG. In addition, MG1 can deliver power to a residential load of 800 kW, and MG2 is capable of supplying a residential load of 600 kW. A 300 kW ESS1 and 300 kW ESS2 have been combined with MG1 and MG2 to provide the MG system with the required inertia utilizing the novel FDVIC technique that has been proposed. The MMG development structure proposed is illustrated in Figure 3.14.

The frequency stability is an effect of the MG's inertia response. During load imbalance or load fluctuation events, inertia plays an important role in maintaining the frequency of the MG system (Rafiee et al., 2021). The first line of defence against load fluctuations, the inertia control stage, acts to minimize frequency deviations within the microgrid.

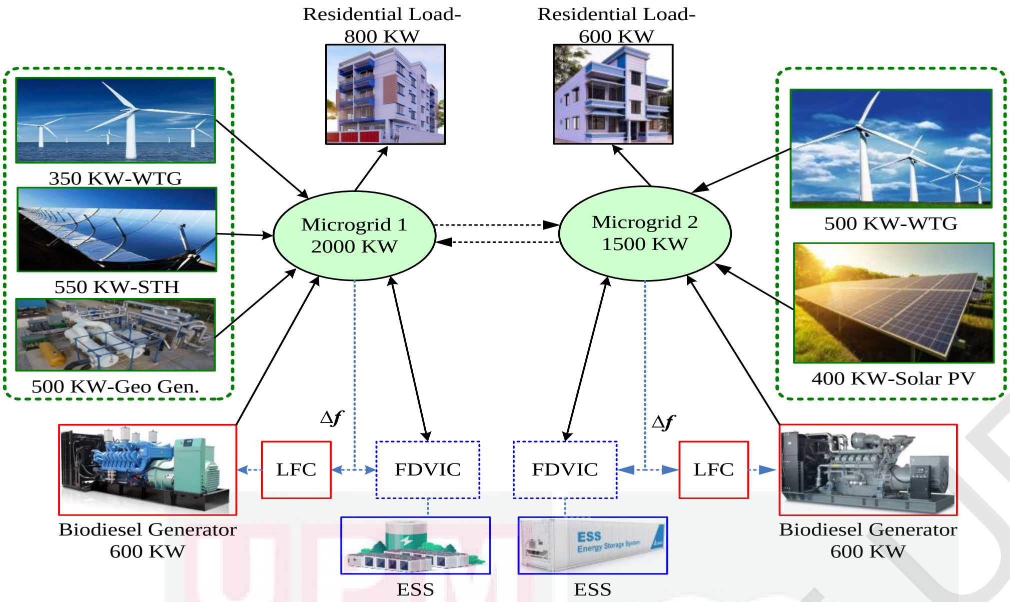

Figure 3.14 : Block diagram of the MMG model

The dynamic response of the generation-load power imbalance is described by the following general swing equation (Saxena et al., 2021):

$$\Delta P_m - \Delta P_{load} = 2H\frac{d\Delta f}{dt} + D\Delta f \tag{3.31}$$

where ΔP_m is the change of mechanical power, ΔP_{load} is the change of demand load, Δf is the rate of change of the MG frequency.

Figure 3.15, shows the proposed dynamic model consisting of the secondary control loop with FOPID, the proposed FDVIC, and DRC. The parameters of the proposed MGs and RESs are illustrated in Appendix A.

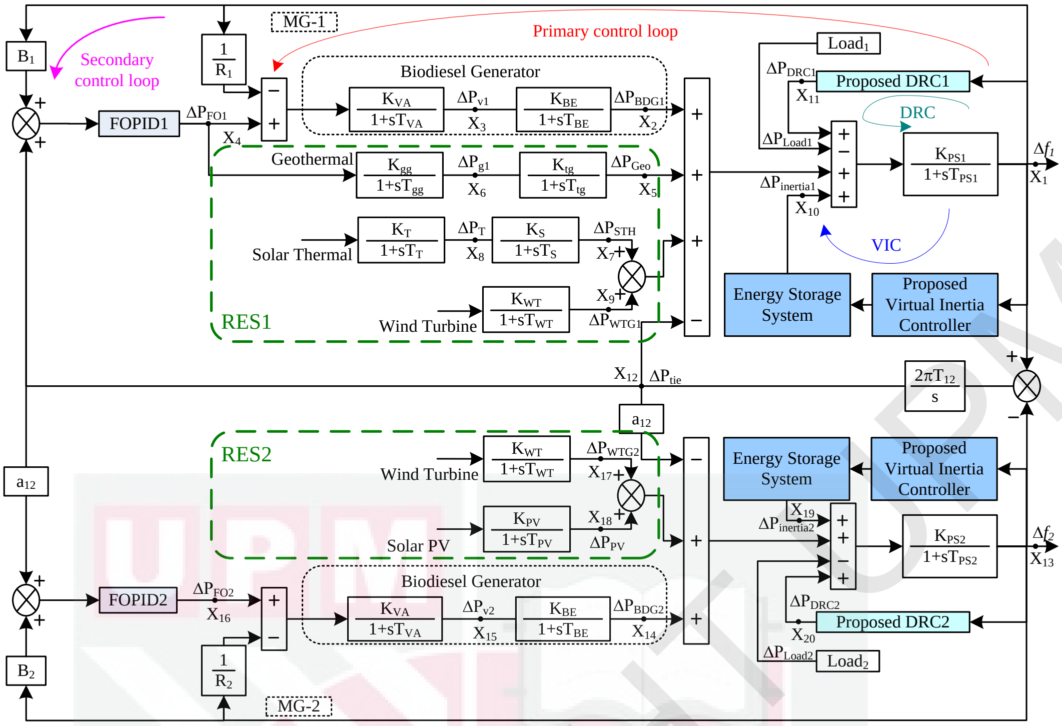

Figure 3.15 : Dynamic model of MMG integrated with RESs

The detailed integration of conventional generators and RESs within the MMG model is outlined as follows:

BDG is made by a chemical process called transesterification, and it has similar qualities to natural diesel despite being made from energy crops that are inexpensive in cost and maintenance (Barik & Das, 2018). It can be utilized in various combinations, including its pure form (B100). The linearized model of the BDG output power can be approximated as follows (Barik & Das, 2019):

$$\Delta P_{BDG} = \frac{K_{VA}}{1+sT_{VA}} \cdot \frac{K_{BE}}{1+sT_{BE}} \tag{3.32}$$

where ΔP_{BDG} is the output power of the BDG, K_{VA}, T_{VA}, K_{BE}, and T_{BE} are valve gain, valve actuator delay, engine gain, and time constants of BDG, respectively.

Wind turbine generators have risen as a critical RESs due to recent technological advancements in power converters, decreased dependency on fossil fuels, environmental consciousness, and cost-efficiency. A pitch control mechanism changes the rotor's pitch as the wind speed changes in order to maintain the steady output of power from the wind energy conversion system. Wind-generated power relies on various factors. The mechanical power of wind turbines is determined by (Tavakoli et al., 2018):

$$\Delta P_{WT} = \frac{1}{2}\rho A_r C_p V_W^3 \tag{3.33}$$

$$C_p = \left(0.44 - 0.0167\beta\right)\sin\left[\frac{\pi(\lambda-3)}{15-0.3\beta}\right] - 0.018(\lambda-3)\beta \tag{3.34}$$

where ΔP_{WT} represents the mechanical power extracted from the wind; ρ is the air density in Kg/m^3; A_r is the swept area of the blades (m^2); V_W is the wind speed, and C_p is a function influenced by both the speed tip ratio (λ) and blade pitch angle (β). The association between mechanical power and β allows for the utilization of this relationship to reserve power. Two WTGs integrated with MG1 and MG2 are considered in this study and illustrated as a first-order transfer function as follows:

$$\Delta P_{WTG} = \frac{K_{WTG}}{1+sT_{WTG}} \tag{3.35}$$

where K_{WTG} and T_{WTG} are the gain constant and time constant of the WTG.

PV power generators, utilizing either crystalline or thin-film panels, are extensively employed in Malaysia's solar-rich environment, where monthly solar radiation ranges from approximately 400 – 600 MJ/m^2 (Mekhilef et al., 2012). This study assumed the

PV generating system operates in a maximum power point tracking mode. The PV output power can be represented as (Fayek & Kotsampopoulos, 2021):

$$P_{solar} = A \times \eta_{solar} \times I \times \left[1-(0.005T_a + 0.125)\right] \tag{3.36}$$

where P_{solar} is the output power of the PV system in Watt, A is the area of the cells (m^2), η_{solar} is the efficiency of the conversion from sunlight to electricity, I is the isolation (Watt/m^2), and T_a is the ambient temperature in ^oC.

The transfer function of the PV power generator can be written as follows:

$$\Delta P_{PV} = \frac{K_{PV}}{1+sT_{PV}} \tag{3.37}$$

where ΔP_{PV} is the output power of the PV, K_{PV} and T_{PV} are the gain constant and time constant of the photovoltaic cell behaviour.

Energy storage system has indeed gained significant attention in recent years as a means to enhance the frequency response of MGs. By quickly responding to imbalances between power generation and demand, ESS can help reduce frequency deviation and contribute to system stability. Lithium-ion batteries are the most common type of battery used in LFC power applications due to their properties (El-Bidairi et al., 2020). It can be rapidly charged and discharged and has a relatively long cycle life both of which have significance for LFC. The proposed control technique in this study is designed to keep the ESS unit fully charged during normal operating conditions and then automatically inject the system with the required active power during the contingencies. The transfer function of the ESS can be written as a first-order lag:

$$\Delta P_{ESS} = \frac{K_{ESS}}{1 + sT_{ESS}} \tag{3.38}$$

where ΔP_{ESS} is the output power of the ESS, K_{ESS} is the gain constant of the ESS, T_{ESS} is the time constant of the ESS.

ii. Proposed Fractional Derivative Virtual Inertia Controller

This section demonstrates a novel design of the FDVIC based on ESS proposed in this study. The objective of this design is to provide inertia and damping impact instantly during high penetration of RESs into the MGs. Short-term ESS, an inverter, and the proposed inertia controller can prove this concept. FDVIC controller operates separately from other control units in the model, such as the primary control loop (droop control) and secondary control loop. As a result, the ESS's energy is completely exploited to enhance stability.

Fractional calculus enables the design of controllers with increased degrees of freedom, resulting in enhanced performance and robustness (Monje et al., 2010). In additions, it involves differentiating and integrating non-integer orders. In control systems, it enhances controller design for improved performance and robustness. The dynamic structure of the proposed FDVIC is presented in Figure 3.16:

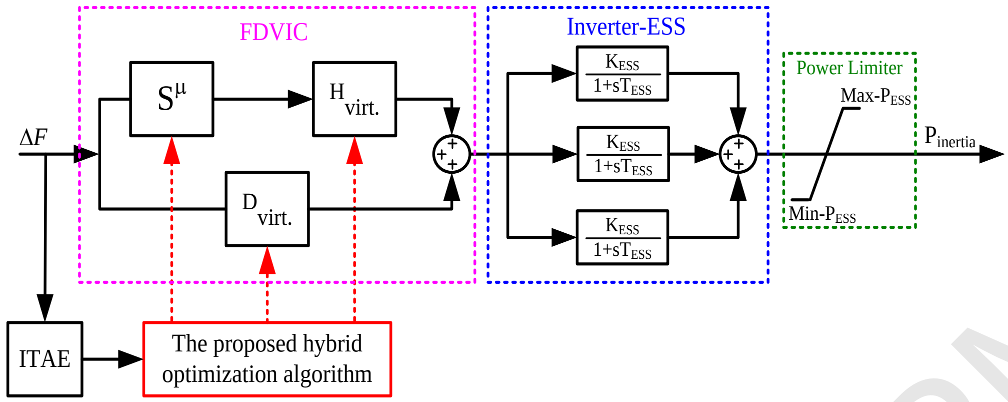

Figure 3.16 : The proposed fractional derivative virtual inertia control system

Caputo introduced an alternate definition for the fractional-order derivative as (Monje et al., 2010):

$$\frac{d^{\mu}e(t)}{dt^{\mu}} = \frac{1}{\Pi(n-\mu)} \cdot \frac{d^{n}}{dt^{n}} \int_{0}^{t} (t-\tau)^{n-\mu-1} e(\tau)\, d\tau \tag{3.39}$$

where Π is the Gamma function, $\frac{d^{n}}{dt^{n}}$ is the nth order derivative, n is the integer part of the derivative, μ is the fractional order of the derivative, $\int_{0}^{t} e(\tau)\, d\tau$ is the fractional integral of the error signal $e(t)$.

The dynamic equation of the proposed FDVIC controller design can be presented as follows:

$$\Delta P_{inertia\,i,j} = \Delta f_{i,j}(s^{\mu vi,j} H_{vir.i,j} + D_{vir.i,j}) \left[\frac{K_{ESS}}{1+sT_{ESS}} \right] \tag{3.40}$$

where $\Delta P_{inertia\ i,j}$ is the change of active power supported to the $MG_{i,j}$ $(i \neq j)$, $s^{\mu vi,j}$ is the fractional derivative, μv is the derivative coefficient factor, $H_{vir.i,j}$ is the virtual inertia constant, $D_{vir.i,j}$ is the virtual damping coefficient constant, K_{ESS} is the gain constant of the inverter based ESS, and T_{ESS} is the time constant of the inverter based ESS.

The FDVIC controller can control the power direction of the ESS. SSAMGO algorithm has been used to tune the value of μv and estimate the optimal value of $H_{vir.}$ and $D_{vir.}$. To include the FDVIC controller impact with the dynamic swing power equation. Equation (3.31) can be modified as follows:

$$\Delta P_m - \Delta P_{load} \pm \Delta P_{inertia} = 2H\frac{d\Delta f}{dt} + D\Delta f \tag{3.41}$$

iii. Demand Response Controller

DRC unit is used to improve system frequency, reduce operational costs, and increase the flexibility of the MGs to deal with the fluctuation and uncertainty of the RESs (Barik & Das, 2019), aligning with the third objective of this study. The conventional dynamic response in Equation (3.31) will be modified to Equation (3.42) to include the DRC loop, where ΔP_{DRC} is the change in the DRC active power. Based on the sign (negative or positive) of the frequency deviation, the binary indicator factor x_{DRC} is activated (1) or deactivated (0).

$$\Delta P_m - \Delta P_{load} \pm x_{DRC}\Delta P_{DRC} = 2H\frac{d\Delta f}{dt} + D\Delta f \tag{3.42}$$

In contrast to conventional control, such as adjusting the position of a valve or gate, DR control is known for its quick response to frequency regulation. In DR, the frequency threshold (Δf_{th}) and appliance shutoff time (T_{off}) are the two most critical factors to determine (Shayeghi et al., 2021). The number of electrical devices that require turning off is dependent on the following:

$$P_{DRC} = \begin{cases} -P_{DRC} & \text{if } \Delta f > \Delta f_{prm} \\ -\dfrac{P_{DRC}}{(\Delta f_{db} - \Delta f_{prm})}(\Delta f_{db} - \Delta f) & \text{if } \Delta f_{db} \le \Delta f \le \Delta f_{prm} \\ 0 & \text{if } -\Delta f_{db} < \Delta f < \Delta f_{db} \\ -\dfrac{P_{DRC}}{(\Delta f_{db} - \Delta f_{prm})}(\Delta f - \Delta f_{db}) & \text{if } -\Delta f_{prm} \le \Delta f \le -\Delta f_{db} \\ P_{DRC} & \text{if } \Delta f < -\Delta f_{prm} \end{cases} \quad (3.43)$$

where Δf_{db} is the dead band frequency for the primary frequency control, Δf_{prm} is the MG's frequency deviation at the end of all primary control reserves delivered.

Assume there are a number (n) of appliances that will be chosen to participate in improving the frequency deviation of the proposed MGs. These appliances will be arranged according to priorities. The controller is designed to switch off the least important devices first. P_1, P_2, ... P_k represents the individual power demands of the listed DR devices. The Δf_{th} parameter can be calculated for the ith appliance by:

$$\Delta f_{th(i)} = \Delta f_{db} - \left[\frac{\Delta f_{db} - \Delta f_{prm}}{P_{DRC}} \cdot \sum_{k=1}^{i} P_k \right] \quad (3.44)$$

The aggregated DR's frequency response characteristics are illustrated in Figure 3.17.

In order to avoid quick switching, the responsive DR appliances (which are turned off because of the frequency deviation) cannot be turned back on before the minimum off-time has elapsed. After that, the responsive DR appliances are progressively turned on if the minimum off-time has elapsed and the frequency has been returned to the nominal value (Bao et al., 2015). The assumed rate of reduction is k_{res} p.u. per second for the responsive DR load. The parameter T_{off} of the ith appliances can be calculated in Equation (3.45):

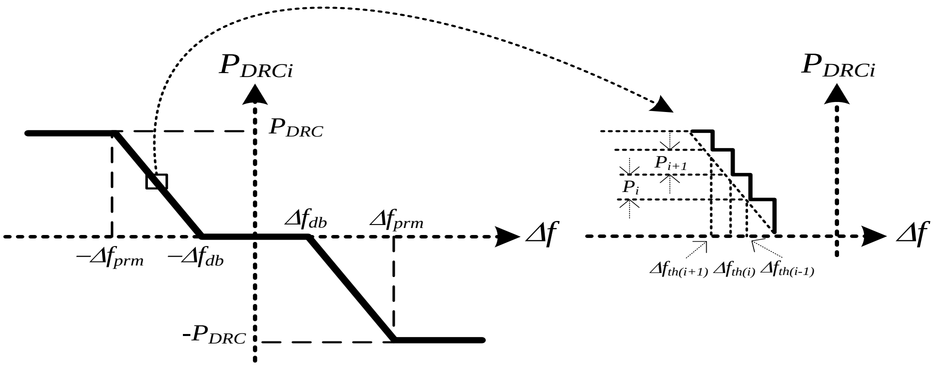

Figure 3.17 : Frequency response behaviour of aggregate DRC

$$T_{off\,(i)} = T_{off\,0} + \frac{1}{k_{res}} \sum_{k=1}^{i} P_k \tag{3.45}$$

where T_{off0} is the first switched minimum off-time of the DR appliance. The value of the k_{res} is evaluated by using SSAMGO algorithm.

The overall control process of the DR controller, aimed at reducing frequency deviations in the proposed MGs, consists of a sequence of actions. Initially, all DR appliances are kept in standby mode. If the system frequency drops below the established dead band frequency, the process advances. Next, DR appliances are progressively switched off as required. The amount of DR load to be shed is estimated using the formula presented in Equation (3.43). Once the system frequency reaches its nadir frequency, the timer T_{off0} is initialized, prompting further actions.

In the following phase, if the timer T_{off0} has elapsed and the frequency deviation Δf exceeds the dead band frequency deviation Δf_{db}, the process moves to the final phase. Conversely, if Δf is less than Δf_{db}, the process loops back to the previous action to reassess the situation.

In the concluding phase, the responding DR appliances that were previously managed are gradually turned back on. Utilizing the rate of reduction k_{res}, the DR load is adjusted until all appliances are fully recovered. If the total demand response capacity P_{DRC} reaches zero, the process returns to the initial phase. Additionally, if the frequency deviation Δf is found to be less than Δf_{db}, the process reverts for further monitoring.

The dynamic structure of the proposed DR controller combined is illustrated in Figure 3.18:

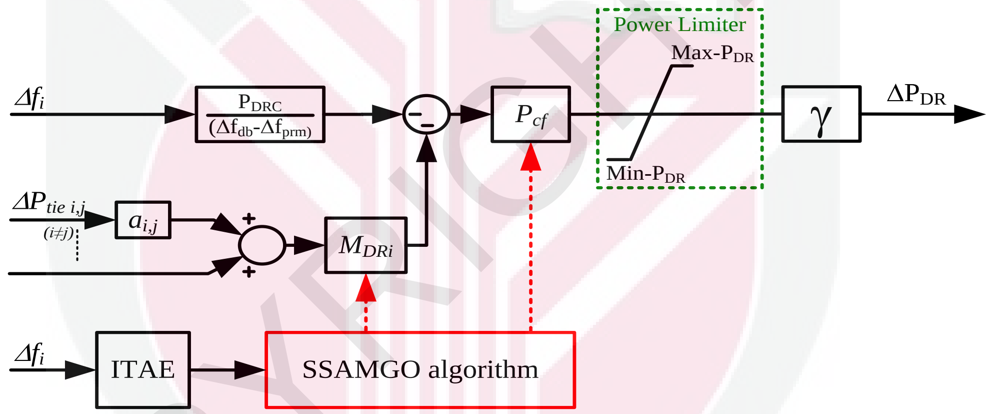

Figure 3.18 : The proposed demand response control system

where P_{cf} is demand contribution factor; and M_{DRi} is intervention coefficient. The proposed hybrid optimization algorithm has been utilized to determine the optimal values for both the demand contribution factor and the intervention coefficient. P_{cf} plays a pivotal role in controlling the gain of active power within the DRC, contributing significantly to its enhanced performance.

The final frequency deviation equation of the MG1 and MG2 has been derived by taking into consideration the relationship between the DGs of the MG integrated with

RESs and including the proposed FDVIC technique with the DRC technique and the demand load of the proposed model depicted in Figure 3.15 as follows:

$$\Delta f_1 = \frac{K_{ps1}}{D_1 + 2H_1 s} \times \left[\Delta P_{BDG1} + \Delta P_{RES1} \pm P_{DRC1} \pm \Delta P_{inertia1} - \Delta P_{load1}\right] \tag{3.46}$$

where $\Delta P_{RES1} = \Delta P_{Geo} + \Delta P_{STH} + \Delta P_{WTG1}$

$$\Delta f_2 = \frac{K_{ps2}}{D_2 + 2H_2 s} \times \left[\Delta P_{BDG2} + \Delta P_{RES2} \pm P_{DRC2} \pm \Delta P_{inertia2} - \Delta P_{load2}\right] \tag{3.47}$$

where $\Delta P_{RES2} = \Delta P_{WTG2} + \Delta P_{PV}$, k_{ps1} and k_{ps2} are the gain constant of the MGs power systems.

The frequency response of the proposed MGs model at steady-state can be represented as in Equation (3.48) (Zaman et al., 2018):

$$\Delta f_{ss} = \frac{\Delta P_{gen,ss} \pm \Delta P_{inertia,ss} \pm \Delta P_{DRC,ss} - \Delta P_{load}}{D + \frac{1}{R}} \tag{3.48}$$

where Δf_{ss} is the frequency deviation at steady-state; $\Delta P_{gen,ss}$ is the change of the total power generated from the BDG and the RESs; $\Delta P_{inertia,ss}$ is the change of the active power supported from ESS; $\Delta P_{DR,ss}$ is the change in demand response power.

The steady-state frequency deviation in Equation (3.48) can be minimized to zero if one or more of the three powers ($\Delta P_{gen,ss}$, $\Delta P_{inertia,ss}$, and $\Delta P_{DR,ss}$) are adequately available to balance the change in demand load ΔP_{load}. Therefore, $\Delta P_{inertia,ss}$ and $\Delta P_{DR,ss}$ are indicated to be used to regulate the frequency deviation in addition to the secondary control loop.

In order to improve the frequency performance in contingency situations, the proposed control strategy has the freedom to decide the optimal power sharing from each control loop. If the shares power of $P_{inertia}$, P_{DRC}, and P_{gen}. are δ, γ, and ξ, respectively, then:

$$\xi = 1 - \delta - \gamma \tag{3.49}$$

If the total sharing power to balance the change in the demand load is ΔP_{total}, then the power contribution from ESS is:

$$\Delta P_{inertia} = \delta \times \Delta P_{total} \tag{3.50}$$

and, the power contribution of the DRC is present as follow:

$$\Delta P_{DRC} = \gamma \times \Delta P_{total} \tag{3.51}$$

The value of γ acts as a pivotal control parameter for the demand response controller, determining its operation in tandem with FDVIC and FOPID by incorporating adjustments based on a predefined percentage.

Finally, the power contribution by the conventional generator integrated with RESs is:

$$\Delta P_{gen} = (1 - \delta + \gamma)\Delta P_{total} \tag{3.52}$$

It should be noted that the steady-state values depend on the proportion between the conventional control loop (ξ), the DR control (γ), and the virtual inertia control (δ), which is decided by the system administrator in negotiations with consumers.

iv. Control Strategy of The MMG based on the Proposed Technique

The closed-loop control technique of MMG can be simplified as depicted in Figure 3.19:

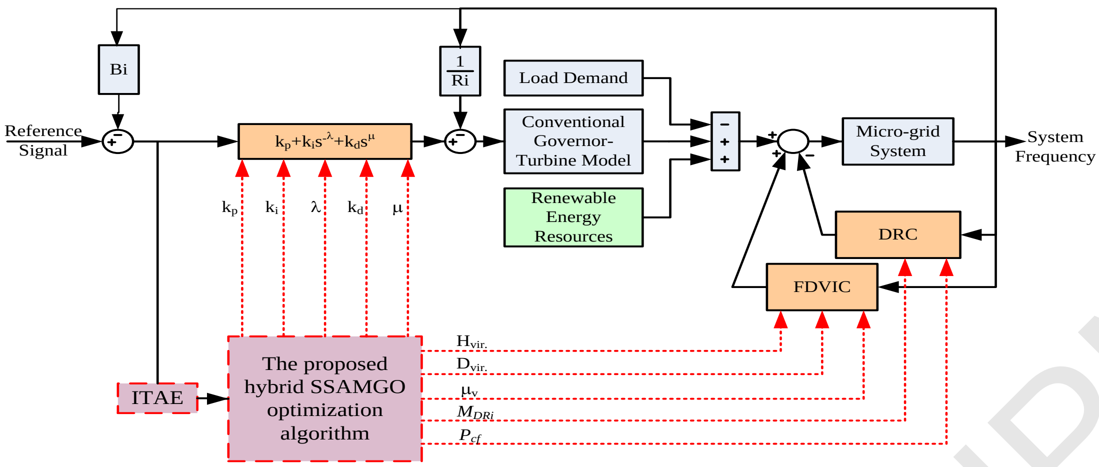

Figure 3.19 : The proposed closed-loop control approach of the MMG

FOPID controller transfer function is given in Equation (3.53) (Irudayaraj et al., 2022b):

$$T_{FOPID} = k_{pi} + \frac{k_{ii}}{s^{\lambda i}} + k_{di} s^{\mu i} \tag{3.53}$$

where k_{pi}, k_{ii}, and k_{di} are proportional, integral, and derivative parameters of FOPID, λi, and μi represent the fractional-order operators and their values tuned in the range (0,1).

In this work, two FOPID controller units have been used in the secondary control loop of the proposed model. Its value is tuned using the hybrid SSAMGO algorithm. Furthermore, in order to provide the proposed model with the required virtual inertia and virtual damping, new FDVIC techniques have been designed to operate independently in low inertia situations. The transfer function of the proposed FDVIC technique is presented as:

$$T_{P_{inertia}i} = H_{vir.i} s^{\mu v,i} + D_{vir.i} \tag{3.54}$$

where $H_{vir.i}$, $D_{vir.i}$, and $\mu v,i$ tuned by using the proposed hybrid algorithm.

While the DR control loop transfer function are given as:

$$T_{DRC} = M_{DRC,i} + P_{cf,i} \tag{3.55}$$

where $M_{DRC,i}$ is the primary DRC control coefficient; $P_{cf,i}$ is the secondary DRC control coefficient.

The selection of the ITAE performance index for controller parameter design in this study is based on its superior performance compared to other indices (Tabak & Duman, 2023). Thus, the fitness function is given as:

$$\mathrm{Min}(J) = \mathrm{ITAE} = \int_0^t t\left\{\left|U_i + \Delta f_i + \Delta P_{tie,ij}\right|\right\} dt \quad i \neq j \tag{3.56}$$

where $U_i(t) = ACE_i \times \left(k_{pi} + \frac{k_{ii}}{s^{\lambda i}} + k_{di} s^{\mu i}\right)$ and $ACE_i = \sum_i^N \Delta P_{tie,i} + B_i \Delta f_i$

where ACE_i is the area control error of the ith area; B_i is the system frequency bias in (p.u MW/Hz). Under the conditions of the following inequalities:

$k_p^{min} < k_{pi} < k_p^{max}$;	$k_i^{min} < k_{ii} < k_i^{max}$;	$k_d^{min} < k_{di} < k_d^{max}$;
$\lambda^{min} < \lambda_i < \lambda^{max}$;	$\mu^{min} < \mu_i < \mu^{max}$;	$H_{vir.}^{min} < H_{vir.i} < H_{vir.}^{max}$;
$D_{vir.}^{min} < D_{vir.i} < D_{vir.}^{max}$;	$\mu v^{min} < \mu_{vi} < \mu v^{max}$	$M_{DRC}^{min} < M_{DRCi} < M_{DRC}^{max}$;
$P_{cf}^{min} < P_{cfi} < P_{cf}^{max}$;		

The maximum and minimum ranges used for tuning the parameters of FOPID controller such as k_p, k_i, and k_d are bounded between [−100, -0.01], λ and μ is selected between [0, 1].

v. Hybrid SSAMGO Algorithm Tuned PID/FOPID, VIC, FDVIC, and DRC

To obtain the optimal values of the three controller parameters (FOPID, FDVIC, and DRC) for an MMG power system, an effort was made to develop a new hybrid metaheuristic algorithm that combines the strengths of swarm-inspired algorithms such as SSA (Xue & Shen, 2020) with MGO.

The development of the new hybrid SSAMGO algorithm considers several key features. One such feature is the poor exploitation tactics of SSA, which can often result in getting trapped in local minima, particularly in complex, multi-modal optimization problems. To address this problem, a solution has been devised by integrating the territorial solitary male's strategy with the utilization of a chaotic map, resulting in the development of the MGO (Abdollahzadeh et al., 2022). Furthermore, within the optimization process, the occurrence of numerous iterations without observable advancements in the fitness function can lead to inadequate stability and low-quality solutions. To address this challenge, a transformation from localized to global zones is suggested. This transformation aims to enhance the capabilities of the proposed optimizer, not only in the exploration phase but also in the exploitation phase, resulting in significant improvements in both aspects. The adoption of this strategy brings about a substantial improvement in the performance of the optimizer during each solution iteration. Instead of relying on crossed lower and upper bounds, this approach replaces them with new, promising areas derived from the information gathered from the best optimal solution obtained up to that point. The proposed SSAMGO offers several key contributions, which can be summarized as follows:

To address the limitation of the location equation in the SSA optimizer algorithm, two strategies are employed. Firstly, in the initial phase, the searching ability is enhanced by leveraging the information from neighboring solutions. This approach allows for a broader exploration of the search space, improving the chances of finding optimal regions. Secondly, in the subsequent phase, a chaotic map is introduced to further amplify the exploration tendencies of the optimizer. By incorporating these tactics, the optimizer can effectively mitigate the issue of premature convergence and exhibit a stronger inclination toward exploration. The aforementioned benefits can be summarized as follows (Shi et al., 2017, 2018):

$$X_{i,j}^{t+1} = \begin{cases} X_{i,j}^{t} \cdot \exp\left(\dfrac{-i}{\alpha \cdot iter_{max}}\right) - X_{i,j}^{t} & \text{if } R_2 < ST \\ X_{best}^{t+1} + M_d & \text{if } R_2 \geq ST \end{cases} \tag{3.57}$$

where m is chosen randomly between the range of [0,1], $M_d = 4 \times (1 - m)$, $X_{i,j}^{t}$ is the previous sparrow location, X_{best}^{t+1} is the global solution's location, R_2 is alarm factor, ST is the safety threshold and it is a value between 0.5 to 1.

The territorial solitary male's strategy in the MGO demonstrates a remarkable ability to amplify both exploration and exploitation phases by combining the information from the best possible solutions with integrated procedures that guide the search towards new optimal regions. This strategy draws inspiration from the intense battles that occur among adult male gazelles as they compete for territorial control and access to females. The MGO's approach leverages this performance to enhance the positioning of the scrounger within the SSA optimizer. The scrounger is represented by a model that utilizes the following framework:

$$X_{i,j}^{t+1} = \begin{cases} X_{best}^{t+1} - \left|(ri_1 \times BH - ri_2 \times X(t)) \times F\right| \times Cof_r & \text{if } i > \dfrac{n}{2} \\ X_p^{t+1} + \left|X_{i,j}^{t} - X_p^{t+1}\right| \cdot A^{+} \cdot L & \text{otherwise} \end{cases} \tag{3.58}$$

where ri_1 and ri_2 are random values between 1 and 2; X_p^{t+1} is the optimal location occupied by the producer; A is a matrix [1 x n] which each element inside assigned 1 or -1; $A^{+}=A^{T}(AA^{T})^{-1}$; L is a matrix [1 x n] which each element inside is 1; when $i > \frac{n}{2}$, it signifies that the ith participant must relocate to another area in order to find food; BH, F, and Cof_r are the coefficients of the young male herd, control parameter, and randomly number updated in each iteration, which may be required to enhance the orientation search capability, as given below (Abdollahzadeh et al., 2022):

$$BH = X_{ra} \times \lfloor r_1 \rfloor + M_{pr} \times \lceil r_2 \rceil, ra = \left\{\left|\frac{N}{3}\right| .... N\right\}, a \tag{3.59}$$

$$F = N_1(D) \times \exp\left(2 - Iter \times \left(\frac{2}{MaxIter}\right)\right), \tag{3.60}$$

and

$$Cof_i = \begin{cases} (a+1) + r_3, \\ a \times N_2(D) \\ r_4(D) \\ N_3(D) \times N_4(D)^2 \times \cos((r_4 \times 2) \times N_3(D)) \end{cases}, \tag{3.61}$$

where X_{ra} is randomly selected within range of ra; M_{Pr} is the average number of search agents picked at random $\left|\frac{N}{3}\right|$; N refers to the total number of solutions; r_1 and

r_2 are numbers randomly chosen between 0 and 1; N_1 denotes to the standard distribution chosen at random; Iter and MaxIter are the current and maximum iterations; r_3 and r_4 are arbitrary numbers between 0 and 1; N_2, N_3, and N_4 are integers drawn at random from the population; while a is computed as follows:

$$a = -1 + \mathrm{Iter} \times \left(\frac{-1}{\mathrm{MaxIter}} \right) \tag{3.62}$$

The mathematical model of sparrows, which possess an awareness of danger, has undergone further refinement in its second part. This refinement involves the introduction of random parameters to enhance their exploratory ability and the elimination of fitness calculations for the best and worst values. These calculations have been identified as potentially harmful during the optimization process. The newly modified equation can be represented as follows:

$$X_{i,j}^{t+1} = \begin{Bmatrix} X_{best}^{t} + \beta \cdot \left| X_{i,j}^{t} - X_{best}^{t} \right| & \text{if} \quad f_i > f_g \\ X_{i,j}^{t} + (2 \times \mathrm{rand}(1) - 1) \times \left(\left| X_{i,j}^{t} - X_{worst}^{t} \right| \right) & \text{if} \quad f_i = f_g \end{Bmatrix} \tag{3.63}$$

where the step size control parameter β follows a normal distribution of random numbers with a mean of 0 and a variance of 1; f_i and f_g are the fitness value of the present sparrow and the current global best, respectively.

To facilitate the transition from local to global areas during the optimization process, a number of newly generated solutions may cross the upper and lower boundaries of the optimization problem. This can be attributed to the utilization of multiple random strategies. The presence of simple lower and upper bounds in most optimization algorithms can potentially impede the convergence speed toward optimal solutions. To address this challenge, we have proposed a mechanism that enables the transformation of solutions from predefined upper and lower bounds to near-optimal regions. This is achieved through the utilization of the following mathematical model (Ridha et al., 2022):

$$X_{i,j} = X_{best}^{t} + \in \times (rand \times (UB_j - LB_j)) \times rand \times LB_j \tag{3.64}$$

where $\in$ is an infinitesimally small value, UB_j and LB_j are denote the lower and upper bounds of the jth position, respectively. The specific steps of the SSAMGO are described in the flowchart shown in Figure 3.20.

The mentioned equations play a crucial role in significantly enhancing the diversity of the best optimal solutions discovered during the optimization process. This implies that not only do the solutions undergo a transition from local areas to optimal regions, but their quality is also improved by incorporating information from the neighbourhood of the best solution.

It is important to highlight that selecting appropriate boundaries for the FOPID, FDVIC, and DRC controller factors contributes to the rapid attainment of the correct position.

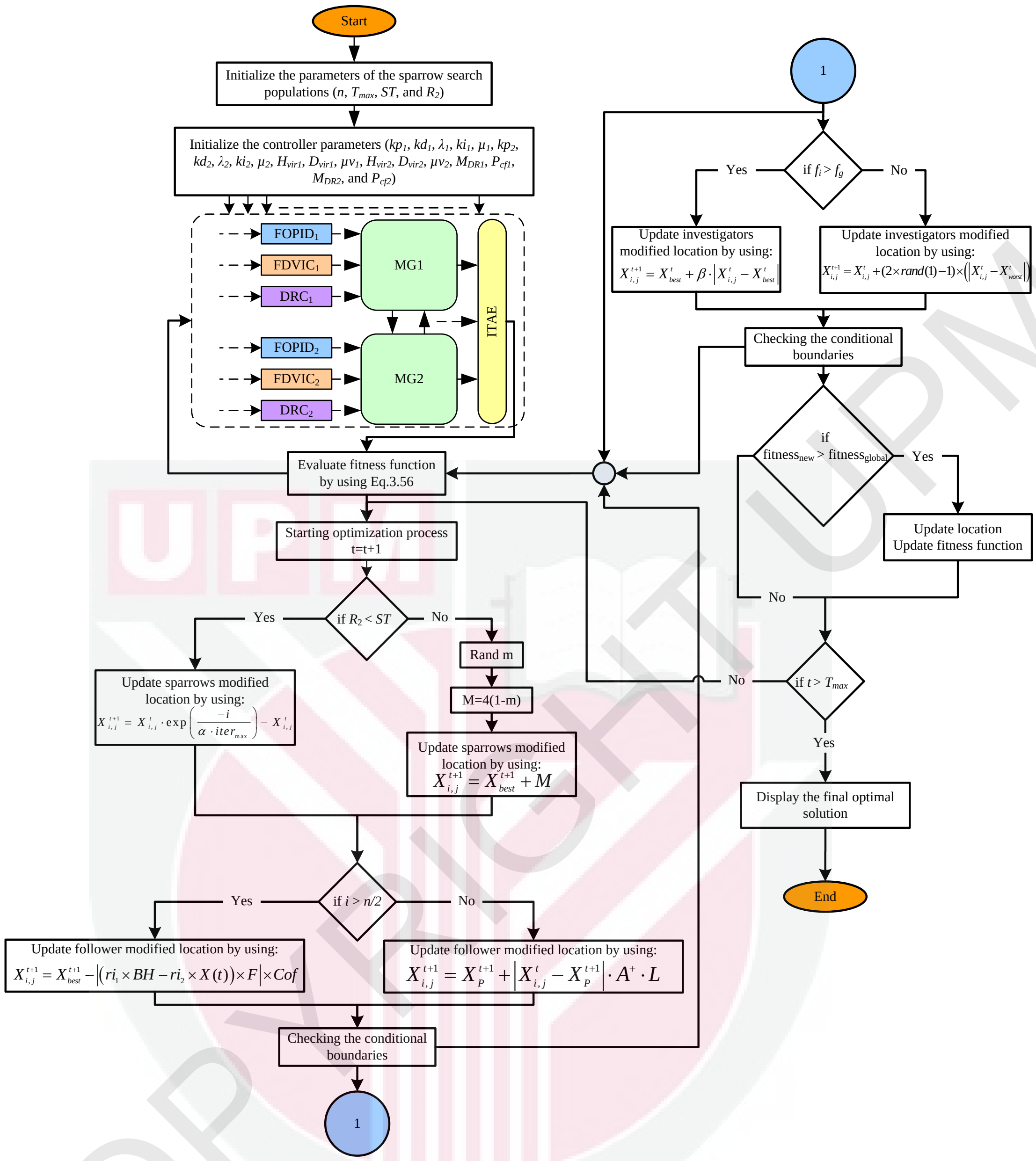

Figure 3.20 : Flow chart of the SSAMGO algorithm technique-tuned the controller parameters

3.4 Validation of the Proposed Control Techniques

The last part of the study delves into the fourth objective, focusing on validating the optimization of the FOPID, FDVIC, and DRC controller parameters using the proposed SSAMGO method. Two validation scenarios are examined. The first scenario involves two interconnected microgrid power systems alongside a large-scale power system (LSPS) operating in grid-connected mode, with consideration given to the capacity of the 39-bus IEEE New England test system. The second scenario entails validating the LSPS and the MMG power system through Real-Time Digital Simulation Experiments utilizing the Opal-RT simulator.

3.4.1 Multi-Microgrid Integrated with Large Scale Power System

This study examines a power system comprising three interconnected areas with varying capacities, as illustrated in Figure 3.21. The system integrates two MG systems that utilize RES and operate in connected modes alongside a large-scale power system (LSPS) with a capacity of 2000 MW. MG1 and MG2 have capacities of 6 MW and 8 MW, respectively.

In Area-1, the LSPS comprises a Hydropower station with a capacity of 1200 MW and a Gas turbine plant with a capacity of 800 MW (Fernández et al., 2022). The nominal demand power in Area-1 is 1000 MW.

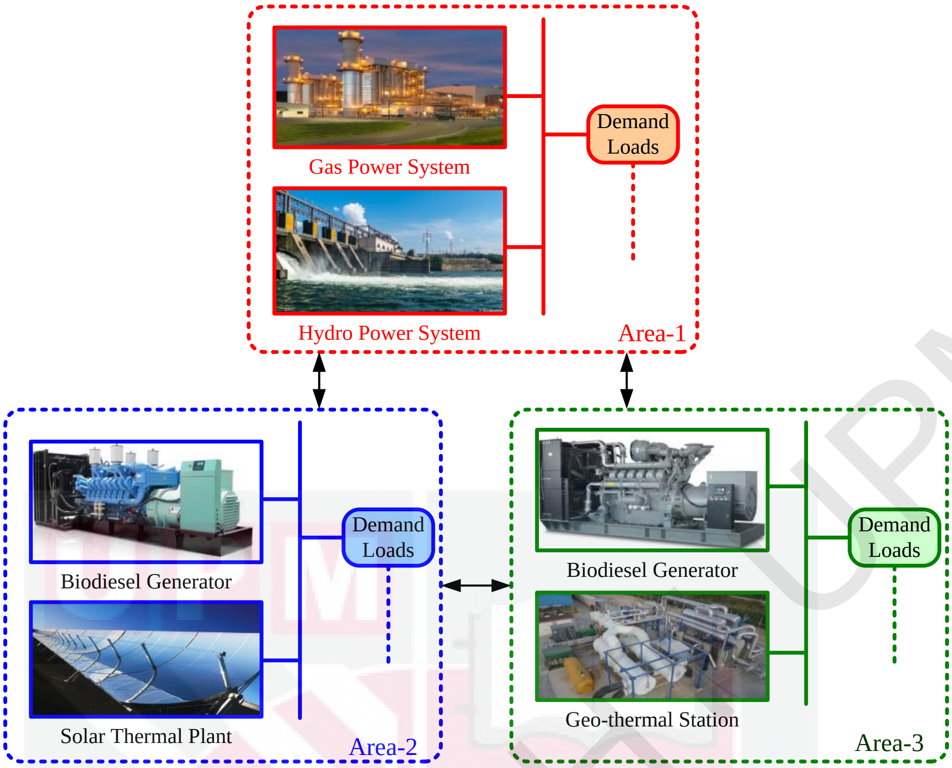

Figure 3.21 : Block diagram of the LSPS interconnected with MG1 and MG2

Area-2 including an MG power system consists of a BDG rated at 3 MW (Barik & Das, 2018), and Solar thermal RESs with a combined rated power of 3 MW (Irudayaraj et al., 2022), and the nominal demand load is 2.75 MW. Meanwhile, Area-3's MG system includes a BDG with a capacity of 3.5 MW and a Geothermal station with a capacity of 4.5 MW (Saha et al., 2022), and the nominal demand load is 3.75 MW. The substantial integration of RESs has a notable influence on the stability and frequency response of the proposed power system, attributed to the absence of total system inertia. To address this, a 300 kW ESS (El-Bidairi et al., 2020) has been integrated with MG1 and MG2, employing the FDVIC technique to support the power system with the necessary inertia. The depicted configuration of the proposed power system is illustrated in Figure 3.22.

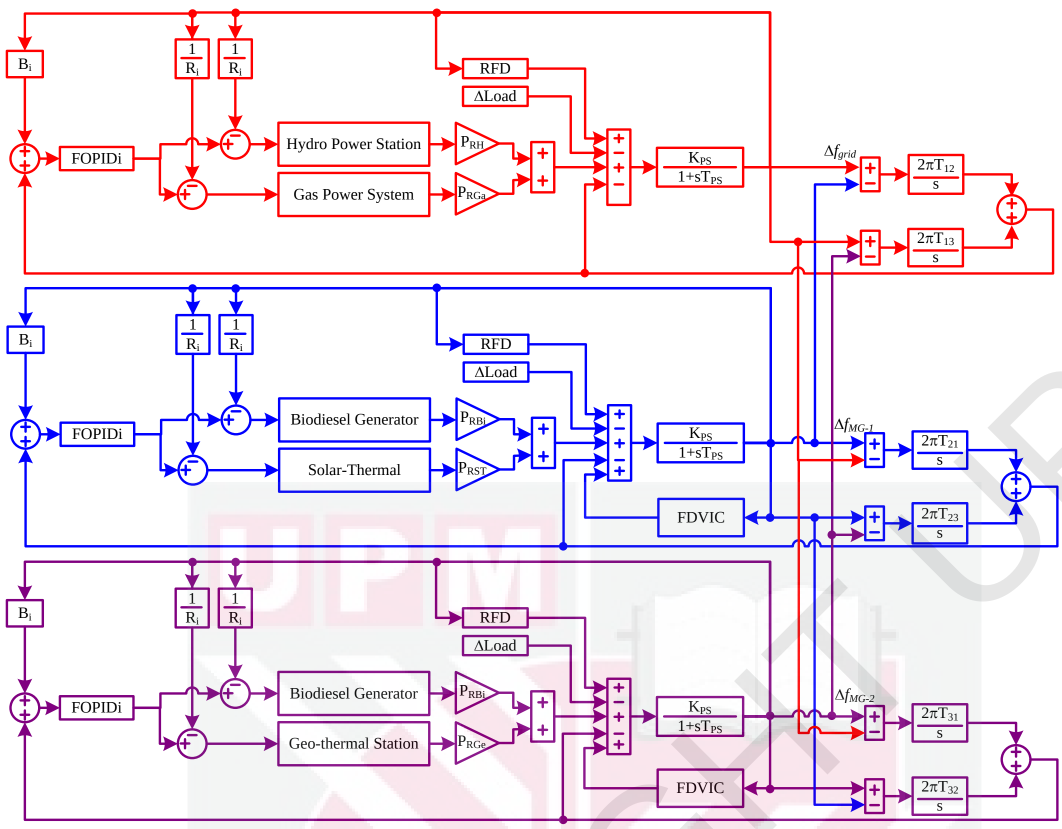

Figure 3.22 : Dynamic model of proposed power system integrated with RESs

The modeling of the integrated RESs of the MMG integrated with the LSPS model is outlined as follows:

i. Hydro Power Station

The turbine speed governor monitors fluctuations in the speed of a hydropower plant and is responsible for adjusting the turbine's valve input accordingly. The turbine receives water through a pipe, and the flow is controlled by a valve gate that introduces a specific level of obstruction (Weldcherkos et al., 2021). Turbine speed regulation commonly involves fly ball governing, which serves to identify alterations in the generator's speed. Hydraulic amplifiers consist of a pilot valve and a dominant piston arrangement, crucial for controlling the water valve in the presence of high-pressure water. Simultaneously, the linkage mechanism facilitates feedback from the gate valve. The speed changer is employed to ensure a consistent output power (Gope et al., 2023). The conventional modeling approach for these turbines considers the following aspects:

1. Negligible hydraulic resistance is presumed in the modeling;
2. The penstock pipe is characterized by its inelasticity, containing water that is considered incompressible;
3. The velocity of water changes in direct proportion to the gate opening and the square root of the net head;
4. The power generated by the turbine is directly proportional to the multiplication of the head and the volume flow.

Given these conditions, the transfer function of the hydro-power turbine is illustrated in Figure 3.23. With P_{ci} denoting the set-point power, T_{Hg} representing the governor's time constant, T_R as the reset time, R_T indicating temporary droop, R_p denoting permanent droop, and T_w serving as the estimated water starting time, as follows (Fernández et al., 2022):

$$T_W = \frac{L \cdot U_0}{ag \cdot H_0} \tag{3.65}$$

In this scenario, where H_0 denotes the initial steady state of the hydraulic head at the gate, U_0 represents the initial steady state of water velocity, ag is the constant of gravity, and L is the length of the conduit, both R_T and T_R can be derived from:

$$R_T = \left[2.3 - (T_W - 1) \times 0.15\right] \cdot \frac{T_W}{2H} \tag{3.66}$$

$$T_R = \left[5 - (T_W - 1) \times 0.5\right] \cdot T_W \tag{3.67}$$

where H is the hydro-power inertia constant. Hydro-power turbine model parameters: T_{Hg} = 28.75s, T_W = 3.06s, T_R = 1, R_T/R_p = 0.3, K_H = 0.5747.

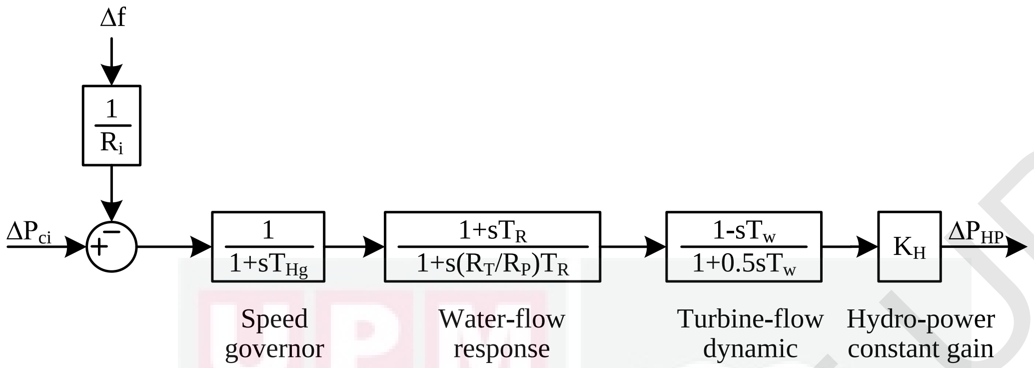

Figure 3.23 : Transfer function model of the Hydro-power station

ii. Gas Power Station

Gas turbines operate by using gases, such as air, carbon dioxide, or helium, as the medium through which they transfer energy (Fernández et al., 2022; Paliwal et al., 2022b). The essential components of a gas turbine power plant include a valve positioner, speed governor, fuel system & combustor, gas turbine, and gas constant gain. Figure 3.24 illustrates the load-frequency model for the gas turbine power plant. Δf in p.u. represents the system frequency deviation, and R_i in Hz/p.u. denotes the governor speed regulation parameters. Within this framework, ΔP_{ci} stands for the reference power setting of the gas plant, and ΔP_{GT} signifies the gas turbine's output power. In the gas turbine generator's block diagram, the constants a and c correspond to the valve positioner, and b represents the valve positioner time constant. The speed governing system is illustrated by a lead-lag compensator, where X_G is the lead time constant of the gas turbine speed governor in sec, and Y_G is the lag time constant of the gas turbine speed governor in sec. The transfer function capturing the fuel system and combustor in the gas turbine is defined by appropriate time constants. In this context, T_F designates the gas turbine fuel time constant in sec, and T_{CR} represents the gas turbine combustion reaction time delay in sec (Hota & Mohanty, 2016). The gas turbine is depicted by a transfer function characterized by a singular time constant, specifically referred to as the gas turbine compressor discharge volume-time constant T_{CD}, measured in sec. Gas Turbine model parameters: a = 1, c = 1, b = 0.05s, X_G = 0.6s, YG = 1s, T_{CR} = 0.01s, T_F = 0.23s, T_{CD} = 0.2s, K_G = 0.1304.

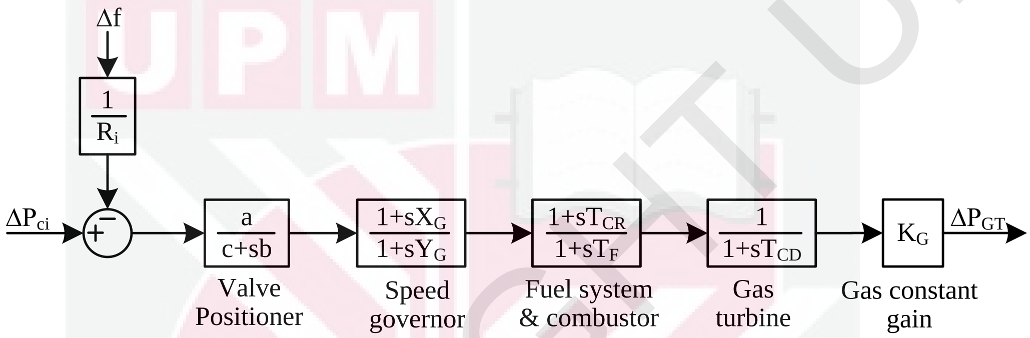

Figure 3.24 : Transfer function model of the Gas Turbine Generator

3.4.2 IEEE-39 New England Test System

The IEEE-39 New England test system is chosen as the platform for validating the proposed control techniques due to its widespread recognition as a reliable benchmark in power system studies. This system offers a realistic and detailed representation of actual power networks, allowing for the effective testing of control strategies under various operating conditions, including the integration of RESs. The decision to divide the system into three areas, while maintaining its behaviour as a single interconnected network, reflects common modeling practices in the literature. This allows for a thorough analysis of how different regions interact and ensures the system's overall stability, even when one area appears to have an undercapacity. The IEEE-39 bus system is particularly well-suited for evaluating the frequency response and stability of the system in the presence of RESs, making it an ideal testbed for the proposed Virtual Inertia Control and supplementary controllers.

In this section, a simulation study investigates the influence of RES units on the frequency of the power system. To conduct this analysis, a network with an identical topology to the renowned IEEE 39-bus test system is chosen as the focal point of the case study (Bevrani, 2014). This system, known for its intricate representation mirroring real-world complexities, is widely recognized in the literature as a pertinent testbed for evaluating a range of control strategies. Figure 3.25 features a single-line diagram that condenses the New England power system, providing an effective tool for analyzing both static and dynamic challenges within the system (Hussain et al., 2022; Singh & Govindarasu, 2021). The investigation of the proposed FDVIC techniques for the MMG incorporates the use of the FOPID controller for supplementary control within the framework of this test system. This model is versatile, accommodating the examination of both static and dynamic issues within the power system. This system includes 10 generators, 19 loads, 34 transmission lines, and 12 transformers. Patel & Beik (2021), presents the simulation parameters for the generators, loads, lines, and transformers in the test system.

The IEEE-39 bus system was divided into three areas in this study to simulate a realistic interconnected power grid with distinct regional characteristics. Each area includes a mix of conventional generation and RESs, reflecting varying load and generation conditions. This division allows for detailed analysis of power sharing between areas and the performance of the proposed control strategies (FOPID, FDVIC, and DRC) in managing frequency deviations. Despite the area-based segmentation, the system operates as a single interconnected network, allowing power flow between areas to maintain stability, even when one area experiences a generation shortfall. This approach provides a comprehensive platform to validate the controllers under real-world-like conditions.

The total installed capacity of 841.2 MW from conventional generation and 45.34 MW from RESs. Area 1 comprises 198.96 MW of conventional generation, 22.67 MW of RES generation, and a load of 265.25 MW. Area 2 includes 232.83 MW of conventional generation and an equivalent load of 232.83 MW. In Area 3, there is 160.05 MW of conventional generation, 22.67 MW of RES generation, and a load of 124.78 MW (Patel & Beik, 2021). In the IEEE-39 bus test system, the divisions into three areas do not strictly limit the power flow. The system behaves effectively like a single area, enabling loads in Area 1 to draw power from generators in other areas, even when cumulative generation seems insufficient to meet local demand. This interconnectivity is vital for maintaining system stability.

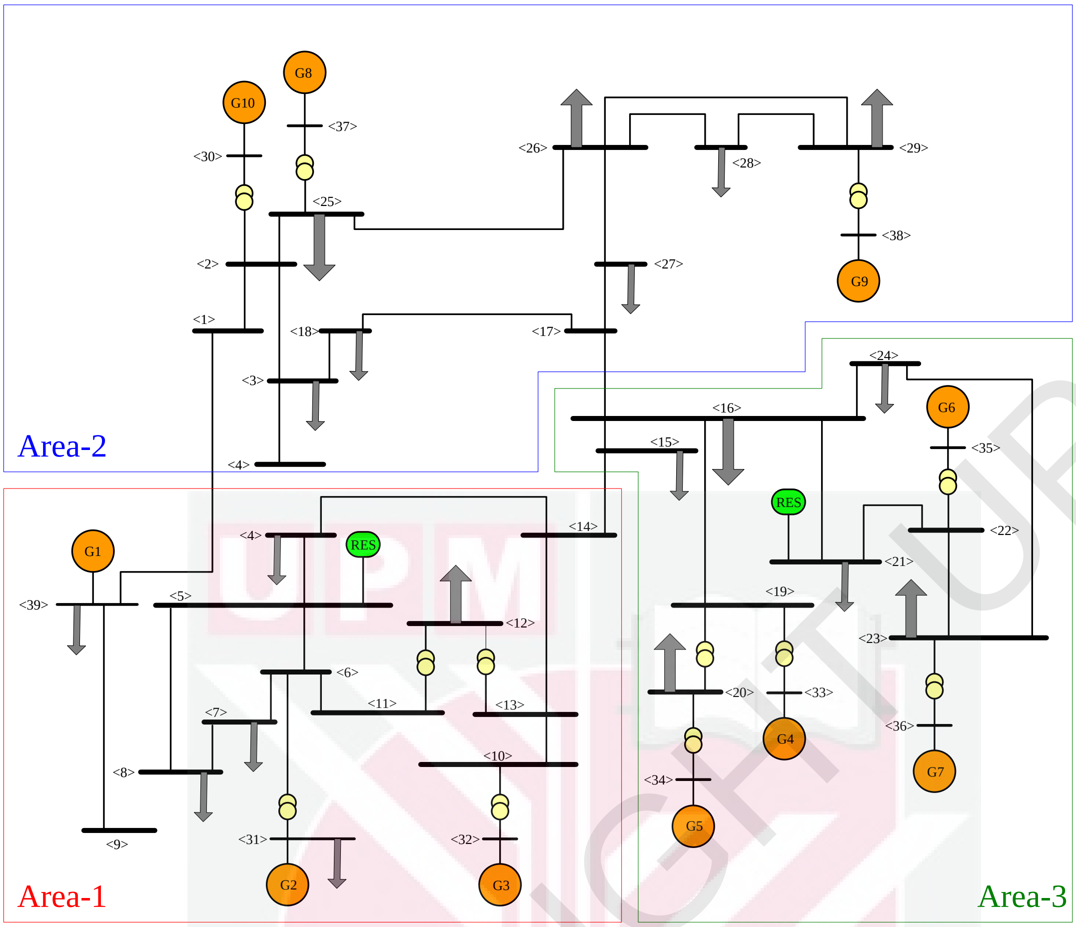

Figure 3.25 : Single-line diagram of the 39-bus test system

To provide further detail, in Area 1, buses 1, 2, and 3 accommodate the generator buses (G1, G2, and G3), whereas in Area 2, buses 8, 9, and 10 function as the generator buses (G8, G9, and G10). Additionally, in Area 3, buses 4, 5, 6, and 7 serve as generator buses (G4, G5, G6, and G7). In this context, the assumption is made that the FOPID controller is tasked with handling the secondary control for two generators within each area, specifically, the conventional generator and the RES station.

3.4.3 Validation through Real-Time Digital Simulation Experiments

The real-time implementation of the proposed SSAMGO-optimized FOPID for the secondary controller and FDVIC for the inertia controller loop of the MMG is experimentally validated using a real-time digital simulator (RTDS). This validation is achieved through hardware-in-the-loop (HIL) simulation conducted in Opal-RT. The OP4510 serves as an introductory-level simulator that integrates the core features of the RT high-performance lab's Rapid Control Prototyping and Hardware-in-the-Loop system for implementation purposes. It provides 128 rapid I/O channels with signal conditioning, additional RS422 channels, and high-speed connectors. Moreover, it is fully integrated with MATLAB/SimPower Systems, enabling seamless communication and control. The integration of upscaled Intel multi-core processors with the efficient Kintex 7 FPGA enhances simulation power, allowing for sub-microsecond simulation time steps.

Opal-RT is a powerful tool for simulating and validating control strategies in dynamic systems, particularly in LFC applications. By accurately modeling power system components, including generators, loads, and controllers, Opal-RT provides a realistic environment for testing and evaluating the performance of the proposed control strategies under various operating conditions. The simulator is equipped to handle complex dynamic models, allowing for real-time processing and rapid feedback, which are essential for effective control in power systems.

In this validation process, the Opal-RT simulator allows for the configuration of a master-slave architecture, where the Opal-RT serves as the master controlling the overall system, while MATLAB simulates the individual components such as the MMG, the LSPS, and the control algorithms. This setup ensures that the interactions between different elements of the power system are accurately represented, providing insights into how each component contributes to overall system stability and performance.

To facilitate the simulation in MATLAB, the power system model is modified to accommodate the master-slave configuration. The Opal-RT simulator acts as the master, orchestrating the communication between various subsystems. The MMG and LSPS are represented as slave models, which receive control commands and provide feedback on system performance. Figure 3.26 illustrates the schematic diagram of the Opal-RT configuration.

1. Modeling the Power System: In MATLAB, the MMG and LSPS are modelled using Simulink, where each component is represented by its respective block. The FOPID controller is implemented within the Simulink environment, designed to manage the secondary control for the generators. The FDVIC controller is also integrated to handle inertia control in response to load disturbances;

2. Communication Protocol: The communication between the Opal-RT master and the slave models in MATLAB is established using real-time communication protocols. This allows for the exchange of data, such as system frequency and load demand, in real-time. The Opal-RT's rapid I/O channels facilitate high-speed data transfer, ensuring minimal latency in control commands;

3. Parameter Tuning: The parameters for the FOPID and FDVIC controllers are optimized using the proposed SSAMGO method before being implemented in the Opal-RT environment. This optimization is critical for achieving the desired performance in load frequency control scenarios;

4. Real-Time Simulation Execution: During the simulation, the Opal-RT master executes the control algorithms in real-time, continuously monitoring system parameters and adjusting the outputs to the slave models. The feedback from

the slaves is used to assess the system's performance, allowing for dynamic adjustments to the control strategies as needed.

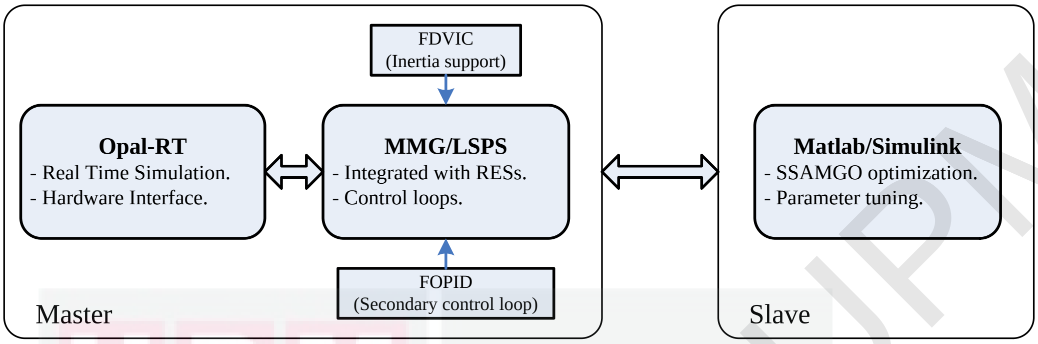

Figure 3.26 : Representation of the Opal RT simulation platform integrated with the hybrid control model implemented in MATLAB

Two validation scenarios have been considered to evaluate the optimization of the designed FDVIC controller parameters through the proposed SSAMGO:

1. Islanded Mode Operation: In the first scenario, the MMG operates in islanded mode, simulating conditions where the system is isolated from the larger grid. This scenario introduces uncertainty in the demand load, allowing for the assessment of how well the control strategies maintain frequency stability under varying load conditions. The Opal-RT simulator facilitates real-time testing of the controllers' responses to load changes and disturbances, ensuring that the designed control techniques effectively manage frequency deviations;

2. Interconnected Mode with LSPS: The second scenario involves two interconnected microgrid systems alongside the LSPS operating in grid-connected mode, considering the capacity of the 39-bus IEEE New England test system. This configuration allows for the examination of inter-area power flows and their impact on frequency stability. The Opal-RT simulator effectively demonstrates how the controllers respond to the dynamics of interconnected systems, providing valuable insights into their performance in real-world applications.

In both scenarios, the Opal-RT's capabilities enable rigorous testing and validation of the proposed control strategies, highlighting their effectiveness in LFC applications.

The combination of Opal-RT simulation and MATLAB modeling provides a robust framework for validating the proposed SSAMGO-optimized FOPID and FDVIC controllers. By simulating real-time scenarios that reflect the complexities of modern power systems, this approach ensures that the control strategies are thoroughly tested and validated for practical implementation. The OPAL-RT validation experiments were conducted at the Centre for TEQIP-III, COE-Alternate Energy Research (AER), funded by the National Project Implementation Unit (NPIU) at Government College of Technology (GCT), Coimbatore, India.

3.5 Summary

This chapter presents the research framework and methodology, which encompasses four objectives centered around virtual inertia control schemes for addressing the LFC problem. The evaluation of decentralized control strategies takes place within the context of an MG/grid power system network. To enhance controller performance, the gain values are tuned using a range of enhanced hybrid optimization algorithms based on the SSA algorithm. Furthermore, validation is conducted via Real-Time Digital Simulation Experiments utilizing the Opal-RT simulator, thereby confirming the efficacy of the designed controller optimization achieved through the proposed hybrid optimization techniques.

CHAPTER 4

RESULTS AND DISCUSSION

4.1 Introduction

This chapter presents a comprehensive analysis of the results obtained from various system models tested to validate the proposed control techniques. It begins with results from a two-area power system integrated with RESs, where decentralized PID controllers and optimization via the SSA algorithm are initially tested. To overcome SSA's limitations, a hybrid SSAGWO algorithm is applied to optimize PID gains, achieving better exploration and stability under parametric uncertainty. Subsequently, for high-penetration MMG systems, a FDVIC approach with three control loops (FOPID, FDVIC, and DRC) is introduced to ensure necessary inertia support. This section also compares the tuning results from the SSAMGO hybrid optimization method with other algorithms to identify the best performing control configuration. The effectiveness of the proposed approach is further validated in a modified IEEE 39-bus New England test system using Real-Time Digital Simulation Experiments on the Opal-RT platform. The findings outline a recommended control strategy with its operational framework, offering a practical solution for LFC in complex, interconnected power systems.

4.2 Simulation Results of SSA Optimized Decentralized PID Controller Deregulated Power System

The power system model present in Figure 3.2 is simulated by using MATLAB/SIMULINK for a reheat turbine generator integrated with RESs under a deregulated power system. The SSA optimization algorithm technique has been used to obtain the optimal value of the PID controller parameters to reduce the frequency deviation for all possible scenarios in the deregulated power market. The results obtained from SSA were compared with those from PSO and GWO. The participation factor of the proposed model is assumed as:

apf_{11} = 0.8, apf_{12} = 0.2, apf_{21} = 0.3, and apf_{22} = 0.7, respectively. Each DISCO's contracted power consumption is assumed to be 0.05 p.u. across all contracts. Three different scenarios of deregulated behaviour are considered, which is poolco, bilateral, and contract violation.

4.2.1 Poolco Transaction

In this scenario, all of the DISCOs get their power demands fulfilled by generation companies (GENCOs) located in the same area. DPM is calculated in this scenario as follows:

$$DPM=\begin{bmatrix} 0.6 & 0.5 & 0 & 0 \\ 0.4 & 0.5 & 0 & 0 \\ 0 & 0 & 0.55 & 0.6 \\ 0 & 0 & 0.45 & 0.4 \end{bmatrix}$$

In the context of the poolco scenario, the values within each cell of the DPM matrix represent the contract participation factor, which specifies the share of power each GENCO contributes to meet the demand of each DISCO. A cpf value of, for instance, 0.6 in a given cell indicates that 60% of the demand of the specified DISCO is sourced from the corresponding GENCO. The matrix structure, with rows corresponding to GENCOs and columns to DISCOs, enables a clear visual representation of these contractual obligations. In this configuration, the sum of each column's values reflects the total demand met by all contributing GENCOs, ensuring the balance of supply and demand across the system.

In this case study, GENCOs of the interconnected power system supply the demand loads as:

$\Delta PG_{11} = 0.006$ p.u. $\Delta PG_{21} = 0.004$ p.u.

$\Delta PG_{12} = 0.005$ p.u. $\Delta PG_{22} = 0.005$ p.u.

$\Delta PG_{33} = 0.0055$ p.u. $\Delta PG_{34} = 0.006$ p.u.

$\Delta PG_{43} = 0.0045$ p.u. $\Delta PG_{44} = 0.004$ p.u.

Figure 4.1 illustrates the dynamic response of the frequency deviation of the two-area power system and the tie-line power flow between areas. The PID controller parameters to maintain the frequency at its nominal value were obtained using the SSA optimization algorithm. These results were then compared with those obtained using PSO and GWO.

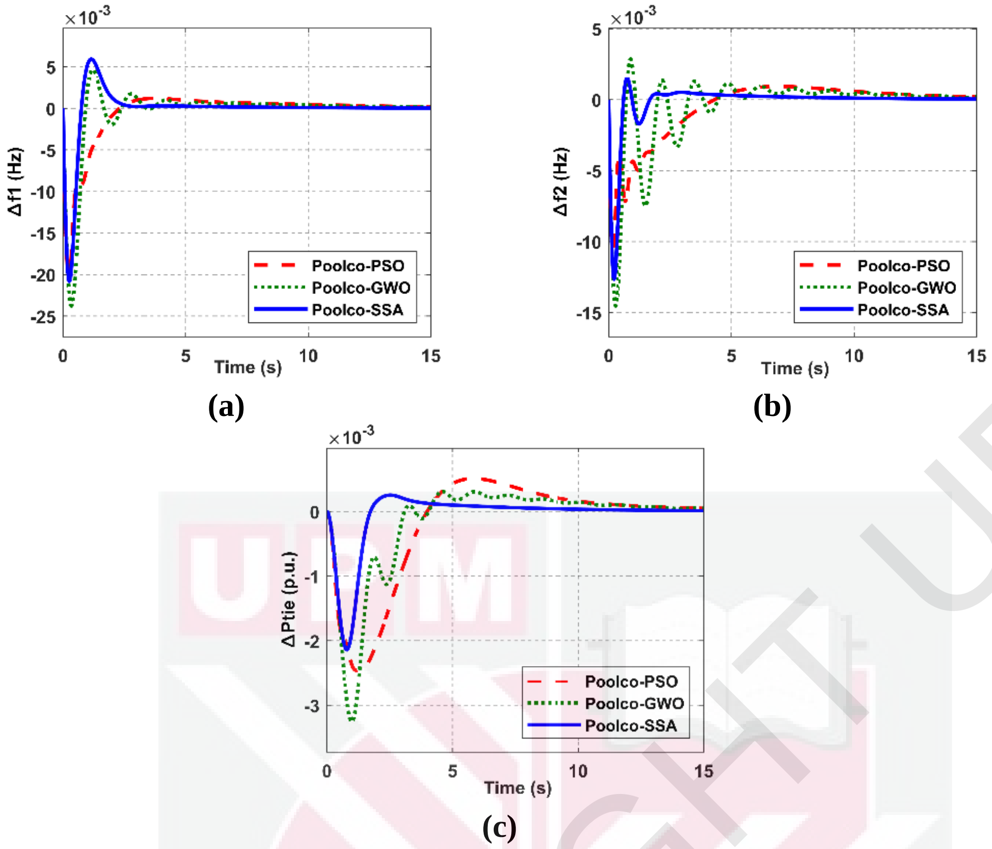

Figure 4.1 : Transient performance response of two-area deregulated power system (a) frequency response in area-1 (b) frequency response in area-2 (c) change in tie-line power deviation

Table 4.1 presents the values of settling time (ST), rise time (RT), and steady-state error (SSE) for the frequency of the areas and tie-line power. Analyzing the results from Table 4.1 reveals that the settling time of the frequency deviation in area 1, a crucial factor in the dynamic performance of the interconnected power system, is minimized when employing the SSA algorithm compared to the results obtained from the PSO and GWO algorithms. Specifically, it is reduced by 71.25% and 65.41% respectively, in comparison to PSO and GWO. Moreover, the rise time decreased by 98.60% and 70.50% respectively, while the steady-state error is reduced by 79.68% and 71.19% respectively. For area 2, the settling time is reduced by 55.26% and 44.88%, the rise time is decreased by 99.26% and 77.04%, and the steady-state error is minimized by 79.36% and 82.28% compared to PSO and GWO respectively. Finally, regarding the tie-line power flow between the two areas, the settling time is decreased by 33.11% and 25.24%, the rise time is reduced by 84.86% and 77.05%, and the steady-state error is minimized by 75.83% and 75.61% when compared to PSO and GWO respectively.

Table 4.1 : Dynamic response results of the poolco scenario

Optimization Algorithm	**ST(s)**	**RT(s)**	**SSE**
		Δf_1	
Poolco-PSO	8.5475	$59.0x10^{-3}$	$17.06x10^{-5}$
Poolco-GWO	7.1040	$2.80x10^{-3}$	$12.03x10^{-5}$
Poolco-SSA	2.4570	$8.25x10^{-4}$	$3.465x10^{-5}$
		Δf_2	
Poolco-PSO	11.4448	$191.5x10^{-3}$	$19.59x10^{-5}$
Poolco-GWO	9.2900	$6.10x10^{-3}$	$22.82x10^{-5}$
Poolco-SSA	5.1202	$1.40x10^{-3}$	$4.042x10^{-5}$
		ΔP_{tie}	
Poolco-PSO	11.8166	$60.8x10^{-3}$	$4.829x10^{-5}$
Poolco-GWO	10.5713	$40.1x10^{-3}$	$4.786x10^{-5}$
Poolco-SSA	7.9031	$9.20x10^{-3}$	$1.167x10^{-5}$

4.2.2 Bilateral Transaction

In this operating scenario, any DISCO can get its demand power from the GENCOs in its area or from GENCOs in other areas. The DPM matrix for this scenario is calculated as follows:

$$DPM=\begin{bmatrix} 0.3 & 0.25 & 0.25 & 0.2 \\ 0.2 & 0.25 & 0 & 0.3 \\ 0.2 & 0.2 & 0.35 & 0.2 \\ 0.3 & 0.3 & 0.4 & 0.3 \end{bmatrix}$$

In bilateral contract, GENCOs of the proposed power system supply the demand loads as:

$\Delta PG_{11} = 0.003$ p.u.	$\Delta PG_{12} = 0.0025$ p.u.	$\Delta PG_{13} = 0.0025$ p.u.	$\Delta PG_{14} = 0.002$ p.u.
$\Delta PG_{21} = 0.002$ p.u.	$\Delta PG_{22} = 0.0025$ p.u.	$\Delta PG_{23} = 0.0000$ p.u.	$\Delta PG_{24} = 0.003$ p.u.
$\Delta PG_{31} = 0.002$ p.u.	$\Delta PG_{32} = 0.0020$ p.u.	$\Delta PG_{33} = 0.0035$ p.u.	$\Delta PG_{34} = 0.002$ p.u.
$\Delta PG_{41} = 0.003$ p.u.	$\Delta PG_{42} = 0.0030$ p.u.	$\Delta PG_{43} = 0.0040$ p.u.	$\Delta PG_{44} = 0.003$ p.u.

The frequency response and the change in tie-line power of the bilateral contract operation scenario shown in Figure 4.2:

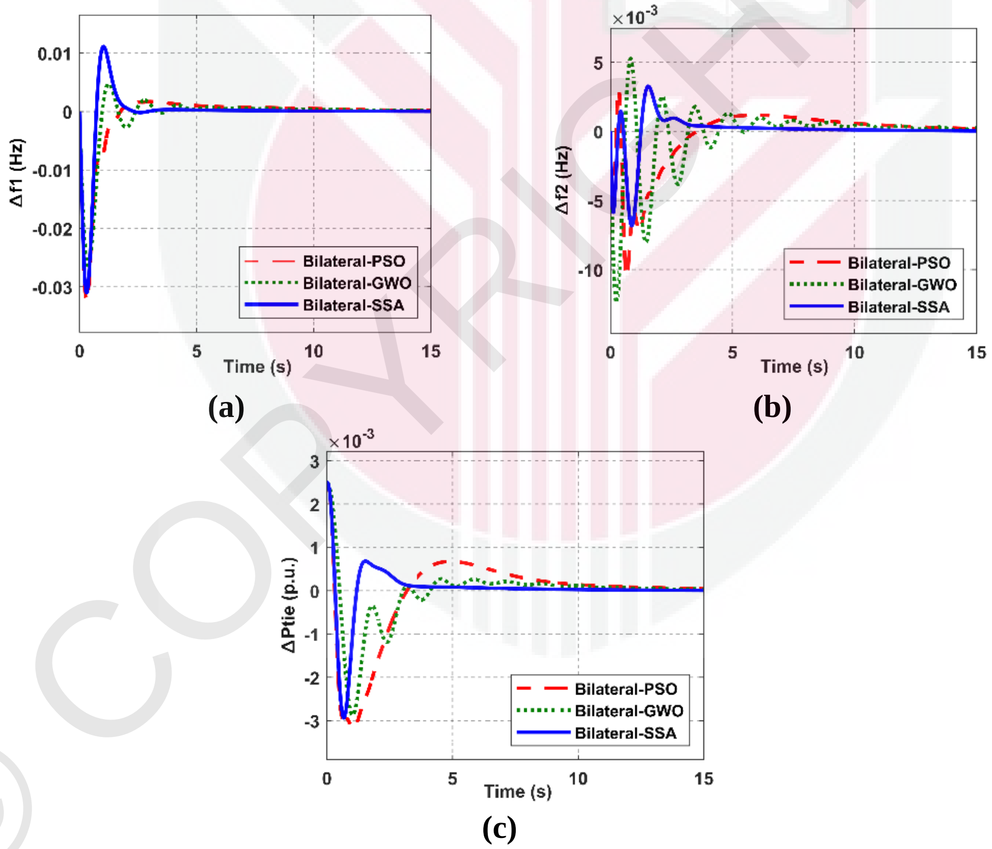

Figure 4.2 : Transient performance response based on bilateral transaction (a) frequency response in area-1 (b) frequency response in area-2 (c) change in tie-line power deviation

Table 4.2 displays the values of settling time, rise time, and steady-state error for the frequency of the areas and tie-line power in bilateral transaction operation scenarios.

Table 4.2 : Dynamic response results of the bilateral scenario

Optimization Algorithm	ST(s)	RT(s)	SSE
		Δf_1	
Bilateral-PSO	6.0726	23.4x10^{-3}	16.73x10^{-5}
Bilateral-GWO	5.8245	2.70x10^{-3}	11.95x10^{-5}
Bilateral-SSA	1.9772	3.58x10^{-4}	3.574x10^{-5}
		Δf_2	
Bilateral-PSO	11.5857	2.8x10^{-3}	19.23x10^{-5}
Bilateral-GWO	10.4548	4.6x10^{-3}	24.47x10^{-5}
Bilateral-SSA	7.5160	1.1x10^{-3}	4.049x10^{-5}
		ΔP_{tie}	
Bilateral-PSO	11.0112	19.22x10^{-2}	4.525x10^{-5}
Bilateral-GWO	10.4579	31.93x10^{-2}	3.518x10^{-5}
Bilateral-SSA	6.0980	17.71x10^{-2}	9.063x10^{-5}

Table 4.2 illustrates that compared to the results obtained from the PSO and GWO algorithms, the SSA method achieves the shortest settling time for the frequency deviation in area 1, which is crucial for the dynamic performance of the interconnected power system. Specifically, it is reduced by 67.44% and 66.05% respectively, compared to PSO and GWO. The shorter settling time achieved by the SSA method for frequency deviation in area 1 can be attributed to the unique features of the SSA algorithm, particularly its efficient exploration and exploitation capabilities when optimizing PID controller parameters in dynamic systems. Unlike PSO and GWO, the SSA algorithm is specifically designed to mimic the natural foraging behavior of sparrows, enabling it to avoid local optima and search more effectively across the solution space.

For a large-scale, two-area interconnected power system with RESs, the SSA's ability to balance global exploration (discovering new areas in the solution space) and local exploitation (fine-tuning parameters in promising regions) ensures that the PID controller parameters are optimally adjusted. This balance minimizes frequency oscillations and leads to faster stabilization following a disturbance. Additionally, SSA's structure allows it to respond more dynamically to parameter variations, which is crucial for maintaining rapid settling times in secondary control loops under deregulated conditions with integrated RESs.

Therefore, the SSA algorithm's combination of robust global search and fine-tuned parameter optimization contributes to a shorter settling time for frequency deviation in area 1, enhancing the system's overall dynamic performance compared to PSO and GWO.

Additionally, the rise time is decreased by 98.46% and 86.72%, while the steady-state error is minimized by 78.63% and 70.09% respectively. In the case of area 2 in this scenario, the settling time of the frequency is reduced by 35.12% and 28.10%, the rise time is decreased by 60.71% and 76.08%, and the steady-state error is minimized by 78.94% and 83.45% compared to PSO and GWO respectively. The response of the tie-line power flow between areas is also improved, with the settling time reduced by 44.62% and 41.69%, the rise time reduced by 7.85% and 44.53%, and the steady-state error minimized by 79.97% and 74.23% compared to the results obtained from PSO and GWO respectively.

4.2.3 Contract Violation

In a contract violation, DISCOs can be very demanding in terms of contract power and commitment. In these cases, the GENCOs in the same area must step in to provide the extra, uncommitted power. In this study assume that a DISCOs located in area 1 has a demand that is 0.1 p.u. more than the contract commitment. Then, the DISCOs demand in area 1 will increase as follows:

ΔP_{D1} = DISCO1 + DISCO2 + 0.1 = 0.01 + 0.01 + 0.1 = 0.12 p.u.

The frequency response and tie-line power deviation of the contract violation scenario are shown in Figure 4.3.

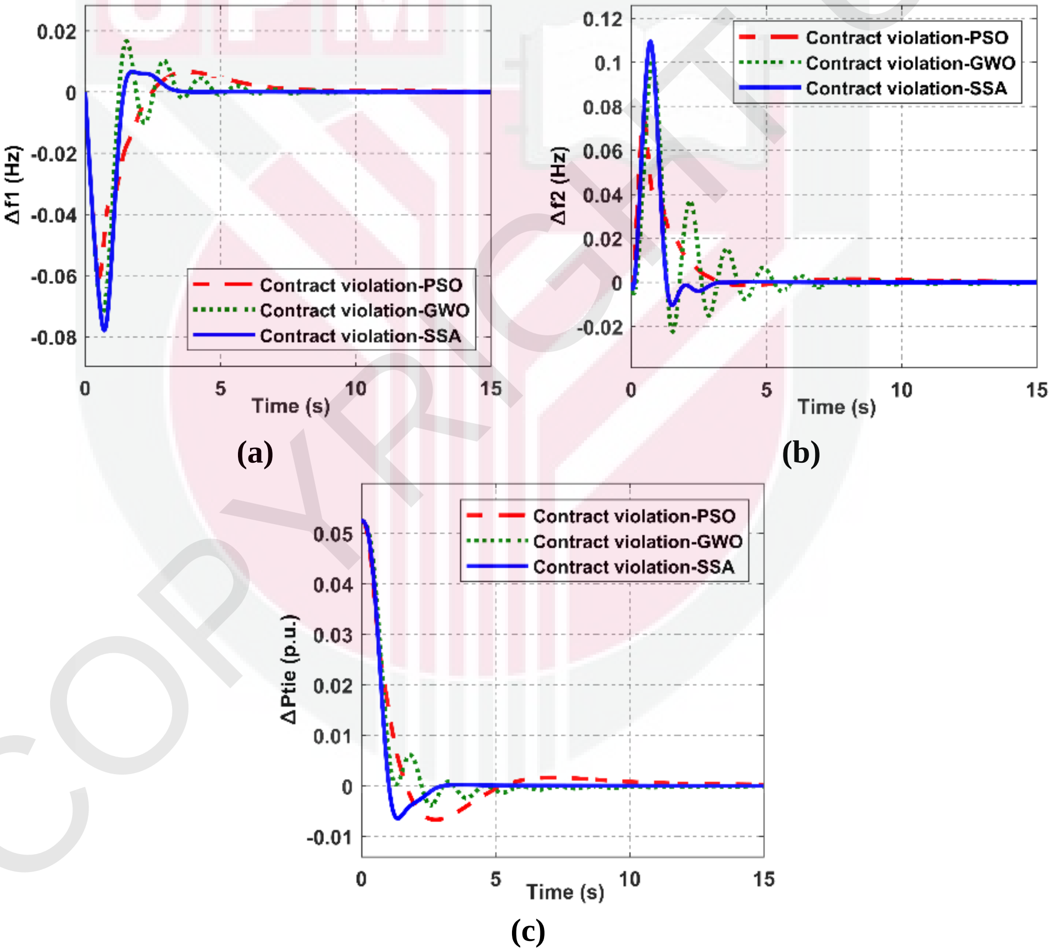

Figure 4.3 : (a) frequency response of area 1, (b) frequency response of area 2, and (c) tie-line power flow between areas, based on contract violation

The results of settling time, rise time, and steady-state error of applying the SSA algorithm compared with PSO and GWO results for the contract violation operation are shown in Table 4.3:

Table 4.3 : Dynamic response results of the contract violation

Optimization Algorithm	ST(s)	RT(s)	SSE
		Δf_1	
Contract violation-PSO	6.9755	99.0×10^{-4}	16.07×10^{-5}
Contract violation-GWO	5.8581	7.64×10^{-4}	14.31×10^{-5}
Contract violation-SSA	3.0417	2.19×10^{-4}	1.612×10^{-5}
		Δf_2	
Contract violation-PSO	4.6796	19×10^{-4}	26.44×10^{-5}
Contract violation-GWO	7.1227	32×10^{-4}	40.33×10^{-5}
Contract violation-SSA	2.8108	1.8×10^{-4}	2.166×10^{-5}
		ΔP_{tie}	
Contract violation-PSO	8.5399	1.0664	26.03×10^{-5}
Contract violation-GWO	5.4328	0.6811	8.791×10^{-5}
Contract violation-SSA	2.5920	0.5995	1.256×10^{-5}

Based on the findings depicted in Figures 4.1, 4.2, and 4.3, as well as Tables 4.1, 4.2, and 4.3, it is evident that the settling time, rise time, and steady-state error reach their minimum values when utilizing the proposed SSA optimization algorithm compared to other optimization techniques. Moreover, the PID controller implemented as a solution in each of these case studies proved to be highly efficient and reliable.

In the initial phase of this study, the focus was primarily on evaluating the performance of the SSA algorithm in optimizing PID controller parameters for the two-area large-scale power system integrated with RESs. Specifically, we examined the impact of RES integration on system dynamics, without incorporating variations in the output of individual sources like geothermal power. The geothermal source's dynamic characteristics were accounted for, but no output adjustments were made. Changes in load demand, however, were considered in subsequent scenarios to further analyze the controllers' adaptability under varying system conditions.

4.3 Simulation Results of SSAGWO Optimized PID Controller of the Integrated Two Area Power System

In this section, the proposed SSAGWO algorithm performance is first evaluated by comparing it with SSA and GWO algorithms in terms of statistical findings using six well-known benchmark functions from the literature. Furthermore, the proposed SSAGWO-tuned PID controller is analyzed for a two-area multi-source interconnected power system shown in Figure 3.4. The proposed SSAGWO optimized PID controller results are compared with SSA and GWO techniques. The obtained results for benchmark functions and various scenarios of the system model considered are discussed in detail in the following sections.

4.3.1 Validation of Benchmark Functions

Six classical benchmark functions with a wide range of characteristics are considered to compare the proposed SSAGWO algorithm's performance to that of GWO and SSA algorithms. The description of the benchmark functions used to verify the performance of various hybrid SSAGWO algorithms is shown in Table C1 in Appendix C. When referring to Table C1, the letter U indicates that the benchmark functions F1-F4 have a single global best and are unimodal. A function is said to be separable if and only if the letter S appears after the letter U in the notation. While if the letter N is written after the letter U, then the function is non-separable(Veerasamy et al., 2022). The exploitation ability of the optimization algorithm is investigated by the functions F1-F4 unimodal benchmark functions, and they indicate that a robust local search capability is necessary for achieving good results. F5 and F6 are multimodal functions. These functions have multiple global bests and are used to investigate the optimization algorithm's exploration ability. The multimodal functions are denoted with the letter M as shown in Table C1. Also, the multimodal functions are classified into separable and non-separable functions (Barshandeh & Haghzadeh, 2021; Narinder & Singh, 2017).

Table 4.4 illustrates the statistical results of the optimization algorithm on the conventional benchmark functions.

Table 4.4 : Benchmark functions statistics

Function	Index	SSAGWO	SSA	GWO
F1	Best	2.2339×10^{-31}	2.7901×10^{-23}	42.0302
	SD	3.3466×10^{-17}	1.8513×10^{-19}	10.11
	Mean	1.0642×10^{-17}	6.6255×10^{-20}	19.9949
	Min	0	2.4457×10^{-47}	8.9247
F2	Best	5.1938×10^{-13}	8.0550×10^{-12}	22.7455
	SD	1.0443×10^{-10}	2.2659×10^{-10}	3.9943
	Mean	3.7025×10^{-11}	7.8765×10^{-11}	9.4191
	Min	1.6096×10^{-80}	4.3857×10^{-55}	5.3553
F3	Best	3.6567×10^{-13}	1.6810×10^{-11}	1.4005
	SD	4.9149×10^{-09}	6.1537×10^{-10}	0.3749
	Mean	1.7859×10^{-09}	3.9256×10^{-10}	1.3875
	Min	8.6574×10^{-58}	1.2831×10^{-24}	0.7203
F4	Best	2.8199×10^{-4}	2.7812×10^{-2}	548.2237
	SD	1.873×10^{-1}	4.97×10^{-2}	492.196
	Mean	1.113×10^{-1}	5.28×10^{-2}	963.3173
	Min	2×10^{-4}	9.3×10^{-3}	435.8797
F5	Best	0	0	76.6652
	SD	0	0	14.1344
	Mean	0	0	61.2244
	Min	0	0	36.401
F6	Best	8.8818×10^{-16}	8.8818×10^{-16}	2.4941
	SD	8.5631×10^{-11}	7.1236×10^{-10}	0.6564
	Mean	4.7806×10^{-11}	3.0156×10^{-10}	3.0160
	Min	8.8817×10^{-16}	8.8817×10^{-16}	1.3413

The results are compared based on the mean, minimum, and standard deviation of reaching the best values. The results were recorded for each algorithm 30 times running. Different benchmark functions are used to assess the algorithms GWO and SSA with SSAGWO by suggesting the algorithm population of 30 and 100 as a number of iterations. The results in Table 4.4 show that the SSAGWO has improved the exploration and exploitation ability compared with other optimization techniques. SSAGWO shows mean, min, and standard deviation less than other algorithms.

4.3.2 Time Domain Analysis of the Integrated Power System

Three cases are presented to analyze the time domain response of the two area power systems integrated with RESs as the following:

Case I: In this case, area 1 is integrated with a PV, and area 2 is integrated with a WTG source. A step load change of 50 MW and 35 MW of the rated power system occurs in area 1 and area 2, respectively. Figure 4.4 shows the frequency deviation of four optimization techniques for tuning PID controller parameters (PSO, GWO, SSA, and SSAGWO) and the Z-N technique. It is clear from the figure that the ST of the proposed SSAGWO-optimized PID controller is much faster than the other optimization-tuned PID controller and Z-N-tuned PID controller. Table 4.5 shows the results of the frequency deviation of area 1 and area 2 and the power deviation in the tie-line power. The ST of the proposed technique is improved by 75.06%, 74.29%, 71.60%, and 71.04% than Z-N, PSO, GWO, and SSA. Moreover, the RT of the frequency deviation of the proposed algorithm is less than other techniques by 85.18%, 78.54%, 73.65%, and 67.38%, respectively. In addition, the value of the undershoot of the frequency deviation is less than other techniques by 9.19%, 0.59%, 7.69%, and 0.59%, respectively. Besides that, the results show that the steady-state error of the power system frequency when using the proposed SSAGWO is less by 85.06%, 78.49%, 73.60%, and 67.34%, respectively, when using other optimization techniques mentioned above. Furthermore, the steady-state values of the performance indices of the frequency deviation are improved by 30.43%, 70.45%, 39.50%, and 64.08% for the ISE, ITSE, IAE, and ITAE, respectively, compared with the best performance index of the optimization techniques presented in Table 4.6. Moreover, the proposed algorithm reduces the controller efforts—defined here as the energy or control actions required by the controller to maintain system stability and minimize frequency deviations in response to disturbances—by 40.67%, 18.60%, 51.70%, and 9.85% for the Z-N, PSO, GWO, and SSA methods, respectively. This reduction indicates a more efficient control response, with fewer and lower-amplitude adjustments needed to stabilize the system, thereby improving energy efficiency and reducing wear on control equipment.

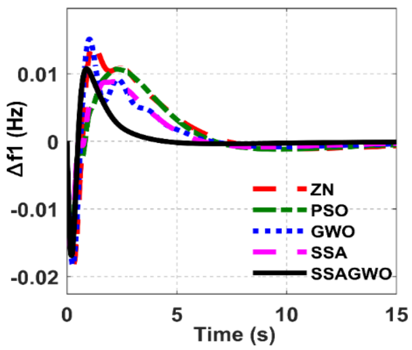

(a)

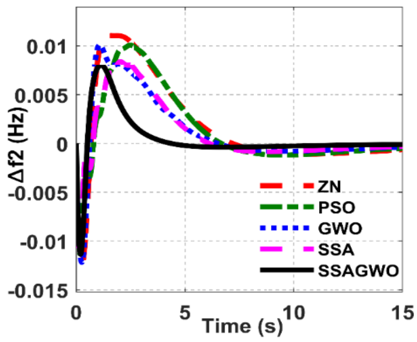

(b)

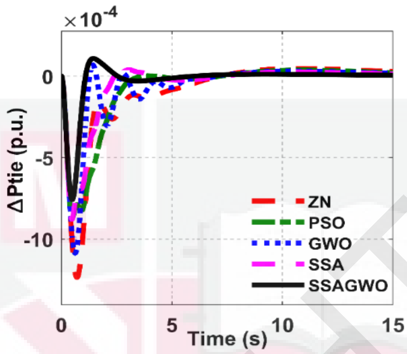

(c)

Figure 4.4 : The frequency deviation responses of the optimization techniques and conventional Z-N method for tuning PID controller parameters for case I: (a) The frequency deviation of area 1; (b) The frequency deviation of area 2; (c) The power deviation of the tie line

Table 4.5 : Frequency and power deviation in the tie-line power of case I

Optimization Technique	Controller Effort	ST (s)	RT (s)	Undershoot	Steady-State Error
		Δf_1			
Z-N	10.03×10^{-2}	15.5747	1.3000×10^{-3}	-1.85×10^{-2}	-2.416×10^{-4}
PSO	7.31×10^{-2}	15.1049	8.9766×10^{-4}	-1.69×10^{-2}	-1.678×10^{-4}
GWO	12.32×10^{-2}	13.6758	7.3107×10^{-4}	-1.82×10^{-2}	-1.367×10^{-4}
SSA	6.60×10^{-2}	13.4111	5.9055×10^{-4}	-1.69×10^{-2}	-1.105×10^{-4}
SSAGWO	$\mathbf{5.95\times10^{-2}}$	**3.8834**	$\mathbf{1.9259\times10^{-4}}$	$\mathbf{-1.68\times10^{-2}}$	$\mathbf{-3.608\times10^{-5}}$
		Δf_2			
Z-N	7.14×10^{-2}	16.7079	1.8×10^{-3}	-1.23×10^{-2}	-2.366×10^{-4}
PSO	7.14×10^{-2}	16.1989	1.3×10^{-3}	-1.14×10^{-2}	-1.643×10^{-4}
GWO	6.24×10^{-2}	15.1067	1.0×10^{-3}	-1.22×10^{-2}	-1.337×10^{-4}
SSA	6.02×10^{-2}	14.7612	8.2627×10^{-4}	-1.14×10^{-2}	-1.081×10^{-4}
SSAGWO	$\mathbf{5.18\times10^{-2}}$	**9.9788**	$\mathbf{2.6857\times10^{-4}}$	$\mathbf{-1.13\times10^{-2}}$	$\mathbf{-3.521\times10^{-5}}$
		ΔP_{tie}			
Z-N	6.6906×10^{-4}	13.6500	2.957×10^{-1}	-1.2×10^{-3}	10.035×10^{-6}
PSO	5.5430×10^{-4}	14.0710	4.0090	-0.8×10^{-3}	7.325×10^{-6}
GWO	3.4650×10^{-4}	11.5746	5.7×10^{-3}	-1.1×10^{-3}	6.509×10^{-6}
SSA	5.3688×10^{-4}	12.0433	2.87×10^{-2}	-0.8×10^{-3}	5.096×10^{-6}
SSAGWO	$\mathbf{1.1460\times10^{-4}}$	**4.9285**	$\mathbf{2.0\times10^{-3}}$	$\mathbf{-0.7\times10^{-3}}$	$\mathbf{1.912\times10^{-6}}$

Table 4.6 : Steady-state indices case I

Performance Index	Δf_1				
	Z-N	**PSO**	**GWO**	**SSA**	**SSAGWO**
ITAE	22.81×10^{-2}	20.45×10^{-2}	14.77×10^{-2}	13.860×10^{-2}	$\mathbf{4.978\times10^{-2}}$
IAE	5.787×10^{-2}	4.785×10^{-2}	4.296×10^{-2}	3.625×10^{-2}	$\mathbf{2.193\times10^{-2}}$
ITSE	9.9×10^{-4}	8.1×10^{-4}	5×10^{-4}	4.4×10^{-4}	$\mathbf{1.3\times10^{-4}}$
ISE	5×10^{-4}	3.4×10^{-4}	3.4×10^{-4}	2.3×10^{-4}	$\mathbf{1.6\times10^{-4}}$
Performance Index	Δf_2				
	Z-N	**PSO**	**GWO**	**SSA**	**SSAGWO**
ITAE	22.22×10^{-2}	20.070×10^{-2}	14.4×10^{-2}	13.64×10^{-2}	$\mathbf{4.845\times10^{-2}}$
IAE	5.236×10^{-2}	4.425×10^{-2}	3.816×10^{-2}	3.322×10^{-2}	$\mathbf{1.862\times10^{-2}}$
ITSE	8.9×10^{-4}	7.5×10^{-4}	4.3×10^{-4}	4×10^{-4}	$\mathbf{1\times10^{-4}}$
ISE	3.8×10^{-4}	2.7×10^{-4}	2.3×10^{-4}	1.7×10^{-4}	$\mathbf{0.997\times10^{-4}}$

Case II: In this case, area 1 and area 2 are integrated with PV resources. Similar to a step change in demand load applied in case I, it occurs in case II. Figure 4.5 shows the frequency deviation of the two areas and the power deviation in tie-line power for tuning PID parameters of the proposed SSAGWO compared with (PSO, GWO, and SSA) and the Z-N technique. The figure demonstrates that the ST of the proposed SSAGWO-optimized PID controller is significantly less than that of the other optimization-tuned PID controller and the Z-N-tuned PID controller.

The results of the frequency deviation and tie-line power of case II are shown in Table 4.7. The ST of the proposed algorithm has been enhanced by 75.94%, 74.23%, 72.53%, and 70.83% compared with the ST of Z-N, PSO, GWO, and SSA, respectively. In addition, the RT of the frequency deviation of the proposed SSAGWO is less than other techniques by 85.63%, 80.60%, 75.24%, and 69.86%, respectively.

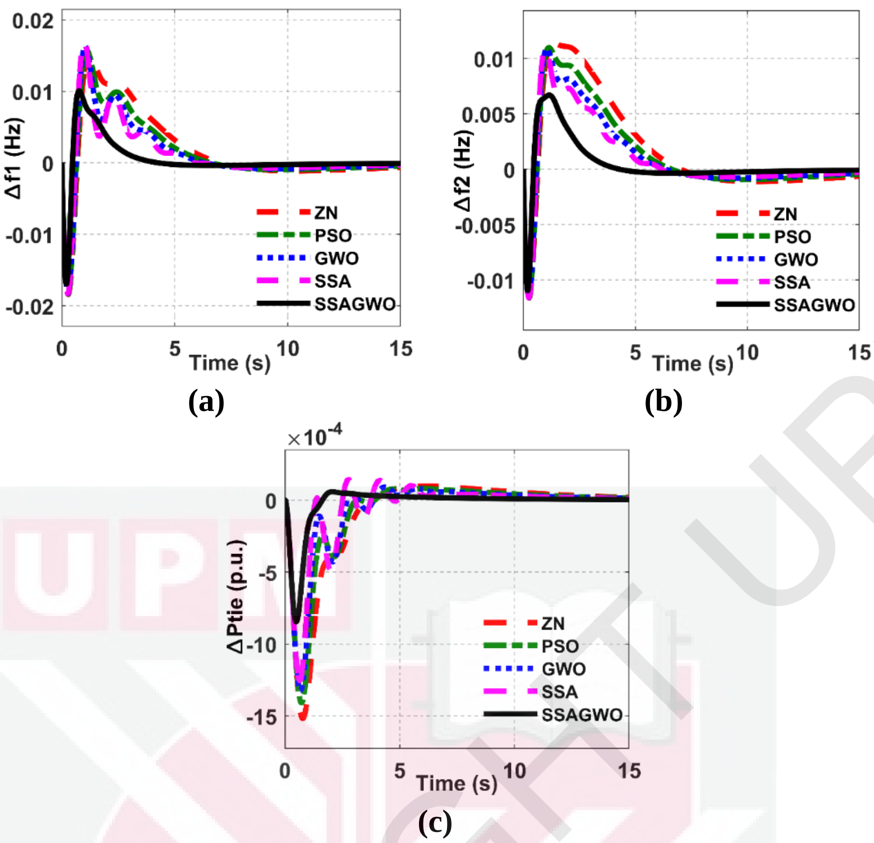

Figure 4.5 : The frequency deviation responses of the optimization techniques and conventional Z-N method for tuning PID controller parameters for case II: (a) The frequency deviation of area 1; (b) The frequency deviation of area 2; (c) The power deviation of the tie line

Moreover, the peak undershoot value of the frequency deviation is less than other techniques by 8.15%, 8.15%, 7.65%, and 7.65%, respectively. Furthermore, the results shown in Table 4.7 depict that the steady-state error of the frequency deviation of the power system is less than other techniques by 85.93%, 80.54%, 75.20%, and 69.83% respectively, when using the proposed SSAGWO to tune PID controller parameters.

Table 4.7 : Frequency and power deviation in the tie-line power of case II

Optimization Technique	Controller Effort	ST (s)	RT (s)	Undershoot	Steady-State Error
		Δf_1			
Z-N	14.71×10^{-2}	15.5119	12.000×10^{-4}	-1.84×10^{-2}	-2.296×10^{-4}
PSO	17.09×10^{-2}	14.4838	8.8905×10^{-4}	-1.84×10^{-2}	-1.661×10^{-4}
GWO	19.04×10^{-2}	13.5912	6.9661×10^{-4}	-1.83×10^{-2}	-1.303×10^{-4}
SSA	20.49×10^{-2}	12.7962	5.7231×10^{-4}	-1.83×10^{-2}	-1.071×10^{-4}
SSAGWO	$\mathbf{8.060\times10^{-2}}$	**3.73260**	$\mathbf{1.7247\times10^{-4}}$	$\mathbf{-1.69\times10^{-2}}$	$\mathbf{-3.231\times10^{-5}}$
		Δf_2			
Z-N	8.96×10^{-2}	16.7318	17.000×10^{-4}	-1.16×10^{-2}	-2.264×10^{-4}
PSO	9.55×10^{-2}	15.9302	13.000×10^{-4}	-1.16×10^{-2}	-1.637×10^{-4}
GWO	10.32×10^{-2}	15.1767	9.8148×10^{-4}	-1.16×10^{-2}	-1.283×10^{-4}
SSA	11.09×10^{-2}	14.4961	8.0590×10^{-4}	-1.16×10^{-2}	-1.054×10^{-4}
SSAGWO	$\mathbf{5.19\times10^{-2}}$	**9.69000**	$\mathbf{2.4235\times10^{-4}}$	$\mathbf{-1.09\times10^{-2}}$	$\mathbf{-3.178\times10^{-5}}$
		ΔP_{tie}			
Z-N	6.8776×10^{-4}	12.0385	6.85×10^{-2}	-1.5×10^{-3}	6.506×10^{-6}
PSO	6.9817×10^{-4}	11.2029	81.85×10^{-2}	-1.3×10^{-3}	5.092×10^{-6}
GWO	8.2955×10^{-4}	10.5142	7.3×10^{-3}	-1.3×10^{-3}	4.183×10^{-6}
SSA	17.000×10^{-4}	9.7186	10.9×10^{-3}	-1.2×10^{-3}	3.547×10^{-6}
SSAGWO	$\mathbf{6.1746\times10^{-4}}$	**6.4993**	$\mathbf{3.6\times10^{-3}}$	$\mathbf{-0.8\times10^{-3}}$	$\mathbf{1.167\times10^{-6}}$

The steady-state values of the ISE, ITSE, IAE, and ITAE all improve when using the proposed SSAGWO upon the best performance index of the optimization strategies shown in Table 4.8 by 57.57%, 74.42%, 46.93%, and 62.58% respectively.

Table 4.8 : Steady-state indices case II

Performance Index	Δf_1				
	Z-N	**PSO**	**GWO**	**SSA**	**SSAGWO**
ITAE	22.71×10^{-2}	17.88×10^{-2}	14.71×10^{-2}	12.45×10^{-2}	$\mathbf{4.658\times10^{-2}}$
IAE	5.845×10^{-2}	4.97×10^{-2}	4.356×10^{-2}	3.899×10^{-2}	$\mathbf{2.069\times10^{-2}}$
ITSE	10.1×10^{-4}	7×10^{-4}	5.3×10^{-4}	4.3×10^{-4}	$\mathbf{1.1\times10^{-4}}$
ISE	5.2×10^{-4}	4.2×10^{-4}	3.6×10^{-4}	3.3×10^{-4}	$\mathbf{1.4\times10^{-4}}$
Performance Index	Δf_2				
	Z-N	**PSO**	**GWO**	**SSA**	**SSAGWO**
ITAE	21.72×10^{-2}	17.07×10^{-2}	14.03×10^{-2}	11.91×10^{-2}	$\mathbf{4.393\times10^{-2}}$
IAE	5.146×10^{-2}	4.32×10^{-2}	3.747×10^{-2}	3.33×10^{-2}	$\mathbf{1.679\times10^{-2}}$
ITSE	8.5×10^{-4}	5.7×10^{-4}	4.1×10^{-4}	3.1×10^{-4}	$\mathbf{0.801\times10^{-4}}$
ISE	3.7×10^{-4}	2.8×10^{-4}	2.2×10^{-4}	1.9×10^{-4}	$\mathbf{0.792\times10^{-4}}$

Moreover, the controller effort was reduced by 45.20%, 52.83%, 57.66%, and 60.66%, respectively, when using SSAGWO compared with other optimization techniques.

Case III: In this case, WTPG resources are integrated into both areas 1 and area 2. Figure 4.6 shows the frequency deviation and tie-line power of the proposed model.

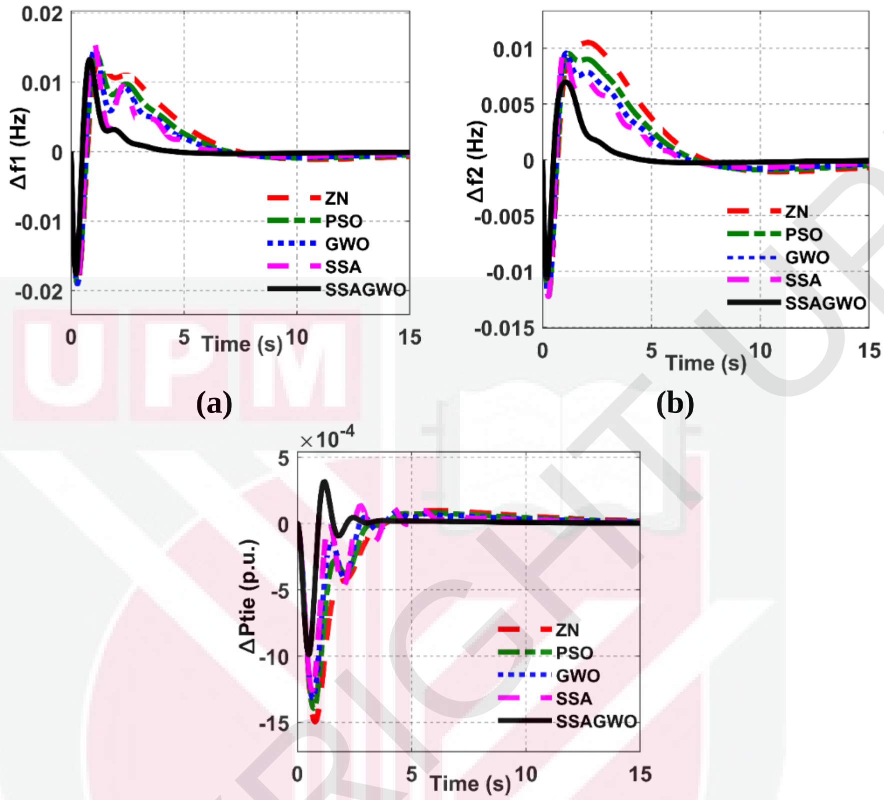

(c)

Figure 4.6 : The frequency deviation responses of the optimization techniques and conventional Z-N method for tuning PID controller parameters for case III: (a) The frequency deviation of area 1; (b) The frequency deviation of area 2; (c) The power deviation of the tie line

The figures show that the ST of the frequency deviation when using SSAGWO is less than the other optimization-tuned PID controller parameters mentioned above. The results of this case in detail are demonstrated in Table 4.9. With the same sequence of comparing the proposed SSAGWO with other optimization techniques illustrated in case I and case II, the ST was improved by 75.40%, 73.66%, 71.88%, and 70.03%, respectively. In addition, the RT of the frequency deviation was reduced by 88.10%, 84.01%, 79.56%, and 75.15%, respectively. There is also a reduction in the peak undershoot value of the frequency deviation of 8.37%, 7.89%, 7.89%, and 7.41 compared to the other techniques. Table 4.9 further demonstrates that using the proposed SSAGWO to tune PID controller parameters decreased the steady-state error of the frequency deviation of the power system by 88.41%, 83.97%, 79.52%, and 75.10%, respectively.

Compared to the best performance index of the optimization strategies presented in Table 4.10, the proposed SSAGWO improves the steady-state values of the ISE, ITSE, IAE, and ITAE by 50%, 74.42%, 49.88%, and 68.96%, respectively. In addition, SSAGWO reduced controller effort by 20.17%, 31.57%, 40.82%, and 19.48% compared to other optimization methods.

Table 4.9 : Frequency and power deviation in the tie-line power of case III

Optimization Technique	Controller Effort	ST (s)	RT (s)	Undershoot	Steady-State Error
		Δf_1			
Z-N	12.84×10^{-2}	15.5405	13.000×10^{-4}	-1.91×10^{-2}	-2.5010×10^{-4}
PSO	14.98×10^{-2}	14.5127	9.6740×10^{-4}	-1.90×10^{-2}	-1.8080×10^{-4}
GWO	17.32×10^{-2}	13.5950	7.5658×10^{-4}	-1.90×10^{-2}	-1.4150×10^{-4}
SSA	12.73×10^{-2}	12.7563	6.2227×10^{-4}	-1.89×10^{-2}	-1.1640×10^{-4}
SSAGWO	$\mathbf{10.25\times10^{-2}}$	**3.8229**	$\mathbf{1.5464\times10^{-4}}$	$\mathbf{-1.75\times10^{-2}}$	$\mathbf{-0.2898\times10^{-4}}$
		Δf_2			
Z-N	8.55×10^{-2}	16.7930	19×10^{-4}	-1.22×10^{-2}	-2.469×10^{-4}
PSO	7.93×10^{-2}	15.9452	14×10^{-4}	-1.22×10^{-2}	-1.783×10^{-4}
GWO	8.88×10^{-2}	15.1851	11×10^{-4}	-1.22×10^{-2}	-1.395×10^{-4}
SSA	9.99×10^{-2}	14.5028	8.7753×10^{-4}	-1.22×10^{-2}	-1.148×10^{-4}
SSAGWO	$\mathbf{6.48\times10^{-2}}$	**8.8496**	$\mathbf{2.1741\times10^{-4}}$	$\mathbf{-1.06\times10^{-2}}$	$\mathbf{-0.285\times10^{-4}}$
		ΔP_{tie}			
Z-N	7.2857×10^{-4}	12.0973	58.7×10^{-3}	-15×10^{-4}	6.501×10^{-6}
PSO	6.2357×10^{-4}	11.2433	34.6×10^{-3}	-14×10^{-4}	5.083×10^{-6}
GWO	8.4564×10^{-4}	10.5482	7.9×10^{-3}	-13×10^{-4}	4.173×10^{-6}
SSA	5.4×10^{-4}	9.9408	9.1×10^{-3}	-12×10^{-4}	3.536×10^{-6}
SSAGWO	$\mathbf{1.7\times10^{-4}}$	**3.8952**	$\mathbf{3.2793\times10^{-3}}$	$\mathbf{-9\times10^{-4}}$	$\mathbf{1.022\times10^{-6}}$

Table 4.10 : Steady-state indices case III

Performance Index	Δf1				
	Z-N	PSO	GWO	SSA	SSAGWO
ITAE	23.42×10^{-2}	18.45×10^{-2}	15.17×10^{-2}	12.87×10^{-2}	**3.995×10^{-2}**
IAE	5.882×10^{-2}	5.01×10^{-2}	4.401×10^{-2}	3.947×10^{-2}	**1.978×10^{-2}**
ITSE	10.3×10^{-4}	7.1×10^{-4}	5.3×10^{-4}	4.3×10^{-4}	**1.1×10^{-4}**
ISE	5.1×10^{-4}	4.1×10^{-4}	3.5×10^{-4}	3.2×10^{-4}	**1.6×10^{-4}**
Performance Index	**Δf2**				
	Z-N	**PSO**	**GWO**	**SSA**	**SSAGWO**
ITAE	22.43×10-2	17.65×10-2	14.51×10-2	12.29×10^{-2}	**3.749×10^{-2}**
IAE	5.18×10^{-2}	4.357×10^{-2}	3.787×10^{-2}	3.366×10^{-2}	**1.524×10^{-2}**
ITSE	8.7×10^{-4}	5.9×10^{-4}	4.2×10^{-4}	3.2×10^{-4}	**0.671×10^{-4}**
ISE	3.6×10^{-4}	2.7×10^{-4}	2.2×10^{-4}	1.8×10^{-4}	**0.731×10^{-4}**

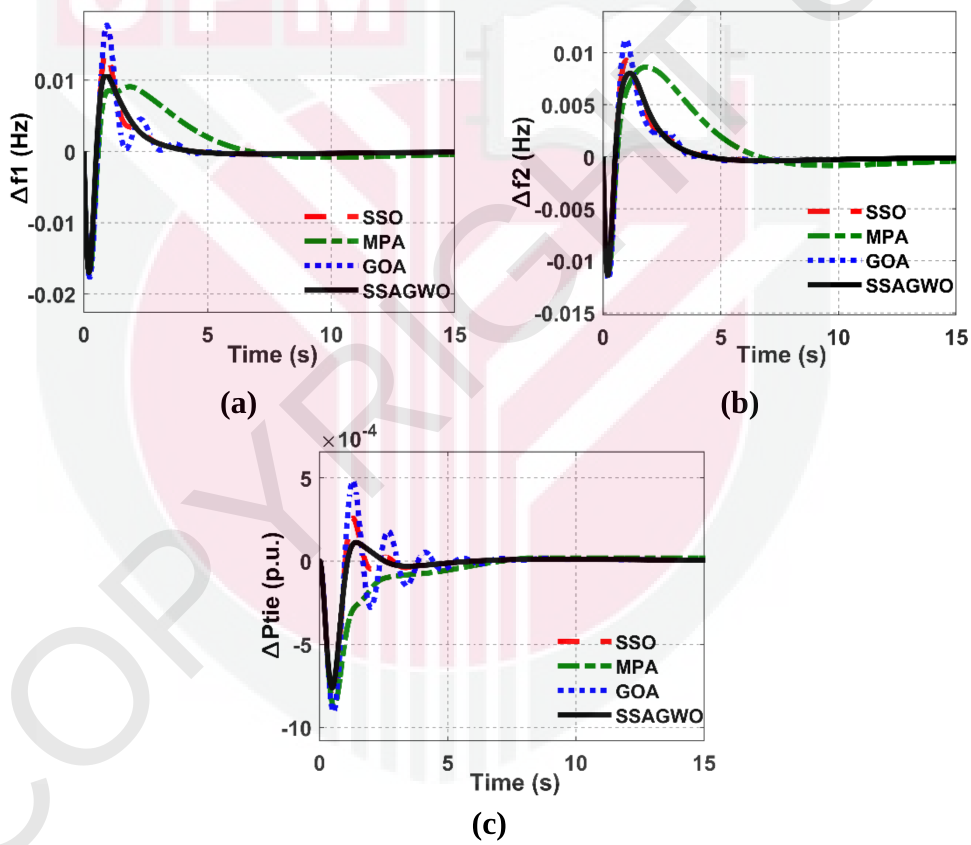

Figure 4.7 : The frequency deviation responses and change in tie line power of SSAGWO compared with GOA, MPA, and SSO for tuning PID controller parameters for case I: (a) The frequency deviation of area 1; (b) The frequency deviation of area 2; (c) The power deviation of the tie line

A comparison of the performance of the proposed hybrid SSAGWO optimization technique with the performance of using the GOA by Nosratabadi et al. (2019), MPA by Sobhy et al. (2021), and SSO (Hasanien & El-Fergany, 2019) has been implemented in order to demonstrate the robustness of the suggested approach. Within the context of this discussion, case I has been utilized as a case study. Figure 4.7 depicts the dynamic response of the proposed power system model to the frequency deviation and the change in tie-line power. When compared with GOA, MPA, and SSO, the results demonstrate that the ST, overshoot, and oscillations of the frequency deviation, as well as the tie-line power, are improved when SSAGWO is utilized.

i. Robustness analysis

To study the effectiveness of the proposed algorithm, a random step change in load demand is applied in area 1, as shown in Figure 4.8. The frequency response of area 1, area 2, and tie line power for this scenario are depicted in Figure 4.9. According to the findings, the proposed algorithm tunes the PID controller response more quickly for a sudden change in load than other optimization techniques do. Additionally, the power supplied by the tie-line changed in response to the changing load demands of the system while keeping a constant level of output despite these changes.

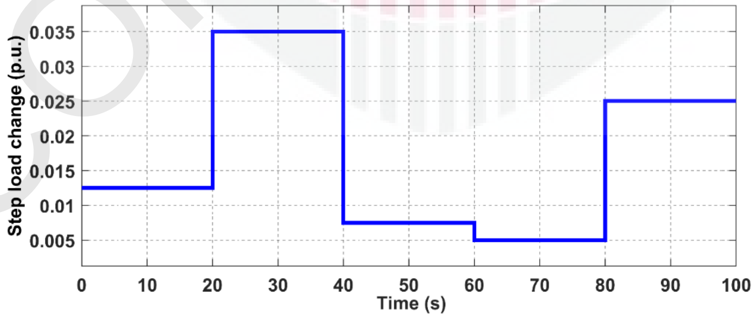

Figure 4.8 : Random change load

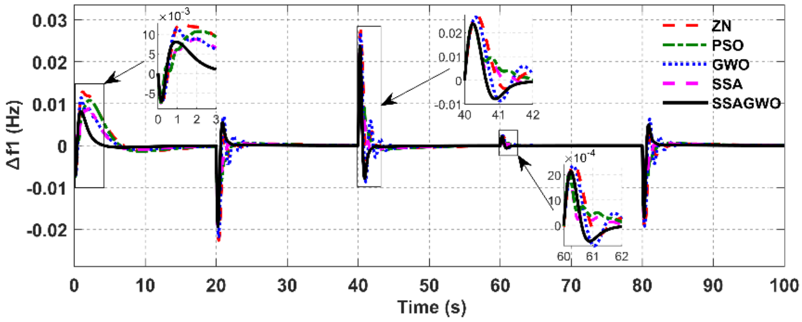

(a)

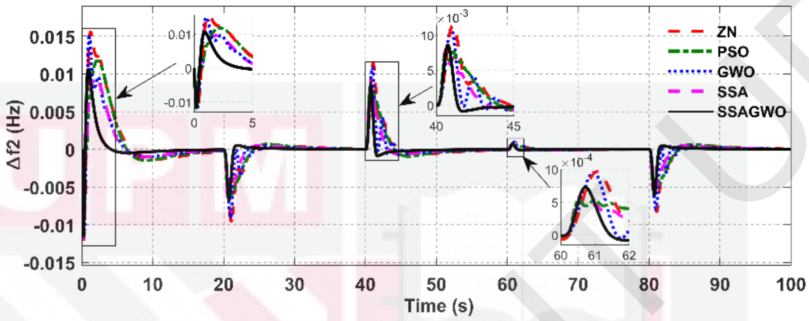

(b)

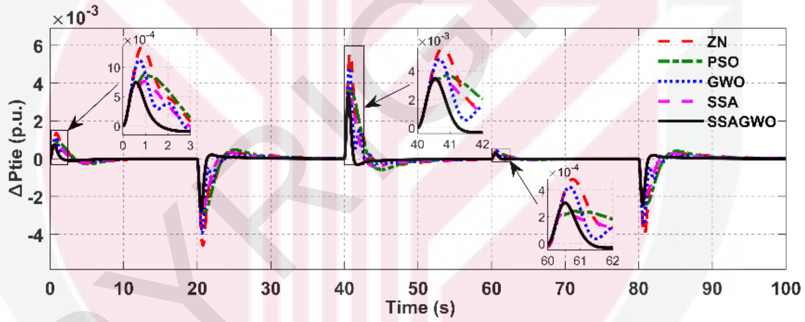

(c)

Figure 4.9 : Dynamic response of the multi-area power system at a random change load: (a) The frequency deviation of area 1; (b) The frequency deviation of area 2; (c) The power deviation of the tie line

ii. Real-time Variation of RES

To further prove the robustness of the proposed technique, solar radiation data collected at Universiti Putra Malaysia, the output power from the PV, is integrated with area 1 . As shown in Figure 4.10, the solar irradiation values were measured from January through December 2014 for a total of 200-time slots of 0.5 seconds. The multi-area power system in case 1 has been chosen to assess the dynamic response for real-time solar power fluctuations with all optimization techniques used in this study. The frequency deviation of area 1 and area 2 is shown in Figure 4.11 for this scenario. It can be deduced that the proffered SSAGWO algorithm-tuned PID controller shows a better and smoother response than other tuning methods, along with minimal undershoot, less ST, RT, steady-state error, and controller efforts.

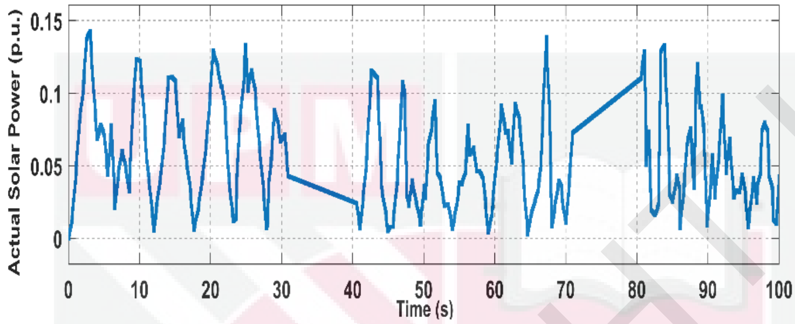

Figure 4.10 : Solar input power from actual data

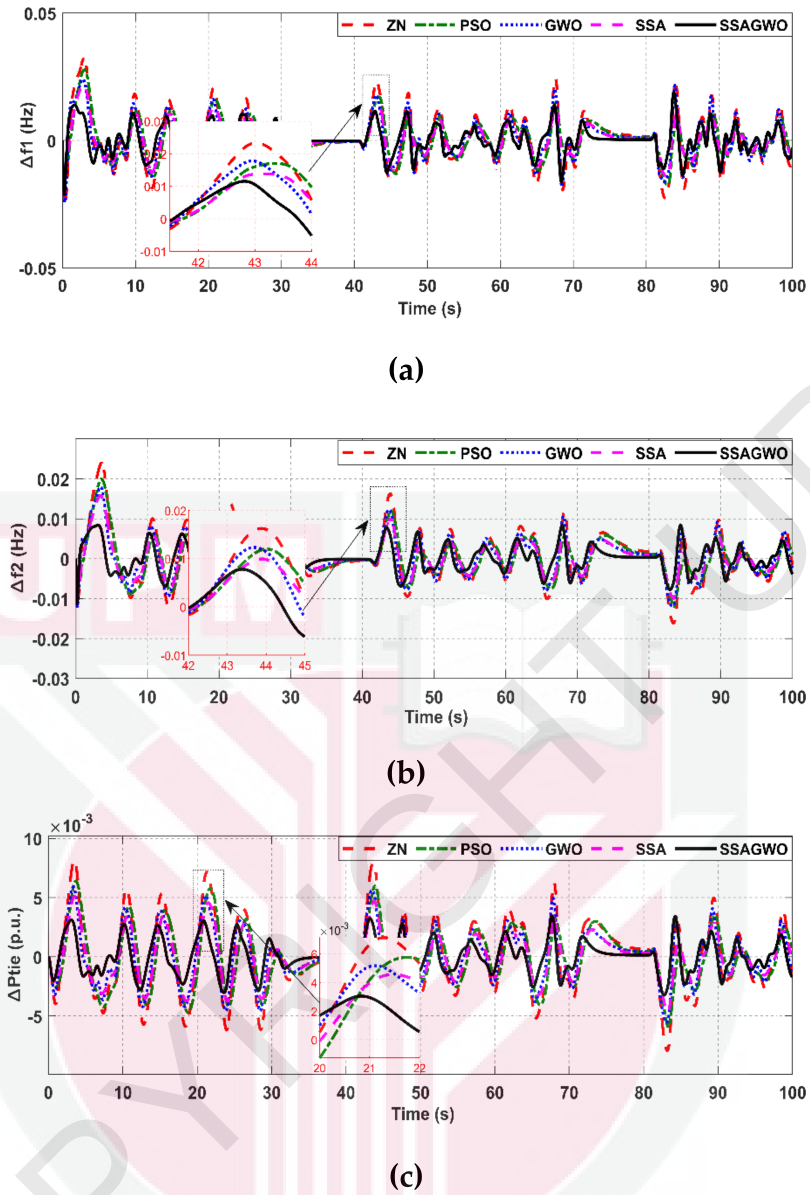

Figure 4.11 : Dynamic response comparison of the multi-area power system using various optimization techniques: (a) The frequency deviation of area 1; (b) The frequency deviation of area 2; (c) The power deviation of the tie line

iii. Sensitivity analysis

The sensitivity analysis of the proposed controller technique has been performed to prove the robustness of the controller parameters obtained under a variation of the inertia constant and change in the nominal loading of the power system. The value of the inertia constant of the power system changed from 75% to 125% of its nominal value (H = 5), and the loading condition changed by ± 25% corresponding to the nominal system loading (50% loading). The controller's efficacy is demonstrated by using the value of the PID controller parameters under the nominal condition. Changing the inertia constant of the power system will affect the value of the time constant Tps. Likewise, the time constant of the power system block Tps and the gain constant Kps are affected by changes in load conditions. Figure 4.12, illustrates the dynamic response of the power system with variation in inertia constant value.

Figure 4.13, represents the dynamic response of the power system under change in the nominal loading. The results demonstrate a high tolerance for a wide range of changes in system parameters, as evidenced by the gain values obtained under nominal conditions. This robustness is achieved because the SSAGWO optimization algorithm effectively tunes the controller parameters to adapt to various system conditions, based on the capacity and characteristics of the proposed system. By accounting for variations in inertia constant and loading conditions during the tuning process, the algorithm generalizes the controller parameters to handle these fluctuations without requiring further adjustments. Because of this, one can conclude that the parameters do not need to be re-tuned even if there is a substantial change in the system's conditions and parameters.

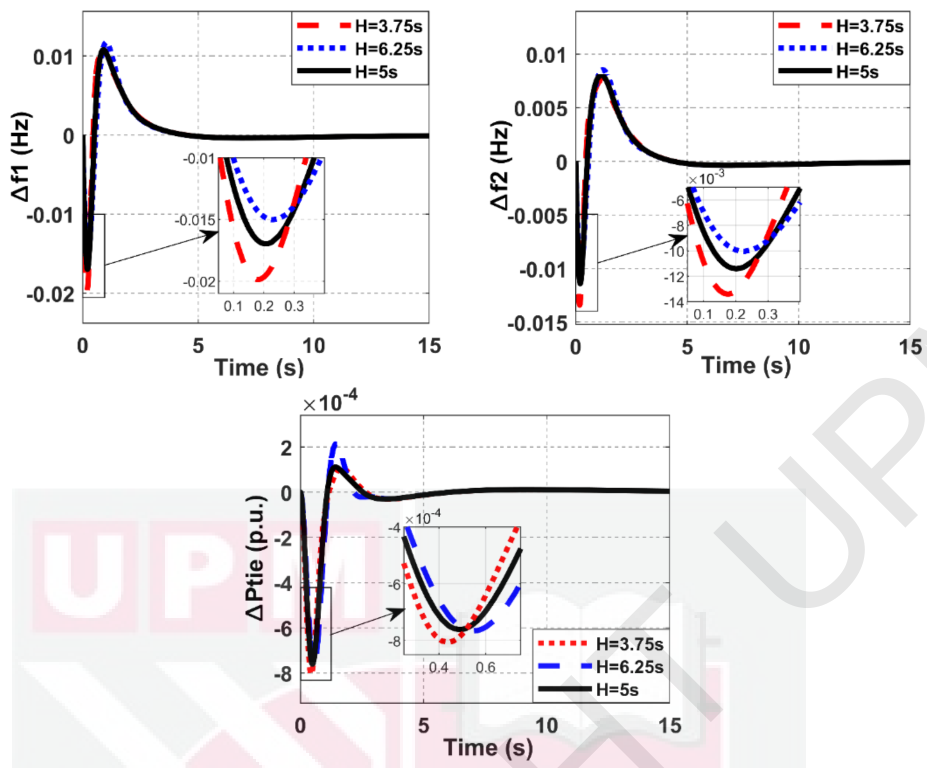

Figure 4.12 : The dynamic response of the power system under different inertia constant (75% and 125% of the nominal value H = 5s)

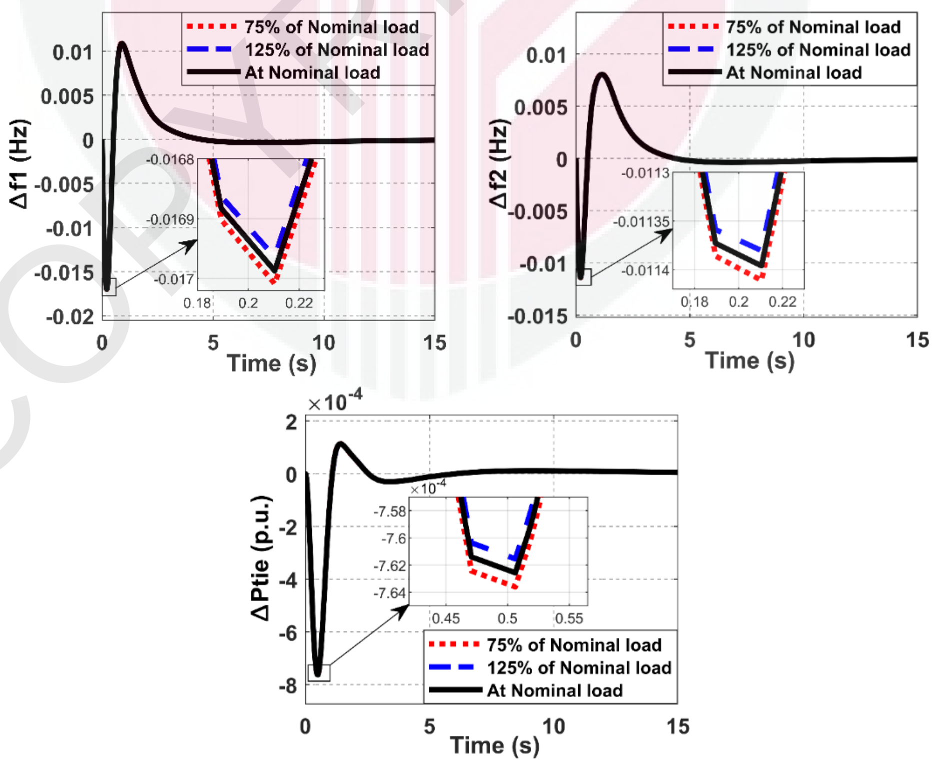

Figure 4.13 : The dynamic response of the power system under different system loading (±25% of the nominal load)

4.3.3 Convergence Curve

This section presents the convergence curves obtained by the proposed SSAGWO algorithm and other optimization algorithms. The convergence curve shows the minimum ITAE of ACE for the model is presented in Figure 4.14. The hybrid SSAGWO approach is shown to converge faster than other optimization methods, proving that the proposed SSAGWO has a better balance between exploration and exploitation than the standard GWO and SSA algorithms.

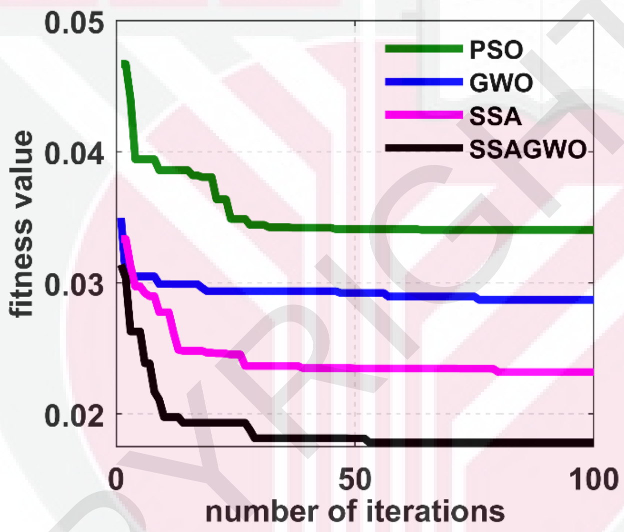

Figure 4.14 : Convergence curve of the algorithms

4.3.4 Stability Analysis of the Hybrid Power System

It is essential to take into consideration the effects of optimization techniques for PID tuning and validation of the stability analysis by calculating the state space of the system based on the Simulink model of the system. To assess the frequency stability of the power system and the proposed model optimized with SSAGWO-tuned PID controller parameters, two scenarios are considered. In scenario 1, area 1 is considered as the input signal of the transfer function; while in scenario 2 area 2 is considered as the input signal of the transfer function. The state-space equations with estimation of the Closed Loop Transfer Function (CLTF) are illustrated in Appendix B.

The closed-loop control of the hybrid power system shown in Figure 3.8, can be simplified as shown in Figure 4.15 in order to estimate the CLTF equation:

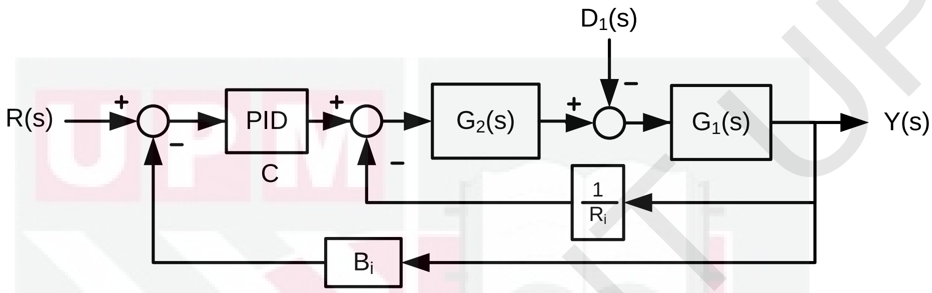

Figure 4.15 : The simplified closed-loop control system for stability analysis

The derivation of the total response of the closed-loop transfer function of the interconnected power system was modelled with PID controller as the following:

$$R(s)G_1(s)G_2(s)C - B_i Y(s)G_1(s)G_2(s)C - Y(s)\frac{1}{R_i}G_1(s)G_2(s) - D_1(s)G_1(s) = Y(s) \tag{4.1}$$

$$Y(s) = \frac{R(s)G_1(s)G_2(s)C}{Z} - \frac{D_1G_1(s)}{Z} \tag{4.2}$$

$$\therefore Y(s) = Y_{11}(s) + Y_{12}(s) \tag{4.3}$$

where

$$Z = 1 + B_iG_1(s)G_2(s)C + \frac{1}{R_i}G_1(s)G_2(s) \tag{4.5}$$

The change in load demand (ΔP_D) is addressed for using the following expression for the CLTF of the system for the proposed controller:

$$\Delta f = \frac{-G_1}{1 + G_1 G_2 \left[CB_i + \frac{1}{R} \right]} \Delta P_D \tag{4.6}$$

The CLTF can be applied to variations in tie-line power, as indicated by the definition of power variation.

$$\Delta f = \frac{CG_1 G_2}{1 + G_1 G_2 \left[CB_i + \frac{1}{R} \right]} \Delta P_{tie} \tag{4.7}$$

By using superposition theorem, the CLTF for the total variations of the frequency response can be defined as:

$$\Delta f = \frac{-G_1 \Delta P_D + CG_1 G_2 \Delta P_{tie}}{1 + G_1 G_2 \left[CB_i + \frac{1}{R} \right]} \tag{4.8}$$

By using the state-space analysis, the CLTF for the two scenarios (i.e. area 1 and area 2) can be presented as:

$$CLTF = \frac{num}{den} \tag{4.9}$$

Appendix B shows the state-space matrix, definition of the num, and den of the proposed hybrid power system model.

Figure 4.16 depicts the frequency response of the Bode plot for the hybrid power system model considering the two scenarios proposed in stability analysis, with a gain margin of 1.57 and 8.71 dB and a gain cross-over frequency of 3.65 and 0.81 (rad/s) for area 1 and area 2 respectively. According to the Bode analysis response, the closed-loop system for the proposed SSAGWO-optimized PID controller of the hybrid power network is stable.

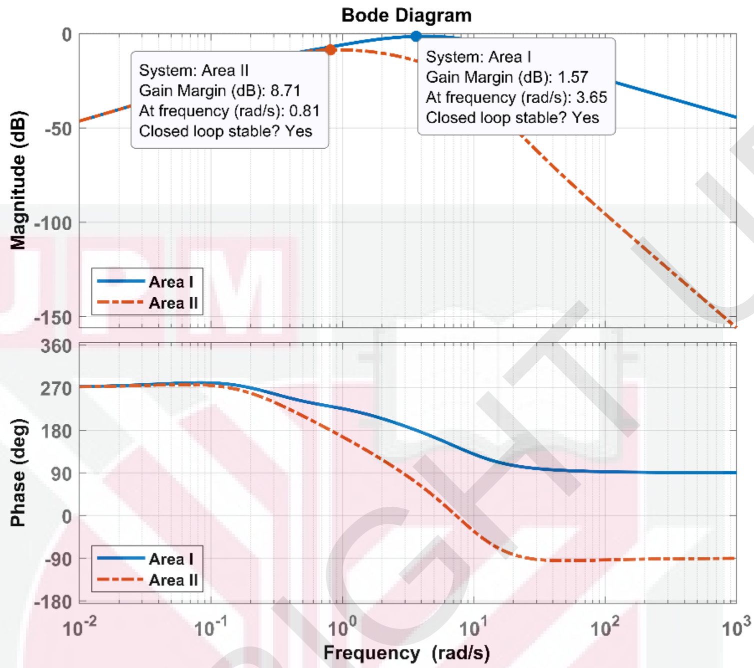

Figure 4.16 : Bode analysis of frequency stability

4.4 Simulation Results of VIC for Frequency Regulation of Microgrid

The dynamic response of the proposed MG model which consists of a BDG integrated with a solar thermal plant and WTG, including the proposed control loops is illustrated in Figure 3.10. The MG system consisted of a 600 kW BDG, 550 kW of a solar thermal plant, 350 kW of a WTG, 300 kW of an ESS capacity, and 600 kW of a residential demand load. Further, the study's model uses the transient demand load change as a disturbance signal to illustrate the performance of the PID and VIC loops under constant RES input power.

A step load change of 225 kW of the rated power occurs in the MG system. The scenario studied presents the optimal tuning parameters of the PID controllers of the secondary loop control and an optimal value of the virtual inertia and virtual damping of the VIC loop. The tuning technique occurs by using the proposed hybrid optimization algorithm SSAMGO and comparing the results with the SSAGWO technique. Figure 4.17, shows the dynamic response of the frequency deviation during a sudden change in the load demand of the optimization techniques for tuning PID parameters.

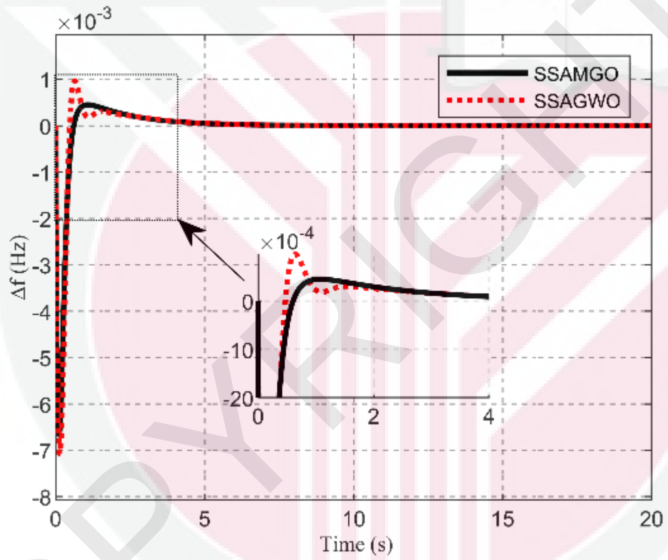

Figure 4.17 : The dynamic response of the frequency deviation of the MG system using the hybrid SSAMGO compared with SSAGWO

It is clear from the results shown in Figure 4.17 that the settling time, rise time, overshoot, undershoot, and peak time of the proposed algorithm are much faster than SSAGWO. More details about the results are illustrated in Table 4.11.

Table 4.11 : Dynamic results illustrating the value of ST, RT, OS, US, and PT

Optimization Technique	ST(s)	RT (s)	OS	US	PT(s)
SSAGWO	3.44	5.59×10^{-6}	9.1×10^{-4}	-7.1×10^{-3}	0.1335
SSAMGO	3.35	2.27×10^{-6}	4.5×10^{-4}	-6.7×10^{-3}	0.1108

where ST, RT, OS, US, and PT are settling time, rise time, overshoot, undershoot, and peak time, respectively.

To illustrate the act of the PID controller and VIC loop, Figure 4.18, presents the details of the energy contributions of all sources of the proposed model. In this scenario, as mentioned previously, supposing the input power of the RESs is a constant value. At t = 0, a sudden change in the load demand occurs.

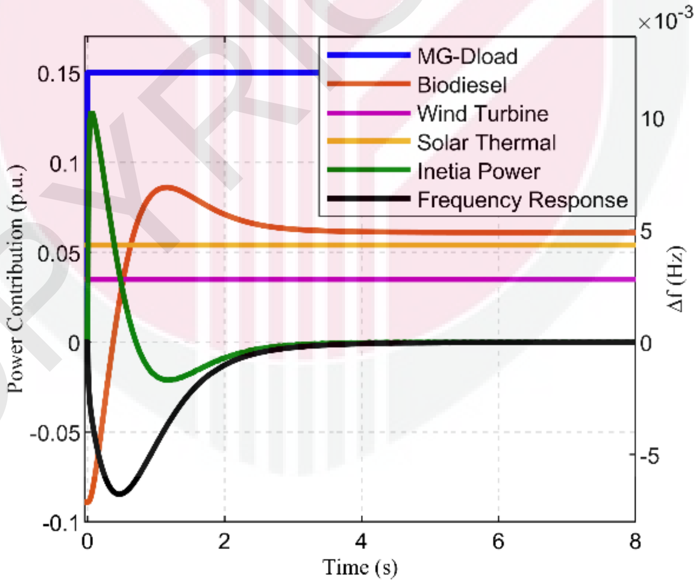

Figure 4.18 : Power contribution and frequency deviation of the microgrid system based on the proposed algorithm

In addition, a drop in the system frequency is a result of an increase in the demand load causing a reduced rotational speed from the synchronous generator to fulfill the additional energy demands. The frequency nadir point is the lowest point in the frequency curve that reaches under an unbalanced load. Frequency control has three stages: inertia control stage, natural droop control (primary control), and secondary frequency control. The inertia control stage is the first line of defence to reduce the frequency deviation during the load imbalance. VIC is acting to compensate the MG system with the required active power by charging/discharging the ESS. The VIC process is depicted as the green curve in Figure 4.18. Consequently, the droop control loop naturally regulates the frequency for balancing between the generation and the demand power. The secondary control stage controls the governor valve position to increase/decrease the speed of the generator turbine. The PID controller process is shown in Figure 4.18 as a brown curve.

The proposed hybrid algorithm is tested and validated by applying a random change in load demand to the MG power system to investigate its efficacy. The frequency response for this case can be observed in Figure 4.19. Simulation results show that the coefficients of the PID have been optimally computed by the proposed SSAMGO algorithm under a sudden change in the load. During this period, the VIC of the ESS compensates for the lack of inertia of the MG.

The convergence curves obtained by the proposed SSAMGO optimization algorithm and the SSAGWO technique were utilized to evaluate the efficacy of the hybrid optimization strategies employed in this research. Figure 4.20, shows the minimum ITAE value of ACE for the MG power system.

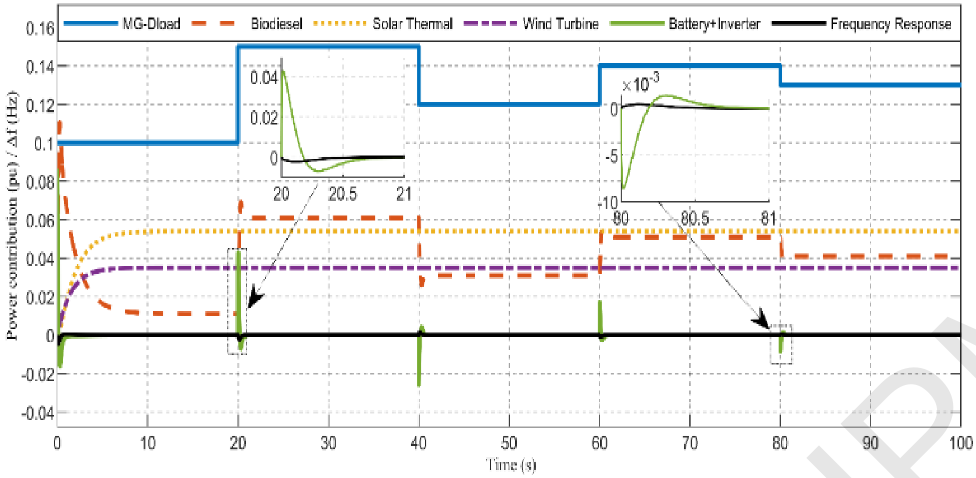

Figure 4.19 : Frequency response of the MG at a step change in the load demand

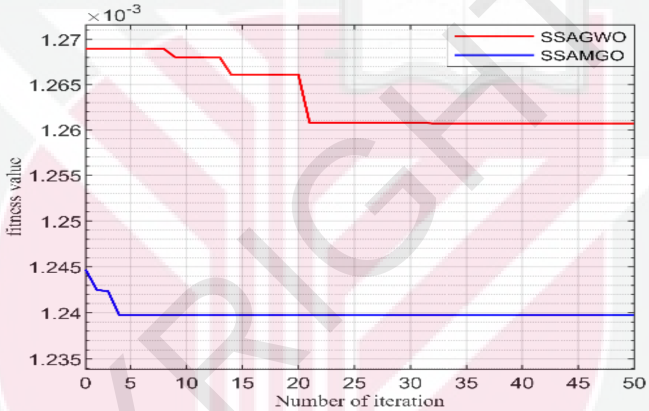

Figure 4.20 : Convergence curve of SSAMGO and SSAGWO algorithms

Convergence to the optimal solution is faster with the proposed algorithmic approach than SSAGWO. SSAMGO's best score was achieved after only four iterations, while SSAGWO required twenty-one iterations. Furthermore, SSAMGO needs 6406 s, and SSAGWO takes 11047 s to identify the global optimal solutions for the given number of populations and iterations assumed. The suggested SSAMGO demonstrates a better balance between exploration and exploitation. The results of the comparison between SSAMGO and SSAGWO are shown in detail in Table 4.12.

Table 4.12 : Dynamic response results

Optimization Technique	Control efforts	Steady-state error	Peak value	Elapsed time (s)	Best score
SSAGWO	$7.3x10^{-4}$	$-4.5x10^{-7}$	$7.1x10^{-3}$	11047	$12.6x10^{-4}$
SSAMGO	$5.9x10^{-4}$	$5.1x10^{-16}$	$6.7x10^{-3}$	6406	$12.4x10^{-4}$

4.4.1 State-Space Model of the Proposed Integrated MG

The system's dynamics are modelled by a set of first-order differential equations that consist of state variables; these are referred to as state equations or a state-space model (Veerasamy et al., 2020a). The state-space analysis governing the MG system integrated with RESs presented in Figure 3.11 is performed in the absence of two controller actions by the proposed secondary control loop and VIC loop. Also, the analysis is shown for the MG system models, considering the change in load disturbances. Appendix B presents the state-space equations of CLTF.

The state-space modeling is derived for the low inertia MG system integrated with RESs. The operation of the BDGs with the RESs during the study resulted in eight state variables, this will lead to the order of the closed-loop transfer function being powered to 6. The proposed model shown in Figure 3.11 can be simplified as shown in Figure 4.21 to illustrate the closed-loop control technique used in this study of the second objective:

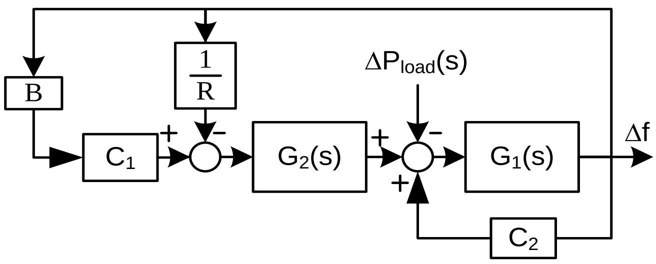

Figure 4.21 : The closed-loop control MG system

The total response of the integrated MG power system was modelled with two controller loops (C1 and C2). The frequency response of the MG can be represented as a function of the change in load demand as follows:

$$\left\{\left[\left(\Delta f \cdot B \cdot C_1\right) - \Delta f \cdot \frac{1}{R}\right] G_2(s) - \Delta P_{load}(s) + \Delta f \cdot C_2\right\} G_1(s) = \Delta f \tag{4.10}$$

$$\therefore \Delta f = \frac{-G_1(s)}{1 - G_1(s)\left[B \cdot C_1 \cdot G_2(s) + \frac{1}{R} \cdot G_2(s) - C_2\right]} \cdot \Delta P_{load} \tag{4.11}$$

Figure 3.22, depicts the bode-plot diagram of the frequency response for the MG power system considering the controller loop effects in stability analysis. The gain margin is 6.66 and the gain cross-over frequency is 8.27 (rad/s) for MG. For the proposed SSAMGO-optimized two-loop controller parameters of the MG power system, the Bode analysis response demonstrates that the closed-loop system is stable.

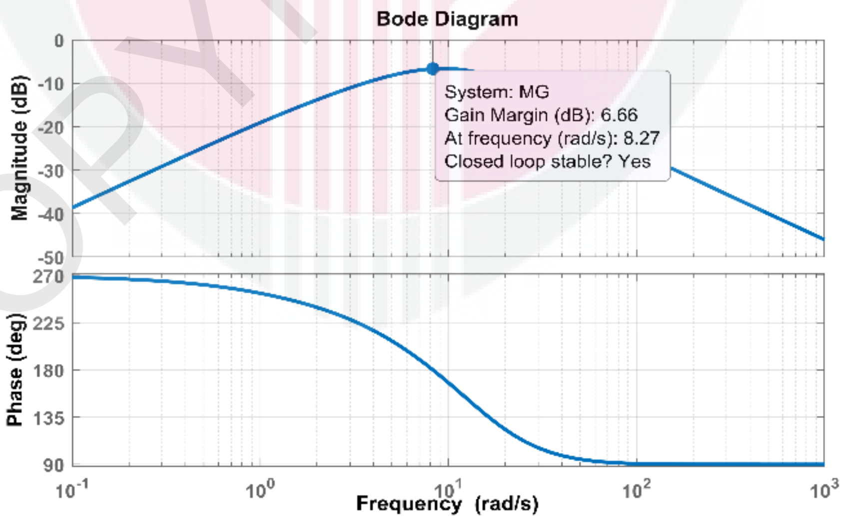

Figure 4.22 : Bode plot analysis of the frequency stability

4.5 Simulation Results of SSAMGO Tuned FDVIC for Frequency Regulation of Multi-Microgrid

The dynamic response of the low-inertia MMG system integrated with RESs for the FOPID, FDVIC, and DRC controllers presented in Figure 3.15 is described in this section. By using five benchmark functions, the proposed hybrid SSAMGO algorithm's performance is evaluated by comparing it with SSAGWO, PSOGSA, MPSOGA, and CPSO algorithms in terms of statistical findings. Furthermore, the proposed SSAMGO-tuned twenty parameters of the three loop controllers are analyzed for the MGs power system (i.e., five parameters for the FOPID controller of MG1, five parameters for the FOPID controller of MG2, three parameters for the FDVIC of MG1, three parameters for the FDVIC of MG2, two parameters for the DRC of MG1, and two parameters for the DRC of MG2). The MG model is developed and implemented using MATLAB/Simulink. The following sub-sections will be described in detail.

4.5.1 Validation of Benchmark Functions

The performance of the SSAMGO algorithm is evaluated against SSAGWO, PSOGSA, MPSOGA, and CPSO algorithms using five benchmark functions with diverse characteristics. This comparison provides a comprehensive assessment of the effectiveness of these algorithms (Barshandeh & Haghzadeh, 2021). The evaluation of hybrid SSAMGO algorithms involves benchmark functions detailed in Table C2 in Appendix C. Specifically, F1 and F2 are categorized as unimodal with a single global best solution ("U"). The table further distinguishes the separability of these functions, using "S" for separable and "N" for non-separable characteristics. Algorithm exploitation ability is assessed using unimodal benchmark functions, indicating the algorithm's proficiency in local search. F8, F10, and F12 denote multimodal functions. These functions, with multiple global best solutions, assess an algorithm's exploration capability. Table C2 categorizes functions labeled with "M" as multimodal, further classifying them as separable or non-separable (Narinder & Singh, 2017). Table 4.13 summarizes statistical results from algorithms on classical benchmarks, comparing mean and standard deviation (SD) for best and worst outcomes. Experiments, conducted independently with 20 runs per algorithm, used recorded results for evaluation. Benchmark functions were assessed with a fixed population size of 30 and 500 iterations. From Table 4.13, SSAMGO shows significant enhancements in the exploration and exploitation phases. Figure 4.23 displays the convergence curves for SSAMGO, SSAGWO, PSOGSA, MPSOGA, and CPSO underscoring its superior performance in tackling optimization challenges posed by benchmark functions.

Table 4.13 : Benchmark functions statistics

Function	Index	SSAMGO	SSAGWO	PSOGSA	MPSOGA	CPSO
F1	Best	**0**	1.1931×10^{-128}	42.7235	$3.5688 \times 10^{+04}$	$4.3911 \times 10^{+04}$
	Mean	**0**	9.1668×10^{-55}	308.3442	$6.6840 \times 10^{+04}$	$6.3669 \times 10^{+04}$
	Worst	**0**	1.8334×10^{-53}	842.9858	$8.0561 \times 10^{+04}$	$7.5209 \times 10^{+04}$
	STD	**0**	4.0995×10^{-54}	215.1169	$9.3496 \times 10^{+03}$	$6.8245 \times 10^{+03}$
F2	Best	$\mathbf{1.5932 \times 10^{-247}}$	7.5080×10^{-118}	2.9194×10^{-08}	$9.0956 \times 10^{+08}$	$2.8587 \times 10^{+05}$
	Mean	$\mathbf{1.0861 \times 10^{-204}}$	1.2279×10^{-30}	43.4564	$8.6502 \times 10^{+12}$	$3.7066 \times 10^{+09}$
	Worst	$\mathbf{1.7743 \times 10^{-203}}$	2.3915×10^{-29}	110.0510	$8.6146 \times 10^{+13}$	$1.9167 \times 10^{+10}$
	STD	**0**	5.3419×10^{-30}	45.6627	$2.3090 \times 10^{+13}$	$6.0154 \times 10^{+09}$
F8	Best	$\mathbf{-1.2569 \times 10^{+04}}$	$-9.5402 \times 10^{+03}$	$-7.1072 \times 10^{+03}$	$-5.4177 \times 10^{+03}$	$-4.5621 \times 10^{+03}$
	Mean	$\mathbf{-1.1847 \times 10^{+04}}$	$-8.4706 \times 10^{+03}$	$-6.2020 \times 10^{+03}$	$-5.4177 \times 10^{+03}$	$-3.9268 \times 10^{+03}$
	Worst	$\mathbf{-9.0163 \times 10^{+03}}$	$-7.4124 \times 10^{+03}$	$-5.4715 \times 10^{+03}$	$-5.4177 \times 10^{+03}$	$-3.5715 \times 10^{+03}$
	STD	$\mathbf{1.4531 \times 10^{+03}}$	556.6444	523.6907	9.3312×10^{-13}	231.9713
F10	Best	$\mathbf{8.8818 \times 10^{-16}}$	$\mathbf{8.8818 \times 10^{-16}}$	0.9313	19.9668	20.1562
	Mean	$\mathbf{8.8818 \times 10^{-16}}$	$\mathbf{8.8818 \times 10^{-16}}$	7.8574	19.9668	20.2579
	Worst	$\mathbf{8.8818 \times 10^{-16}}$	$\mathbf{8.8818 \times 10^{-16}}$	18.4607	19.9668	20.3541
	STD	**0**	**0**	5.7494	7.2900×10^{-15}	0.0565
F12	Best	$\mathbf{1.2062 \times 10^{-16}}$	1.0660×10^{-15}	7.7209	$2.3417 \times 10^{+08}$	$1.9415 \times 10^{+08}$
	Mean	$\mathbf{4.0462 \times 10^{-14}}$	7.2378×10^{-13}	12.2799	$5.9084 \times 10^{+08}$	$5.6059 \times 10^{+08}$
	Worst	$\mathbf{3.5152 \times 10^{-13}}$	5.2621×10^{-12}	19.5074	$7.7045 \times 10^{+08}$	$7.7634 \times 10^{+08}$
	STD	$\mathbf{8.4222 \times 10^{-14}}$	1.3653×10^{-12}	3.3100	$1.5266 \times 10^{+08}$	$1.3508 \times 10^{+08}$

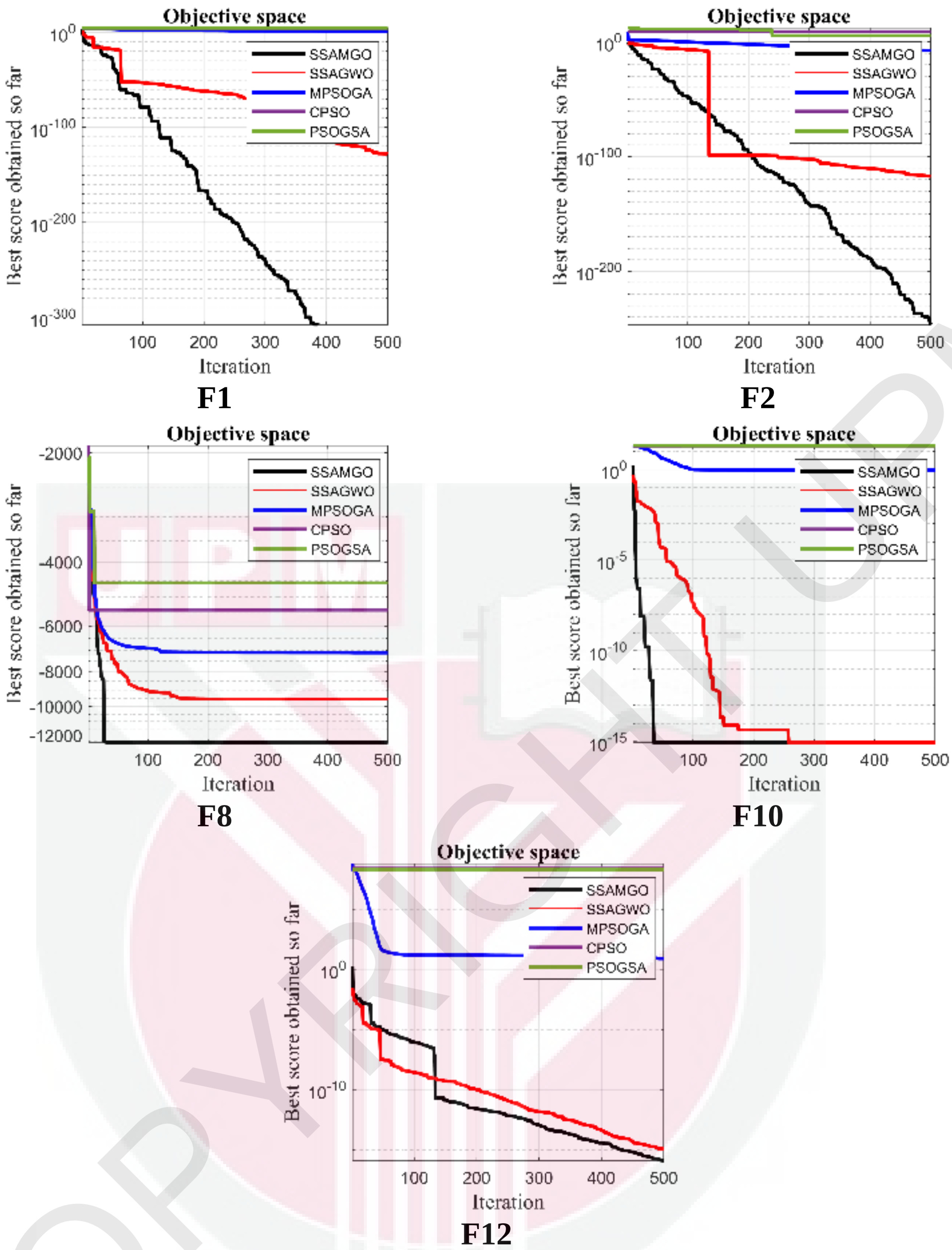

Figure 4.23 : Convergence characteristics for the proposed SSAMGO compared with other hybrid optimization algorithms

4.5.2 Time Domain Analysis of MMG Power System

In this subsection, the virtual inertia constant and virtual damping coefficient have been estimated by using the proposed SSAMGO and compared with other hybrid optimization techniques. Table 4.14 illustrates the optimal value of the H_{vir}, D_{vir}, and μ for the FDVIC of MG1 and MG2, respectively. The results show that the value of the virtual inertia and virtual damping when using SSAMGO is less than other optimization techniques by (65.62%, 44.82%, 48.05%, and 48.61%) for H_{vir1} and (70.53%, 17.46%, 45.60%, and 47.97%) for D_{vir1} and (69.43%, 42.00%, 43.53%, and 36.07%) for H_{vir2} and (70.99%, 45.66%, 37.94%, and 40.73%) for D_{vir2}. The estimated value of the virtual inertia constant has a very significant impact on the size of the capacity of the ESS that is used to support the MG power system with instant active power to reduce the value of the frequency nadir. In other words, the minimum value of the virtual inertia constant means reducing the size of the battery and leading to a reduction in the cost.

Table 4.14 : Virtual inertia and virtual damping for FDVIC of MG1 and MG2

Performance Index	FDVIC-1 (MG1)			FDVIC-2 (MG2)		
	H_{vir-1}	D_{vir-1}	μ_1	H_{vir-2}	D_{vir-2}	μ_2
SSAGWO-FDVIC	3.5230	4.8590	0.0125	3.6670	4.5670	0.0136
PSOGSA-FDVIC	2.1948	1.7349	0.1146	1.9329	2.4386	0.1298
MPSOGA-FDVIC	2.3310	2.6319	0.3571	1.9850	2.1350	0.5682
CPSO-FDVIC	2.3565	2.7523	0.7752	1.7536	2.2354	0.2704
SSAMGO-FDVIC	1.2110	1.4320	0.6326	1.1210	1.3250	0.5001

The proposed MG model is simulated under two scenarios. The first scenario shows the effect of the proposed new FDVIC technique on the dynamic performance of the MGs. In addition, proves the effectiveness of the proposed MG model under uncertainty in the load, variable virtual inertia, variable virtual damping, variable nominal load, uncertainties due to input real power of the PV and WTG. While the second scenario demonstrates the dynamic performance of the MG power system after combining the proposed DRC technique with the FDVIC on the system frequency deviations and the stress on the ESS.

The time domain response analysis of the MG is presented as follows. MG1 consists of a BDG integrated with a geothermal power station, solar thermal power station, and WTG. While MG2 consists of a BDG integrated with PV and WTG. Fractional derivative virtual inertia control is used to control the active power support from the ESS to compensate for the lack of microgrid inertia in MG1 and MG2, respectively. A step load change of 0.12 p.u. (240 kW) and 0.1 p.u. (150 kW) of the rated power occurs in MG1 and MG2, respectively. Table 4.15 presents the optimized values of the FOPID controller using the proposed SSAMGO, in comparison with other hybrid optimization algorithms, for the MMG power system in both the first and second scenarios.

Table 4.15 : FOPID controller parameters for MMG

Optimization Algorithm Technique	k_p	k_d	μ	k_i	λ	Execution Time (s)
SSAGWO-MG1	-50.2456	-52.5241	0.2832	-48.2465	0.5710	15536.9
SSAGWO-MG2	-35.1550	-0.0156	0.0100	-49.9990	0.9990	15536.9
PSOGSA-MG1	-4.2541	-11.0444	0.0568	-79.1746	0.7746	7353.7
PSOGSA-MG2	-5.7592	-7.7631	0.0105	-50.1111	0.7634	7353.7
MPSOGA-MG1	-93.4000	-16.2695	0.5598	-91.3346	0.5889	6857.6
MPSOGA-MG2	-1.5502	-53.2872	0.4307	-79.6204	0.9761	6857.6
CPSO-MG1	-10.0000	-2.4455	0.9886	-7.9373	0.9990	8239.9
CPSO-MG2	-10.0000	-7.1898	0.0768	-10.0000	0.9990	8239.9
SSAMGO-MG1	-4.9727	-19.8355	0.2621	-79.9185	0.9981	6640.9
SSAMGO-MG2	-9.9983	-19.9996	0.2077	-79.9151	0.9609	6640.9

A. The First Scenario

In this section, the impact of the proposed FDVIC technique on the dynamic performance of MGs is demonstrated.

i. Dynamic Performance Comparative

To provide further evidence of the superior performance of the SSAMGO algorithm in optimizing the FOPID and FDVIC parameters for MG1 and MG2, a comprehensive comparison was conducted with several widely used meta-heuristic hybrid algorithms found in the existing literature.

The algorithms considered for this comparison included SSAGWO, PSOGSA, MPSOGA, and CPSO. These algorithms were employed to optimize the parameters of the FOPID and FDVIC controllers in the multi-MG model integrated with high penetration RESs, as discussed in the first scenario. By comparing the results obtained from the SSAMGO algorithm with those obtained from the other algorithms, we aimed to validate the effectiveness and superiority of the SSAMGO approach in achieving optimal parameter settings for the given system. To maintain fairness in the comparison, all algorithms were implemented in MATLAB, utilizing a system configuration consisting of an Intel Core i7 7th generation processor and 8 GB of RAM. In order to create a consistent evaluation framework, the maximum number of iterations and the population size were uniformly set to 100 and 30, respectively, for all the algorithms being compared. By establishing these standardized parameters, we ensured that each algorithm was assessed under the same computational conditions when optimizing the FOPID and FDVIC controller parameters for the multi-MG model incorporating high penetration RESs. Figure 4.24, illustrates the frequency deviation of the proposed SSAMGO for tuning FOPID controller parameters for the secondary control loop of the MG1 and MG2, and for tuning FDVIC parameters of the MG1 and MG2 compared with (SSAGWO, PSOGSA, MPSOGA, and CPSO) hybrid optimization algorithms.

The results of the frequency deviation of MG1 and MG2 and the change of the tie line power are presented in Table 4.16. It is clear from Figure 4.24 and the results illustrated in Table 4.16, that ST, SSE, US, and Best Score (BS) for the proposed SSAMGO algorithm optimized FOPID and FDVIC are much faster than other optimization-tuned FOPID and FDVIC controllers. ET and ITAE are elapsed time, and integrated time absolute error performance index respectively.

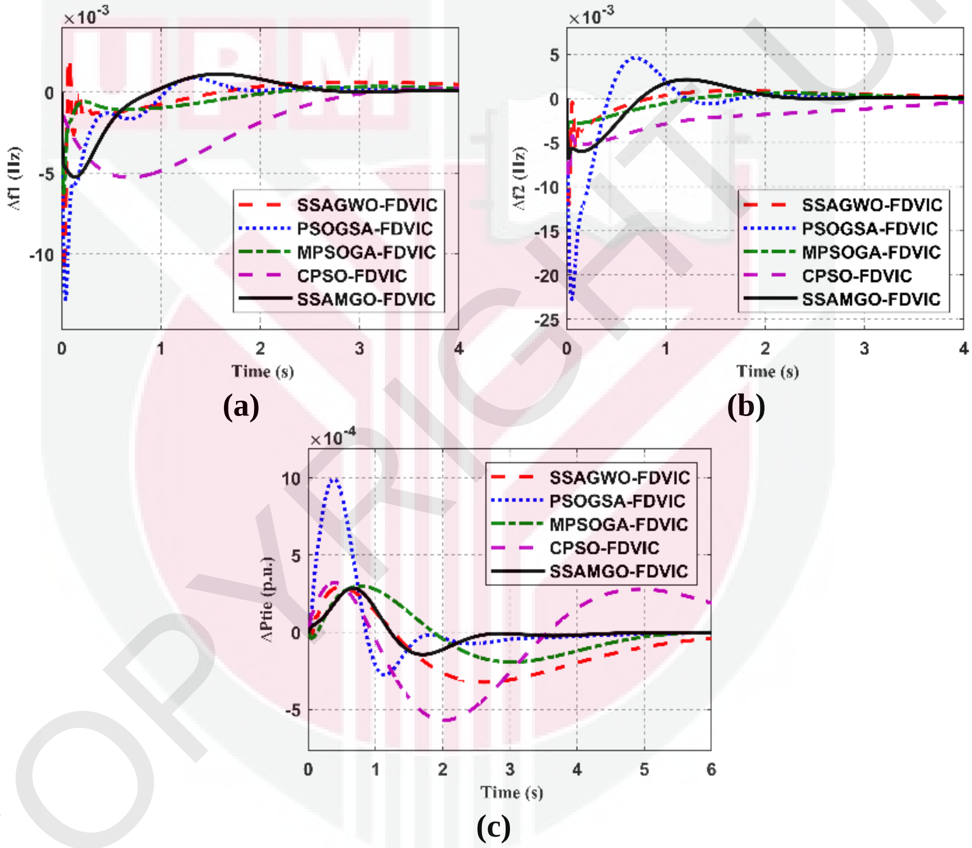

Figure 4.24 : The dynamic response of SSAMGO compared to other optimization techniques for tuning FOPID controller parameters and FDVIC parameters: (a) The frequency deviation of MG1; (b) The frequency deviation of MG2; (c) The power deviation of the tie line

Table 4.16 : Frequency deviation and the change in tie line power of MG1 and MG2 of the first scenario

Optimization Algorithm Technique	ST(s)	SSE	US	BS	ET(s)	ITAE	IAE	ISE	ITSE
					Δf_1				
SSAGWO-FDVIC	5.55	5.1×10^{-7}	107×10^{-4}	34.2×10^{-3}	15536.9	10.7×10^{-3}	3.8×10^{-3}	11.2×10^{-6}	3.8×10^{-6}
PSOGSA-FDVIC	7.77	77×10^{-7}	127×10^{-4}	23.0×10^{-3}	7353.7	23.6×10^{-3}	4.5×10^{-3}	1.5×10^{-5}	3.9×10^{-6}
MPSOGA-FDVIC	4.52	110×10^{-7}	62×10^{-4}	28.0×10^{-3}	6857.6	25.8×10^{-3}	3.9×10^{-3}	14.3×10^{-6}	4.2×10^{-6}
CPSO-FDVIC	10.72	1.5×10^{-7}	56×10^{-4}	47.2×10^{-3}	8239.9	21.5×10^{-3}	9.8×10^{-3}	3.4×10^{-5}	3.2×10^{-5}
SSAMGO-FDVIC	4.18	1.4×10^{-7}	52×10^{-4}	5.30×10^{-3}	6640.9	4.2×10^{-3}	3.7×10^{-3}	9.8×10^{-6}	3.5×10^{-6}
					Δf_2				
SSAGWO-FDVIC	3.78	5.3×10^{-7}	120×10^{-4}	34.2×10^{-3}	15536.9	8.3×10^{-3}	4.9×10^{-3}	7.9×10^{-6}	3.4×10^{-6}
PSOGSA-FDVIC	4.15	76×10^{-7}	227×10^{-4}	23.0×10^{-3}	7353.7	24.4×10^{-3}	7.8×10^{-3}	6.7×10^{-6}	7.3×10^{-6}
MPSOGA-FDVIC	5.59	120×10^{-7}	34×10^{-4}	28.0×10^{-3}	6857.6	26.4×10^{-3}	5.7×10^{-3}	4.3×10^{-6}	2.6×10^{-6}
CPSO-FDVIC	7.94	1.4×10^{-7}	90×10^{-4}	47.2×10^{-3}	8239.9	26.9×10^{-3}	10.5×10^{-3}	2.8×10^{-5}	2.5×10^{-5}
SSAMGO-FDVIC	2.17	1.3×10^{-7}	67×10^{-4}	5.30×10^{-3}	6640.9	4.6×10^{-3}	4.8×10^{-3}	1.6×10^{-6}	1.7×10^{-6}
					ΔP_{tie}				
SSAGWO-FDVIC	7.91	2.3×10^{-7}	3.2×10^{-4}	34.2×10^{-3}	15536.9	3.7×10^{-3}	1.2×10^{-3}	2.6×10^{-7}	6.6×10^{-7}
PSOGSA-FDVIC	4.95	9.6×10^{-7}	2.7×10^{-4}	23.0×10^{-3}	7353.7	3.2×10^{-3}	0.8×10^{-3}	4.3×10^{-7}	2.1×10^{-7}
MPSOGA-FDVIC	18.87	48×10^{-7}	1.9×10^{-4}	28.0×10^{-3}	6857.6	11.1×10^{-3}	1.1×10^{-3}	1.4×10^{-7}	3.3×10^{-7}
CPSO-FDVIC	11.08	0.9×10^{-7}	5.6×10^{-4}	47.2×10^{-3}	8239.9	7.9×10^{-3}	1.9×10^{-3}	5.9×10^{-7}	1.6×10^{-6}
SSAMGO-FDVIC	4.71	0.6×10^{-7}	1.4×10^{-4}	5.30×10^{-3}	6640.9	0.7×10^{-3}	0.3×10^{-3}	5.8×10^{-8}	5.3×10^{-8}

The ST of the SSAMGO tuned the FOPID and tuned the proposed FDVIC for the frequency response of MG1 is improved by (24.68%, 46.20%, 7.52%, and 61.01%) and for the frequency deviation of MG2 enhanced by (42.59%, 47.71%, 61.18%, and 72.67%) and for the change in the tie line power ameliorated by (40.45%, 4.85%, 75.04%, and 57.49%) from SSAGWO, PSOGSA, MPSOGA, and CPSO, respectively. Moreover, the SSE of the frequency deviation of the SSAMGO for MG1 is better than other hybrid optimization techniques by (72.56%, 98.18%, 98.73%, and 6.67%) and for frequency response of MG2 raises by (75.47%, 98.29%, 98.92%, and 7.14%) and for the tie line power deviation improved by (73.91%, 93.75%, 98.75%, and 33.33%), respectively. Furthermore, the proposed FDVIC technique in this work reduces the US of the frequency deviations which has a significant impact on the frequency nadir and system stability, it is enhanced by (105.76%, 144.23%, 19.23%, and 7.69%) than the other optimization techniques used to tune FDVIC parameters.

Moreover, there is a significant enhancement in the steady-state values of the performance indices for frequency deviations and the change in tie-line power. Specifically, for the frequency deviation of the MG1, improvements are observed: 60.74% for ITAE, 2.63% for IAE, 12.5% for ISE, and 7.89% for ITSE. For frequency deviation of MG2, enhancements are noted: 44.57% for ITAE, 2.04% for IAE, 62.79% for ISE, and 34.62% for ITSE. Similarly, for the change in tie-line power, considerable advancements are registered: 78.12% for ITAE, 62.5% for IAE, 58.47% for ISE, and 74.76% for ITSE. These results show that the studied MG has improved its load-frequency characteristic as intended.

ii. Comparative between the Proposed FDVIC and Conventional VIC

The frequency response of MG1 and MG2, as depicted in Figure 4.25, demonstrates an improvement in dynamic performance. Specifically, the proposed FDVIC techniques enhance MG1 frequency undershoot by 40.37%, MG2 frequency undershoot by 66.62%, and tie line power undershoot by 31.74% when compared to the conventional VIC technique under the same operating conditions. Furthermore, the proposed FDVIC techniques have also led to improvements in several performance metrics. The rise time (RT), SSE, overshoot (OS), and the steady-state value of ITAE of the frequency deviations, as well as the change in tie line power, have all shown enhancements.

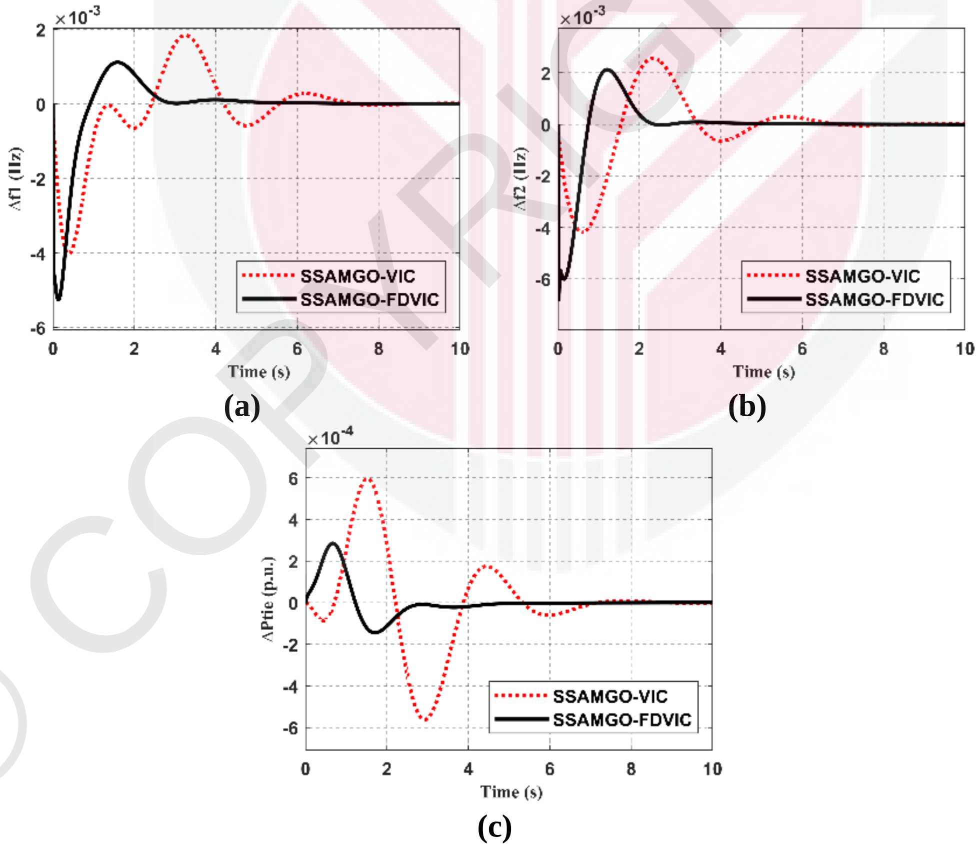

Figure 4.25 : The dynamic response of the SSAMGO-tuned FDVIC compared with SSAMGO-tuned conventional VIC: (a) The frequency deviation of MG1; (b) The frequency deviation of MG2; (c) The power deviation of the tie line

Moreover, the SSAMGO-tuned FDVIC technique requires less time to achieve optimal values compared to the SSAMGO-tuned conventional VIC technique. The elapsed time for obtaining the optimal values using the FDVIC approach is significantly shorter than that required by the conventional VIC technique. A comprehensive breakdown of these results can be found in Table 4.17.

Table 4.17 : Frequency deviation and the change in tie line power of MG1 and MG2 of proposed FDVIC compared with conventional VIC

Optimization Algorithm Technique	ST(s)	RT(s)	SSE	OS	BS	ET(s)	ITAE
				Δf_1			
SSAMGO-VIC	7.01	227.5×10^{-6}	7.92×10^{-7}	18×10^{-4}	50.9×10^{-3}	11478.6	13.83×10^{-3}
SSAMGO-FDVIC	4.18	19.6×10^{-6}	1.47×10^{-7}	11×10^{-4}	5.3×10^{-3}	6640.9	4.19×10^{-3}
				Δf_2			
SSAMGO-VIC	6.50	57.0×10^{-6}	3.99×10^{-7}	25×10^{-4}	50.9×10^{-3}	11478.6	15.77×10^{-3}
SSAMGO-FDVIC	2.17	13.3×10^{-6}	1.38×10^{-7}	21×10^{-4}	5.3×10^{-3}	6640.9	4.57×10^{-3}
				ΔP_{tie}			
SSAMGO-VIC	6.90	2500×10^{-6}	1.68×10^{-7}	5.9×10^{-4}	50.9×10^{-3}	11478.6	3.967×10^{-3}
SSAMGO-FDVIC	4.71	680.2×10^{-6}	0.59×10^{-7}	2.8×10^{-4}	5.3×10^{-3}	6640.9	0.75×10^{-3}

iii. Dynamic Performance of FDVIC

The proposed FDVIC technique implemented in an MG power system effectively emulates the behaviour of conventional synchronous generators, which possess inherent inertia. Figure 4.26, depicts the comparison between using FDVIC to compensate MG with inertia and without using any technique for inertia controller. It is clear from the results, that the FDVIC technique approach improves the transient response of the MG. Moreover, it reduces the frequency fluctuations and enhances the system's ability to handle the rapid change in power demand. The results demonstrated in Table 4.18 show that FDVIC has faster response times, and reduces settling time by 8.33%, undershoot by 51.24%, and overshoot by 66.67% for the frequency of MG1. While reducing the ST, US, and OS by 63.52%, 71.53%, and 66.67% for the frequency of MG2, respectively.

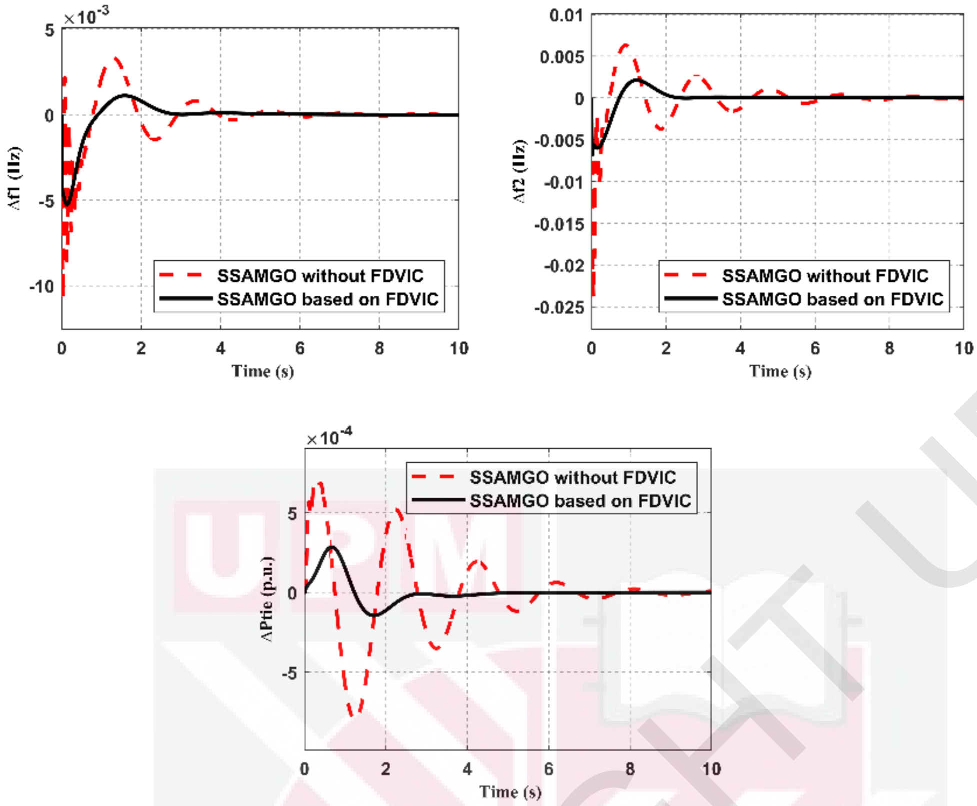

Figure 4.26 : The dynamic response of the SSAMGO tuned FDVIC compared with SSAMGO without virtual inertia controller

Table 4.18 : Frequency deviation and the change in tie line power of MG1 and MG2 of proposed FDVIC compared without VIC

Optimization Algorithm Technique	**ST(s)**	**RT(s)**	**SSE**	**OS**	**BS**	**ET(s)**	**ITAE**
				Δf_1			
SSAMGO-without VIC	4.56	-107.78×10^{-4}	33×10^{-4}	3.48×10^{-7}	9.3×10^{-3}	6837.5	12.13×10^{-3}
SSAMGO-FDVIC	4.18	19.6×10^{-6}	1.47×10^{-7}	11×10^{-4}	5.3×10^{-3}	6640.9	4.19×10^{-3}
				Δf_2			
SSAMGO-without VIC	5.95	-239.01×10^{-4}	63×10^{-4}	3.69×10^{-7}	9.3×10^{-3}	6837.5	27.82×10^{-3}
SSAMGO-FDVIC	2.17	13.3×10^{-6}	1.38×10^{-7}	21×10^{-4}	5.3×10^{-3}	6640.9	4.57×10^{-3}
				ΔP_{tie}			
SSAMGO-without VIC	9.18	-7.99×10^{-4}	7.1×10^{-4}	1.44×10^{-7}	9.3×10^{-3}	6837.5	4.37×10^{-3}
SSAMGO-FDVIC	4.71	680.2×10^{-6}	0.59×10^{-7}	2.8×10^{-4}	5.3×10^{-3}	6640.9	0.75×10^{-3}

Significant enhancements in frequency stability, transient responsiveness, and overall system stability result from incorporating the proposed virtual inertia control into an

MG. It allows MG systems to function reliably and efficiently by reducing the challenges caused by renewable energy's lack of inherent inertia.

iv. Performance Evaluation of Estimated Virtual Inertia and Virtual Damping

In the simulations mentioned above, the virtual inertia constant and the virtual damping coefficient are determined optimally using the SSAMGO algorithm for the FDVIC controller. In order to assess the robustness of the proposed FDVIC approach based on the SSAMGO algorithm, the values of the optimal H_{vir} and D_{vir} were varied within the range of 50% to 150%. The effectiveness of the controller is showcased by utilizing the FOPID controller parameters of MG1 and MG2 under normal operating conditions. The dynamic response of the MG with varying values of the virtual inertia constant is depicted in Figure 4.27.

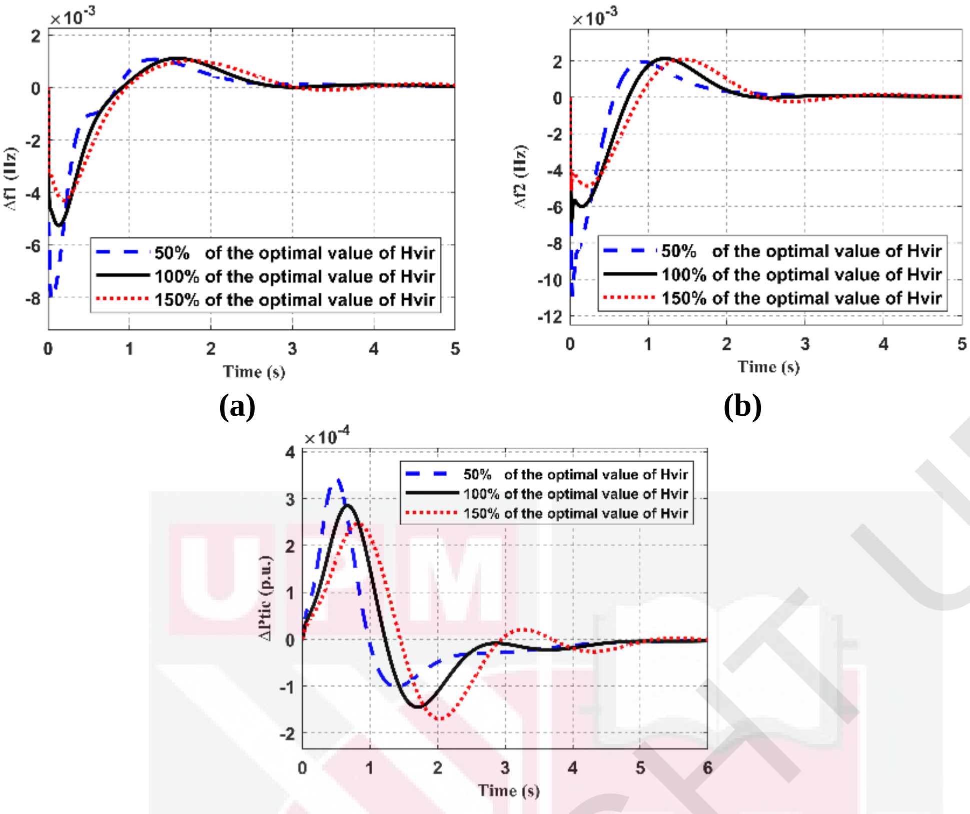

Figure 4.27 : The dynamic response of the MG1 and MG2 under different virtual inertia constants (50% 150% from its optimal value) using SSAMGO algorithm: (a) The frequency deviation of MG1; (b) The frequency deviation of MG2; (c) The power deviation of the tie line

Similarly, Figure 4.28 displays the dynamic response of the MG when the virtual damping coefficient is changed.

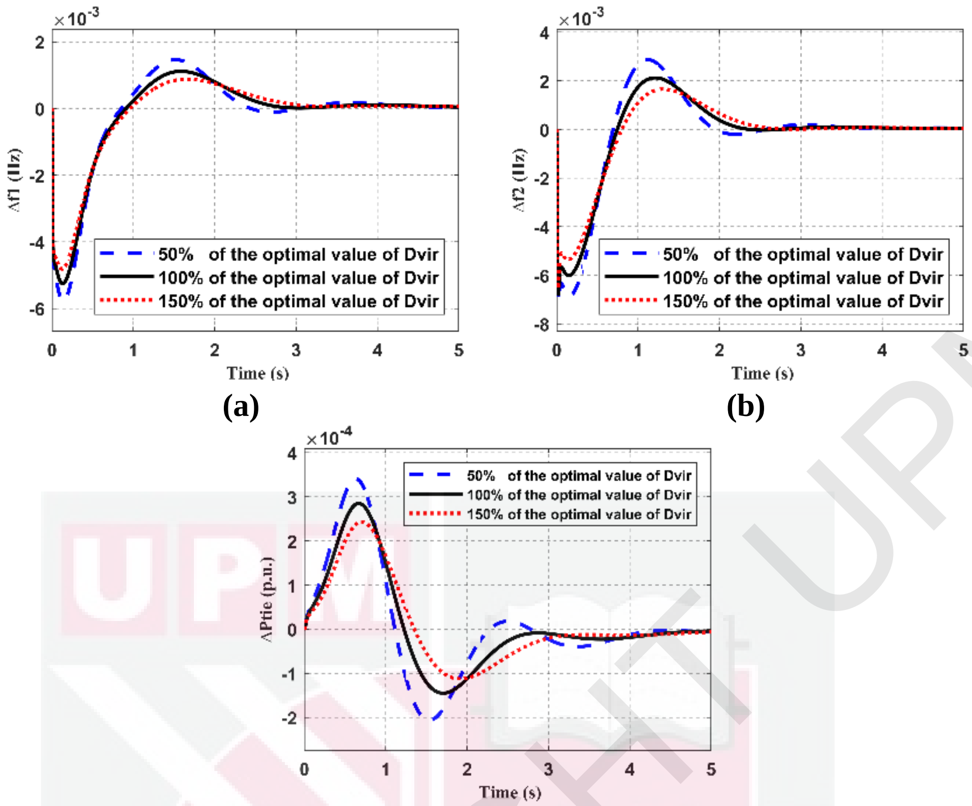

(c)

Figure 4.28 : The dynamic response of the MG1 and MG2 under different virtual damping coefficients (50% 150% from its optimal value) using SSAMGO algorithm: (a) The frequency deviation of MG1; (b) The frequency deviation of MG2; (c) The power deviation of the tie line

Based on the observations from these figures, we can draw the conclusion that the proposed FDVIC controller, utilizing optimal values, exhibits robustness against uncertainties in the parameters. It effectively maintains the MG frequency and tie-line power at their reference values within short time intervals.

v. Performance Evaluation Under Random Load Demand Variation

Figure 4.29 demonstrates the application of a random step change in load demand to MG1, serving as a means to evaluate the effectiveness of the proposed SSAMGO compared with other hybrid optimization algorithms. To assess the system's response, Figure 4.30 displays the frequency response of MG1, MG2, and tie-line power. This analysis aims to evaluate the performance of the proposed algorithm in maintaining system stability and regulating power distribution in response to load variations. Based on the findings, it is evident that the proposed algorithm exhibits faster tuning of the FOPID and FDVIC responses compared to other optimization techniques when subjected to sudden load changes. Furthermore, the tie-line power supplied by the system demonstrates the ability to adjust in response to varying load demands while maintaining a consistent output level. These results highlight the effectiveness of the proposed algorithm in dynamically adapting to changes in the system, ensuring stability and optimal performance.

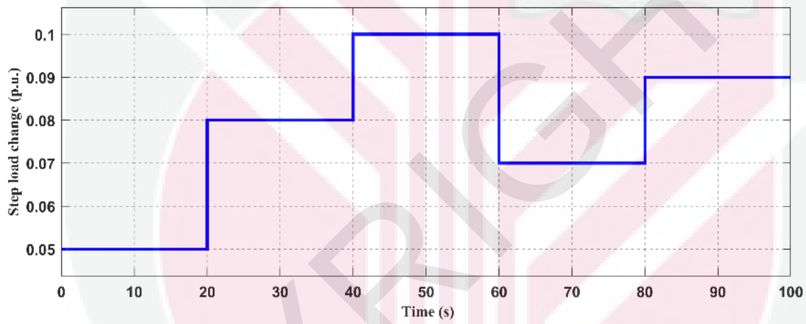

Figure 4.29 : Random step change load demand

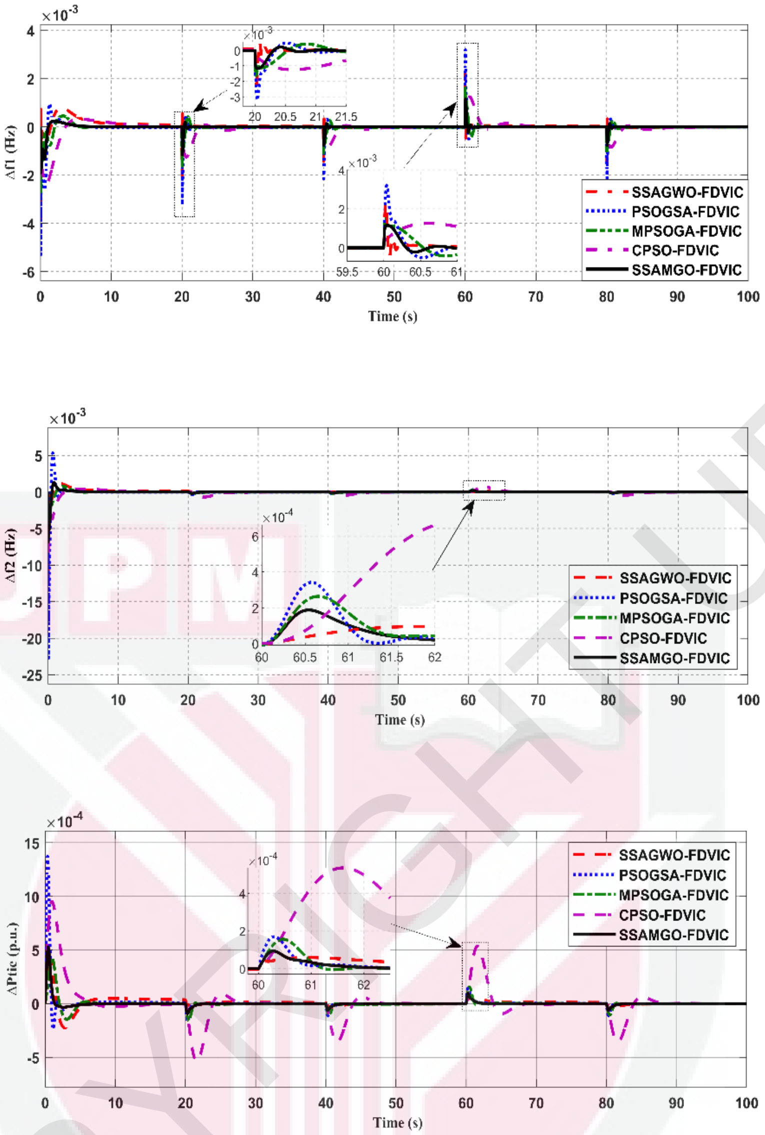

Figure 4.30 : Dynamic response of MG1 and MG2 at a random change load

vi. Real-time Variation of RESs Performance Evaluation

In this scenario, the case focuses on analyzing the variation in power output of PV units using real-time monthly average irradiance data collected from the Subang meteorological center was specifically recorded at Universiti Putra Malaysia (Irudayaraj et al., 2022a). The data spans from January to December 2014 and comprises 200 time slots of 0.5 seconds each, as depicted in Figure 4.31.

To assess the performance of the developed MMG model, real-time variations in solar power are tested. The dynamic response of the system is recorded and presented in Figure 4.32, where the proposed SSAMGO algorithm is compared with other hybrid optimization algorithms.

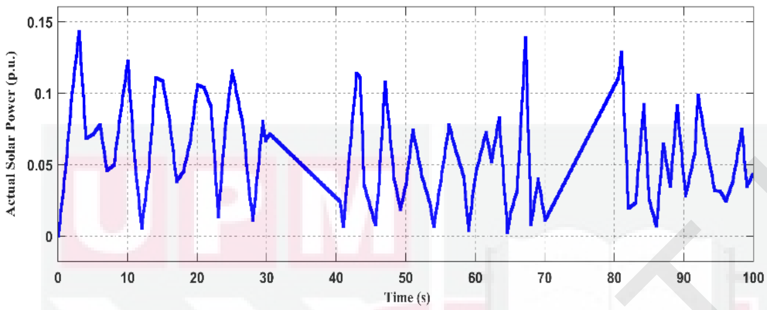

Figure 4.31 : Real-time Solar Input Power

Figure 4.32 : Dynamic response of the MMG power system under real-time solar input power

The results indicate that the SSAMGO-tuned parameters for the FOPID and FDVIC controllers exhibit superior and more consistent responses, characterized by minimal overshoot and undershoot. This finding suggests that the SSAMGO algorithm outperforms other tuning methods in achieving smoother and more efficient control of the MG system.

The Malaysian Meteorological Department in Kuala Terengganu collects real-time data on wind power variation by monitoring changes in wind speed throughout the year. The location of the department is specified by the coordinates 5°23' N latitude and 103°06' E longitude, with an elevation of 5.2 meters (Ali Kadhem et al., 2019). To evaluate the reliability of the controller, the wind power variation data is converted into seconds. Figure 4.33 illustrates this process. Additionally, Figure 4.34 displays the frequency response and tie-line power deviation resulting from the aforementioned wind power variation. The analysis reveals that the SSAMGO algorithm exhibits minimal frequency oscillations and achieves lower SSE compared to other hybrid optimization algorithms. Based on this observation, it can be inferred that the proposed SSAMGO algorithm, which tunes the FOPID and FDVIC parameters, produces a superior and smoother response compared to other tuning methods. Furthermore, it demonstrates minimal undershooting, reduced SSE, and real-time responsiveness under variations in RESs input power.

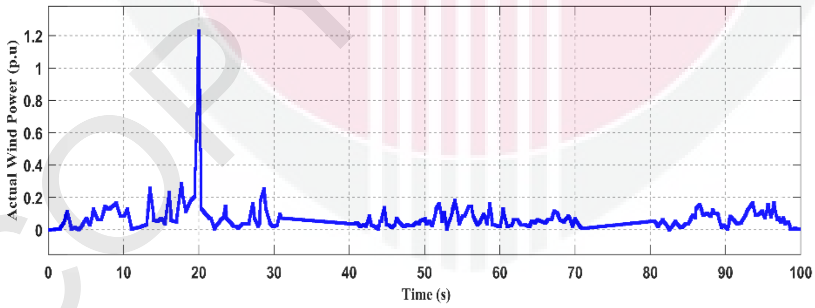

Figure 4.33 : Real-time Wind-turbine Input Power

Figure 4.34 : Dynamic response of the MMG power system under real-time wind input power

B. The Second Scenario

In this section, the impact of the combination of the proposed FDVIC and DRC technique based on the proposed hybrid SSAMGO on the dynamic performance of MGs is demonstrated and explained.

In order to evaluate the performance of the proposed MMG power system model, the simulation incorporates the combination of the FDVIC techniques from the first scenario with the DRC controller. The responses of this combined system are then simulated and analyzed. In the analysis of the proposed model, it is subjected to sudden changes in load demand. Specifically, a load demand changes of 0.12 p.u. is applied to MG1, while MG2 experiences a load demand change of 0.1 p.u. The maximum demand response load available in the analyzed MGs is 0.036 p.u., which corresponds to 30% of the total nominal load of MG1 (240 kW). Similarly, MG2 has a maximum demand response load of 0.025 p.u., which accounts for 25% of its total nominal load (187.5 kW). The value of T_{off0} is configured as 10 seconds. Additionally, Δf_{db} is set to -0.05 Hz and Δf_{prm} is set to -0.55 Hz. In the DR control loop for frequency regulation, 10%, 30%, and 50% of the responsive loads are utilized. The proposed SSAMGO algorithm has been utilized to achieve the optimal value of the DRC parameters. The frequency response of MG1 and MG2, along with the corresponding change in tie line power, is depicted in Figure 4.35. The findings strongly suggest that the combination of FDVIC and DRC techniques in the examined system offers notable advantages in terms of frequency regulation. The improvements in frequency responses, tie-line power changes, and reduction in frequency oscillations, as illustrated in Figure 4.35 and Table 4.19, highlight the effectiveness of incorporating DRC units into the system. These results further demonstrate the system's ability to successfully mitigate frequency fluctuations, particularly in scenarios with increased renewable energy penetration, through the integration of demand response support in isolated MGs.

The efficacy of the proposed virtual inertia controller technique is illustrated in Figure 4.36, showcasing the effective energy participation from the batteries during the inertia compensation process in the presence of sudden load changes. These results highlight the rapid and efficient charging and discharging of the batteries, validating the effectiveness of the employed method in minimizing frequency deviation and enhancing power system inertia. It is important to note that combining the DRC approach with the FDVIC results in a substantial reduction in active power charging and discharging of the ESS. This reduction significantly improves the lifespan of the ESS, indicating the beneficial impact of the integrated approach.

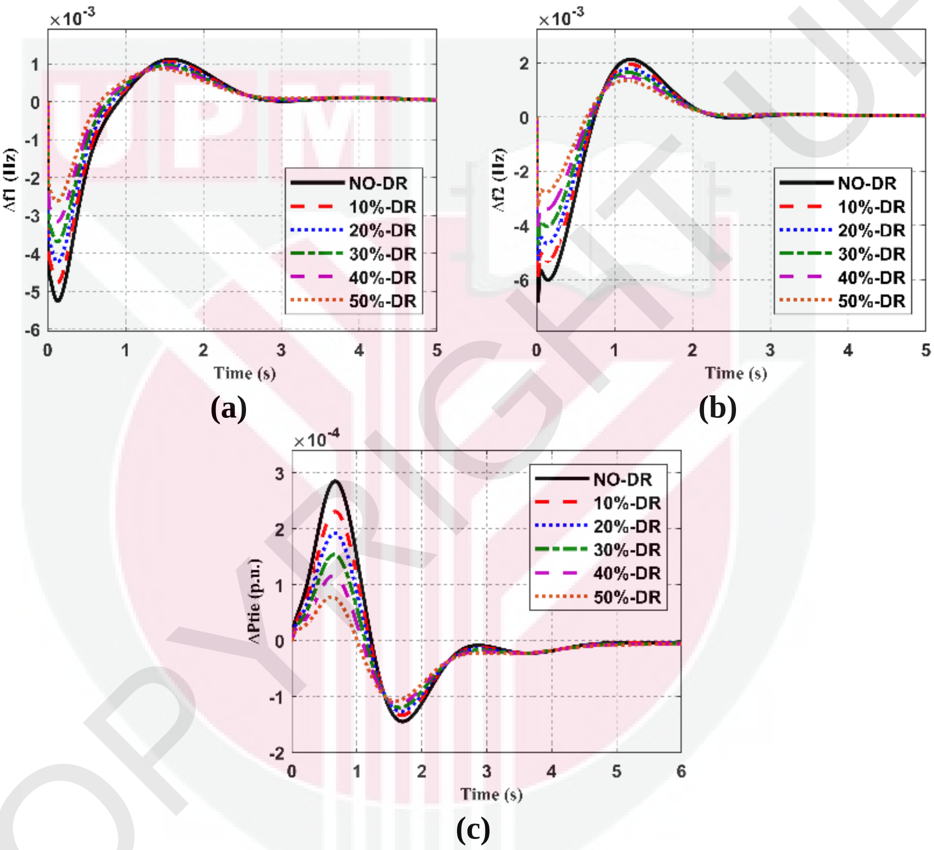

Figure 4.35 : Dynamic response of the MG with a variation of DRC: (a) Frequency deviation of the MG1; (b) Frequency deviation of the MG2; (c) The changing power of the tie line

Table 4.19 : Dynamic response of MG1 and MG2 of FDVIC combined with DRC

Optimization Algorithm Technique	ST(s)	RT(s)	US	OS	SSE	ITAE
				Δf_1		
NO-DRC	4.19	$2.5x10^{-7}$	$-5.25x10^{-3}$	$1.16x10^{-3}$	$1.83x10^{-7}$	$4.19x10^{-3}$
10% turn-off of the DR appliance	4.30	$1.6x10^{-7}$	$-4.77x10^{-3}$	$1.06x10^{-3}$	$1.07x10^{-7}$	$3.83x10^{-3}$
20% turn-off of the DR appliance	4.43	$6.4x10^{-8}$	$-4.23x10^{-3}$	$1.01x10^{-3}$	$3.77x10^{-8}$	$3.54x10^{-3}$
30% turn-off of the DR appliance	4.55	$1.1x10^{-5}$	$-3.69x10^{-3}$	$0.95x10^{-3}$	$3.17x10^{-8}$	$3.65x10^{-3}$
40% turn-off of the DR appliance	4.71	$3.3x10^{-5}$	$-3.15x10^{-3}$	$0.91x10^{-3}$	$1.01x10^{-7}$	$3.83x10^{-3}$
50% turn-off of the DR appliance	4.92	$5.4x10^{-5}$	$-2.62x10^{-3}$	$0.86x10^{-3}$	$1.71x10^{-7}$	$4.02x10^{-3}$
				Δf_2		
NO-DRC	2.17	$1.4x10^{-7}$	$-6.79\ x10^{-3}$	$2.13\ x10^{-3}$	$1.38x10^{-7}$	$4.56x10^{-3}$
10% turn-off of the DR appliance	2.21	$7.7x10^{-8}$	$-6.04x10^{-3}$	$1.94x10^{-3}$	$7.06x10^{-8}$	$4.08x10^{-3}$
20% turn-off of the DR appliance	2.23	$1.1x10^{-8}$	$-5.35x10^{-3}$	$1.79x10^{-3}$	$8.56x10^{-9}$	$3.69x10^{-3}$
30% turn-off of the DR appliance	3.54	$6.0x10^{-6}$	$-4.67x10^{-3}$	$1.64x10^{-3}$	$5.35x10^{-8}$	$3.69x10^{-3}$
40% turn-off of the DR appliance	3.79	$1.5x10^{-5}$	$-3.99x10^{-3}$	$1.49x10^{-3}$	$1.15x10^{-7}$	$3.75x10^{-3}$
50% turn-off of the DR appliance	4.06	$2.5x10^{-5}$	$-3.30x10^{-3}$	$1.35x10^{-3}$	$1.77x10^{-7}$	$3.81x10^{-3}$
				ΔP_{tie}		
NO-DRC	4.71	$5.5x10^{-4}$	$-1.45x10^{-4}$	$2.85x10^{-4}$	$5.95x10^{-8}$	$0.75x10^{-3}$
10% turn-off of the DR appliance	5.78	$3.2x10^{-4}$	$-1.34x10^{-4}$	$2.31x10^{-4}$	$2.94x10^{-8}$	$0.61x10^{-3}$
20% turn-off of the DR appliance	6.19	$2.6x10^{-5}$	$-1.27x10^{-4}$	$1.92x10^{-4}$	$2.14x10^{-9}$	$0.50x10^{-3}$
30% turn-off of the DR appliance	6.59	$4.67x10^{-5}$	$-1.19x10^{-4}$	$1.54x10^{-4}$	$2.51x10^{-8}$	$0.59x10^{-3}$
40% turn-off of the DR appliance	7.36	$1.12x10^{-4}$	$-1.13x10^{-4}$	$1.15x10^{-4}$	$5.24x10^{-8}$	$0.69x10^{-3}$
50% turn-off of the DR appliance	8.03	$2.04x10^{-4}$	$-1.08x10^{-4}$	$0.78x10^{-4}$	$7.97x10^{-8}$	$0.81x10^{-3}$

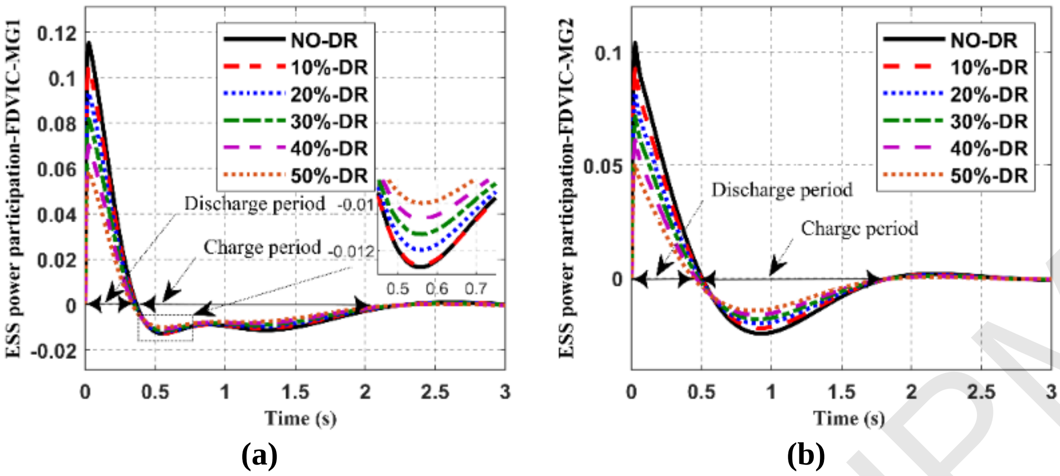

Figure 4.36 : Power participation in the ESS of the FDVIC controller loop: (a) ESS of the MG1; (b) ESS of the MG2

4.5.3 State-Space Model of MMG Power System (Stability Analysis)

The system's dynamics are modeled by a set of first-order differential equations that consist of state variables; these are referred to as state equations or a state-space model (Alhelou et al., 2023; Veerasamy et al., 2020). The state-space analysis governing the MMG system integrated with RESs presented in Figure 3.15 is performed in the absence of the three controllers' actions proposed secondary control loop, virtual inertia control loop, and demand-side response loop. Also, the analysis is shown for the two MG system models, considering the change in load disturbances in MG1 and MG2. The state-space modeling is derived for the low inertia MMG system integrated with RESs. The state space model equations are illustrated in detail in Appendix B.

The operation of the BDGs with the RESs during the study of the first scenario and second scenario control technique resulted in 20 state variables, this will lead to the order of the closed loop transfer function being powered to 35. The proposed model shown in Figure 3.15 can be simplified as shown in Figure 4.37 to illustrate the closed-loop control technique used in this study.

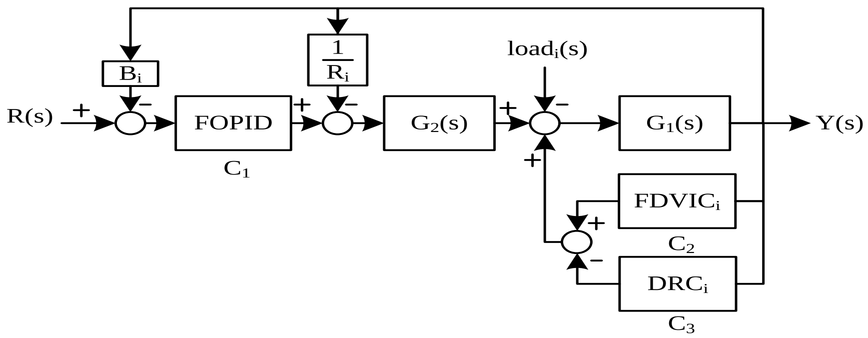

Figure 4.37 : Closed loop control of the proposed MMG

The total response of the interconnected MGs system was modeled with three controller's loops (C1, C2, and C3) as the following:

$$\begin{gathered} R(s)C_1 G_1(s)G_2(s) - B_i Y(s)C_1 G_1(s)G_2(s) - \frac{1}{R_i} Y(s)G_1(s) \\ G_2(s) - D_i(s)G_1(s) + Y(s)C_2 G_1(s) - Y(s)C_3 G_1(s) = Y(s) \end{gathered} \tag{4.12}$$

$$\therefore Y(s) = Y_{11}(s) + Y_{12}(s) \tag{4.13}$$

where

$$Y_{11}(s) = \frac{R(s)C_1 G_1(s)G_2(s)}{B_i C_1 G_1(s)G_2(s) + \frac{1}{R_i} G_1(s)G_2(s) - C_2 G_1(s) + C_3 G_1(s)} \tag{4.14}$$

and

$$Y_{12}(s) = \frac{-D_i(s)G_1(s)}{B_i C_1 G_1(s)G_2(s) + \frac{1}{R_i} G_1(s)G_2(s) - C_2 G_1(s) + C_3 G_1(s)} \tag{4.15}$$

The closed-loop transfer function of the proposed model shown in Figure 4.37 is used to address the change in the load demand and the variation in tie-line power in Equation (4.16) and (4.17) respectively.

$$\Delta f\big|_{\Delta P_{load}} = \frac{-G_1}{1+G_1\left[B_iC_1G_2 + \frac{1}{R_i}G_2 - C_2 + C_3\right]}\Delta P_{load} \tag{4.16}$$

$$\Delta f\big|_{\Delta P_{tie}} = \frac{C_1G_1G_2}{1+G_1\left[B_iC_1G_2 + \frac{1}{R_i}G_2 - C_2 + C_3\right]}\Delta P_{tie} \tag{4.17}$$

By applying the superposition theorem, the closed-loop transfer function for the total variations of the frequency response of the proposed MMG can be represented as follows:

$$\Delta f = \frac{-G_1\Delta P_{load} + C_1G_1G_2\Delta P_{tie}}{1+G_1\left[B_iC_1G_2 + \frac{1}{R_i}G_2 - C_2 + C_3\right]} \tag{4.18}$$

Figure 4.38, depicts the bode-plot diagram of the frequency response for the MMG power system considering the three controller loop effects in stability analysis. For the first scenario, the gain margin of 23.3 and 26.4 dB and a gain cross-over frequency of 7.5 and 2.25 (rad/s) for MG1 and MG2, respectively. For the second scenario, 27.7 and 40.1 dB of the gain margin and 7.26 and 6.27 (rad/s) of cross-over frequency for MG1 and MG2 respectively. For the proposed SSAMGO-optimized three-loop controller parameters of the MMG power system, the Bode analysis response demonstrates that the closed-loop system is stable.

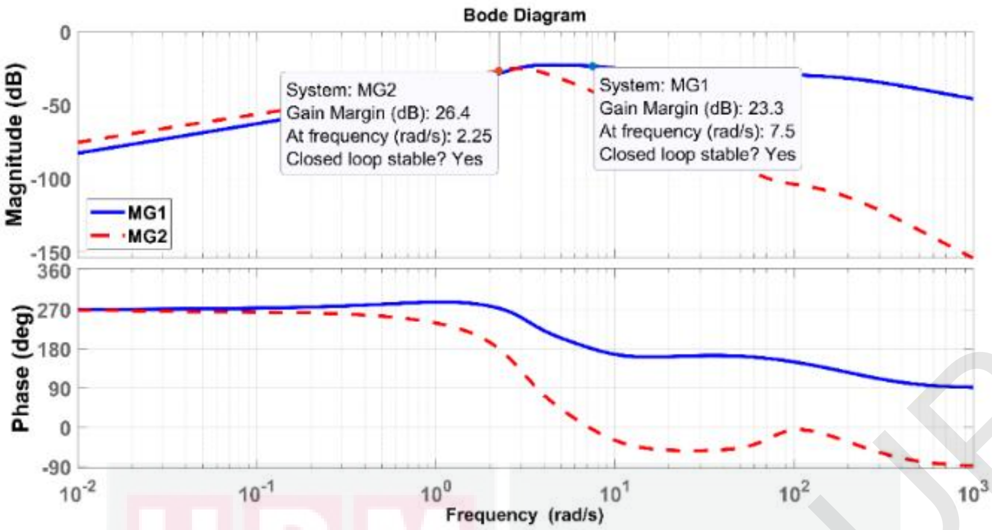

(a)

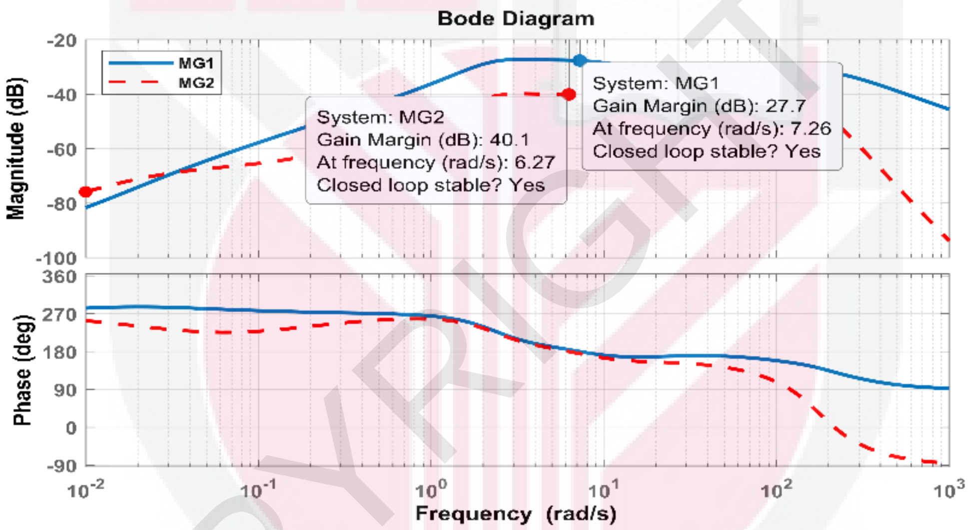

(b)

Figure 4.38 : Bode analysis of frequency stability: (a) the first scenario, (b) the second scenario

4.6 Simulation Results of the MMG Grid Connected Mode

In this section, the results derived from the LSPS simulation conducted in MATLAB/Simulink, as well as the validation of the proposed control approach using the IEEE-39 New England test system and the Opal-RT, will be demonstrated. Simulation is conducted on the power system model depicted in Figure 3.21. This simulation specifically targets a three-area power system, which incorporates the integration of an LSPS with two low-inertia MGs integrated with RESs. Figure 3.22 depicts the block diagram configuration of the analyzed power system. The SSAMGO hybrid optimization algorithm was applied to determine the optimal values for the parameters of the FOPID controller in the secondary control of the three-area power system. Simultaneously, it was utilized to optimize the parameters of the FDVIC for the virtual controller in the MG system. This optimization aims to provide the necessary inertia support to minimize frequency deviation across various scenarios.

The optimized parameters for the FOPID controller and the FDVIC technique in the context of a MMG power system connected with an LSPS are provided in Table 4.20:

Table 4.20 : Controller parameters for the proposed model

Controller Technique Based on SSAMGO Algorithm		FOPID					FDVIC		
		k_p	k_d	μ	k_i	λ	H_{vir}	D_{vir}	μ_{vir}
SSAMGO-FDVIC	Grid	-21.85	-26.71	0.99	-86.23	0.591	---	---	---
	MG1	-10.33	-97.82	0.52	-20.92	0.973	0.9806	1.1454	0.1390
	MG2	-20.66	-29.26	0.83	-14.18	0.958	1.9884	1.8824	0.9964
SSAMGO-VIC	Grid	-20.54	-30.03	0.99	-99.17	0.556	---	---	---
	MG1	-75.91	-74.37	0.25	-23.82	0.386	3.3253	4.200	---
	MG2	-78.82	-60.08	0.59	-25.38	0.993	3.5871	4.9851	---
SSAMGO-Without VIC	Grid	-42.83	-22.27	0.17	-13.06	0.890	---	---	---
	MG1	-8.12	-3.17	0.58	-32.58	0.849	---	---	---
	MG2	-7.62	-13.61	0.69	-98.43	0.740	---	---	---

The results display frequency deviations and tie-line power changes for the Grid, MG1, and MG2, achieved through the SSAMGO algorithm fine-tuning FOPID controllers in the Multi-area power system's secondary control loop. SSAMGO also optimized FDVIC parameters for MG1 and MG2 to compensate for system inertia. Figure 4.39 and Figure 4.40 show frequency deviation and tie-line power changes in response to sudden changes in the demand load, comparing FDVIC with conventional VIC and no inertia controller implementation.

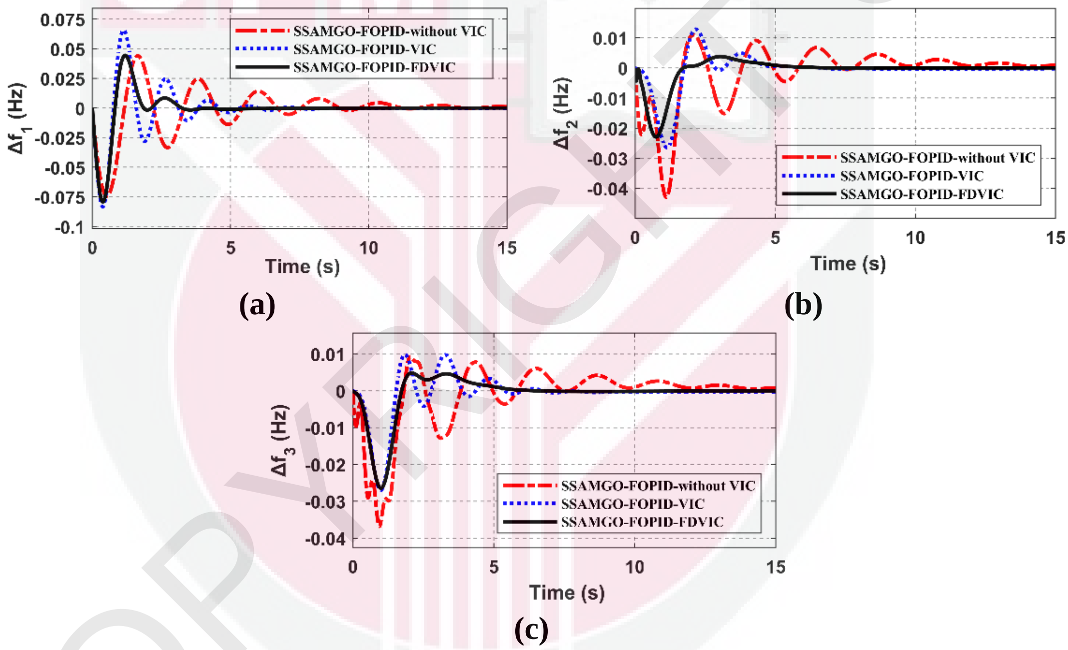

Figure 4.39 : Comparing the frequency deviations, (a): The frequency fluctuation of the Grid, (b): The frequency fluctuation of the MG1, and (c): The frequency fluctuation of the MG2

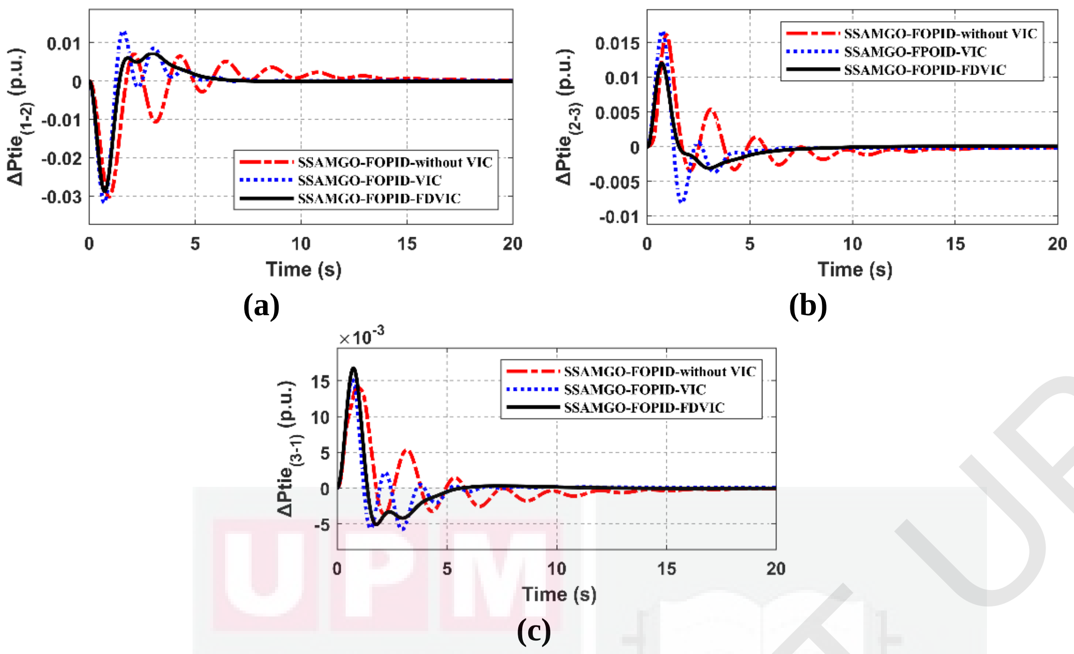

Figure 4.40 : Comparing the change in tie line power, (a): The frequency fluctuation of the Grid, (b): The frequency fluctuation of the MG1, and (c): The frequency fluctuation of the MG2

Table 4.21 and Table 4.22 present a comprehensive breakdown of the results, specifically detailing the frequency fluctuations and changes in tie-line power for the proposed model. The comparison results reveal that the ST, RT, US, OS, SSE, and ITAE for the FOPID and FDVIC optimized by the SSAMGO algorithm demonstrate significantly faster performance compared to conventional VIC techniques and scenarios where no virtual inertia controller is employed.

Table 4.21 : Frequency deviation of the LSPS, MG1, and MG2 of the FDVIC compared with VIC and without any inertia controller

Controller Technique Based on SSAMGO Algorithm		Δf					
		ST (s)	RT (s)	US	OS	SSE	ITAE
SSAMGO-FDVIC	Δf_1	3.6181	2.23×10^{-5}	-7.92×10^{-2}	4.43×10^{-2}	8.340×10^{-6}	0.10040
	Δf_2	5.4563	3.56×10^{-5}	-2.29×10^{-2}	0.38×10^{-2}	8.330×10^{-6}	0.05908
	Δf_3	5.4628	4.59×10^{-5}	-2.64×10^{-2}	0.48×10^{-2}	8.440×10^{-6}	0.08244
SSAMGO-VIC	Δf_1	5.7734	5.69×10^{-4}	-8.32×10^{-2}	6.57×10^{-2}	213.3×10^{-6}	0.46510
	Δf_2	5.6262	3330×10^{-5}	-2.64×10^{-2}	1.28×10^{-2}	212.0×10^{-6}	0.36440
	Δf_3	6.5948	5380×10^{-5}	-2.70×10^{-2}	0.98×10^{-2}	213.5×10^{-6}	0.37090
SSAMGO-Without VIC	Δf_1	12.9394	2.14×10^{-5}	-8.32×10^{-2}	6.56×10^{-2}	4.250×10^{-6}	0.52660
	Δf_2	15.1518	6.30×10^{-5}	-4.30×10^{-2}	1.09×10^{-2}	5.192×10^{-6}	0.33700
	Δf_3	15.4337	6.51×10^{-5}	-3.68×10^{-2}	0.92×10^{-2}	4.984×10^{-6}	0.31770

Table 4.22 : The change in tie line power of the LSPS, MG1, and MG2 of the FDVIC compared with VIC and without any inertia controller

Controller Technique Based on SSAMGO Algorithm		Δf					
		ST (s)	**RT (s)**	**US**	**OS**	**SSE**	**ITAE**
SSAMGO-FDVIC	tie_{1-2}	6.0056	$4.3x10^{-3}$	$-2.87x10^{-2}$	$0.72x10^{-2}$	$4.19x10^{-6}$	0.09107
	tie_{2-3}	8.1593	$2.4x10^{-3}$	$-0.31x10^{-2}$	$1.20x10^{-2}$	$2.21x10^{-6}$	0.05903
	tie_{3-1}	5.1647	$2.8x10^{-3}$	$-0.51x10^{-2}$	$1.67x10^{-2}$	$1.98x10^{-6}$	0.05590
SSAMGO-VIC	tie_{1-2}	6.2462	$8.9x10^{-4}$	$-3.18x10^{-2}$	$1.31x10^{-2}$	$213.3x10^{-6}$	0.46510
	tie_{2-3}	6.1197	$3.5x10^{-3}$	$-8.20x10^{-2}$	$1.67x10^{-2}$	$169.1x10^{-6}$	0.26740
	tie_{3-1}	6.3403	$23x10^{-3}$	$-0.58x10^{-2}$	$1.52x10^{-2}$	$89.7x10^{-6}$	0.16140
SSAMGO-Without VIC	tie_{1-2}	15.5256	$3.1x10^{-4}$	$-3.02x10^{-2}$	$0.71x10^{-2}$	$15.24x10^{-6}$	0.29800
	tie_{2-3}	15.4691	$4.9x10^{-4}$	$-0.34x10^{-2}$	$1.61x10^{-2}$	$10.08x10^{-6}$	0.15680
	tie_{3-1}	15.5828	$1.9x10^{-4}$	$-0.37x10^{-2}$	$1.41x10^{-2}$	$5.16x10^{-6}$	0.14160

The ST of the frequency deviation of the proposed model using SSAMGO tuned the FOPID and tuned FDVIC, for the frequency response of LSPS is reduced by (37.33% and 72.04%), for the frequency deviation of MG1 is decreased by (3.02% and 63.99%), and for the frequency deviation of MG2 is lowered by (17.16% and 64.60%) when compared to conventional VIC and scenarios without VIC, respectively. While, the ST of the change in tie-line power within the interconnected power system using the proposed approach, specifically for tie-line fluctuation between LSPS and MG1, is decreased by (3.85% and 61.32%) in comparison to conventional VIC and scenarios without VIC, respectively. The tie-line power deviation between MG1 and MG2 is increased by 24.99% compared to conventional VIC and decreased by 47.25% compared to scenarios without VIC. Additionally, for the tie-line power between MG2 and LSPS, the ST is reduced by (18.54% and 66.85%) when compared to conventional VIC and scenarios without VIC, respectively.

Furthermore, the RT of the frequency deviation for LSPS is reduced by 96.08% compared to conventional VIC and increased by 4.03% compared to scenarios without VIC, and for the frequency response of MG1, it is decreased by (99.89% and 43.49%), and for the frequency response of MG2, it is decreased by (99.91% and 29.49%) when compared with conventional VIC and scenarios without VIC, respectively. Even though there is an observed increase in the ST of tie-line power deviation compared to conventional VIC and an increase in the RT of frequency deviation compared to scenarios without VIC in some instances, it is crucial to note the presence of oscillations in the waveform and increasing in OS and US. Consequently, the performance of the proposed controller techniques with SSAMGO is deemed superior.

The FDVIC technique employed to provide the necessary inertia in MG1 and MG2 effectively diminishes both US and OS in the frequency deviations, thereby exerting a notable influence on the frequency nadir and overall system stability. Specifically, the US of the frequency deviation in LSPS decreased by (4.81% and 4.81%), and the OS decreased by (32.57% and 32.46%) in comparison to conventional VIC and scenarios without VIC, respectively. Moreover, the US in the frequency deviation of MG1 is notably reduced by (13.26% and 46.74%) and the OS reduced by (70.31% and 65.14%) when compared to conventional VIC and scenarios without VIC, respectively. In the case of MG2, there is a reduction of (2.22% and 28.26%) in the US and a decrease of (51.02% and 47.83%) in OS when compared to conventional VIC and scenarios without VIC, respectively. The findings indicate that the analyzed interconnected power system, employing the proposed controller approach, has successfully enhanced its load-frequency characteristic as intended.

4.6.1 Validation of the Proposed Techniques Based on IEEE-39 New England Test System

This section investigates the impact of RES units on the frequency of the power system through simulation results. To conduct this analysis, a network with the same topology as the well-known IEEE 10 generators 39-bus test system is selected as the focus of the case study.

Table 4.23 displays the capacity of the three-area power system and presents the transfer function parameters adjusted according to the standard capacity of the IEEE-39 New England test system.

Table 4.23 : The capacity of the three-area power system integrated with RESs based on IEEE-39 bus system

Total installed capacity = 841.2 MW				
	Conventional Generator (MW)	**RESs (MW)**	**Loads (MW)**	**Power System (T.F)**
Area 1	198.96	22.67	265.25	$\mathrm{T.F} = \dfrac{158.56}{31.695s + 1}$
Area 2	232.83	----	232.83	$\mathrm{T.F} = \dfrac{180.64}{36.13s + 1}$
Area 3	160.05	22.67	124.78	$\mathrm{T.F} = \dfrac{337.07}{67.41s + 1}$
Total	591.84	45.34	622.86	
Total generation (conventional +RESs) = 637.18 MW				

Area 1 experiences a load demand increase of 42.06 MW, while Area 2 and Area 3 face increases of 23.133 MW and 14.721 MW, respectively. Figure 4.41 depicts the frequency deviation achieved by optimizing the gain of the FOPID and FDVIC controller using the SSAMGO algorithm in a 39-bus system.

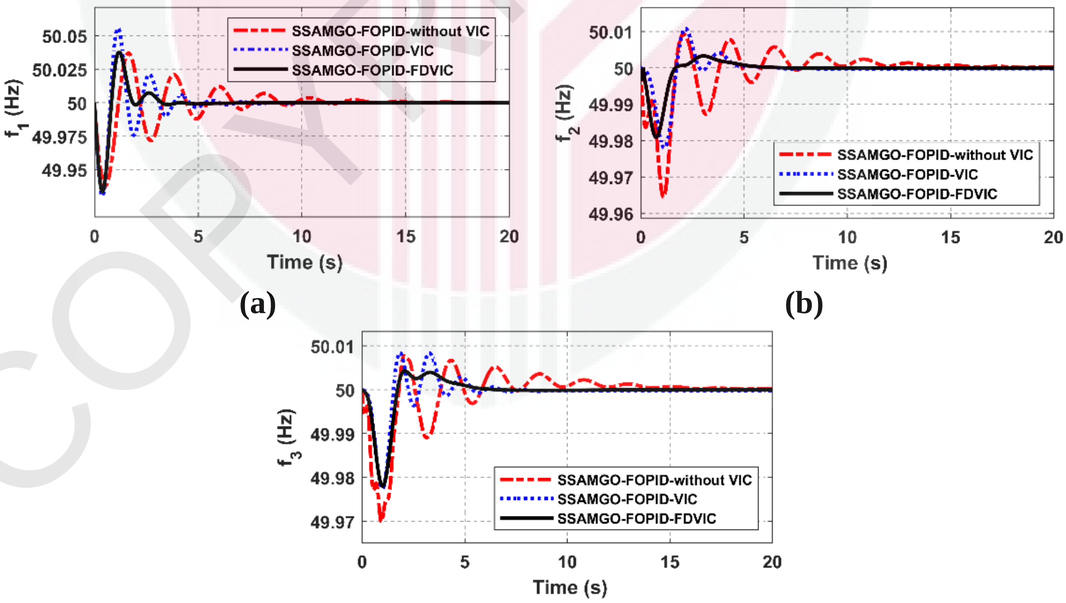

Figure 4.41 : Comparing the frequency deviations, (a): The frequency fluctuation of the Grid, (b): The frequency fluctuation of the MG1, and (c): The frequency fluctuation of the MG2

This illustration includes a comparison with the conventional VIC approach, as well as a scenario without any inertial controller. The optimization algorithm proposed clearly fine-tunes the FOPID controller, and the suggested FDVIC controller demonstrates a faster settling time and reduced oscillations when compared to both the conventional VIC and strategies without any inertia control.

Figure 4.42 illustrates the variation in tie-line power between interconnected areas, achieved by optimizing FOPID and FDVIC controller gains using the SSAMGO algorithm in an IEEE-39 bus system. This visualization includes a comparison with the conventional VIC approach and a scenario without any inertial controller. The implementation of the SSAMGO algorithm for fine-tuning the FOPID controller and the proposed FDVIC controller demonstrates faster settling times and reduced oscillations in comparison to both the conventional VIC and strategies without any inertia control.

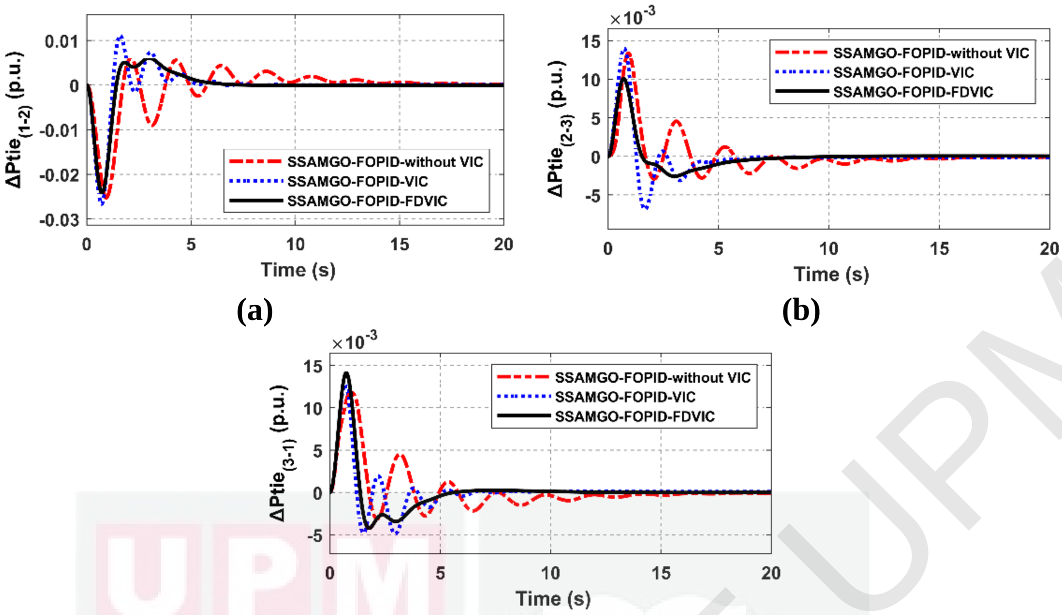

Figure 4.42 : Comparing the change in tie line power, (a): The frequency fluctuation of the Grid, (b): The frequency fluctuation of the MG1, and (c): The frequency fluctuation of the MG2

4.6.2 Experimental Validation Based on Opal-RT Lab

This section illustrates the experimental validation of the real-time implementation of the proposed SSAMGO-optimized FOPID for the secondary controller and FDVIC for the inertia controller loop of the MMG using an RTDS. Two validation scenarios have been analyzed to confirm the optimization of the FDVIC controller parameters using the proposed SSAMGO method. In the first scenario, the MMG power system operates in islanded mode, introducing demand load uncertainty as outlined in the second objective. The second scenario entails two interconnected microgrid power systems with a large-scale power system in grid-connected mode, considering the capacity of the 39-bus IEEE New England test system.

Figure 4.43 presents the response of frequency and tie-line power deviations for the first scenario, and Figure 4.44 demonstrates the frequency deviation of the grid and

MMG system in the second scenario. These measurements are acquired using RTDS through an oscilloscope. The results demonstrate that the frequency deviations obtained through MATLAB simulation for both scenarios correspond with the response observed in RTDS. In Figure 4.45, a real-time depiction is presented, illustrating FDVIC of the low inertia MMG system operating in islanded and grid-connected modes.

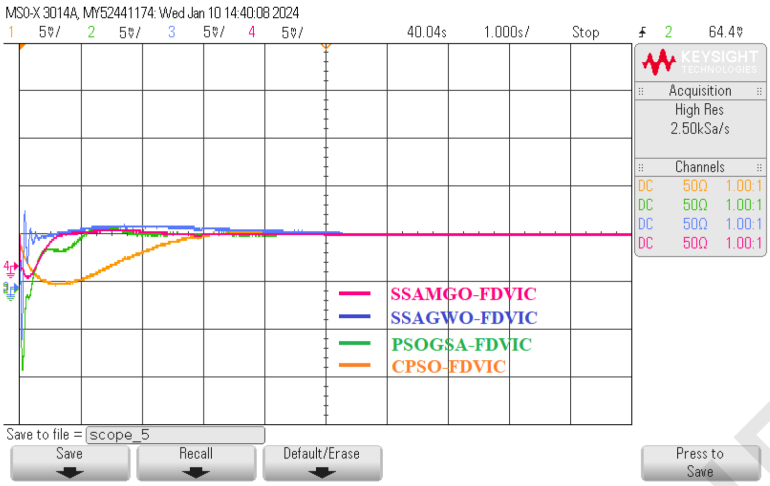

(a)

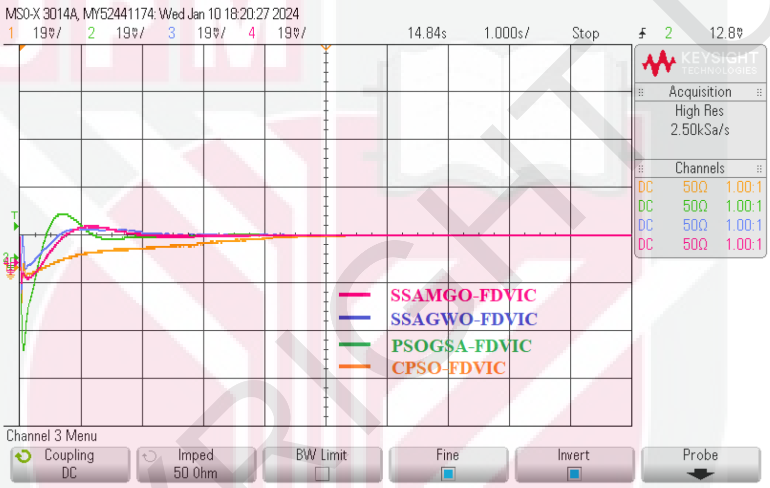

(b)

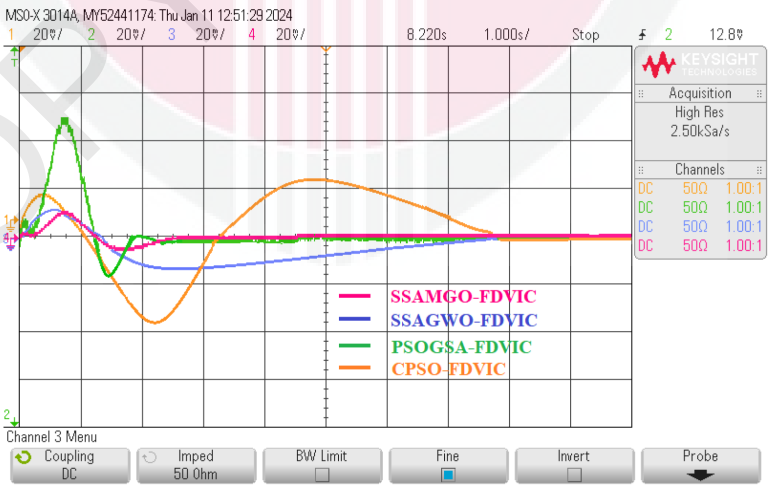

(c)

Figure 4.43 : RTDS output of MMG power system for the first scenario (a) frequency response of MG-1 (b) frequency response of MG-2 (c) tie-line power deviation

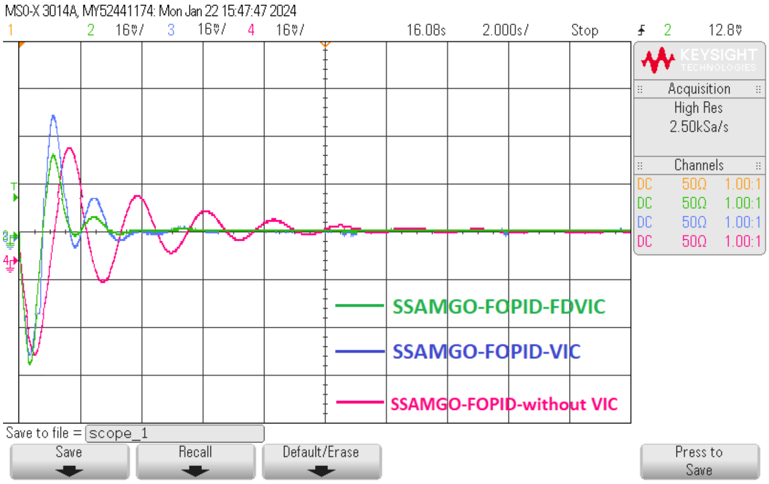

(a)

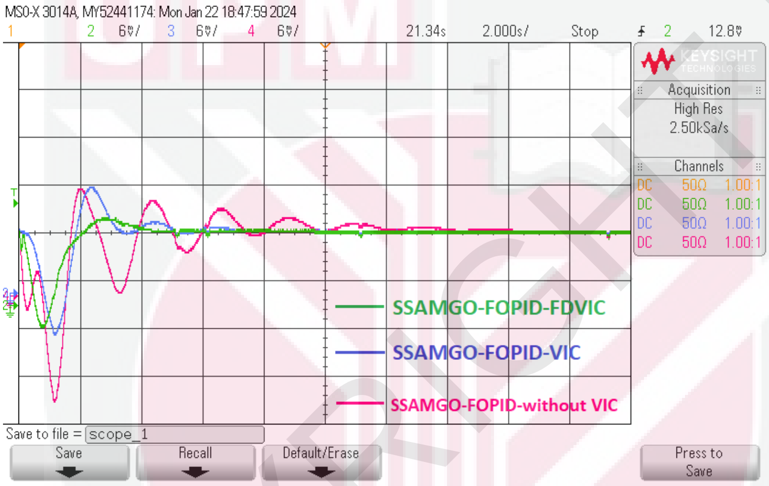

(b)

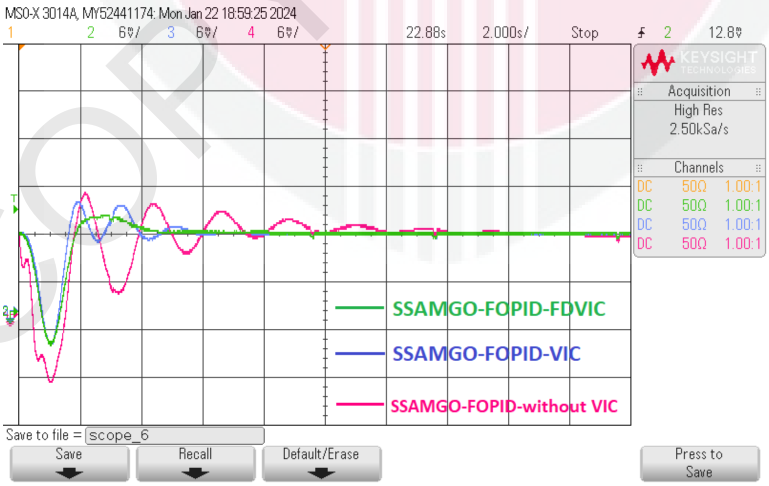

(c)

Figure 4.44 : RTDS output of MMG power system-grid connected mode (39-bus IEEE New England test system) for the second scenario (a) frequency response of area-1 (b) frequency response of area-2 (c) frequency response of area-3

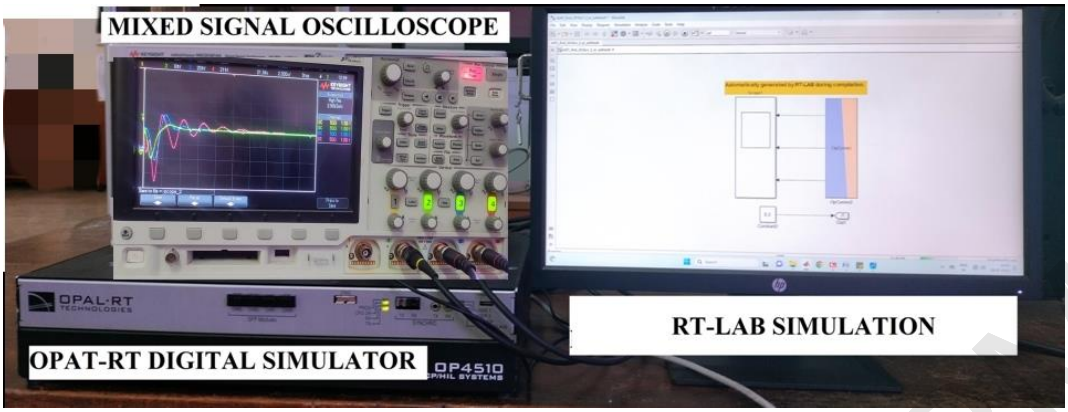

Figure 4.45 : Hardware-in-the-loop digital simulator setup of MMG system operating in islanded/grid-connected mode

4.7 Summary

This section provides a detailed overview of the estimated virtual inertia constant and virtual damping coefficient using the hybrid optimization algorithm proposed, alongside the implementation of the virtual inertia control strategy for frequency regulation as outlined in the thesis. The results presented aim to achieve the four objectives of the thesis. Initially, a decentralized PID controller is developed to manage the frequency of the two-area integrated power system. Subsequently, a hybrid SSAGWO algorithm is introduced to optimize the gain values of the controller. The study assesses the robustness of this proposed technique, focusing on its capability to address parametric uncertainty within the system. Then, a novel virtual inertia controller is devised to bolster the low inertia MMG system, ensuring sufficient inertia to mitigate frequency fluctuations during uncertain conditions. This controller integrates demand response control with inertia control to alleviate stress on the ESS during active periods of inertia control. Furthermore, the performance of the control technique is augmented through the introduction of a hybrid SSAMGO algorithm, with results compared to those obtained using SSAGWO. Finally, the devised controller strategy, utilizing the SSAMGO algorithm, is applied to integrate MMG into a large-scale power system. The modified New England IEEE 39 bus system is specifically chosen as the test platform to validate the effectiveness of the proposed approach.

CHAPTER 5

CONCLUSIONS AND RECOMMENDATIONS FOR FUTURE RESEARCH

5.1 Conclusions

This section consolidates the conclusions drawn from each objective and presents a summary of the key findings resulting from this research. Furthermore, it discusses the contributions made to the field and offers recommendations for future research to enhance our understanding of the ongoing inquiry. A new approach combining virtual inertia control with the impact of damping coefficients, alongside a demand response controller, was developed to maintain the frequency stability of the integrated power system. To achieve optimal dynamic performance of the controller, numerous hybrid intelligence-based control techniques were employed to identify the most suitable values for the controller parameters.

This research introduces a decentralized PID control strategy for managing a multi-area power network integrated with RESs in a deregulated environment. The controller's gain values are optimized using a SSA algorithm. The close loop controller is designed to reduce the frequency deviation and the change in the tie-line power of the power system. Three different scenarios of deregulated behaviour are studied, which is Poolco, Bilateral, and Contract violation. The dynamic performance of the SSA optimization algorithm was implemented and compared with other optimization algorithms in terms of transient (settling time and rise time) and steady-state ITAE performance index of the power system frequency and tie-line power deviation under different scenarios conditions. During scenario 1 of the frequency control response (at Poolco operation condition), It was observed that the settling time with the SSA technique achieves zero state faster than PSO and GWO by 59.66% and 47.13%, respectively. Furthermore, the SSE and transient state indices were significantly improved with the SSA-tuned PID controller when compared to other techniques, as shown by the results of the analyses of scenarios 2 and scenario 3 (bilateral, and contract violation operation condition). The simulation results show that the ST, RT, and SSE were enhanced when applying the proposed algorithm compared with PSO and GWO optimization techniques. Further analysis revealed that while the SSA technique demonstrates strong exploration capabilities, allowing it to broadly search the solution space, it lacks effective exploitation abilities. This limitation becomes evident when using SSA in complex two-area systems integrated with RESs, where high uncertainty and nonlinearity impact performance. In such systems, SSA's weaker exploitation capacity can lead to stagnation in local optima, as it struggles to fine-tune solutions in promising areas under these challenging conditions. To address this challenge, hybridization with GWO is introduced, enhancing both the global convergence speed and the exploration-exploitation capabilities of the optimization process. The proposed SSAGWO optimization algorithm was utilized to enhance the parameter of the PID controller to minimize the frequency devotion in the presence of the PV system, wind turbine system generation, and load disturbance. The proposed power system includes a high nonlinearity reheat steam station integrated with various RERs. To enhance the robustness of the PID controller with SSAGWO against the integration of RESs and the nonlinearities of conventional plants in the hybrid power system, modifications were made to the constraints and boundaries of the algorithm. This adjustment, accomplished through the utilization of both the SSA and GWO algorithms, aims to minimize the complexity of fitness functions, thereby optimizing the performance of the SSAGWO algorithm. This modified approach improves the dynamic performance of the LFC, considering the reduced order of the entire transfer function for the sensitivity and stability analyses. In order to validate the dynamic performance and rigidity of the proposed optimization algorithm, a state-space model of the high-order close loop transfer function was computed in this work. Furthermore, the dynamic performance of the optimization algorithm was compared with PSO, GWO, SSA, GOA, MPA, and SSO. It is concluded that the SSAGWO achieved the best performance (i.e. settling time is 3.8834 seconds) in comparison with PSO, GWO, and SSA; where the settling time values are 15.1049 seconds, 13.6758 seconds, and 13.4111 seconds, respectively.

The conclusions drawn from the second and third objective are as follows, the greater adoption of RESs within MGs has a discernible influence on the stability of the system's frequency. This is primarily attributed to the reduction in the overall system inertia, which subsequently results in significant challenges related to frequency stability. Therefore, a novel approach known as FDVIC is presented, which pertains to a virtual inertia control scheme. This method is designed to improve the dynamic response for the low-inertia MMGs integrated with high penetration of RESs. Furthermore, an adapted DRC has been integrated with the proposed FDVIC technique to mitigate the frequency fluctuations and alleviate the strain on the ESS of the FDVIC during both discharge and charge cycles. The stress on the ESS of the FDVIC for MG1 and MG2 has seen a decrease of 49.15% and 51.37%, respectively, during the discharging period. Furthermore, the power necessary to charge the ESS of the FDVIC has been reduced by 21.34% for MG1 and 41.47% for MG2. Additionally, FOPID controllers have been implemented to govern the active power output of both the BDGs and the Geothermal station of the proposed MG. The optimal parameters for the three-loop controller were determined through the utilization of the SSAMGO algorithm. An extensive assessment of SSAMGO's performance was conducted, comparing it to various other optimization algorithms in different scenarios. The controllers' robustness was further confirmed through testing under concurrent alterations in wind power, PV irradiation, and load fluctuations. The proposed controllers notably minimized both the OS, US, ST, RT, and SSE of frequency and tie-line power deviations. The stability analysis of two scenarios, conducted through Bode analysis, demonstrates that the calibrated gain values for the three-loop controllers are apt for maintaining the system's stable operation. The simulation results clearly show that the FDVIC technique proposed in this study provides adequate inertia to maintain MG stability. The controller's robustness was assessed by examining how it responds to fluctuations in system parameters. Its real-time viability was confirmed through validation, using meteorological data from Malaysia to simulate uncertain variations in both solar thermal and wind power.

The fourth objective focuses on validating the optimization of FOPID and FDVIC controller parameters using the proposed SSAMGO method. Two validation scenarios were explored. In the first scenario, two interconnected microgrid power systems, alongside an LSPS operating in grid-connected mode, were considered, with a capacity analysis based on the 39-bus IEEE New England test system. Results indicate significant improvements in various performance metrics such as ST, RT, US, OS, and SSE of frequency deviations, as well as changes in tie line power when employing the SSAGWO algorithm-optimize FOPID and FDVIC controllers compared to conventional inertia controllers or absence of inertia control techniques. Specifically, enhancements in settling time were observed for MG1 frequency deviation by 37.33%

and 72.04%, for MG2 frequency deviation by 3.02% and 63.98%, and for LSPS frequency deviation by 17.16% and 64.6%, respectively, in comparison to conventional virtual inertia controllers and absence of inertia control techniques. The second scenario involved the validation of two models through Real-Time Digital Simulation Experiments, conducted using the Opal-RT simulator. The first model simulated the MMG integrated power system operating in islanded mode, while the second model represented the three-area interconnected MMG with LSPS operating in grid-connected mode. Measurements acquired via RTDS and an oscilloscope revealed a close correspondence between the frequency deviations observed in MATLAB simulations and those recorded in RTDS for both scenarios. This validation reinforces the efficacy and accuracy of the proposed SSAMGO method in optimizing FOPID and FDVIC controller parameters across various operational modes and system configurations.

5.2 Contributions of the Research

The thesis provides several significant contributions and findings, outlined as follows:

- The hybridization of the SSA algorithm with GWO has led to the creation of a new methodology called hybrid SSAGWO, aimed at optimizing the gain values of decentralized PID controllers. This innovative method significantly improves the regulation of frequency in hybrid power systems integrated with RESs. By leveraging diversified chaotic sequences, it effectively mitigates premature convergence, a common challenge encountered in standard SSA algorithms.

- An FDVIC controller, incorporating the damping coefficient's effect, is introduced for the first time. This innovation aims to support integrated power systems by virtually estimating optimal values for inertia and damping coefficient constants, thereby enhancing frequency regulation in both islanded and grid-connected MMG systems. This contribution utilizes an advanced hybrid optimization technique, SSAMGO. Furthermore, the controller is integrated with demand-side management techniques to enhance frequency response across MMG while minimizing active power drawn from ESS.

- To validate the proposed FDVIC controller and its associated hybrid optimization algorithm, experiments were conducted using a three-area large-scale power system model based on the 39-bus New England IEEE test system. Additionally, real-time simulations were performed using the Opal-RT lab simulator. These validation steps confirmed the effectiveness of the virtual inertia control scheme in enhancing frequency regulation across the integrated power system. The results underscored the viability of the proposed approach in practical applications, demonstrating its potential for improving grid stability and efficiency.

5.3 Recommendations for Future Research

Based on the research findings, several recommendations can be made for future endeavors aimed at advancing the field of virtual inertia controllers in LFC studies:

- The hybrid metaheuristic algorithms introduced in this research can be advanced through additional hybridization with deep learning algorithms. This integration aims to capitalize on the complementary strengths of both methodologies, thereby enhancing the optimization performance of the proposed virtual inertia control scheme.

- An intriguing direction for advancement could entail deploying the proposed controller to uphold the stability of grid-connected microgrid systems, integrating Phasor Measurement Units (PMUs) for real-time measurements.

- Utilizing a centralized controller to regulate frequency fluctuations and provide inertia support for integrated hybrid power systems presents a promising avenue for further investigation. This approach aims to enhance overall system stability and performance by employing centralized control mechanisms to manage frequency variations, ensuring grid stability amidst the integration of diverse energy sources.

REFERENCES

Abazari, A., Monsef, H., & Wu, B. (2018). Load frequency control by de-loaded windfarm using the optimal fuzzy-based PID droopcontroller. *IET Renewable Power Generation*, *13*(1), 180–190.

Abbassi, R., Saidi, S., Urooj, S., Alhasnawi, B. N., Alawad, M. A., & Premkumar, M. (2023). An Accurate Metaheuristic Mountain Gazelle Optimizer for Parameter Estimation of Single- and Double-Diode Photovoltaic Cell Models. *Mathematics*, *11*(22), 4565.

Abdelsattar, M., Mesalam, A., Fawzi, A., & Hamdan, I. (2024). Mountain gazelle optimizer for standalone hybrid power system design incorporating a type of incentive-based strategies. *Neural Computing and Applications*.

Abdollahzadeh, B., Gharehchopogh, F. S., Khodadadi, N., & Mirjalili, S. (2022a). Mountain Gazelle Optimizer: A new Nature-inspired Metaheuristic Algorithm for Global Optimization Problems. *Advances in Engineering Software*, *174*(May), 103282.

Abdollahzadeh, B., Gharehchopogh, F. S., Khodadadi, N., & Mirjalili, S. (2022b). Mountain Gazelle Optimizer: A new Nature-inspired Metaheuristic Algorithm for Global Optimization Problems. *Advances in Engineering Software*, *174*(October), 103282.

Abou El-Ela, A. A., El-Sehiemy, R. A., Shaheen, A. M., & Diab, A. E.-G. (2021). Enhanced coyote optimizer-based cascaded load frequency controllers in multi-area power systems with renewable. *Neural Computing and Applications*, *33*(14), 8459–8477.

Abubakr, H., Guerrero, J. M., & Vasquez, J. C. (2021). Modified Virtual Inertia Mechanism Based ESS for A real Multi-Source Power System Application: the Egyptian Grid. *IECON 2021 – 47th Annual Conference of the IEEE Industrial Electronics Society*, *2021-Octob*, 1–6.

Abubakr, H., Mohamed, T. H., Hussein, M. M., Guerrero, J. M., & Agundis-Tinajero, G. (2021). Adaptive frequency regulation strategy in multi-area microgrids including renewable energy and electric vehicles supported by virtual inertia. *International Journal of Electrical Power & Energy Systems*, *129*(January), 106814.

Acharya, S., Moursi, M. S. El, & Al-Hinai, A. (2018). Coordinated Frequency Control Strategy for an Islanded Microgrid With Demand Side Management Capability. *IEEE Transactions on Energy Conversion*, *33*(2), 639–651.

Akram, U., Nadarajah, M., Shah, R., & Milano, F. (2020). A review on rapid responsive energy storage technologies for frequency regulation in modern power systems. *Renewable and Sustainable Energy Reviews*, *120*, 109626.

Agwa, A., Abdeen, M., & M. Shaaban, S. (2022). Optimal FOPID Controllers for LFC Including Renewables by Bald Eagle Optimizer. *Computers, Materials & Continua*, *73*(3), 5525–5541.

Al-Hinai, A., Alyammahi, H., & Haes Alhelou, H. (2021). Coordinated intelligent frequency control incorporating battery energy storage system, minimum variable contribution of demand response, and variable load damping coefficient in isolated power systems. *Energy Reports*, *7*, 8030–8041.

Al-Humaid, Y. M., Khan, K. A., Abdulgalil, M. A., & Khalid, M. (2021). Two-Stage Stochastic Optimization of Sodium-Sulfur Energy Storage Technology in Hybrid Renewable Power Systems. *IEEE Access*, *9*, 162962–162972.

Alahmadi, A. A. Al, Belkhier, Y., Ullah, N., Abeida, H., Soliman, M. S., Khraisat, Y. S. H., & Alharbi, Y. M. (2021). Hybrid Wind/PV/Battery Energy Management-Based Intelligent Non-Integer Control for Smart DC-Microgrid of Smart University. *IEEE Access*, *9*, 98948–98961.

Alayi, R., Zishan, F., Seyednouri, S. R., Kumar, R., Ahmadi, M. H., & Sharifpur, M. (2021). Optimal Load Frequency Control of Island Microgrids via a PID Controller in the Presence of Wind Turbine and PV. *Sustainability*, *13*(19), 10728.

Alhelou, H. H., Nagpal, N., Kassarwani, N., & Siano, P. (2023). Decentralized Optimized Integral Sliding Mode-Based Load Frequency Control for Interconnected Multi-Area Power Systems. *IEEE Access*, *11*(March), 32296–32307.

Ali Kadhem, A., Abdul Wahab, N. I., & N. Abdalla, A. (2019). Wind Energy Generation Assessment at Specific Sites in a Peninsula in Malaysia Based on Reliability Indices. *Processes*, *7*(7), 399.

Almotairi, K. H., & Abualigah, L. (2022). Hybrid Reptile Search Algorithm and Remora Optimization Algorithm for Optimization Tasks and Data Clustering. *Symmetry*, *14*(3), 458.

Alonso Sørensen, D., Vázquez Pombo, D., & Torres Iglesias, E. (2023). Energy storage sizing for virtual inertia contribution based on ROCOF and local frequency dynamics. *Energy Strategy Reviews*, *47*, 101094.

Ashnani, M. H. M., Johari, A., Hashim, H., & Hasani, E. (2014). A source of renewable energy in Malaysia, why biodiesel? *Renewable and Sustainable Energy Reviews*, *35*, 244–257.

Åström, K. J., & Hägglund, T. (2001). The future of PID control. *Control Engineering Practice*, *9*(11), 1163–1175.

Ates, A., & Akpamukcu, M. (2022). Optimization to optimization (OtoO): optimize monarchy butterfly method with stochastics multi-parameter divergence method for benchmark functions and load frequency control. *Engineering with Computers*, *38*(S3), 1735–1754.

Babu, N. R., & Saikia, L. C. (2021). Load frequency control of a multi-area system incorporating realistic high-voltage direct current and dish-Stirling solar thermal system models under deregulated scenario. *IET Renewable Power Generation*, *15*(5), 1116–1132.

Bagheri-Sanjareh, M., Nazari, M. H., & Hosseinian, S. H. (2021). Energy management of islanded microgrid by coordinated application of thermal and electrical energy storage systems. *International Journal of Energy Research*, *45*(4), 5369–5385.

BAO, Y.-Q., LI, Y., WANG, B., HU, M., & CHEN, P. (2017). Demand response for frequency control of multi-area power system. *Journal of Modern Power Systems and Clean Energy*, *5*(1), 20–29.

Bao, Y., Li, Y., Hong, Y., & Wang, B. (2015). Design of a hybrid hierarchical demand response control scheme for the frequency control. *IET Generation, Transmission & Distribution*, *9*(15), 2303–2310.

Barakat, M. (2022). Novel chaos game optimization tuned-fractional-order PID fractional-order PI controller for load–frequency control of interconnected power systems. *Protection and Control of Modern Power Systems*, *7*(1), 16.

Barik, A. K., & Das, D. C. (2018). Expeditious frequency control of solar photovoltaic/biogas/biodiesel generator based isolated renewable microgrid using grasshopper optimisation algorithm. *IET Renewable Power Generation*, *12*(14), 1659–1667.

Barik, A. K., & Das, D. C. (2019). Proficient load-frequency regulation of demand response supported bio-renewable cogeneration based hybrid microgrids with quasi-oppositional selfish-herd optimisation. *IET Generation, Transmission & Distribution*, *13*(13), 2889–2898.

Barshandeh, S., & Haghzadeh, M. (2021). A new hybrid chaotic atom search optimization based on tree-seed algorithm and Levy flight for solving optimization problems. *Engineering with Computers*, *37*(4), 3079–3122.

Bevrani, H. (2014). *Robust Power System Frequency Control*. Springer International Publishing.

Bharti, K., Singh, V. P., & Singh, S. P. (2022). Impact of Intelligent Demand Response for Load Frequency Control in Smart Grid Perspective. *IETE Journal of Research*, *68*(4), 2433–2444.

Bhowmik, P., & Rout, P. (2019). Emulation of Virtual Inertia with the Dynamic Virtual Damping in Microgrids. *2019 International Conference on Applied Machine Learning (ICAML)*, 130–133.

Biswas, S., Roy, P. K., & Chatterjee, K. (2023). FACTS-based 3DOF-PID Controller for LFC of Renewable Power System Under Deregulation Using GOA. *IETE Journal of Research*, *69*(3), 1486–1499.

Boopathi, D., Jagatheesan, K., Anand, B., Samanta, S., & Dey, N. (2023). Frequency Regulation of Interlinked Microgrid System Using Mayfly Algorithm-Based PID Controller. *Sustainability*, *15*(11), 8829.

Bose, R. B., & Auxillia, D. J. (2021). A robust predictive feedback <scp>FPID</scp> controller using elephant herd virtual inertia optimization control algorithm in Islanded microgrid. *International Journal of Numerical Modelling: Electronic Networks, Devices and Fields*, *34*(5), 1–21.

Bubshait, A., & G. Simões, M. (2018). Optimal Power Reserve of a Wind Turbine System Participating in Primary Frequency Control. *Applied Sciences*, *8*(11), 2022.

Cai, G., Zhou, S., Liu, C., Zhang, Y., Guo, S., & Cao, Z. (2023). Hierarchical under frequency load shedding scheme for inter-connected power systems. *Protection and Control of Modern Power Systems*, *8*(1), 34.

Chandra, A., & Pradhan, A. K. (2021). An Adaptive Underfrequency Load Shedding Scheme in the Presence of Solar Photovoltaic Plants. *IEEE Systems Journal*, *15*(1), 1235–1244.

D’silva, S., Shadmand, M., Bayhan, S., & Abu-Rub, H. (2020). Towards Grid of Microgrids: Seamless Transition between Grid-Connected and Islanded Modes of Operation. *IEEE Open Journal of the Industrial Electronics Society*, *1*, 66–81.

Daraz, A., Malik, S. A., Azar, A. T., Aslam, S., Alkhalifah, T., & Alturise, F. (2022). Optimized Fractional Order Integral-Tilt Derivative Controller for Frequency Regulation of Interconnected Diverse Renewable Energy Resources. In *IEEE Access* (Vol. 10, pp. 43514–43527).

Dashtdar, M., Flah, A., Hosseinimoghadam, S. M. S., & El-Fergany, A. (2022). Frequency control of the islanded microgrid including energy storage using soft computing. *Scientific Reports*, *12*(1), 20409.

Delille, G., Francois, B., & Malarange, G. (2012). Dynamic Frequency Control Support by Energy Storage to Reduce the Impact of Wind and Solar Generation on Isolated Power System’s Inertia. *IEEE Transactions on Sustainable Energy*, *3*(4), 931–939.

Dhandapani, L., Abdulkareem, P., & Muthu, R. (2018). Two-area load frequency control with redox flow battery using intelligent algorithms in a restructured scenario. *TURKISH JOURNAL OF ELECTRICAL ENGINEERING & COMPUTER SCIENCES*, *26*(1), 330–346.

Dokht Shakibjoo, A., Moradzadeh, M., Moussavi, S. Z., Mohammadzadeh, A., & Vandevelde, L. (2022). Load frequency control for multi-area power systems: A new type-2 fuzzy approach based on Levenberg–Marquardt algorithm. *ISA Transactions*, *121*, 40–52.

Donde, V., Pai, M. A., & Hiskens, I. A. (2001). Simulation and optimization in an AGC system after deregulation. *IEEE Transactions on Power Systems*, *16*(3), 481–489.

Dutta, A., & Prakash, S. (2022). Utilizing Electric Vehicles and Renewable Energy Sources for Load Frequency Control in Deregulated Power System Using Emotional Controller. *IETE Journal of Research*, *68*(2), 1500–1511.

El-Bidairi, K. S., Nguyen, H. D., Mahmoud, T. S., Jayasinghe, S. D. G., & Guerrero, J. M. (2020). Optimal sizing of Battery Energy Storage Systems for dynamic frequency control in an islanded microgrid: A case study of Flinders Island, Australia. *Energy*, *195*, 117059.

Elmelegi, A., Mohamed, E. A., Aly, M., Ahmed, E. M., Mohamed, A.-A. A., & Elbaksawi, O. (2021). Optimized Tilt Fractional Order Cooperative Controllers for Preserving Frequency Stability in Renewable Energy-Based Power Systems. *IEEE Access*, *9*, 8261–8277.

Farooq, Z., Rahman, A., Suhail Hussain, S. M., & Ustun, T. S. (2022). Power Generation Control of Renewable Energy Based Hybrid Deregulated Power System. *Energies*, *15*(2), 1–19.

Fathy, A., & Alharbi, A. G. (2021). Recent Approach Based Movable Damped Wave Algorithm for Designing Fractional-Order PID Load Frequency Control Installed in Multi-Interconnected Plants With Renewable Energy. *IEEE Access*, *9*, 71072–71089.

Fayek, H. H., & Kotsampopoulos, P. (2021). Central Tunicate Swarm NFOPID-Based Load Frequency Control of the Egyptian Power System Considering New Uncontrolled Wind and Photovoltaic Farms. *Energies*, *14*(12), 3604.

Fernández-Guillamón, A., Muljadi, E., & Molina-García, A. (2022). Frequency control studies: A review of power system, conventional and renewable generation unit modeling. *Electric Power Systems Research*, *211*, 108191.

Gharehpasha, S., Masdari, M., & Jafarian, A. (2021). Power efficient virtual machine placement in cloud data centers with a discrete and chaotic hybrid optimization algorithm. *Cluster Computing*, *24*(2), 1293–1315.

Ghasemi-Marzbali, A. (2020a). Multi-area multi-source automatic generation control in deregulated power system. *Energy*, *201*, 117667.

Gheisarnejad, M., & Khooban, M. H. (2019). Secondary load frequency control for multi-microgrids: HiL real-time simulation. *Soft Computing*, *23*(14), 5785–5798.

Gope, S., Hemakumar Reddy, G., & Millaner Singh, K. (2023). Frequency regulation analysis for renewable bio generated autonomous multi-microgrid using moth flame optimized fractional order controller. *Materials Today: Proceedings*, *80*, 753–761.

Guha, D., Roy, P. K., & Banerjee, S. (2016). Load frequency control of interconnected power system using grey wolf optimization. *Swarm and Evolutionary Computation*, *27*, 97–115.

Guha, D., Roy, P. K., & Banerjee, S. (2020). Whale optimization algorithm applied to load frequency control of a mixed power system considering nonlinearities and PLL dynamics. *Energy Systems*, *11*(3), 699–728.

Guha, D., Roy, P. K., Banerjee, S., Padmanaban, S., Blaabjerg, F., & Chittathuru, D. (2020). Small-Signal Stability Analysis of Hybrid Power System With Quasi-Oppositional Sine Cosine Algorithm Optimized Fractional Order PID Controller. *IEEE Access*, *8*, 155971–155986.

Gupta, D. K., Jha, A. V., Appasani, B., Srinivasulu, A., Bizon, N., & Thounthong, P. (2021). Load Frequency Control Using Hybrid Intelligent Optimization Technique for Multi-Source Power Systems. *Energies*, *14*(6), 1581.

Hadi, S. (1999). *Power system analysis* (Vol.2). McGraw-hill.

Hasanien, H. M., & El-Fergany, A. A. (2019). Salp swarm algorithm-based optimal load frequency control of hybrid renewable power systems with communication delay and excitation cross-coupling effect. *Electric Power Systems Research*, *176*(October 2018), 105938.

Hassanzadeh, M. E., Nayeripour, M., Hasanvand, S., & Waffenschmidt, E. (2020). Decentralized control strategy to improve dynamic performance of micro-grid and reduce regional interactions using BESS in the presence of renewable energy resources. *Journal of Energy Storage*, *31*(May).

Hatziargyriou, N., Milanovic, J., Rahmann, C., Ajjarapu, V., Canizares, C., Erlich, I., Hill, D., Hiskens, I., Kamwa, I., Pal, B., Pourbeik, P., Sanchez-Gasca, J., Stankovic, A., Van Cutsem, T., Vittal, V., & Vournas, C. (2021). Definition and Classification of Power System Stability – Revisited & Extended. *IEEE Transactions on Power Systems*, *36*(4), 3271–3281.

Hosseini, S. A., Toulabi, M., Ashouri-Zadeh, A., & Ranjbar, A. M. (2022). Battery energy storage systems and demand response applied to power system frequency control. *International Journal of Electrical Power & Energy Systems*, *136*(October 2021), 107680.

Hota, P. K., & Mohanty, B. (2016). Automatic generation control of multi source power generation under deregulated environment. *International Journal of Electrical Power & Energy Systems*, *75*, 205–214.

Hou, X., Sun, Y., Zhang, X., Lu, J., Wang, P., & Guerrero, J. M. (2020). Improvement of Frequency Regulation in VSG-Based AC Microgrid Via Adaptive Virtual Inertia. *IEEE Transactions on Power Electronics*, *35*(2), 1589–1602.

Hussain, T., Ishaq, S., Liaqat, S., Zia, M. F., Al-Durra, A., Khan, B., & Guerrero, J. M. (2022). Load Shed Recovery With Transmission Switching and Intentional Islanding Methods After (N-2) Line Contingencies. *IEEE Access*, *10*, 98403–

98413.

Irudayaraj, A. X. R., Wahab, N. I. A., Premkumar, M., Radzi, M. A. M., Sulaiman, N. Bin, Veerasamy, V., Farade, R. A., & Islam, M. Z. (2022). Renewable sources-based automatic load frequency control of interconnected systems using chaotic atom search optimization. *Applied Soft Computing*, *119*, 108574.

Irudayaraj, A. X. R., Wahab, N. I. A., Umamaheswari, M. G., Mohd Radzi, M. A., Sulaiman, N. Bin, Veerasamy, V., Prasanna, S. C., & Ramachandran, R. (2020). A Matignon's Theorem Based Stability Analysis of Hybrid Power System for Automatic Load Frequency Control Using Atom Search Optimized FOPID Controller. *IEEE Access*, *8*, 168751–168772.

Irudayaraj, A. X. R., Wahab, N. I. A., Veerasamy, V., Premkumar, M., Radzi, M. A. M., Sulaiman, N. Bin, & Tan, W. (2023). Distributed intelligence for consensus-based frequency control of multi-microgrid network with energy storage system. *Journal of Energy Storage*, *73*(PD), 109183.

Jagatheesan, K., Anand, B., Samanta, S., Dey, N., Ashour, A. S., & Balas, V. E. (2017). Particle swarm optimisation-based parameters optimisation of PID controller for load frequency control of multi-area reheat thermal power systems. *International Journal of Advanced Intelligence Paradigms*, *9*(5/6), 464.

Jain, D., & Bhaskar, M. K. (2024). Optimization of controllers using soft computing technique for load frequency control of multi-area deregulated power system. *International Journal of Applied Power Engineering (IJAPE)*, *13*(1), 52.

Jirdehi, M. A., Tabar, V. S., Ghassemzadeh, S., & Tohidi, S. (2020). Different aspects of microgrid management: A comprehensive review. *Journal of Energy Storage*, *30*, 101457.

Kalyan, C. H. N. S., & Rao, G. S. (2021). Impact of communication time delays on combined LFC and AVR of a multi-area hybrid system with IPFC-RFBs coordinated control strategy. *Protection and Control of Modern Power Systems*, *6*(1), 7.

Karad, S. G., Thakur, R., Alotaibi, M. A., Khan, M. J., Malik, H., Márquez, F. P. G., & Hossaini, M. A. (2024). Optimal Design of Fractional Order Vector Controller Using Hardware-in-Loop (HIL) and Opal RT for Wind Energy System. *IEEE Access*, *12*, 35033–35047.

Karnavas, Y. L., & Nivolianiti, E. (2023). Optimal Load Frequency Control of a Hybrid Electric Shipboard Microgrid Using Jellyfish Search Optimization Algorithm. *Applied Sciences*, *13*(10), 6128.

Kerdphol, T., Qudaih, Y., & Mitani, Y. (2016). Optimum battery energy storage system using PSO considering dynamic demand response for microgrids. *International Journal of Electrical Power & Energy Systems*, *83*, 58–66.

Kerdphol, T., Rahman, F., & Mitani, Y. (2018). Virtual Inertia Control Application to Enhance Frequency Stability of Interconnected Power Systems with High Renewable Energy Penetration. *Energies*, *11*(4), 981.

Kerdphol, T., Rahman, F. S., Mitani, Y., Watanabe, M., & Kufeoglu, S. (2018). Robust Virtual Inertia Control of an Islanded Microgrid Considering High Penetration of Renewable Energy. *IEEE Access*, *6*, 625–636.

Kerdphol, T., Rahman, F. S., Phunpeng, V., Watanabe, M., & Mitani, Y. (2018c). Demonstration of Virtual Inertia Emulation Using Energy Storage Systems to Support Community-Based High Renewable Energy Penetration. *2018 IEEE Global Humanitarian Technology Conference (GHTC)*, 1–7. https://doi.org/10.1109/GHTC.2018.8601755

Kerdphol, T., Rahman, F. S., Watanabe, M., & Mitani, Y. (2021). Virtual Inertia Synthesis and Control. In *Power Systems*. Springer International Publishing.

Kerdphol, T., Rahman, F. S., Watanabe, M., Mitani, Y., Hongesombut, K., Phunpeng, V., Ngamroo, I., & Turschner, D. (2021). Small-signal analysis of multiple virtual synchronous machines to enhance frequency stability of grid-connected high renewables. *IET Generation, Transmission & Distribution*, *15*(8), 1273–1289.

Kerdphol, T., Rahman, F. S., Watanabe, M., Mitani, Y., Turschner, D., & Beck, H.-P. (2019). Enhanced Virtual Inertia Control Based on Derivative Technique to Emulate Simultaneous Inertia and Damping Properties for Microgrid Frequency Regulation. *IEEE Access*, *7*, 14422–14433.

Kerdphol, T., Watanabe, M., Hongesombut, K., & Mitani, Y. (2019). Self-Adaptive Virtual Inertia Control-Based Fuzzy Logic to Improve Frequency Stability of Microgrid With High Renewable Penetration. *IEEE Access*.

Kerdphol, T., Watanabe, M., Mitani, Y., & Phunpeng, V. (2019). Applying Virtual Inertia Control Topology to SMES System for Frequency Stability Improvement of Low-Inertia Microgrids Driven by High Renewables. *Energies*, *12*(20), 3902.

Khayat, Y., Naderi, M., Shafiee, Q., Batmani, Y., Fathi, M., Guerrero, J. M., & Bevrani, H. (2019). Decentralized Optimal Frequency Control in Autonomous Microgrids. *IEEE Transactions on Power Systems*, *34*(3), 2345–2353.

Khokhar, B., Dahiya, S., & Parmar, K. P. S. (2021). Load frequency control of a microgrid employing a 2D Sine Logistic map based chaotic sine cosine algorithm. *Applied Soft Computing*, *109*, 107564.

Khooban, M. H. (2021). An Optimal Non-Integer Model Predictive Virtual Inertia Control in Inverter-Based Modern AC Power Grids-Based V2G Technology. *IEEE Transactions on Energy Conversion*, *36*(2), 1336–1346.

Kumar, A., Gupta, D. K., Ghatak, S. R., Appasani, B., Bizon, N., & Thounthong, P. (2022). A Novel Improved GSA-BPSO Driven PID Controller for Load

Frequency Control of Multi-Source Deregulated Power System. *Mathematics*, *10*(18), 3255.

Kumar, A., & Pan, S. (2022). Design of fractional order PID controller for load frequency control system with communication delay. *ISA Transactions*, *129*, 138–149.

Kumar, R., & Sharma, V. K. (2020). Whale Optimization Controller for Load Frequency Control of a Two-Area Multi-source Deregulated Power System. *International Journal of Fuzzy Systems*, *22*(1), 122–137.

Kumari, S., & Shankar, G. (2020). Maiden application of cascade tilt-integral-derivative controller in load frequency control of deregulated power system. *International Transactions on Electrical Energy Systems*, *30*(3), 1–23.

Kundur, P. (1965). Transient Phenomena in Electrical Power Systems. In *McGraw-Hill*. Elsevier.

Kundur, P., Paserba, J., Ajjarapu, V., Andersson, G., Bose, A., Canizares, C., Hatziargyriou, N., Hill, D., Stankovic, A., Taylor, C., Van Cursem, T., & Vittal, V. (2004). Definition and Classification of Power System Stability IEEE/CIGRE Joint Task Force on Stability Terms and Definitions. *IEEE Transactions on Power Systems*, *19*(3), 1387–1401.

Kuttomparambil Abdulkhader, H., Jacob, J., & Mathew, A. T. (2019). Robust type-2 fuzzy fractional order PID controller for dynamic stability enhancement of power system having RES based microgrid penetration. *International Journal of Electrical Power & Energy Systems*, *110*(July 2018), 357–371.

Latif, A., Das, D. C., Barik, A. K., & Ranjan, S. (2019). Maiden coordinated load frequency control strategy for ST-AWEC-GEC-BDDG-based independent three-area interconnected microgrid system with the combined effect of diverse energy storage and DC link using BOA-optimised PFOID controller. *IET Renewable Power Generation*, *13*(14), 2634–2646.

Latif, A., Hussain, S. M. S., Das, D. C., Ustun, T. S., & Iqbal, A. (2021). A review on fractional order (FO) controllers' optimization for load frequency stabilization in power networks. *Energy Reports*, *7*, 4009–4021.

Li, C., Wu, Y., Sun, Y., Zhang, H., Liu, Y., Liu, Y., & Terzija, V. (2020). Continuous Under-Frequency Load Shedding Scheme for Power System Adaptive Frequency Control. *IEEE Transactions on Power Systems*, *35*(2), 950–961.

Liu, G., Shu, C., Liang, Z., Peng, B., & Cheng, L. (2021). A Modified Sparrow Search Algorithm with Application in 3d Route Planning for UAV. *Sensors*, *21*(4), 1224.

Lu, P., Ye, L., Zhao, Y., Dai, B., Pei, M., & Tang, Y. (2021). Review of meta-heuristic algorithms for wind power prediction: Methodologies, applications and challenges. *Applied Energy*, *301*(April), 117446.

Lucas, A., & Chondrogiannis, S. (2016). Smart grid energy storage controller for frequency regulation and peak shaving, using a vanadium redox flow battery. *International Journal of Electrical Power & Energy Systems*, *80*, 26–36.

Magdy, G., Ali, H., & Xu, D. (2021). Effective control of smart hybrid power systems: Cooperation of robust LFC and virtual inertia control system. *CSEE Journal of Power and Energy Systems*, *8*(6), 1583–1593.

Magdy, G., Shabib, G., Elbaset, A. A., Kerdphol, T., Qudaih, Y., Bevrani, H., & Mitani, Y. (2019). Tustin's technique based digital decentralized load frequency control in a realistic multi power system considering wind farms and communications delays. *Ain Shams Engineering Journal*, *10*(2), 327–341.

Mahmud, I., Masood, N.-A., & Jawad, A. (2023). Optimal deloading of PV power plants for frequency control: A techno-economic assessment. *Electric Power Systems Research*, *221*, 109457.

Mandal, R., & Chatterjee, K. (2021). Virtual inertia emulation and RoCoF control of a microgrid with high renewable power penetration. *Electric Power Systems Research*, *194*(February), 107093.

Mekhilef, S., Safari, A., Mustaffa, W. E. S., Saidur, R., Omar, R., & Younis, M. A. A. (2012). Solar energy in Malaysia: Current state and prospects. *Renewable and Sustainable Energy Reviews*, *16*(1), 386–396.

Mishra, D. K., Li, L., Zhang, J., & Hossain, M. J. (2023). Power System Frequency Control. In *ELSEVIER*. Elsevier.

Mohamed, E. A., & Mitani, Y. (2019). Load frequency control enhancement of islanded micro-grid considering high wind power penetration using superconducting magnetic energy storage and optimal controller. *Wind Engineering*, *43*(6), 609–624.

Mohamed, M. A., Diab, A. A. Z., Rezk, H., & Jin, T. (2020). A novel adaptive model predictive controller for load frequency control of power systems integrated with DFIG wind turbines. *Neural Computing and Applications*, *32*(11), 7171–7181.

Mohseni, N. A., & Bayati, N. (2022). Robust Multi-Objective H2/H∞ Load Frequency Control of Multi-Area Interconnected Power Systems Using TS Fuzzy Modeling by Considering Delay and Uncertainty. *Energies*, *15*(15), 5525.

Monje, C. A., Chen, Y., Vinagre, B. M., Xue, D., & Feliu, V. (2010). Fractional-order Systems and Controls. In *Journal of Chemical Information and Modeling*. Springer London.

Moradi, M. H., & Amiri, F. (2021). Virtual inertia control in islanded microgrid by using robust model predictive control (RMPC) with considering the time delay. *Soft Computing*, *25*(8), 6653–6663.

Murugesan, K., J., Shah, P., & Sekhar, R. (2023). Fractional order PI D controller for microgrid power system using cohort intelligence optimization. *Results in Control and Optimization*, *11*(January), 100218.

Mythreyee, M., & A. Nalini, D. (2023). Genetic Algorithm Based Smart Grid System for Distributed Renewable Energy Sources. *Computer Systems Science and Engineering*, *45*(1), 819–837.

Naderipour, A., Abdul-Malek, Z., Davoodkhani, I. F., Kamyab, H., & Ali, R. R. (2021). Load-frequency control in an islanded microgrid PV/WT/FC/ESS using an optimal self-tuning fractional-order fuzzy controller. *Environmental Science and Pollution Research*, *30*(28), 71677–71688.

Naidu, K., Mokhlis, H., Bakar, A. H. A., Terzija, V., & Illias, H. A. (2014). Application of firefly algorithm with online wavelet filter in automatic generation control of an interconnected reheat thermal power system. *International Journal of Electrical Power and Energy Systems*, *63*, 401–413.

Nikolaidis, P., & Poullikkas, A. (2018). Cost metrics of electrical energy storage technologies in potential power system operations. *Sustainable Energy Technologies and Assessments*, *25*, 43–59.

Nosratabadi, S. M., Bornapour, M., & Gharaei, M. A. (2019). Grasshopper optimization algorithm for optimal load frequency control considering Predictive Functional Modified PID controller in restructured multi-resource multi-area power system with Redox Flow Battery units. *Control Engineering Practice*, *89*(April 2018), 204–227.

Nour, M., Magdy, G., Bakeer, A., Telba, A. A., Beroual, A., Khaled, U., & Ali, H. (2023). A New Fractional-Order Virtual Inertia Support Based on Battery Energy Storage for Enhancing Microgrid Frequency Stability. *Fractal and Fractional*, *7*(12), 855.

Okwu, M. O., & Tartibu, L. K. (2021). Grey Wolf Optimizer. In *Studies in Computational Intelligence* (Vol. 927, pp. 43–52).

Oshnoei, S., Aghamohammadi, M., Oshnoei, S., Oshnoei, A., & Mohammadi-Ivatloo, B. (2021). Provision of Frequency Stability of an Islanded Microgrid Using a Novel Virtual Inertia Control and a Fractional Order Cascade Controller. *Energies*, *14*(14), 4152.

Oshnoei, S., Aghamohammadi, M. R., Oshnoei, S., Sahoo, S., Fathollahi, A., & Khooban, M. H. (2023). A novel virtual inertia control strategy for frequency regulation of islanded microgrid using two-layer multiple model predictive control. *Applied Energy*, *343*, 121233.

Oshnoei, S., Oshnoei, A., Mosallanejad, A., & Haghjoo, F. (2021). Novel load frequency control scheme for an interconnected two-area power system including wind turbine generation and redox flow battery. *International Journal of Electrical Power & Energy Systems*, *130*(March), 107033.

Ouyang, C., Zhu, D., & Wang, F. (2021). A Learning Sparrow Search Algorithm. *Computational Intelligence and Neuroscience*, *2021*.

Paliwal, N., Srivastava, L., & Pandit, M. (2022). Application of grey wolf optimization algorithm for load frequency control in multi-source single area power system. *Evolutionary Intelligence*, *15*(1), 563–584.

Patel, M. R., & Beik, O. (2021). Wind Power Systems. In *Wind and Solar Power Systems* (pp. 37–62). CRC Press.

Peddakapu, K., Mohamed, M. R., Srinivasarao, P., & Leung, P. K. (2022). Simultaneous controllers for stabilizing the frequency changes in deregulated power system using moth flame optimization. *Sustainable Energy Technologies and Assessments*, *51*, 101916.

Pozna, C., Precup, R.-E., Horvath, E., & Petriu, E. M. (2022). Hybrid Particle Filter–Particle Swarm Optimization Algorithm and Application to Fuzzy Controlled Servo Systems. *IEEE Transactions on Fuzzy Systems*, *30*(10), 4286–4297.

Rafiee, A., Batmani, Y., Ahmadi, F., & Bevrani, H. (2021). Robust Load-Frequency Control in Islanded Microgrids: Virtual Synchronous Generator Concept and Quantitative Feedback Theory. *IEEE Transactions on Power Systems*, *36*(6), 5408–5416.

Rai, A., & Das, D. K. (2020). Optimal PID Controller Design by Enhanced Class Topper Optimization Algorithm for Load Frequency Control of Interconnected Power Systems. *Smart Science*, *8*(3), 125–151.

Rakhshani, E., Remon, D., Mir Cantarellas, A., & Rodriguez, P. (2016). Analysis of derivative control based virtual inertia in multi-area high-voltage direct current interconnected power systems. *IET Generation, Transmission & Distribution*, *10*(6), 1458–1469.

Ramachandran, R., Madasamy, B., Veerasamy, V., & Saravanan, L. (2018). Load frequency control of a dynamic interconnected power system using generalised Hopfield neural network based self-adaptive PID controller. *IET Generation, Transmission and Distribution*, *12*(21), 5713–5722.

Ramachandran, R., Satheesh Kumar, J., Madasamy, B., & Veerasamy, V. (2021). A hybrid MFO-GHNN tuned self-adaptive FOPID controller for ALFC of renewable energy integrated hybrid power system. *IET Renewable Power Generation*, *15*(7), 1582–1595.

Rezaei, J., Golshan, M. E. H., & Alhelou, H. H. (2022). Impacts of integration of very large-scale photovoltaic power plants on rotor angle and frequency stability of power system. *IET Renewable Power Generation*, *16*(11), 2384–2401.

Ridha, H. M., Hizam, H., Mirjalili, S., Othman, M. L., Ya'acob, M. E., Ahmadipour, M., & Ismaeel, N. Q. (2022). On the problem formulation for parameter extraction of the photovoltaic model: Novel integration of hybrid evolutionary algorithm and Levenberg Marquardt based on adaptive damping parameter formula. *Energy Conversion and Management*, *256*(January), 115403.

Rojin, R., & Mary Linda, M. (2022). Hybrid Microgrid based on PID Controller with the Modified Particle Swarm Optimization. *Intelligent Automation & Soft Computing*, *33*(1), 245–258.

Roy, N. K., Islam, S., Podder, A. K., Roy, T. K., & Muyeen, S. M. (2022). Virtual Inertia Support in Power Systems for High Penetration of Renewables—Overview of Categorization, Comparison, and Evaluation of Control Techniques. *IEEE Access*, *10*, 129190–129216.

Sabahi, K., Tavan, M., & Hajizadeh, A. (2021). Adaptive type-2 fuzzy PID controller for LFC in AC microgrid. *Soft Computing*, *25*(11), 7423–7434.

Saeed Uz Zaman, M., Bukhari, S., Hazazi, K., Haider, Z., Haider, R., & Kim, C.-H. (2018). Frequency Response Analysis of a Single-Area Power System with a Modified LFC Model Considering Demand Response and Virtual Inertia. *Energies*, *11*(4), 787.

Safari, A., Babaei, F., & Farrokhifar, M. (2021). A load frequency control using a PSO-based ANN for micro-grids in the presence of electric vehicles. *International Journal of Ambient Energy*, *42*(6), 688–700.

Saha, A., Dash, P., Babu, N. R., Chiranjeevi, T., Venkateswararao, B., & Knypiński, Ł. (2022). Impact of Spotted Hyena Optimized Cascade Controller in Load Frequency Control of Wave-Solar-Double Compensated Capacitive Energy Storage Based Interconnected Power System. *Energies*, *15*(19), 6959.

Sahu, R. K., Gorripotu, T. S., & Panda, S. (2015). A hybrid DE-PS algorithm for load frequency control under deregulated power system with UPFC and RFB. *Ain Shams Engineering Journal*, *6*(3), 893–911.

Saleh, A., Omran, W. A., Hasanien, H. M., Tostado-Véliz, M., Alkuhayli, A., & Jurado, F. (2022). Manta Ray Foraging Optimization for the Virtual Inertia Control of Islanded Microgrids Including Renewable Energy Sources. *Sustainability*, *14*(7), 4189.

Sanki, P., Mazumder, S., Basu, M., Pal, P. S., & Das, D. (2021). Moth Flame Optimization Based Fuzzy-PID Controller for Power–Frequency Balance of an Islanded Microgrid. *Journal of The Institution of Engineers (India): Series B*, *102*(5), 997–1006.

Santhoshkumar, T., & Senthilkumar, V. (2020). Transient and small signal stability improvement in microgrid using AWOALO with virtual synchronous generator control scheme. *ISA Transactions*, *104*, 233–244.

Sarangi, P., & Mohapatra, P. (2023). Evolved opposition-based Mountain Gazelle Optimizer to solve optimization problems. *Journal of King Saud University - Computer and Information Sciences*, *35*(10), 101812.

Saxena, A., & Shankar, R. (2022). Improved load frequency control considering dynamic demand regulated power system integrating renewable sources and hybrid energy storage system. *Sustainable Energy Technologies and Assessments*, *52*(PC), 102245.

Saxena, P., Singh, N., & Pandey, A. K. (2020). Enhancing the dynamic performance of microgrid using derivative controlled solar and energy storage based virtual inertia system. *Journal of Energy Storage*, *31*(June), 101613.

Saxena, P., Singh, N., & Pandey, A. K. (2021). Investigating the frequency fault ride through capability of solar photovoltaic system: Replacing battery via virtual inertia reserve. *International Transactions on Electrical Energy Systems*, *31*(3), 1–18.

Saxena, P., Singh, N., & Pandey, A. K. (2021). Self-Regulated Solar PV Systems: Replacing Battery via Virtual Inertia Reserve. *IEEE Transactions on Energy Conversion*, *36*(3), 2185–2194.

Saxena, S., & Hote, Y. V. (2016). Decentralized PID load frequency control for perturbed multi-area power systems. *International Journal of Electrical Power & Energy Systems*, *81*, 405–415.

Sen, S., & Kumar, V. (2018). Microgrid control: A comprehensive survey. *Annual Reviews in Control*, *45*(March), 118–151.

Shafei, M. A. R., Ibrahim, D. K., & Bahaa, M. (2022). Application of PSO tuned fuzzy logic controller for LFC of two-area power system with redox flow battery and PV solar park. *Ain Shams Engineering Journal*, *13*(5), 101710.

Shair, J., Li, H., Hu, J., & Xie, X. (2021). Power system stability issues, classifications and research prospects in the context of high-penetration of renewables and power electronics. *Renewable and Sustainable Energy Reviews*, *145*, 111111.

Shakibjoo, A. D., Moradzadeh, M., Din, S. U., Mohammadzadeh, A., Mosavi, A. H., & Vandevelde, L. (2022). Optimized Type-2 Fuzzy Frequency Control for Multi-Area Power Systems. *IEEE Access*, *10*, 6989–7002.

Shankar, R., Chatterjee, K., & Bhushan, R. (2016). Impact of energy storage system on load frequency control for diverse sources of interconnected power system in deregulated power environment. *International Journal of Electrical Power and Energy Systems*, *79*, 11–26.

Shayeghi, H., Rahnama, A., & Alhelou, H. H. (2021). Frequency control of fully-renewable interconnected microgrid using fuzzy cascade controller with demand response program considering. *Energy Reports*, *7*, 6077–6094.

Shi, K., Tang, Y., Liu, X., & Zhong, S. (2017). Non-fragile sampled-data robust synchronization of uncertain delayed chaotic Lurie systems with randomly occurring controller gain fluctuation. *ISA Transactions*, *66*, 185–199.

Shi, K., Tang, Y., Zhong, S., Yin, C., Huang, X., & Wang, W. (2018). Nonfragile asynchronous control for uncertain chaotic Lurie network systems with Bernoulli stochastic process. *International Journal of Robust and Nonlinear Control*, *28*(5), 1693–1714.

Shiva, C. K., & Mukherjee, V. (2016). Design and analysis of multi-source multi-area deregulated power system for automatic generation control using quasi-oppositional harmony search algorithm. *International Journal of Electrical Power and Energy Systems*, *80*, 382–395.

Shuai, Z., Sun, Y., Shen, Z. J., Tian, W., Tu, C., Li, Y., & Yin, X. (2016). Microgrid stability: Classification and a review. *Renewable and Sustainable Energy Reviews*, *58*, 167–179.

Singh, J., Chattterjee, K., & Vishwakarma, C. B. (2018). Two degree of freedom internal model control-PID design for LFC of power systems via logarithmic approximations. *ISA Transactions*, *72*, 185–196.

Singh, K. M., & Gope, S. (2021). Renewable energy integrated multi-microgrid load frequency control using grey wolf optimization algorithm. *Materials Today: Proceedings*, *46*, 2572–2579.

Singh, N., & Singh, S. (2017). A Modified Mean Gray Wolf Optimization Approach for Benchmark and Biomedical Problems. *Evolutionary Bioinformatics*, *13*, 117693431772941.

Singh, V. K., & Govindarasu, M. (2021). A Cyber-Physical Anomaly Detection for Wide-Area Protection Using Machine Learning. *IEEE Transactions on Smart Grid*, *12*(4), 3514–3526.

Siti, M. W., Tungadio, D. H., Nsilulu, N. T., Banza, B. B., & Ngoma, L. (2022). Application of load frequency control method to a multi-microgrid with energy storage system. *Journal of Energy Storage*, *52*(PA), 104629.

Sitompul, S., Hanawa, Y., Bupphaves, V., & Fujita, G. (2020). State of charge control integrated with load frequency control for BESS in islanded microgrid. *Energies*, *13*(18).

Sobhy, M. A., Abdelaziz, A. Y., Hasanien, H. M., & Ezzat, M. (2021). Marine predators algorithm for load frequency control of modern interconnected power systems including renewable energy sources and energy storage units. *Ain Shams Engineering Journal*, *12*(4), 3843–3857.

Sockeel, N., Gafford, J., Papari, B., & Mazzola, M. (2020). Virtual Inertia Emulator-Based Model Predictive Control for Grid Frequency Regulation Considering High Penetration of Inverter-Based Energy Storage System. *IEEE Transactions on Sustainable Energy*, *11*(4), 2932–2939.

Stroe, D. I., Knap, V., Swierczynski, M., Stroe, A. I., & Teodorescu, R. (2017). Operation of a grid-connected lithium-ion battery energy storage system for primary frequency regulation: A battery lifetime perspective. *IEEE*

Transactions on Industry Applications, *53*(1), 430–438.

Sun, X., Hu, C., Lei, G., Guo, Y., & Zhu, J. (2020). State Feedback Control for a PM Hub Motor Based on Gray Wolf Optimization Algorithm. *IEEE Transactions on Power Electronics*, *35*(1), 1136–1146.

Sundararaju, N., Vinayagam, A., Veerasamy, V., & Subramaniam, G. (2022). A Chaotic Search-Based Hybrid Optimization Technique for Automatic Load Frequency Control of a Renewable Energy Integrated Power System. *Sustainability*, *14*(9), 5668.

Sureshkumar, V., Balasubramaniam, S., Ravi, V., & Arunachalam, A. (2022). A hybrid optimization algorithm-based feature selection for thyroid disease classifier with rough type-2 fuzzy support vector machine. *Expert Systems*, *39*(1), 18.

Tabak, A., & Duman, S. (2023). Maiden application of TID μ 1 ND μ 2 controller for effective load frequency control of non-linear two-area power system. *IET Renewable Power Generation*.

Tan, W., Zhang, H., & Yu, M. (2012). Decentralized load frequency control in deregulated environments. *International Journal of Electrical Power & Energy Systems*, *41*(1), 16–26.

Tavakoli, M., Pouresmaeil, E., Adabi, J., Godina, R., & Catalão, J. P. S. (2018). Load-frequency control in a multi-source power system connected to wind farms through multi terminal HVDC systems. *Computers & Operations Research*, *96*, 305–315.

Teng, Q., Xu, D., Yang, W., Li, J., & Shi, P. (2021). Neural network-based integral sliding mode backstepping control for virtual synchronous generators. *Energy Reports*, *7*, 1–9.

Tepljakov, A., Alagoz, B. B., Yeroglu, C., Gonzalez, E. A., Hosseinnia, S. H., Petlenkov, E., Ates, A., & Cech, M. (2021). Towards Industrialization of FOPID Controllers: A Survey on Milestones of Fractional-Order Control and Pathways for Future Developments. *IEEE Access*, *9*, 21016–21042.

Tripathi, S., Singh, V. P., Kishor, N., & Pandey, A. S. (2023). Load frequency control of power system considering electric Vehicles' aggregator with communication delay. *International Journal of Electrical Power & Energy Systems*, *145*(October 2022), 108697.

Veerasamy, V., Abdul Wahab, N. I., Ramachandran, R., Othman, M. L., Hizam, H., Satheesh Kumar, J., & Irudayaraj, A. X. R. (2022). Design of single- and multi-loop self-adaptive PID controller using heuristic based recurrent neural network for ALFC of hybrid power system. *Expert Systems with Applications*, *192*, 116402.

Veerasamy, V., Abdul Wahab, N. I., Ramachandran, R., Vinayagam, A., Othman, M. L., Hizam, H., & Satheeshkumar, J. (2019). Automatic Load Frequency

Control of a Multi-Area Dynamic Interconnected Power System Using a Hybrid PSO-GSA-Tuned PID Controller. *Sustainability*, *11*(24), 6908.

Veerasamy, V., Wahab, N. I. A., Ramachandran, R., Othman, M. L., Hizam, H., Irudayaraj, A. X. R., Guerrero, J. M., & Kumar, J. S. (2020). A Hankel Matrix Based Reduced Order Model for Stability Analysis of Hybrid Power System Using PSO-GSA Optimized Cascade PI-PD Controller for Automatic Load Frequency Control. *IEEE Access*, *8*, 71422–71446.

Wang, H., Pourmousavi, S. A., Soong, W. L., Zhang, X., & Ertugrul, N. (2023). Battery and energy management system for vanadium redox flow battery: A critical review and recommendations. *Journal of Energy Storage*, *58*, 106384.

Wang, P., Zhang, Y., & Yang, H. (2021). Research on Economic Optimization of Microgrid Cluster Based on Chaos Sparrow Search Algorithm. *Computational Intelligence and Neuroscience*, *2021*.

Wang, X., Wang, Y., & Liu, Y. (2020). Dynamic load frequency control for high-penetration wind power considering wind turbine fatigue load. *International Journal of Electrical Power & Energy Systems*, *117*(November 2019), 105696.

Wang, Z., Liu, Y., Yang, Z., & Yang, W. (2021). Load Frequency Control of Multi-Region Interconnected Power Systems with Wind Power and Electric Vehicles Based on Sliding Mode Control. *Energies*, *14*(8), 2288.

Weldcherkos, T., Salau, A. O., & Ashagrie, A. (2021). Modeling and design of an automatic generation control for hydropower plants using Neuro-Fuzzy controller. *Energy Reports*, *7*, 6626–6637.

Wu, W., Chen, Y., Luo, A., Zhou, L., Zhou, X., Yang, L., Dong, Y., & Guerrero, J. M. (2017). A Virtual Inertia Control Strategy for DC Microgrids Analogized With Virtual Synchronous Machines. *IEEE Transactions on Industrial Electronics*, *64*(7), 6005–6016.

Xie, Q., Guo, Z., Liu, D., Chen, Z., Shen, Z., & Wang, X. (2021). Optimization of heliostat field distribution based on improved Gray Wolf optimization algorithm. *Renewable Energy*, *176*, 447–458.

Xiong, L., Yang, S., Li, P., Huang, S., Wang, C., & Wang, J. (2020). Discrete specified time consensus control of aggregated energy storage for load frequency regulation. *International Journal of Electrical Power and Energy Systems*, *123*(August), 106224.

Xu, Q., Dragicevic, T., Xie, L., & Blaabjerg, F. (2021). Artificial Intelligence-Based Control Design for Reliable Virtual Synchronous Generators. *IEEE Transactions on Power Electronics*, *36*(8), 9453–9464.

Xue, J., & Shen, B. (2020). A novel swarm intelligence optimization approach: sparrow search algorithm. *Systems Science & Control Engineering*, *8*(1), 22–34.

Yakout, A. H., Attia, M. A., & Kotb, H. (2021). Marine Predator Algorithm based Cascaded PIDA Load Frequency Controller for Electric Power Systems with Wave Energy Conversion Systems. *Alexandria Engineering Journal*, *60*(4), 4213–4222.

Yan, Z., & Xu, Y. (2020). A Multi-Agent Deep Reinforcement Learning Method for Cooperative Load Frequency Control of a Multi-Area Power System. *IEEE Transactions on Power Systems*, *35*(6), 4599–4608.

Yang, L., Hu, Z., Xie, S., Kong, S., & Lin, W. (2019). Adjustable virtual inertia control of supercapacitors in PV-based AC microgrid cluster. *Electric Power Systems Research*, *173*(August 2018), 71–85.

Yildirim, B., Gheisarnejad, M., & Khooban, M. H. (2022). A New Parameter Tuning Technique for Noninteger Controllers in Low-Inertia Modern Power Grids. *IEEE Journal of Emerging and Selected Topics in Industrial Electronics*, *3*(2), 279–288.

Yu, C., Huang, S., Xu, H., Yan, J., Rong, K., & Sun, M. (2024). Optimal charging of lithium-ion batteries based on lithium precipitation suppression. *Journal of Energy Storage*, *82*, 110580.

Yuan, J., Zhao, Z., Liu, Y., He, B., Wang, L., Xie, B., & Gao, Y. (2021). DMPPT Control of Photovoltaic Microgrid Based on Improved Sparrow Search Algorithm. *IEEE Access*, *9*, 16623–16629.

Zhang, C., Wei, Y.-L., Cao, P.-F., & Lin, M.-C. (2018). Energy storage system: Current studies on batteries and power condition system. *Renewable and Sustainable Energy Reviews*, *82*, 3091–3106.

Zhang, J., Zhang, G., Chen, Z., Dai, H., Hu, Q., Liao, S., & Sun, S. (2020). Emerging applications of atomic layer deposition for lithium-sulfur and sodium-sulfur batteries. *Energy Storage Materials*, *26*, 513–533.

Zhang, Z., Fang, J., Dong, C., Jin, C., & Tang, Y. (2023). Enhanced Grid Frequency and DC-Link Voltage Regulation in Hybrid AC/DC Microgrids Through Bidirectional Virtual Inertia Support. *IEEE Transactions on Industrial Electronics*, *70*(7), 6931–6940.

Zhu, Y., & Yousefi, N. (2021). Optimal parameter identification of PEMFC stacks using Adaptive Sparrow Search Algorithm. *International Journal of Hydrogen Energy*, *46*(14), 9541–9552.

Zishan, F., Akbari, E., Montoya, O. D., Giral-Ramírez, D. A., & Molina-Cabrera, A. (2022). Efficient PID Control Design for Frequency Regulation in an Independent Microgrid Based on the Hybrid PSO-GSA Algorithm. *Electronics*, *11*(23), 3886.

Zou, C., Zhang, L., Hu, X., Wang, Z., Wik, T., & Pecht, M. (2018). A review of fractional-order techniques applied to lithium-ion batteries, lead-acid batteries, and supercapacitors. *Journal of Power Sources*, *390*, 286–296.

APPENDICES

Appendix A

In chapter 3, in section 3.2.1, system model parameters of the model presented in Figure 3.2:

Base rated power $P_{R1} = P_{R2} = 2000MW$, $K_{P1} = K_{P2} = 120Hz/p.u.$, $T_{P1} = T_{P2} = 0.08s$, $T_{T1} = T_{T2} = 0.3s$, $T_{r1} = T_{r2} = 10s$, $K_{r1} = K_{r2} = 0.5s$, $R_1 = R_2 = 2.4Hz/p.u.$, $B_1 = B_2 = 0.425$ p.u./Hz, $D_1 = D_2 = 0.00833$ p.u./Hz, $T_{12} = T_{21} = 0.08674$ p.u./rad. Boiler parameters: $K_1 = 0.85$, $K_2 = 0.095$, $K_3 = 0.92$, CB = 200, TD = 0, $K_{IB} = 0.03$, $T_{IB} = 26$, $T_{RB} = 69$, TF = 10.

In chapter 3, in section 3.2.2-a, system model parameters of the model presented in Figure 3.4:

Base Rated Power of area 1 and area 2 $P_{R1} = P_{R2} = 2000$ MW; The gains of power system $K_{p1} = K_{p2} = 120$ Hz/p.u.; The time constant of the power system $T_{P1} = T_{P2} = 0.08$ s; The turbine time constant $T_{T1} = T_{T2} = 0.3$ s; The time constant of the Reheat $T_{r1} = T_{r2} = 10$ s; The gains of the Reheat $K_{r1} = K_{r2} = 0.5$; The governor adjustment deviation coefficients $R_1 = R_2 = 2.4$ Hz/p.u.; The frequency response coefficients $B_1 = B_2 = 0.425$ p.u./Hz; The system damping coefficient $D_1 = D_2 = 0.00833$ p.u./Hz; The time constants of tie-line flow $T_{12} = T_{21} = 0.08674$ p.u./rad; System inertia $H_1 = H_2 = 5$ s; Solar PV time constant $T_{PV} = 1.3$; Wind turbine time constant $T_{WT} = 1.5$; Boiler parameters, $K_1 = 0.85$, $K_2 = 0.095$, $K_3 = 0.92$, $C_B = 200$, $T_D = 0$, $K_{IB} = 0.03$, $T_{IB} = 26$, $T_{RB} = 69$, $T_F = 10$.

In chapter 3, in section 3.3.1-a, the parameters of the proposed MG integrated with RESs presented in Figure 3.11:

Microgrid capacity $P_r = 1500$ kW; Microgrid system gain $K_{ps} = 125$ Hz/p.u.; Microgrid system time constant $T_{ps} = 25$ s; Biodiesel valve gain $K_{VA} = 1$; Biodiesel valve actuator delay $T_{VA} = 0.05$ s; Biodiesel engine gain $K_{BE} = 1$; Time constants of biodiesel $T_{BE} = 0.5$ s; Droop constant $R = 2.4$ Hz/p.u.; Frequency bias constant $B = 0.4267$ p.u./Hz; Gain constant of WTG $K_{WT} = 1$; Time constant of WTG $T_{WT} = 1.5$ s; Gain of the turbine of solar thermal $K_T = 1$; Charging time constant of the turbine of solar thermal $T_T = 0.3$ s; Solar collector gain $K_S = 1.8$; Solar collector time constant $T_S = 1.8$ s; Gain constant of the ESS $K_{BESS} = 1$; Time constant of the ESS $T_{BESS} = 0.026$ s.

In chapter 3, in section 3.3.2-i, the parameters of the proposed MMG integrated with RESs presented in Figure 3.15:

MG rated power: $P_{r1} = 2000$ kW, $P_{r2} = 1500$ kW; Power system gains constant: $k_{p1} = 125$ Hz/p.u., $k_{p2} = 100$ Hz/p.u.; Power system time constant: $T_{p1} = 25$ s, $T_{p2} = 12$ s; Frequency bias factor: $B_1 = B_2 = 0.4267$ p.u./Hz; Damping coefficient: $D_1 = 0.00833$ p.u./Hz, $D_2 = 0.01$ p.u./Hz; Droop control: $R_1 = R_2 = 2.4$ Hz/p.u.; Equivalent system inertia: $H_{eq.1} = 3.5106$ s, $H_{eq.2} = 0.75$ s; Tie-line power flow time constants: $T_{12} = T_{21} = 0.08674$ p.u./rad; Biodiesel valve gain: $K_{VA1} = K_{VA2} = 1$; Biodiesel valve actuator delay: $T_{VA1} = T_{VA2} = 0.05$ s; Biodiesel engine gain: $K_{BE1} = K_{BE2} = 1$; Time constants of biodiesel: $T_{BE1} = T_{BE2} = 0.5$ s; Gain constant of WT: $K_{WT1} = K_{WT2} = 1$; Time constant of WT: $T_{WT1} = T_{WT2} = 1.5$ s; Gain constant of PV: $K_{PV1} = K_{PV2} = 1$; Time constant of PV: $T_{PV1} = T_{PV2} = 1.8$ s; Gain of the turbine of solar thermal: $K_T = 1$;

Charging time constant of the turbine of solar thermal: T_T = 0.3 s; Solar collector gain: K_S = 1.8; Solar collector time constant: T_S = 1.8 s; Gain constant of the ESS: K_{BESS1} = K_{BESS2} = 1; Time constant of the ESS: T_{BESS1} = T_{BESS2} = 0.026 s.

Appendix B

The state-space equations with an estimation of the CLTF of the model in Chapter 3, in Section 3.2.2-a, Figure 3.4, and in Chapter 4, in section 4.3.4 are illustrated as the following:

Let, $\Delta f_i = X_1$, $\Delta P_{Ti} = X_2$, $\Delta T_T = X_3$, $\Delta P_{tie,i} = X_5$, $\Delta P_{WT} = X_6$, $\Delta P_{PV} = X_7$, and $\Delta P_{RFB} = X_8$

The vector form of the state variables of the proposed model is present in Equation (B.1).

$$X = \left[X_1, X_2, X_3, X_4, X_5, X_6, X_7, X_8\right]^T \tag{B.1}$$

System parameters and their associated state variables are shown as below:

$$X = \left[\Delta f_i \quad \Delta X_{1T} \quad \Delta X_{1RE} \quad \Delta P_{tie,i}\right]^T \tag{B.2}$$

where

$$X_{1T} = \left[\Delta P_T \quad \Delta T_T \quad \Delta G_T\right] \tag{B.3}$$

$$X_{1RE} = \left[\Delta P_{WT} \quad \Delta P_{PV} \quad \Delta P_{RFB}\right] \tag{B.4}$$

The state-space equation of the hybrid power system is illustrated as follows:

$$\dot{X}_1 = \frac{K_{pi}}{T_{pi}}\left[-X_1 + X_2 + X_3 + X_4 + X_5 + X_6 + X_7 - X_8 - \Delta P_{Di}\right] \tag{B.5}$$

The state-space modeling of the reheat turbine generator is also derived in Equations (B.6), (B.7), and (B.8).

$$\dot{X}_2 = -\frac{X_2}{T_{ti}} + \frac{X_3}{T_{ti}} \tag{B.6}$$

$$\dot{X}_3 = -\frac{X_3}{T_{ri}} + \left[\frac{1}{T_{ri}} - \frac{K_r}{T_{Gi}}\right] X_4 + \frac{1}{T_{ri}} \Delta P_{ci} - \frac{X_1}{T_{ri} R_i} \tag{B.7}$$

$$\dot{X}_4 = -\frac{X_4}{T_{Gi}} + \frac{\Delta P_{ci}}{T_{Gi}} - \frac{1}{R_i T_{Gi}} X_1 \tag{B.8}$$

In general, the state-space of the tie line power can be emulated as follows:

$$\dot{X}_5 = \Delta P_{tie,i} = 2\pi \left[\sum_{i=1, i \neq j}^{n} T_{ij} X_i\right] \tag{B.9}$$

The wind turbine model in state space is given in Equation (B.10).

$$\dot{X}_6 = -\frac{X_6}{T_{WT}} + K_{WT} P_{WT} \tag{B.10}$$

The PV model in state space is obtained in Equation (B.11).

$$\dot{X}_7 = -\frac{X_7}{T_{PV}} + K_{PV} P_{PV} \tag{B.11}$$

The state-space model of the RFB is shown below:

$$\dot{X}_8 = -\frac{X_8}{T_{RFB}} + K_{RFB} P_{RFB} \tag{B.12}$$

The general state-space representation is given below:

$$\dot{X} = AX + Bu \tag{B.13}$$

The control input can be presented as:

$$u = \left[\Delta P_{ci}\right]^T \tag{B.14}$$

The definition of the output matrix of the proposed system is:

$$Y = CX \tag{B.15}$$

where A is the state matrix, B is the input matrix, and C is the output matrix. According to the previous mathematical steps, A, B, and C can be calculated.

$$A = \begin{bmatrix} -4.07 & 0 & -0.44 & 4.81 & 0.04 & 0 & 0 & 0 & 0 & 0 & 0 & 0.77 & 0 \\ 0 & -4.07 & 0.44 & 0 & 0 & 4.81 & 0.04 & 0 & 0 & 0 & 0 & 0 & 0.67 \\ 6 & -6 & 0 & 0 & 0 & 0 & 0 & 0 & 0 & 0 & 0 & 0 & 0 \\ -10.2 & 0 & -1.43 & -12.5 & 0 & 0 & 0 & -0.22 & 0.8 & 0 & 0 & 0 & 0 \\ 0 & 0 & 0 & 12.5 & -0.1 & 0 & 0 & 0 & 0 & 0 & 0 & 0 & 0 \\ 0 & -10.2 & 1.43 & 0 & 0 & -12.5 & 0 & 0 & 0 & -0.22 & 0.8 & 0 & 0 \\ 0 & 0 & 0 & 0 & 0 & 12.5 & -0.1 & 0 & 0 & 0 & 0 & 0 & 0 \\ -0.05 & 0 & -0.01 & 0 & 0 & 0 & 0 & -0.28 & 0 & 0 & 0 & 0 & 0 \\ -10.2 & 0 & -1.78 & 0 & 0 & 0 & 0 & 0 & 0 & 0 & 0 & 0 & 0 \\ 0 & -0.05 & 0.01 & 0 & 0 & 0 & 0 & 0 & 0 & -0.28 & 0 & 0 & 0 \\ 0 & -10.2 & 1.78 & 0 & 0 & 0 & 0 & 0 & 0 & 0 & 0 & 0 & 0 \\ 0 & 0 & 0 & 0 & 0 & 0 & 0 & 0 & 0 & 0 & 0 & -0.77 & 0 \\ 0 & 0 & 0 & 0 & 0 & 0 & 0 & 0 & 0 & 0 & 0 & 0 & -0.67 \end{bmatrix}$$

$$B = \begin{bmatrix} -1 & 0 & 0 & 0 & 0 & 0 & 0 & 0 & 0 & 0 & 0 & 0 & 0 \end{bmatrix}^T$$

$$C = \begin{bmatrix} 6 & 0 & 0 & 0 & 0 & 0 & 0 & 0 & 0 & 0 & 0 & 0 & 0 \end{bmatrix}$$

The numerator and denominator of the CLTF in Equation 4.8 is as follow:

$$\begin{aligned} num = & -6s^{10} - 179s^{9} - 1991s^{8} - 9844s^{7} - 1.591\times10^{4}s^{6} - 1.231\times10^{4}s^{5} \\ & - 5013s^{4} - 1088s^{3} - 117s^{2} + 4.747s \end{aligned}$$

$$\begin{aligned} den = & s^{11} + 33.9s^{10} + 505s^{9} + 4006s^{8} + 1.739\times10^{4}s^{7} + 3.727\times10^{4}s^{6} \\ & + 4.061\times10^{4}s^{5} + 2.468\times10^{4}s^{4} + 8800s^{3} + 1837s^{2} + 208.3s + 9.932 \end{aligned}$$

The state-space equations with an estimation of the model in Chapter 3, in Section 3.3.1-a, Figure 3.11, and in Chapter 4, in section 4.4.1 are illustrated as the following:

The model will include a total of eight modelled state variables, and its vector form is as follows:

$$X = \left[X_1, X_2, X_3, X_4, X_5, X_6, X_7, X_8\right]^T \tag{B.16}$$

The state variables that relate to the system parameters are denoted as:

$$X = \left[\Delta f, \Delta P_{BDG}, \Delta P_v, \Delta P_{con}, \Delta P_{STH}, \Delta P_T, \Delta P_{WTG}, \Delta P_{inertia}\right]^T \tag{B.17}$$

where ΔP_{BDG} is the output power of the biodiesel generator, ΔP_V is the output of the biodiesel turbine valve, ΔP_{con} is the output of the controller signal, ΔP_{STH} is the output power of the solar thermal generator, ΔP_T is the output of the solar thermal turbine, ΔP_{WTG} is the output power of the WTG, and $\Delta P_{inertia}$ is the active power supporting to the MG system from the ESS through VIC.

Following is a description of the state-space equations of the proposed model:

$$\dot{X}_1 = \frac{-D}{2H} X_1 + \frac{K_{ps}}{2H} X_2 + \frac{K_{ps}}{2H} X_5 + \frac{K_{ps}}{2H} X_7 + \frac{K_{ps}}{2H} X_8 \tag{B.18}$$

The biodiesel generator state-space model of MG is as follows:

$$\dot{X}_2 = \frac{-1}{T_{BE}} X_2 + \frac{K_{BE}}{T_{BE}} X_3 \tag{B.19}$$

$$\dot{X}_3 = \frac{-K_{VA}}{RT_{VA}} X_1 - \frac{1}{T_{VA}} X_3 + \frac{K_{VA}}{T_{VA}} X_4 \tag{B.20}$$

The state-space model of the solar thermal power generator is as:

$$\dot{X}_5 = \frac{-1}{T_s} X_5 + \frac{K_s}{T_s} X_6 \tag{B.21}$$

$$\dot{X}_6 = \frac{-1}{T_T} X_6 + \frac{K_T}{T_T} P_{solar-thermal} \tag{B.22}$$

The state-space model of the wind-turbine generator of MG is as:

$$\dot{X}_7 = \frac{-1}{T_{WTG}} X_7 + \frac{K_{WTG}}{T_{WTG}} P_{wind-turbine} \tag{B.23}$$

The state space of the VIC controller based on ESS of the MG is as:

$$\dot{X}_8 = \frac{-1}{T_{ESS}} X_8 + \frac{K_{ESS}}{T_{ESS}} X_1 \cdot \Delta P_{VIC} \tag{B.24}$$

MG disturbance signals considered in this model include the change in wind power (P_{wind}), solar thermal power ($P_{solar\text{-}thermal}$), and load power (P_{load}):

$$W = \begin{bmatrix} \Delta P_{solar-thermal} & \Delta P_{wind-turbine} & \Delta P_{load} \end{bmatrix}^T \tag{B.25}$$

The control signals of the proposed model are as follows:

$$u = \begin{bmatrix} \Delta P_{con} & \Delta P_{inertia} \end{bmatrix}^T \tag{B.26}$$

The definition of the numerator and denominator of the closed- loop transfer function of the MG by using the state space analysis is demonstrated as follows:

$$TF_{CL-MG} = \frac{Num_{MG}}{Den_{MG}} \tag{B.27}$$

where

$$Num_{MG} = -5s^5 - 2942s^4 - 1.64\times10^5 s^3 - 2.347\times10^6 s^2 - 4.061\times10^6 s$$

$$\mathrm{Den}_{MG} = s^6 + 588.4s^5 + 3.32\times10^4 s^4 + 7.191\times10^5 s^3 + 7.392\times10^6 s^2 + 3.107\times10^7 s + 3.466\times10^7$$

The state-space equations with an estimation of the model in Chapter 3, in Section 3.3.2-i, Figure 3.15, and in Chapter 4, in section 4.5.3 are illustrated as the following:

The state-space model of the proposed MMG model is given as:

$$X^{\bullet} = AX + B_1W + B_2u \tag{B.28}$$

$$Y = CX \tag{B.29}$$

where A matrix is represented as:

$$A = \begin{bmatrix} a_{11} & a_{12} & a_{13} & \cdots & a_{1\,20} \\ a_{21} & a_{22} & a_{23} & \cdots & a_{2\,20} \\ a_{31} & a_{32} & a_{33} & \cdots & a_{3\,20} \\ . & . & . & \cdots & . \\ a_{20\,1} & a_{20\,2} & a_{20\,3} & \cdots & a_{20\,20} \end{bmatrix} \tag{B.30}$$

The model will include a total of 20 modeled state variables, and its vector form is as follows:

$$X = \left[X_1, X_2, X_3, \ldots\ldots\ldots\ldots, X_{20}\right]^T \tag{B.31}$$

The state variables that relate to the system parameters are denoted as:

$$X = [\Delta f_1, \Delta P_{BDG1}, \Delta P_{v1}, \Delta P_{FO1}, \Delta P_{Geo}, \Delta P_{g1}, \Delta P_{STH}, \Delta P_T, \Delta P_{WTG1}, \Delta P_{inertia1}, \Delta P_{DRC1}, \Delta P_{tie,i}, \Delta f_2, \Delta P_{BDG2}, \Delta P_{v2}, \Delta P_{FO2}, \Delta P_{WTG2}, \Delta P_{PV}, \Delta P_{inertia2}, \Delta P_{DRC2}]^T \tag{B.32}$$

Following is a description of the state-space equations of the proposed model:

$$X_1^\bullet = \left[a_{11}X_1 + a_{12}X_2 + a_{15}X_5 + a_{17}X_7 + a_{19}X_9 \pm a_{110}X_{10} \pm a_{111}X_{11} - \Delta P_{load1}\right] \quad \text{(B.33)}$$

where

$$a_{11} = \frac{-D_1}{2H_1},\ a_{12} = a_{15} = a_{17} = a_{19} = a_{110} = a_{111} = \frac{K_{ps1}}{2H_1}$$

The biodiesel generator state-space model of MG1 is as follows:

$$X_2^\bullet = a_{22}X_2 + a_{23}X_3 = \frac{-1}{T_{BE1}}X_2 + \frac{K_{BE1}}{T_{BE1}}X_3 \quad \text{(B.34)}$$

$$X_3^\bullet = a_{31}X_1 + a_{33}X_3 + a_{34}X_4 = \frac{-K_{VA1}}{R_1T_{VA1}}X_1 - \frac{1}{T_{VA1}}X_3 + \frac{K_{VA1}}{T_{VA1}}X_4 \quad \text{(B.35)}$$

Geothermal generator state-space model is depicted as:

$$X_5^\bullet = a_{55}X_5 + a_{56}X_6 = \frac{-1}{T_{tg}}X_5 + \frac{K_{tg}}{T_{tg}}X_6 \quad \text{(B.36)}$$

$$X_6^\bullet = a_{64}X_4 + a_{66}X_6 = \frac{K_{gg}}{T_{gg}}X_4 - \frac{1}{T_{gg}}X_6 \quad \text{(B.37)}$$

The state-space model of the solar thermal power generator is as:

$$X_7^\bullet = a_{77}X_7 + a_{78}X_8 = \frac{-1}{T_s}X_7 + \frac{K_s}{T_s}X_8 \quad \text{(B.38)}$$

$$X_8^\bullet = a_{88}X_8 + \frac{K_T}{T_T}P_{solar-thermal} = \frac{-1}{T_T}X_8 + \frac{K_T}{T_T}P_{solar-thermal} \quad \text{(B.39)}$$

The state-space model of the wind-turbine generator of MG1 is as:

$$X_9^\bullet = a_{99}X_9 + \frac{K_{WTG1}}{T_{WTG1}}P_{wind} = \frac{-1}{T_{WTG1}}X_9 + \frac{K_{WTG1}}{T_{WTG1}}P_{wind} \quad \text{(B.40)}$$

The state-space of the proposed FDVIC controller based on ESS in the MG1 is as:

$$X_{10}^{\bullet} = a_{10\,1} X_1 \cdot \Delta P_{FDVIC1} + a_{10\,10} X_{10} = \frac{K_{ESS}}{T_{ESS}} X_1 \cdot \Delta P_{FDVIC1} - \frac{1}{T_{ESS}} X_{10} \qquad \text{(B.41)}$$

The tie-lines of the interconnected MGs system are portrayed as follows:

$$X_{12}^{\bullet} = \Delta P_{tie,i} = 2\pi \left[\sum_{i=1, i \neq j}^{n} T_{ij} X_i \right] \qquad \text{(B.42)}$$

The state-space of the frequency deviation of MG2 is as:

$$X_{13}^{\bullet} = \left[a_{13\,13} X_{13} + a_{13\,14} X_{14} + a_{13\,17} X_{17} + a_{13\,18} X_{18} \pm a_{13\,19} X_{19} \pm a_{13\,20} X_{20} - \Delta P_{load2} \right] \qquad \text{(B.43)}$$

where

$$a_{13\,13} = \frac{-D_2}{2H_2},\ a_{13\,14} = a_{13\,17} = a_{13\,18} = a_{13\,19} = a_{13\,20} = \frac{K_{ps2}}{2H_2}$$

The biodiesel generator state-space model of MG2 is as follows:

$$X_{14}^{\bullet} = a_{14\,14} X_{14} + a_{14\,15} X_{15} = \frac{-1}{T_{BE2}} X_{14} + \frac{K_{BE2}}{T_{BE2}} X_{15} \qquad \text{(B.44)}$$

$$X_{15}^{\bullet} = a_{15\,13} X_{13} + a_{15\,15} X_{15} + a_{15\,16} X_{16} = \frac{-K_{VA2}}{R_2 T_{VA2}} X_{13} - \frac{1}{T_{VA2}} X_{15} + \frac{K_{VA2}}{T_{VA2}} X_{16} \qquad \text{(B.45)}$$

The state-space model of the wind-turbine generator of MG2 is as:

$$X_{17}^{\bullet} = a_{17\,17} X_{17} + \frac{K_{WTG2}}{T_{WTG2}} P_{wind} = \frac{-1}{T_{WTG2}} X_{17} + \frac{K_{WTG2}}{T_{WTG2}} P_{wind} \qquad \text{(B.46)}$$

The state-space model of the solar photovoltaic RES is as follow:

$$X_{18}^{\bullet} = a_{18\,18} X_{18} + \frac{K_{PV}}{T_{PV}} P_{solar} = \frac{-1}{T_{PV}} X_{18} + \frac{K_{PV}}{T_{PV}} P_{solar} \qquad \text{(B.47)}$$

The state-space of the proposed FDVIC controller based on ESS in the MG2 is as:

$$\dot{X}_{19} = a_{19\,1}X_{13} \cdot \Delta P_{FDVIC2} + a_{19\,19}X_{19} = \frac{K_{ESS}}{T_{ESS}}X_{13} \cdot \Delta P_{FDVIC2} - \frac{1}{T_{ESS}}X_{19} \qquad (B.48)$$

MG disturbance signals considered in this study article include the change in wind power (P_{wind}), solar radiation power (P_{solar}), solar thermal power ($P_{solar\text{-}thermal}$), and load power (P_{load}):

$$X = [\Delta P_{wind}, \Delta P_{solar}, \Delta P_{solar-thermal}, \Delta P_{load}]^T \qquad (B.49)$$

The control signals of the MMG model is as follow:

$$u = [\Delta P_{FO1}, \Delta P_{FO2}, \Delta P_{inertia1}, \Delta P_{inertia2}, \Delta P_{DRC1}, \Delta P_{DRC2}]^T \qquad (B.50)$$

The output matrix model of the MG is defined as:

$$\begin{aligned} Y = [&\Delta f_1, \Delta P_{BDG1}, \Delta P_{Geo}, \Delta P_{STH}, \Delta P_{WTG1}, \Delta P_{inertia1}, \Delta P_{DRC1}, \\ &\Delta f_2, \Delta P_{BDG2}, \Delta P_{WTG2}, \Delta P_{PV}, \Delta P_{inertia2}, \Delta P_{DRC2}]^T \end{aligned} \qquad (B.51)$$

$$\therefore Y = [1\ 0\ 0\ 0\ 0\ 1\ 0\ 0\ 0\ 0]^T \cdot [X]^T \qquad (B.52)$$

For the first scenario, the closed loop transfer function is:

$$TF_{CL-MG1} = \frac{Num_{MG1}}{Den_{MG1}}$$

$$\begin{aligned} Num_{MG1} = &-5s^{34} - 9851s^{33} - 8.522\times10^{06}s^{32} - 4.319\times10^{09}s^{31} - 1.44\times10^{12}s^{30} \\ &- 3.355\times10^{14}s^{29} - 5.671\times10^{16}s^{28} - 7.114\times10^{18}s^{27} - 6.725\times10^{20}s^{26} \\ &- 4.841\times10^{22}s^{25} - 2.673\times10^{24}s^{24} - 1.137\times10^{26}s^{23} - 3.745\times10^{27}s^{22} \\ &- 9.557\times10^{28}s^{21} - 1.894\times10^{30}s^{20} - 2.916\times10^{31}s^{19} - 3.493\times10^{32}s^{18} \\ &- 3.262\times10^{33}s^{17} - 2.378\times10^{34}s^{16} - 1.358\times10^{35}s^{15} - 6.079\times10^{35}s^{14} \\ &- 2.135\times10^{36}s^{13} - 5.858\times10^{36}s^{12} - 1.244\times10^{37}s^{11} - 2.009\times10^{37}s^{10} \\ &- 2.388\times10^{37}s^{9} - 1.992\times10^{37}s^{8} - 1.094\times10^{37}s^{7} - 3.705\times10^{36}s^{6} \\ &- 7.601\times10^{35}s^{5} - 9.388\times10^{34}s^{4} - 6.778\times10^{33}s^{3} - 2.622\times10^{32}s^{2} \\ &- 4.181\times10^{30}s \end{aligned}$$

$$\begin{aligned}Den_{MG1} = {} & s^{35} + 1970s^{34} + 1.769\times10^{06}s^{33} + 9.585\times10^{08}s^{32} + 3.506\times10^{11}s^{31} \\ & + 9.168\times10^{13}s^{30} + 1.773\times10^{16}s^{29} + 2.588\times10^{18}s^{28} + 2.89\times10^{20}s^{27} \\ & + 2.487\times10^{22}s^{26} + 1.658\times10^{24}s^{25} + 8.588\times10^{25}s^{24} + 3.46\times10^{27}s^{23} \\ & + 1.085\times10^{29}s^{22} + 2.655\times10^{30}s^{21} + 5.075\times10^{31}s^{20} + 7.612\times10^{32}s^{19} \\ & + 9.014\times10^{33}s^{18} + 8.486\times10^{34}s^{17} + 6.395\times10^{35}s^{16} + 3.879\times10^{36}s^{15} \\ & + 1.902\times10^{37}s^{14} + 7.55\times10^{37}s^{13} + 2.426\times10^{38}s^{12} + 6.273\times10^{38}s^{11} \\ & + 1.291\times10^{39}s^{10} + 2.071\times10^{39}s^{9} + 2.513\times10^{39}s^{8} + 2.194\times10^{39}s^{7} \\ & + 1.28\times10^{39}s^{6} + 4.55\times10^{38}s^{5} + 9.666\times10^{37}s^{4} + 1.223\times10^{37}s^{3} \\ & + 8.984\times10^{35}s^{2} + 3.518\times10^{34}s + 5.658\times10^{32}\end{aligned}$$

$$TF_{CL-MG2} = \frac{Num_{MG2}}{Den_{MG2}}$$

$$\begin{aligned}Num_{MG2} = {} & -18.51s^{32} - 3.647\times10^{04}s^{31} - 3.10247\times10^{07}s^{30} - 1.51947\times10^{10}s^{29} \\ & - 4.82547\times10^{12}s^{28} - 1.06547\times10^{15}s^{27} - 1.7147\times10^{17}s^{26} - 2.06947\times10^{19}s^{25} \\ & - 1.92947\times10^{21}s^{24} - 1.40647\times10^{23}s^{23} - 8.04647\times10^{24}s^{22} - 3.61647\times10^{26}s^{21} \\ & - 1.27247\times10^{28}s^{20} - 3.48447\times10^{29}s^{19} - 7.38647\times10^{30}s^{18} - 1.20547\times10^{32}s^{17} \\ & - 1.50147\times10^{33}s^{16} - 1.42147\times10^{34}s^{15} - 1.01647\times10^{35}s^{14} - 5.46747\times10^{35}s^{13} \\ & - 2.20147\times10^{36}s^{12} - 6.58647\times10^{36}s^{11} - 1.44347\times10^{37}s^{10} - 2.25647\times10^{37}s^{9} \\ & - 2.40147\times10^{37}s^{8} - 1.61647\times10^{37}s^{7} - 6.27247\times10^{36}s^{6} - 1.41247\times10^{36}s^{5} \\ & - 1.86847\times10^{35}s^{4} - 1.42847\times10^{34}s^{3} - 5.8247\times10^{32}s^{2} - 9.76547\times10^{30}s \\ & + 2.25347\times10^{17}\end{aligned}$$

$$\begin{aligned}Den_{MG2} = {} & s^{35} + 1970s^{34} + 1.769\times10^{06}s^{33} + 9.585\times10^{08}s^{32} + 3.506\times10^{11}s^{31} \\ & + 9.168\times10^{13}s^{30} + 1.773\times10^{16}s^{29} + 2.588\times10^{18}s^{28} + 2.89\times10^{20}s^{27} \\ & + 2.487\times10^{22}s^{26} + 1.658\times10^{24}s^{25} + 8.588\times10^{25}s^{24} + 3.46\times10^{27}s^{23} \\ & + 1.085\times10^{29}s^{22} + 2.655\times10^{30}s^{21} + 5.075\times10^{31}s^{20} + 7.612\times10^{32}s^{19} \\ & + 9.014\times10^{33}s^{18} + 8.486\times10^{34}s^{17} + 6.395\times10^{35}s^{16} + 3.879\times10^{36}s^{15} \\ & + 1.902\times10^{37}s^{14} + 7.55\times10^{37}s^{13} + 2.426\times10^{38}s^{12} + 6.273\times10^{38}s^{11} \\ & + 1.291\times10^{39}s^{10} + 2.071\times10^{39}s^{9} + 2.513\times10^{39}s^{8} + 2.194\times10^{39}s^{7} \\ & + 1.28\times10^{39}s^{6} + 4.55\times10^{38}s^{5} + 9.666\times10^{37}s^{4} + 1.223\times10^{37}s^{3} \\ & + 8.984\times10^{35}s^{2} + 3.518\times10^{34}s + 5.658\times10^{32}\end{aligned}$$

For the second scenario, the close loop transfers function of the proposed model including DRC is:

$$TF_{CL-MG1} = \frac{Num_{MG1}}{Den_{MG1}}$$

$$
\begin{aligned}
Num_{MG1} = &-5s^{34} - 9966s^{33} - 8.829\times10^{06}s^{32} - 4.667\times10^{09}s^{31} - 1.664\times10^{12}s^{30} \\
&- 4.27\times10^{14}s^{29} - 8.184\times10^{16}s^{28} - 1.194\times10^{19}s^{27} - 1.337\times10^{21}s^{26} \\
&- 1.154\times10^{23}s^{25} - 7.701\times10^{24}s^{24} - 3.99\times10^{26}s^{23} - 1.61\times10^{28}s^{22} \\
&- 5.077\times10^{29}s^{21} - 1.253\times10^{31}s^{20} - 2.422\times10^{32}s^{19} - 3.664\times10^{33}s^{18} \\
&- 4.325\times10^{34}s^{17} - 3.968\times10^{35}s^{16} - 2.813\times10^{36}s^{15} - 1.529\times10^{37}s^{14} \\
&- 6.293\times10^{37}s^{13} - 1.931\times10^{38}s^{12} - 4.314\times10^{38}s^{11} - 6.794\times10^{38}s^{10} \\
&- 7.191\times10^{38}s^{9} - 4.787\times10^{38}s^{8} - 1.862\times10^{38}s^{7} - 4.273\times10^{37}s^{6} \\
&- 5.882\times10^{36}s^{5} - 4.831\times10^{35}s^{4} - 2.258\times10^{34}s^{3} - 5.265\times10^{32}s^{2} \\
&- 4.181\times10^{30}s
\end{aligned}
$$

$$
\begin{aligned}
Den_{MG1} = &\, s^{35} + 2013s^{34} + 1.872\times10^{06}s^{33} + 1.069\times10^{09}s^{32} + 4.21\times10^{11}s^{31} \\
&+ 1.215\times10^{14}s^{30} + 2.658\times10^{16}s^{29} + 4.498\times10^{18}s^{28} + 5.938\times10^{20}s^{27} \\
&+ 6.136\times10^{22}s^{26} + 4.964\times10^{24}s^{25} + 3.144\times10^{26}s^{24} + 1.56\times10^{28}s^{23} \\
&+ 6.07\times10^{29}s^{22} + 1.854\times10^{31}s^{21} + 4.447\times10^{32}s^{20} + 8.388\times10^{33}s^{19} \\
&+ 1.244\times10^{35}s^{18} + 1.452\times10^{36}s^{17} + 1.333\times10^{37}s^{16} + 9.616\times10^{37}s^{15} \\
&+ 5.427\times10^{38}s^{14} + 2.384\times10^{39}s^{13} + 8.083\times10^{39}s^{12} + 2.093\times10^{40}s^{11} \\
&+ 4.071\times10^{40}s^{10} + 5.789\times10^{40}s^{9} + 5.759\times10^{40}s^{8} + 3.738\times10^{40}s^{7} \\
&+ 1.455\times10^{40}s^{6} + 3.393\times10^{39}s^{5} + 4.813\times10^{38}s^{4} + 4.141\times10^{37}s^{3} \\
&+ 2.08\times10^{36}s^{2} + 5.489\times10^{34}s + 5.658\times10^{32}
\end{aligned}
$$

$$
TF_{CL-MG2} = \frac{Num_{MG2}}{Den_{MG2}}
$$

$$
\begin{aligned}
Num_{MG2} = &-1.85\times10^{04}s^{32} - 3.645\times10^{07}s^{31} - 3.077\times10^{10}s^{30} - 1.476\times10^{13}s^{29} \\
&- 4.505\times10^{15}s^{28} - 9.285\times10^{17}s^{27} - 1.344\times10^{20}s^{26} - 1.403\times10^{22}s^{25} \\
&- 1.081\times10^{24}s^{24} - 6.25\times10^{25}s^{23} - 2.748\times10^{27}s^{22} - 9.273\times10^{28}s^{21} \\
&- 2.417\times10^{30}s^{20} - 4.881\times10^{31}s^{19} - 7.649\times10^{32}s^{18} - 9.295\times10^{33}s^{17} \\
&- 8.736\times10^{34}s^{16} - 6.321\times10^{35}s^{15} - 3.495\times10^{36}s^{14} - 1.462\times10^{37}s^{13} \\
&- 4.56\times10^{37}s^{12} - 1.038\times10^{38}s^{11} - 1.675\times10^{38}s^{10} - 1.841\times10^{38}s^{9} \\
&- 1.306\times10^{38}s^{8} - 5.691\times10^{37}s^{7} - 1.535\times10^{37}s^{6} - 2.603\times10^{36}s^{5} \\
&- 2.774\times10^{35}s^{4} - 1.796\times10^{34}s^{3} - 6.434\times10^{32}s^{2} - 9.765\times10^{30}s \\
&- 2.412\times10^{16}
\end{aligned}
$$

$$
\begin{aligned}
\mathrm{Den}_{MG2} = {} & s^{35} + 2013s^{34} + 1.872\times10^{06}s^{33} + 1.069\times10^{09}s^{32} + 4.21\times10^{11}s^{31} \\
& + 1.215\times10^{14}s^{30} + 2.658\times10^{16}s^{29} + 4.498\times10^{18}s^{28} + 5.938\times10^{20}s^{27} \\
& + 6.136\times10^{22}s^{26} + 4.964\times10^{24}s^{25} + 3.144\times10^{26}s^{24} + 1.56\times10^{28}s^{23} \\
& + 6.07\times10^{29}s^{22} + 1.854\times10^{31}s^{21} + 4.447\times10^{32}s^{20} + 8.388\times10^{33}s^{19} \\
& + 1.244\times10^{35}s^{18} + 1.452\times10^{36}s^{17} + 1.333\times10^{37}s^{16} + 9.616\times10^{37}s^{15} \\
& + 5.427\times10^{38}s^{14} + 2.384\times10^{39}s^{13} + 8.083\times10^{39}s^{12} + 2.093\times10^{40}s^{11} \\
& + 4.071\times10^{40}s^{10} + 5.789\times10^{40}s^{9} + 5.759\times10^{40}s^{8} + 3.738\times10^{40}s^{7} \\
& + 1.455\times10^{40}s^{6} + 3.393\times10^{39}s^{5} + 4.813\times10^{38}s^{4} + 4.141\times10^{37}s^{3} \\
& + 2.08\times10^{36}s^{2} + 5.489\times10^{34}s + 5.658\times10^{32}
\end{aligned}
$$

Appendix C

Table C1 : Benchmark functions

Function Name		Type	Formulae	Dimension (d)	Range
Sphere	F1	US	$f(x)=\sum_{i=1}^{d} x_i^{2}$	30	[-100,100]
Schwefel 2.21	F2	US	$f(x)=\max_i \{\lvert x_i\rvert, 1 \le i \le d\}$	30	[-100,100]
Schwefel 2.22	F3	UN	$f(x)=\sum_{i=1}^{d} \lvert x_i\rvert + \Pi_{i=1}^{d} \lvert x_i\rvert$	30	[-10,10]
Rosenbrock	F4	UN	$f(x)=\sum_{i=1}^{d-1}\left[100(x_{i+1}-x_i^2)^2+(x_i-1)^2\right]$	30	[-30,30]
Rastrigin	F5	MS	$f(x)=10d+\sum_{i=1}^{d}\left[x_i^d-10\cos(2\pi x_i)\right]$	30	[-5.12,5.12]
Ackley	F6	MN	$f(x)=-20\exp\left(-0.2\sqrt{\frac{1}{d}\sum_{i=1}^{d} x_i^2}\right) -\exp\left(\frac{1}{d}\sum_{i=1}^{d}\cos 2\pi x_i\right)+20+e$	30	[-32,32]

Table C2 : Benchmark functions

Function Name		Type	Formulae	Dimension (d)	Range
Sphere	F1	US	$f(x)=\sum_{i=1}^{d} x_i^{2}$	30	[-100,100]
Schwefel 2.22	F2	UN	$f(x)=\sum_{i=1}^{d} \lvert x_i\rvert + \Pi_{i=1}^{d} \lvert x_i\rvert$	30	[-10,10]
Schwefel 2.26	F8	MS	$f(x)=-\sum_{i=1}^{d}\left(x_i \sin\left(\sqrt{\lvert x_i\rvert}\right)\right)$	30	[-500,500]
Ackley	F10	MN	$f(x)=-20\exp\left(-0.2\sqrt{\frac{1}{d}\sum_{i=1}^{d} x_i^2}\right) -\exp\left(\frac{1}{d}\sum_{i=1}^{d}\cos 2\pi x_i\right)+20+e$	30	[-32,32]
Penalized	F12	MN	$f(x)=0.1\sin^2(3\pi x_i) +0.1\sum_{i=1}^{d}(x_i-1)^2\left[1+\sin^2(3\pi x_i+1)\right] +0.1(x_d-1)^2\left[1+\sin^2(3\pi x_d)\right] +\sum_{i=1}^{d}U(x_i,5,100,4)$	30	[-50,50]

LIST OF PUBLICATIONS

Journal Articles

Fadheel, B. A., Wahab, N. I. A., Manoharan, P., Mahdi, A. J., Radzi, M. A. B. M., Soh, A. B. C., Ridha, H. M., Alsoud, A. R., Veerasamy, V., Irudayaraj, A. X. R., & Derebew, B. (2024). A Hybrid Sparrow Search Optimized Fractional Virtual Inertia Control for Frequency Regulation of Multi-Microgrid System. IEEE Access, 12(April), 1–1. https://doi.org/10.1109/ACCESS.2024.3376468.

Fadheel, B. A., Wahab, N. I. A., Mahdi, A. J., Radzi, M. A. B. M., Soh, A. B. C., Ridha, H. M., & Veerasamy, V. (2024). Optimal Tuning of Virtual Inertia Control for Frequency Regulation of Microgrid. IEEE Canadian Journal of Electrical and Computer Engineering, 47(2), 60–69. https://doi.org/10.1109/ICJECE.2024.3351152.

Fadheel, B. A., Wahab, N. I. A., Mahdi, A. J., Premkumar, M., Radzi, M. A. B. M., Soh, A. B. C., Veerasamy, V., & Irudayaraj, A. X. R. (2023). A Hybrid Grey Wolf Assisted-Sparrow Search Algorithm for Frequency Control of RE Integrated System. Energies, 16(3), 1177. https://doi.org/10.3390/en16031177.

Proceedings /Conference

Fadheel, B. A., Wahab, N. I. A., Radzi, M. A. B. M., Soh, A. B. C., & Irudayaraj, A. X. R. (2024). An SSA algorithm for LFC of two-area power systems integrated with renewable energy sources in a deregulated environment. AIP Conference Proceedings, 040013. https://doi.org/10.1063/5.0204669.

Fadheel, B. A., Izzri Abdul Wahab, N., Mahdi, A. J., Amran Bin Mohd Radzi, M., & Che Soh, A. B. (2021). Review of the Virtual Inertia Strategies from Intermittent Renewable Energy Resources on the Power System. 2021 12th International Renewable Energy Congress, IREC 2021, Irec. https://doi.org/10.1109/IREC52758.2021.9624801.